Application of Strain Hardening Cementitious Composites for retrofitting unreinforced masonry

K. Kuipers

TU Delft

Application of Strain Hardening Cementitious Composites for retrofitting unreinforced masonry

by

K. Kuipers

to obtain the degree of Master of Science
at the Delft University of Technology,
to be defended publicly on Wednesday January 15, 2020 at 16:00.

Student number:	4622243	
Project duration:	February 11, 2019 – January 15, 2020	
Thesis committee:	Dr. M. Lukoviç,	TU Delft (Daily supervisor)
	Dr. R. Esposito,	TU Delft (Daily supervisor)
	Dr. ir. C.B.M. Blom,	TU Delft

This thesis is confidential and cannot be made public until January 15, 2020.

An electronic version of this thesis is available at `http://repository.tudelft.nl/`.

TU Delft

Summary

Starting from the late eighties induced seismic activity is present in the Northern part of the Netherlands. Cause of these earthquakes is the extraction of natural gas. In this region, most of the building stock comprises out of unreinforced masonry (URM) buildings. Multiple experimental campaigns are performed since 2014 to investigate the structural integrity of these type of structures. Both static and dynamic, full-scale and small-scale, experiments are executed to identify both in-plane and out-of-plane failure mechanisms. Strengthening, or retrofitting, of these already existing structures, is of interest and different researchers propose multiple techniques. From the literature, it is found that the application of strain hardening cementitious composites (SHCC) results in the required improved structural performance of the retrofitted masonry. The SHCC material is characterised by high ductility in the range of 3-7%, tight crack widths of around 60 μm and a relatively low fibre content equal to 2% (maximum by volume). In this experimental campaign small-scale, both in-plane and out-of-plane (i.e. shear strength and flexural strength, respectively), experiments are performed on masonry samples retrofitted using a single-sided applied SHCC overlay. Different thicknesses of this overlay, masonry surface preparations, and overlay curing conditions are considered. With the help of these experiments the material properties of retrofitted masonry are investigated.

From the initial shear strength experiments, it is concluded that the retrofitting approach did not work as intended. Results of all the different specimen examined shows similar capacities to the non-retrofitted masonry triplets. With the help of digital image correlation, it is shown that for all of the retrofitted specimen, the overlay material is not activated during the tests. Additional experiments and numerical simulations are performed to investigate the several parameters possibly influencing these experiments. The bond strength of the interface between the SHCC and the masonry substrate is determined to be too low. This is one of the main factors resulting in the absence of cracks in the retrofitting overlay. Additionally, the high cracking strength of the SHCC mixture considered, and the applied pre-compression, have influenced the cracking behaviour of the retrofitting overlay.

Besides the shear strength of the retrofitted masonry material also the flexural strength is investigated with multiple out-of-plane four-point bending tests. Retrofitted masonry beams are used for these experiments. The plain masonry beams are not able to carry their self-weight, therefore all of the additional capacity is accommodated to the applied overlay. The experimental results are governed by shear failure. For eight out of ten specimens debonding of the masonry units is prevalent. Two of the retrofitted masonry beams showed flexural failure. A thicker overlay will result in higher flexural strength. Again, the bond strength between the overlay and the masonry substrate seems to be governing. No numerical analyses are performed to analyse these experiments in more detail.

From this research, it is concluded that a single-sided SHCC overlay can be a very attractive method for retrofitting unreinforced masonry. However, both the interfacial bond strength and the material properties of the SHCC material must be taken into account. The bond strength must be sufficiently high, and the cracking strength of the overlay material sufficiently low, for the overlay to be activated. With the help of numerical simplified micro-models, the requirements of both parameters can be estimated.

Acknowledgements

Choosing a research topic to finalize my study career was difficult. In the beginning, I felt limited because of my selected track, Concrete Structures. However, the enthusiasm of Mladena and the possibility to work on an earthquake-related subject was the decisive factor.

I am very grateful for a lot of people. First, I want to thank Mladena, the chair of my committee. Your positive, but also professional and precise, work ethic helped me a lot. Our, almost daily, meetings were beneficial for the quality of this report. Rita, thank you for your supervision and knowledge regarding the used experimental setups, the masonry material, and the professional writing skills required for the final report. Finally, I would like to express my gratitude to Kees. Your critical view of my report was essential.

Besides the committee members, I want to thank several people from the Stevin-2 Laboratory. Ton, Maiko, Albert, and all the other employees that helped me during my experimental campaign. Without you, my tight schedule was not possible.

Furthermore, I want to thank all friends who motivated me during these last couple of months. Special thanks to Tim and Marc for the daily coffee-breaks. Also, I cannot forget to mention Shozab, who helped me during my last week with numerical modelling.

This acknowledgement is not complete before I express my gratitude to my parents. I cannot thank you enough for all the support you have given me during my study in Delft. Last, but certainly not least, I want to thank my girlfriend, Lotte. Your positive attitude and loving care during these last couple of months were crucial for the success of this thesis.

K. Kuipers
Delft, 13 December 2019

Contents

Abbreviations and Symbols

Abbreviations

SHCC	Strain Hardening Cementitious Composites
URM	Unreinforced Masonry
PVA	Polyvinyl Alcohol
LVDT	Lineair Variable Differential Transformer
DIC	Digital Image Correlation
C.o.V.	Coefficient of Variation
FE	Finite Elements
FEA	Finite Element Analysis
N.A.	Neutral Axis
TU Delft	Delft University of Technology

Symbols

c_0	Cohesion	N/mm^2
f_{v0}	Initial shear strength	N/mm^2
$f_{v0,res}$	Residual shear strength	N/mm^2
Φ	Initial friction angle coefficient	
Φ_{res}	Residual friction angle coefficient	
ψ	Dilatancy angle	
G_f^{II}	Mode-II fracture energy	N/mm

1 Introduction

In this chapter, a general introduction into the topic of interest is provided to create a stable foundation for the reader for the subsequent chapters. Current difficulties, with respect to the investigation in the structural performance of unreinforced masonry (URM) structures under seismic loading, are mentioned. Additionally, the current status of research into this particular topic (i.e. retrofitting of URM structures to increase their structural performance under seismic activity) is summarized. Hereafter, both the motivation and scope of this research are provided.

1.1. Problem statement

Since the year of 1963 the Nederlandse Aardolie Maatschappij (NAM) is extracting natural gas from the gas-field situated in the Northern province Groningen in the Netherlands. In the early days no negative influence, e.g. induced earthquakes, were present. The first major earthquake (3.0 on the Richter scale) occured in 1986. Since this year more than 1000 earthquakes are measured, see Figure (1.1) below. In this figure it is shown that the bulk of the seismic events have a magnitude smaller than 2.0 on the scale of Richter. These induced earthquakes are related to the reservoir compaction resulting from the gas extraction. For more in depth information related to the measuring methods used, the geology of the specific area, and the seismicity the reader is referred to [34].

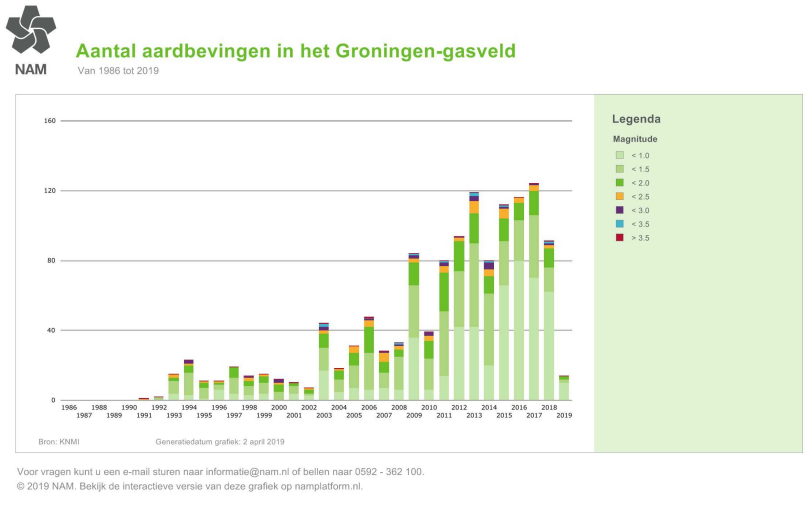

Figure 1.1: Amount of earthquakes near gasfield in Groningen, source: NAM.

Due to this inceased seismic activity, and the resulting damages observed to buildings and structures in the surroundings, concerns are raised with respect to the resistance of the structures subjected to these events. This research is focussed on the unreinforced masonry (URM) structures, e.g. residential housing. These type

of structures are of particular interest due to their very brittle behaviour, as caused by the material properties of the unreinforced masonry. The URM buildings of interest are built in different time periods, before or after the second world war (WW2), which influences both the building materials and construction methods used. Research performed at the Delft Universtity of Technology (TU Delft) characterized the differences in building materials and construction methods corresponding to these different periods in time [26].

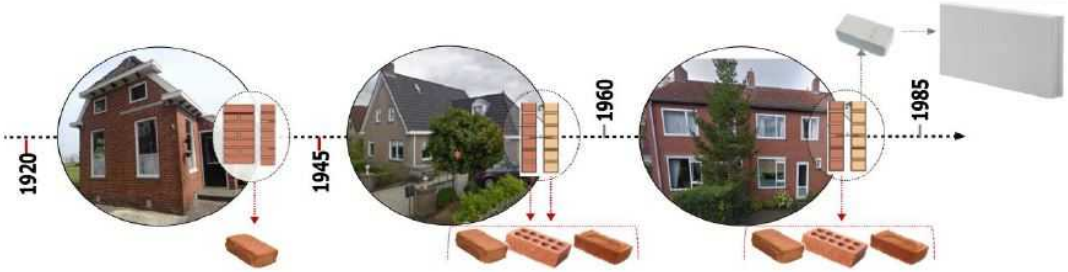

Figure 1.2: Different building typologies and construction materials [26].

From the figure above it is concluded the buildings, as built before WW2, predominantly use single or double whyte solid clay bricks for the internal and perimeter loadbearing walls. After WW2, the use of calcium silicate (CS) masonry for the inner leaf and clay brick masonry for the outer leaf, is used more often. This inner and outer leaf are connected together via steel ties.

Nationaal Coordinator Groningen (NCG), a Dutch govenmental agency, is leading the investigation in possible strengthening methods for these structures. At the moment some of these URM buildings are being retrofitted by means of strengthening the floors, walls, wall-floor connections, and/or the foundation. In Figure (1.3) different retrofitting approaches are presented. These strengthening methods are preventive and primarily focussed on eliminating the global collapse of the specific structure. Thus, reducing the probability on severe damages and possible deaths. However, up to now, no quantitative insight is known regarding the actual structural influence and the possible reduction in risk of these applied strengthening methods (BuildinG Kennisagenda). Also, the methods shown in Figure (1.3) can be very time consuming (especially strengthening of the foundation).

(a) URM residential housing strengthened by means of timber struts. Source: Trouw.

(b) URM residential housing strengthened by means of the QuakeShield. Photo: Archief Huisman Media.

(c) URM monumental building strengthened by means of a 'base isolation'. Source: Dagblad van het Noorden.

Figure 1.3: Examples strengthening methods URM residential housing in Groningen.

New retrofitting methods for these URM structures are widely being researched, some of which are discussed in the following literature review. For a retrofitting method to be succesfull multiple structural influences (e.g. increase in ductility) should be taken into account, however, the speed and ease of application must also be considered.

Different researchers, worldwide, are investigating possible retrofitting methods for URM structures. For example, at the TU Delft and the European Centre for Training and Research in Earthquake Engineering (EU-Centre) extensive multiscale experimental campaigns are conducted to investigate the behaviour of URM at the material, component (e.g. walls), and even structural level (e.g. full scale two-storey residential buildings) [17, 26]. Both cyclic quasi-static and full dynamical experiments are performed to characterize the structural behaviour. It is concluded that different components of the residential buildings examined are of interest in the retrofitting approach (e.g. URM walls, timber diaphragms, wall-floor and wall-wall connections). This research is soley focussed on retrofitting the unreinforced masonry material.

Multiple retrofitting methods for the URM material are investigated, see for example [4, 8, 11, 20, 31]. In this study retrofitting of the URM, by means of a Strain Hardening Cementitious Composite (SHCC) overlay, is investigated. With the help of an extensive literature study different retrofitting methods are examined. However, when compared to the SHCC overlay method, these methods have some disadvantages. For example, the use of Fibre Reinforced Polymers (FRP) is widely recognised, however, this material is limited by the properties of the epoxy matrix used to embed and bond the fibers [4]. Another option is Textile Reinforced Concrete (TRC), also known as Textile Reinforced Mortars (TRM). This retrofitting approach consists out of several layers of mortar material with textile mats in between, acting as reinforcement. Other methods, like shotcrete, can be considered as well. A sprayable concrete mixture is sprayed on top of the base material. Steel reinforcement is used to ensure sufficient tensile capacity. However, as reported in literature, relatively thick reinforced shotcrete overlays are required to generate a succesfull retrofitting [13]. Using large amounts of material will influence the mass of the structure significantly which, in turn, directly influences the dynamical behaviour of the total structure and the requirements of the foundation. The different retrofitting methods are discussed in more detail in the literature review, see Chapter (2).

The use of SHCC for strengthening URM structures is being researched by different researchers and shows great potential [6, 8, 9, 14]. Strain Hardening Cementitious Composite (SHCC), also referred to as Engineered Cementitious Composite (ECC), is a type of fiber reinforced concrete systematically engineered to achieve high ductility under both tensile and shear loading conditions. This high ductility makes it an interesting material for retrofitting brittle materials (e.g. masonry and 'ordinary' reinforced concrete). A relatively low fiber content of 2% and a ductility in the range of 3-7% is characteristic for this type of material. During loading this material shows very small crack widths (up to 100 μm) which will increase the durability of the retrofitted material and give rise to the potential of self healing of the SHCC. Due to this diffuse crack pattern high amount of energy can be absorbed by the material, which is highly interesting for seismic loading conditions. For the retrofitting of masonry structures different methods of applications are considered, e.g. casting and spraying. For the practical implementation of this retrofitting method a sprayable SHCC mixture is optimal. It should be noted that in this graduation project the main objective is the deteremination of the material performance of the SHCC overlay with respect to the unreinforced masonry. A sprayable SHCC mixture is not considered, however, from literature it is concluded this type of mixture can be obtained via adjusting the mixture composition [37].

1.2. Research Strategy

A single-sided overlay method is determined to be most interesting for this research due to its practical implementation, since only the outside of a masonry wall is accessible. Via small-scale experiments (e.g. in-plane and out-of-plane tests, i.e. shear triplet tests and four-point bending tests, respectively) the material properties of the retrofitted masonry is investigated. Different parameters (e.g. overlay thickness) are considered to investigate their possible influence in the material behaviour of the retrofitted solid clay masonry. In this research only solid clay masonry units are investigated. General purpose mortar is used for all the specimen. Both of which are representative of URM housing built with double (or single) whyte masonry walls.

By means of well-designed displacement-controlled testing set-ups, the full non-linear shear-sliding behaviour of the masonry units and the bending behaviour in one orthogonal direction are determined. Only

destructive tests will be examined.

The shear strength properties of the unreinforced masonry are determined by performing shear tests on triplets conform EN 1052-3:2002. Both the initial shear parameters and the residual shear strength are determined based on the Coulomb friction criterion. The experiments on the non-retrofitted masonry are conducted by another researcher at the TU Delft. However, these experiments are performed in the same period, using the same materials. By using the same experimental setup the shear strength of the retrofitted triplets are investigated. Finally, the experimental results of the URM and the retrofitted masonry are compared. The masonry (URM and retrofitted) bending properties are studied by performing four-point out-of-plane bending tests. Masonry beams specimen consisting out of seven masonry units and six mortar joints, built with a stacked bond pattern, are examined. The designed experimental setup is derived from the literature review. Additionally, a Digital Image Correlation (DIC) measurement system is used to investigate the failure modes observed in more detail. The experimental setups are described in more detail in Chapter (3).

Different parameters are investigated in the experimental campaign. The possible influence of the thickness of the SHCC overlay is examined by two different thicknesses (i.e. 10 mm and 30 mm). Both full bond and partial debonding of the overlay material is researched to examine the consequences in crack propagation in the overlay. Finally, differences in performance due to sealed and non-sealed curing conditions of the casted overlay material are investigated. Additionally, both the free and restrained shrinkage of the SHCC mixture are measured.

With the help of numerical analyses, the failure mechanisms of the shear strength tests are examined further. A simplified micro-model is used to model the retrofitted triplet specimen. The numerical analyses are presented in Chapter (5).

1.3. Goal of Research

By means of small-scale experiments the material properties of the retrofitted URM is investigated. Both in-plane and out-of-plane failure modes are examined, i.e. shear-sliding and out-of-plane bending. With the help of this research it might be concluded that retrofitting residential housing, built with loadbearing solid clay masonry walls, is of interest.

"What is the influence of a single-sided SHCC overlay on the material performance of small scale URM samples?"

By means of the following steps the mentioned research question is answered:

- A literature study is performed. Focus of this study is the current status of research with respect to the retrofitting of unreinforced masonry structures. Multiple retrofitting methods (currently used and proposed) are discussed. Retrofitting URM by means of SHCC is investigated in great detail. The material characteristics of both the URM and SHCC are summarized.
- The material behaviour of (non-)retrofitted unreinforced masonry is examined via an experimental campaign (e.g. in-plane and out-of-plane tests, i.e. shear triplet tests and four-point bending tests, respectively). Multiple parameters are investigated and their influence on the experimental results are reported. A Digital Image Correlation technique is employed to examine the failure modes (and crack propagation) in greater detail;
- Numerical simulations are used to investigate the failure modes of the retrofitted masonry triplet specimen in more depth. Only the shear strength experiments are considered; and
- Finally, analysis and discussion of both the experimental and numerical results are combined to provide a qualitative understanding with respect to the influence of the retrofitting approach considered.

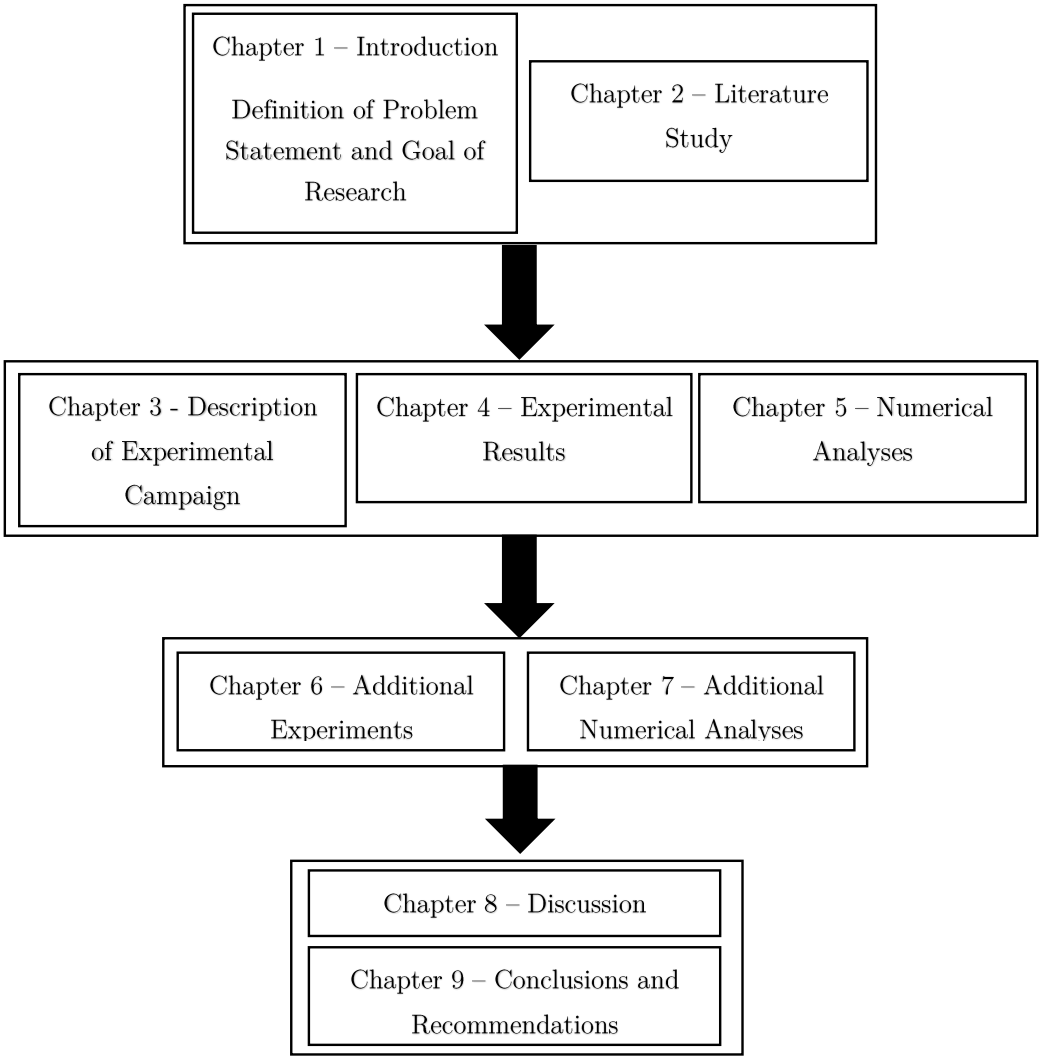

Figure 1.4: Goal of Research

2

Literature Review

This literature study is conducted to obtain a better understanding of the current knowledge concerning the retrofitting of unreinforced masonry structures. The following subjects are highlighted.

- Problem definition: why apply seismic retrofitting?;
- Material (and Structural) behaviour unreinforced masonry (URM);
- Common retrofitting measures;
- Material behaviour Strain Hardening Cementitious Composites (SHCC);
- Experimental campaigns focussed on retrofitting URM by means of SHCC;
  - Type of experiments performed and corresponding experimental results.
- Numerical modelling approaches for URM specimen at the material level.

In this chapter, the results of the literature review are summarized. The different mentioned subjects above are provided in individual sections. Firstly, the problem definition is provided to give a sound explanation about why this research is required. Hereafter, the material properties of unreinforced masonry are summarized, followed by the structural behaviour of this material. Different retrofitting approaches, as reported in the literature, are discussed. The material properties of the SHCC are discussed in detail. Known research focussed on retrofitting URM using a SHCC overlay is summarized, and the experimental results are analysed. Finally, the numerical modelling approach for micro-scale modelling of the (retrofitted) masonry specimen is presented.

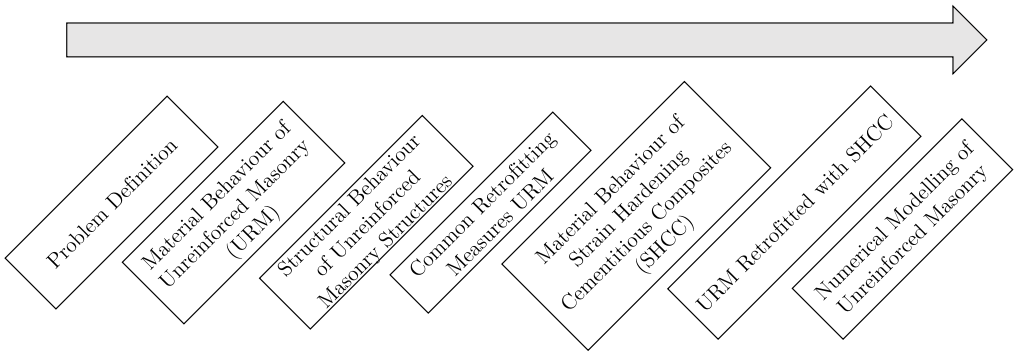

2.1. Problem Definition: why apply seismic retrofitting?

The seismic assessment of unreinforced masonry (URM) structures is a worldwide investigated subject. In recent years it has become a popular topic in the Netherlands as well, due to induced seismic activity in the Northern province of Groningen, resulting from gas drilling in this area. Seismic loading conditions are not taken into account when designing these buildings. In recent years many research is performed to characterize the structural integrity of these Dutch URM structures [19, 26]. Since 2014 an extensive multiscale testing program is performed at Delft University of Technology (TU Delft). Part of this testing program is developed at the European Centre for Training and Research in Earthquake Engineering (EUCentre). Both research programs are designed to characterize the behaviour of URM buildings at multiple levels of interest, i.e. material up to structural level.

Unreinforced masonry structures, as built in the Northern part of the Netherlands, mostly consist out of load-bearing URM walls which support both the roof and the floors. Different wall layouts are possible, depending on the era in which the structure is built. Retrofitting of different structural components of these houses is being investigated [26]. For example, retrofitting of the floor system is of interest to ensure the structural box behaviour of the total system. This influences, and might avoid, local out-of-plane failure mechanisms to occur in the unreinforced masonry loadbearing walls.

This study is focussed on retrofitting single wythe solid clay masonry material. Retrofitting of these loadbearing walls influences both the global in-plane and local out-of-plane failure mechanisms observed in URM houses. With the help of small-scale experiments, the material behaviour of retrofitted clay masonry specimen is investigated.

2.2. Material Behaviour of Unreinforced Masonry (URM)

Masonry is a composite material consisting out of unit bricks with mortar joints in between which has a quasi-brittle behaviour. Characterization of the material properties of unreinforced masonry can be done at different levels. In, for example, [33], very detailed descriptions are present concerning the determination of the material properties of URM, at the material level. These material properties are determined via the execution of experiments at the same (small-scale) level. The output of these experiments is required for further numerical analyses. In Figure (2.1) an overview is provided of a masonry sample to clarify the different terms used in this report (e.g. bed joint).

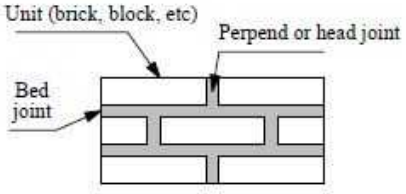

Figure 2.1: Terminology masonry [23].

2.2.1. Tensile Behaviour

The post-peak behaviour characterizes the behaviour of units, mortar and the unit-mortar interface under tension, strain softening, and mode I fracture energy [23]. In Figure (2.2) the material behaviour of masonry (or any other quasi-brittle material) under uniaxial loading and compression is shown. The fracture energy is defined as the amount of energy per unit of area required to create a crack in which no tensile stresses can be transferred anymore. The behaviour prior to the maximum load can reasonably be approached with a linear behaviour. The post-peak behaviour can be described in different manners (e.g. linear, exponential and nonlinear softening curves), see [10]. In [33] an approach, which has been proven to be successful for plain concrete, is followed. Finite element programs, like DIANA, offers multiple softening functions to simulate the post-peak behaviour of a material. More information, related to these numerical models, is provided in section 2.7.

The individual components need to be tested to establish the behaviour of masonry components. Testing is possible for units, but not for mortar joints because their properties are influenced considerably by the interaction between the mortar and unit during hardening. Due to this fact, the characteristics of this mortar and mortar-unit interface should be derived from the behaviour of a masonry specimen (i.e. a composition consisting out of units and mortar joints).

Two different methods for obtaining the tensile characteristics of masonry (i.e. direct tensile tests and flexural tests) are described in the literature chapter. It is mentioned that the flexural bond strength is 1.2 up to 1.5 times greater than the average tensile bond strength. Generally, a factor of 1.5 is assumed. This factor arises when the flexural bond strength is derived by dividing the ultimate bending moment by the elastic section modulus of the failing cross-section. However, this way of calculation assumes a linear stress distribution at failure, which is an assumption concerning the actual non-linear stress distribution, shown in Figure (2.3). The differences between these two stress distributions explain the differences between the tensile and flexural strength. Notice that the factor 1.5, which is generally used, must be seen as a crude approximation.

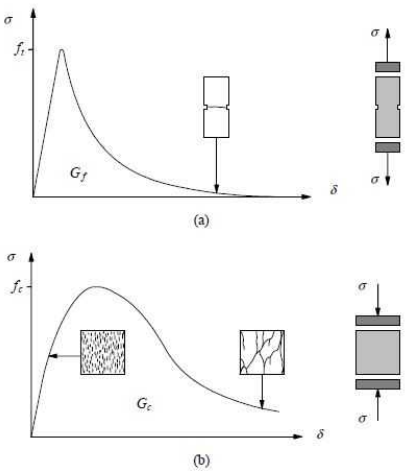

Figure 2.2: Typical behaviour of quasi-brittle materials under uniaxial loading and defintion of fracture energy: (a) tensile loading (f_t denotes the tensile strength); (b) compressive loading (f_c denotes the compressive strength) [23].

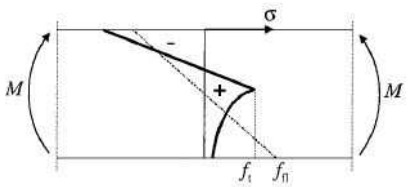

Figure 2.3: Non-linear stress distribution (solid line) due to bending and the fictitious elastic distribution (dashed line) at the maximum load level [33].

2.2.2. Shear Behaviour

In [33] the behaviour of masonry under combined shear and normal-tension or compression is described. Through experiments, these characteristics can be obtained. The reference mentioned so-called couplets (two stacked units with mortar joint in between) that were tested in a deformation-controlled manner. Most tests are carried out under constant normal stress and increasing shear deformation, as measured over the joint. The following properties are derived via these tests: shear strength f_{v0}, mode II fracture energy G_f^{II}, cohesion softening, and dilatancy ψ. See Figure (2.4) for the typical behaviour of masonry under shear.

The shear strength equals the shear stresses in the mortar-unit interface at peak resistance. The total area under the curve, denoted in the figure by G_f^{II}, equals the mode-II fracture energy. A more detailed description of the dilatancy is provided hereafter.

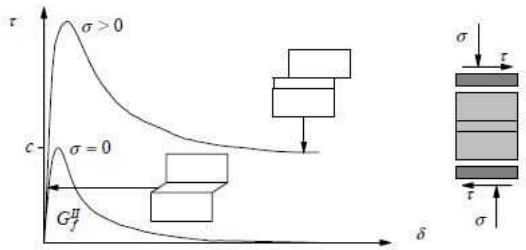

Figure 2.4: Behaviour of masonry under shear and definition of mode II fracture energy G_f^{II} (c denotes the cohesion) [23].

It should be noted that other failure mechanisms than shear failure of the joint and joint-unit interface can govern the shear failure of masonry. Four different failure mechanisms, as a function of of the normal stress, are mentioned in [33], i.e. bond failure of the interface, the masonry compressive strength, and the tensile strength of both bond and the units. Five different failure modes are mentioned in [23] and are depicted in Figure (2.5).

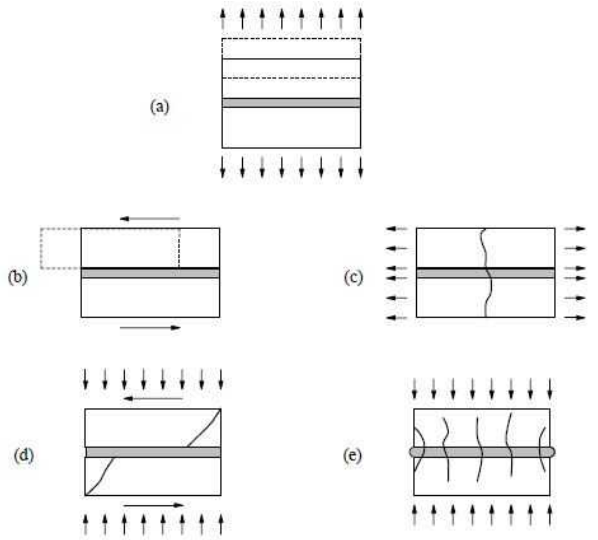

Figure 2.5: Masonry failure mechanisms: (a) joint tensile cracking; (b) joint slipping; (c) unit direct tensile cracking; (d) unit diagonal tensile cracking; (e) masonry crushing [23].

The bond failure of the interface is analysed as a function of the normal stress based on Coulomb's friction failure criterion.

$$\tau_u = c_o - \tan(\varphi) \cdot \sigma \tag{2.1}$$

Where:

τ_u : shear strength of the test;
c_o : cohesion or shear bond strength, i.e. the shear strength at $\sigma = 0$ (f_{v0} conform EN 1052-3:2002);
φ : angle of interal friction.

Comparing Figure (2.2.a) with Figure (2.4) great similarity is found. However, the tail of the latter shown figure does not fall back to zero but becomes stable at a certain shear stress level (τ_{fr}). This specific level corresponds to the dry friction level between the two, non-bonded, surfaces of the masonry unit and the mortar joint. The descending branch, between τ_u and τ_{fr}, is referred to as the so-called cohesion softening [33]. Figure (2.7) is taken from this reference and gives additional information related to the parameters corresponding to the shear behaviour of masonry.

An essential phenomenon in the shear test is the occurrence of a normal displacement u perpendicular to the imposed shear displacement v that occurs beyond the peak load. This phenomenon is referred to as dilatancy and occurs because the crack surface is not perfectly smooth, so shearing of this face introduces an uplift. The tangent of the angle ($\tan(\psi)$) is defined as the ratio between the plastic normal and shear displacements. The maximum uplift, however, is limited. In literature, the importance of dilatancy in numerical models is mentioned. From [33] it is known that a constant value for the dilatancy angle higher than zero leads to infinite shear strength of a joint when the masonry specimen is perfectly constrained in normal direction, see Figure (2.6). Thus, a correct formulation of the dilatancy is required to obtain realistic results. In [35] a formulation for numerical simulation of the dilatancy is described, including both the confining normal stress and the plastic shear displacement.

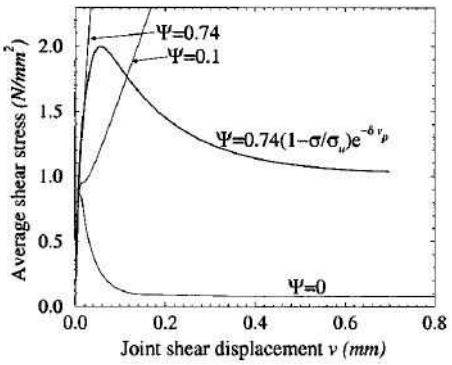

Figure 2.6: Modeling results of different dilatancy angles [35].

In [33] several parameters are determined from the experiments, see Figure (2.7). The initial shear stiffness G_0 requires the Poissons' ratio. This value is derived from compressional tests. The shear strength of the specimen is derived by the division of the maximum measured load by the cross-sectional area of the mortar-unit interface. Based on the Coulomb criterium, the cohesion is determined via linear regression of all the experimental results, i.e. the shear strength plotted for each level of pre-compression. In this reference the dry friction coefficient μ is determined by dividing the mean shear stress with the mean normal stress, corresponding to the last twenty measurement points in the horizontal part of the tail, see Figure (2.7). The dilatancy angle is defined as:

$$\Delta \tan(\psi) = \frac{\Delta u_{pl}}{\Delta v_{pl}} \tag{2.2}$$

Where:

Δu_{pl}: incremental plastic deformation in normal direction;
Δv_{pl}: incremental plastic deformation in shear direction.

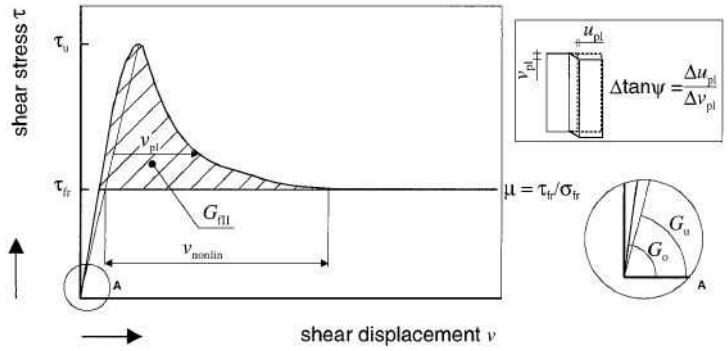

Figure 2.7: Schematic diagram of deformation (v) controlled shear test with shear test quantities analysed [33]

For the specimen loaded by both shear and compression, the following important phenomena are derived:

- The shear strength f_{v0} and dry friction level μ are dependent on the compression level applied; and
- The descending branch after the peak load becomes less steep with increasing pre-compression. Consequently, the fracture energy also increases with the level of pre-compression.

These conclusions are based on the following figure.

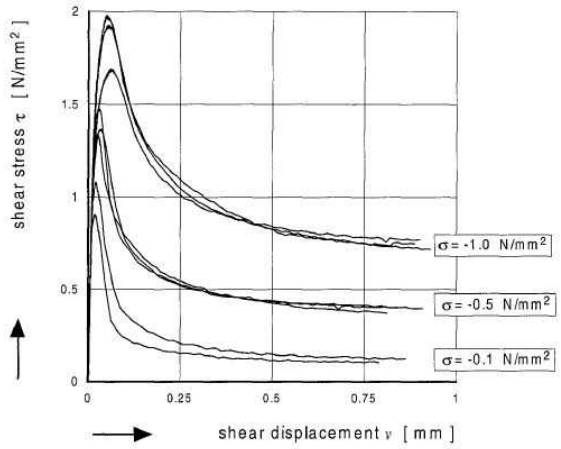

Figure 2.8: Example of $\tau - v$ diagrams of a test series under shear and compression [33].

2.3. Structural Behaviour of Unreinforced Masonry Structures

Researchers performed extensive research to investigate both the material and the structural behaviour of URM structures. The following references also describe experiments related to masonry components, or even full-scale housing [18, 19, 26]. All of these tests performed are related to Dutch buildings.

The experimental campaign, performed at the testing laboratory Stevin II at the Delft University of Technology in 2015, is initiated by the induced earthquakes in the province of Groningen and provided detailed information regarding the material behaviour on both the material and the structural level. Part of this campaign at TU Delft was the characterisation of the material properties of Dutch unreinforced masonry, aimed at developing a guideline and providing a database of material properties related to masonry structures which can be used for numerical models as well as analytical design methods. At the component level, both in-plane and out-of-plane tests are conducted on URM walls. Several influence parameters (e.g. material, geometry, and boundary conditions) are examined. Additionally, two quasi-static cyclic tests on full-scale two-storey buildings are performed. These two-storey buildings are corresponding to terraced houses built with calcium silicate masonry bricks or calcium silicate elements. This test is specifically designed to investigate the global in-plane behaviour of these type of structures.

In [15] the results of the experimental campaign, conducted at Delft University of Technology, are discussed. The results of the calcium silicate (CS) brick masonry assemblage and the calcium silicate element masonry assemblage are compared. In conclusion, the CS brick masonry assemblage shows a higher displacement capacity, while the CS element masonry assemblage shows a higher maximum base shear force. In both cases, the in-plane damage of the facade piers at the ground level governs the failure mechanism, see Figure (2.9). However, this was expected beforehand. Also, for both cases, the diagonal/vertical cracking occurred first in the head and bed joints. In the case of the CS element masonry assemblage, however, larger out-of-plane deformations, up to failure of the piers, occurred. This failure is caused by the large size of the masonry units. The transversal walls deformed out-of-plane accommodates the in-plane deformation of the piers, which indicates the effectiveness of the wall-to-wall connection. At peak load, the damages in the piers of the CS element masonry assemblage promoted local deformation at the end of the transversal walls.

Figure 2.9: Main damage in wide piers at ground floor: (a) CS brick masonry assemblage; (b) CS element masonry assemblage [15].

As mentioned earlier, not only in the Netherlands, experiments are performed to investigate the material and/or structural behaviour of URM. For example, in Italy, at the European Centre for Training and Research in Earthquake Engineering (EUCentre), full-scale shake table tests are performed [30]. These dynamical tests give a good understanding of the structural behaviour of the URM structures under dynamical conditions, which are representative of the induced events in the northern part of the Netherlands.

In this reference, the experiments conducted on a two-storey full-scale URM building performed at the EUCentre are discussed. The structure tested is constructed with cavity walls and without any particular seismic design or detailing. The cavity walls consisted of an inner loadbearing and an outer leaf, the latter having aesthetic and weather-protection functions. The load-bearing inner leaf is composed out of CS bricks. Each of the two storeys has a reinforced concrete floor, and the roof consisted out of a pitched timber structure.

Two distinct ground motions, corresponding with the induced events in Groningen, are used for a sequence of incremental dynamical tests. The intensity of the two ground motions (EQ1 and EQ2) is gradually increased. These two ground motions relate to two main scenarios with a return period of 50 and 500 years, respectively.

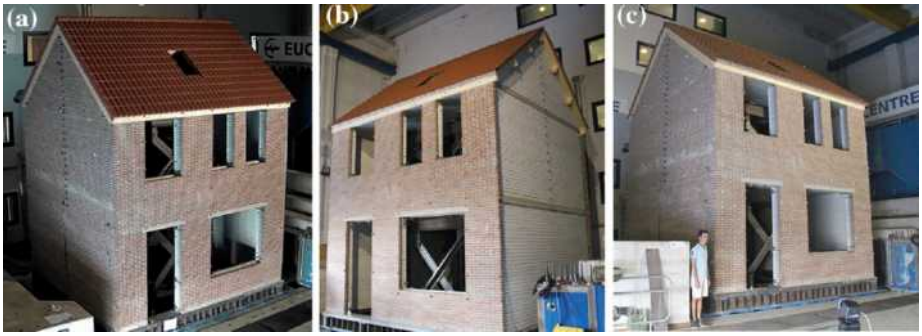

Figure 2.10: Three different views of full-scale two-storey URM building [18].

For the first ground motion (EQ1) at the different load levels (25% up to 150%), no noticeable damages are observed. The first slight damages became visible after testing with EQ2 at a load level of 100%. After the test with the second ground motion at an intensity of 150%, significant cracks were observed in the CS masonry of the second storey. A horizontal crack was observed in one of the longitudinal walls in a wide pier at the second storey level, which indicates the so-called "bending-rocking" response of this structural component. Up to this intensity level (150%), no damage in the two transverse walls was detected. At the highest intensity level (EQ2-200%), a substantial level of damage was observed. Global response of the structure is triggered, resulting in the formation of new cracks or the elongation of the pre-existing ones. Under the openings, corresponding to windows, at the second storey level, in the longitudinal walls, wide diagonal cracks are observed, causing for sliding of the mortar joints and de-cohesion of the blocks. Damages in the transversal walls consisted of the formation of 45° stair-stepped diagonal cracks, which could be associated with the activation of an out-of-plane two-way bending mechanism. This specific mechanism is discussed in detail in [28]. The final failure patterns of the two-storey cavity wall building are shown below. For a more detailed description of these failure patterns, one is referred to article [18].

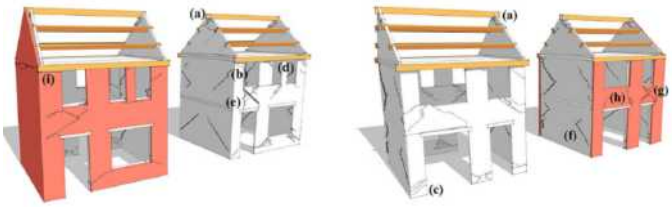

Figure 2.11: Final failure patterns observed. Red material is outer masonry leaf (not loadbearing) and white material is CS bricks (loadbearing) [18].

From the literature, it is expected that both in-plane and out-of-plane failure modes under seismic conditions. However, globally, in-plane failure is governing. Out-of-plane failure modes, i.e. local failure of the transversal walls, is depending on multiple factors, e.g. stiffness of the floor system. The structure profoundly depends on the stiffness of this structural element. Sufficient amount of stiffness is required to ensure the box-type behaviour of the entire structure. Not only the diaphragmic behaviour of the floor is governing, but also the wall-floor connection is of interest. Experiments on the material level do not provide direct results for the additional seismic capacity of structural elements.

2.4. Common Retrofitting Measures

As mentioned, this thesis is solely focussed on the retrofitting of URM elements. Strengthening methods for floors, roofs, and connections are not discussed. Different materials for retrofitting URM are researched (e.g.

ferrocement, shotcrete, grout/epoxy injection, fibre reinforced polymers (FRPs), ordinary fibre reinforced concretes (FRC), textile reinforced concrete (TRC), and strain hardening cementitious composites (SHCC)). Below, some of the different retrofitting approaches are discussed shortly to create a broad overview. The most common mentioned problems for these retrofitting approaches are: time-consumption of application, reduced available space, disturbance to occupancy, affects to the aesthetics of the existing wall, and also the added mass of the measure, directly affecting the dynamical behaviour of the structure.

Both in-plane and out-of-plane failure modes are investigated for some of the retrofitting measures. However, most of the literature is focussed on the global in-plane failure modes of the retrofitted URM.

2.4.1. Fibre Reinforced Plastic (FRP)

Using fibre reinforced plastics (FRP) for retrofitting URM structures is investigated by multiple researchers, see for example [12, 31]. In the former reference, a summary of most of the published work and its significant findings related to this type of retrofitting procedure is presented. Most of the problems mentioned above, concerning conventional retrofitting measures, may be overcome with the usage of fibre-reinforced plastic (FRP). In this reference, both the in-plane and out-of-plane failure mechanisms are discussed. With the help of quasi-static cyclic tests, this approach for retrofitting URM structures is examined. Different retrofitting configurations are investigated. For the in-plane behaviour of the URM walls, inclined plates (BW1, BW2, BW6) and a full-surface coverage (BW7) performs best, see Figure (2.12).

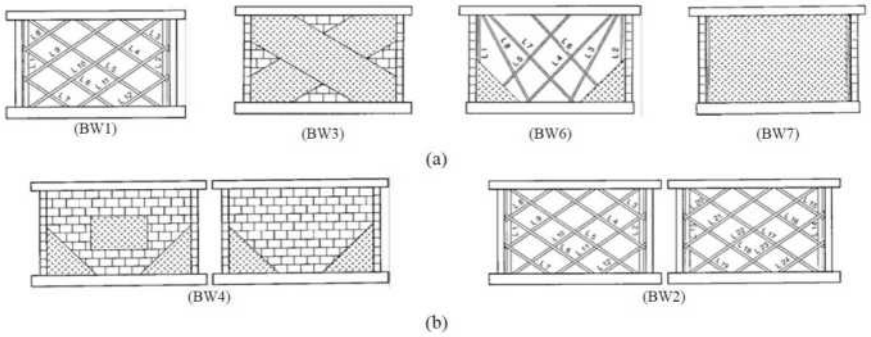

Figure 2.12: Different Retrofitting Schemes (a) Single Side, and (b) Double Sides [12].

The energy dissipation of the URM-FRP system depends on many factors which require more research. With the help of dynamic tri-axial shaking table tests, it is shown that the FRP overlay enhances the seismic resistance of retrofitted walls. However, premature failure reduces the positive influence of the retrofitting measure drastically.

With the help of monotonic and static cyclic loading (both in-plane and out-of-plane), it is shown that retrofitting of the URM walls using FRP dramatically increases the flexural strength. The results show an increase in the retrofitted specimen by a factor of approximately 20 for in-plane failure. The out-of-plane deflection is about 1/60 of the wall height. A lower increase, by a factor of 7.5, in out-of-plane resistance is observed for the retrofitted specimen tested in the static cyclic environment.

A more recent study [31] also shows good results for both the in-plane and out-of-plane behaviour of URM specimen retrofitted by FRP. For both failure modes, FRP elements are installed on (or inside) the masonry substrate.

2.4.2. Textile Reinforced Concrete (TRC)

Textile reinforced concrete (TRC) combines suitable fine-grained mortar with textile fabrics. Research in retrofitting URM structures using this material is limited, as mentioned in [4]. In this reference, the experimental campaign is focussed on the in-plane behaviour of URM walls retrofitted by TRC strips. Although only two walls were tested, the results show a positive influence on the contribution of TRC strips to the structural performance of these URM walls.

The application of the TRC system requires multiple steps, i.e. cleaning of the masonry surface, application of mortar layer, placing of the textile onto the fresh mortar layer, adding a second mortar layer, etc. If the retrofitting system requires multiple layers of reinforcement, the last two steps of this procedure have to be repeated. Besides this multi-step application, an anchorage system of the textile mats to the foundation is required. The investigated retrofitting layout is depicted in Figure (2.13) below.

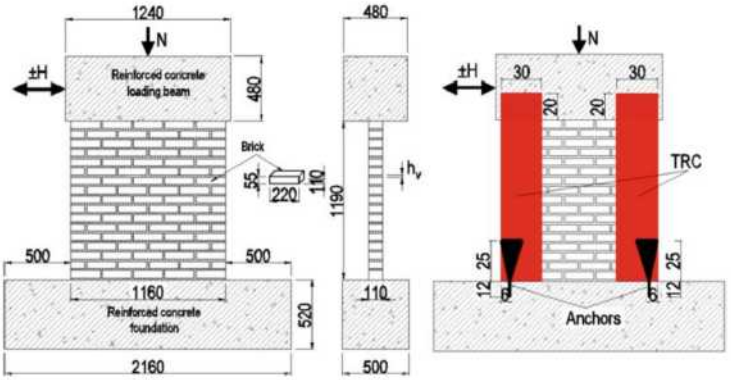

Figure 2.13: Left: Unreinforced masonry wall (URW), and right: TRC-repaired wall (TRCRW) [4].

The URM-TRC system showed an increase in residual strength equal to 36% and a deformation capacity increase of 25%. Also, out-of-plane failure mechanisms are prevented via this retrofitting technique. However, it is concluded that a low strengthening ratio of TRC doesn't bring very high efficiency. Application of multiple reinforcement layers is required to obtain satisfying results and reduces the disease of application for this retrofitting approach.

2.4.3. Shotcrete

In [13] the strengthening of URM walls through a shotcrete overlay is investigated, in which a total of three specimens (one reference and two retrofitted half-scale walls) are tested to determine the influence on their in-plane behaviour. Both single-side and double-side application of a 40 mm and 20 mm thick layer, respectively, are examined.

A mesh of small reinforcing bars is applied to the surface of the masonry substrate, onto which the shotcrete overlays are sprayed, see Figure (2.14a). The thickness of the overlay can be adapted to the seismic demand. Generally, the minimal thickness equals 60 mm. Different researchers question the requirement for shear dowels, which are drilled into the masonry substrate, or a bonding agent to ensure the transfer of shear stress across the shotcrete-masonry interface [13]. Figure (2.14b) shows the details of this retrofitting procedure (for the double-side application specimen).

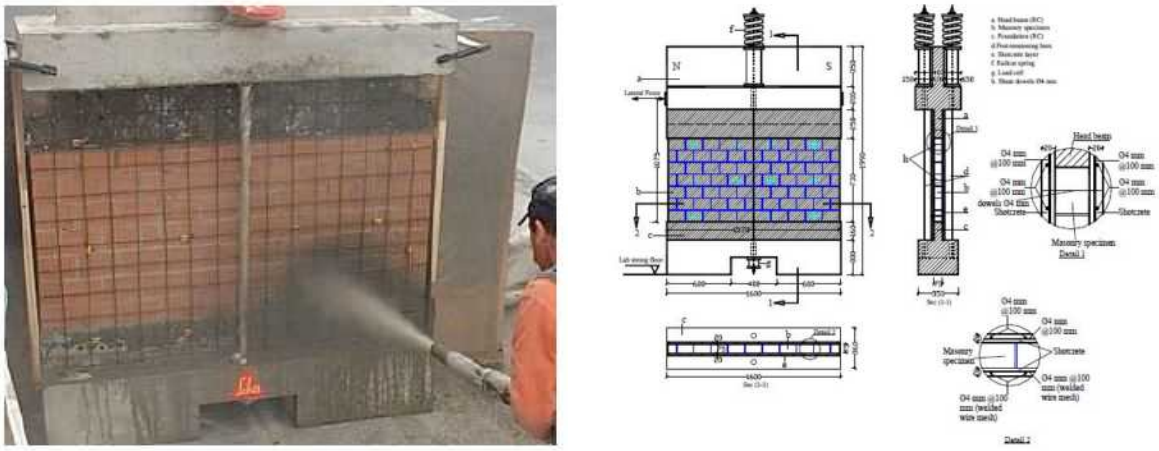

Figure 2.14: Left: application of shotcrete to masonry substrate. Right: details retrofitting approach Shotcrete-URM, [13].

The same researcher examined and mentioned that the application of the shotcrete overlay is more time consuming for the FRP variant, in an earlier experimental campaign [12]. Besides the additional time required, the procedure created a lot of cement dust. These facts are taken into account when considering different retrofitting procedures.

From the experiments, it is concluded that both retrofitted specimen reached a lateral strength of approximately 3.6 times the strength of the reference specimen. For both the peak strength and initial stiffness, there is no significant influence of single or double-side retrofitting. Finally, it is concluded that the double-side approach shows a more ductile failure and higher energy dissipation. No experiments on smaller specimens are performed.

2.4.4. Concluding remarks

In the previous paragraphs different retrofitting measures are discussed, all with promising characteristics and experimental results. However, several drawbacks are present. URM-FRP systems shouldn't be used in harmful environments and are prone to fire conditions. These limitations are related to the epoxy matrix used to embed and bond the fibres [4]. It is also mentioned that the FRP material generally behaves elastically up to the point of failure and potential debonding failure (brittle) is likely to take place through FRP debonding from the masonry wall [9]. Additionally, this reference mentions the need for surface preparation, anchor systems, and the high costs of this retrofitting approach. It can be concluded, taken into account the former statements, that different strengthening materials might be considered.

Both the TRC and shotcrete retrofitting approach shows to be time-consuming, especially the latter. Also, it is noted that the thickness required for the overlay of the shotcrete retrofitting method is quite substantial. This increases the weight of the retrofitted structure resulting in changes of the dynamical behaviour of the structural behaviour.

In addition to the discussed retrofitting approaches the use of Strain Hardening Cementitious Composites is also investigated by multiple researchers [6, 14, 38]. The results of these experimental campaigns are promising for future application of SHCC for masonry retrofitting. If applied correctly, the material shows ductile failure behaviour. A more in-depth description of the material characteristics of the SHCC is provided hereafter.

2.5. Material Behaviour of Strain Hardening Cementitious Composites (SHCC)

Strain hardening cementitious composites (SHCC) has been researched in many different fields of application, as reported in [25]. The high flexural capacity of the material makes it interesting to investigate SHCC as retrofitting material for the strengthening of brittle materials (e.g. concrete) or composites (e.g. masonry). Usage of SHCC as repair material increases the durability of the structure due to the very small crack widths occurring in this overlay material. Additionally, because of a fine diffuse crack pattern, high amounts of energy can be absorbed by the material. The latter is interesting for structures loading by seismic activity.

The term ECC is equivalent to SHCC. In this thesis, the term SHCC is used. This group of materials is characterized by high ductility in the range of 3-7%, tight crack widths of around 60 μm and a relatively low fibre content equal to 2% (maximum by volume) [41].

2.5.1. Mixture Composition

Concerning the environmental impact due to the global production of cement for concrete, many research is done to investigate the possibility of lowering cement contents in concrete mixtures, maintaining sufficient material characteristics like strength and durability. Different names are given to these newly designed materials, with lower cement contents, like engineered cementitious composites (ECC) [25]. A known, and researched, SHCC mixture is used for this research. This mixture is described in [41] under the name M6 and contains Portland cement, limestone powder, and blast furnace slag. This mixture contains a Portland cement-to-BFS (PC/BFS) ratio of 0.43 and showed the best mechanical properties. In all mixtures considered PVA fibres are used, with a fibre content of 2% by volume. The length of the fibres equals 8 mm, and the diameter is 40 μm. The tensile strength of the PVA fibre used is 1600 MPa, and the density is 1,300kg/m^3. The surface of the fibre is coated with oil (1.2%) to reduce the fibre-matrix and friction bond.

Table 2.1: Mix proportions of the ECCs with Portland cement, limestone powder and BFS (weight %) [41].

Mix Number	CEM I 42.5 N	Limestone Powder	BFS	Water/Powder ratio	Super-plasticizer	PVA fiber (by volume, %)
M6	0.6	2	1.4	0.26	0.020	2

After casting the specimen are cured in moulds covered with plastic foil for one day. After 24 hours these specimens are demoulded and cured under sealed conditions at a temperature of 27°C for another 27 days. Different mixtures, including this M6, are tested in the Microlab in Delft University of Technology. These tests consisted of 4-point bending, uniaxial tensile, and compressive tests. For the four-point-bending tests, four pieces of ECC are sawn into the dimensions of 120 mm x 30 mm x 10 mm. The free span between the supports of the bending tests is 110 mm and the distance between the two loading points 30 mm. The experimental setup used is shown below.

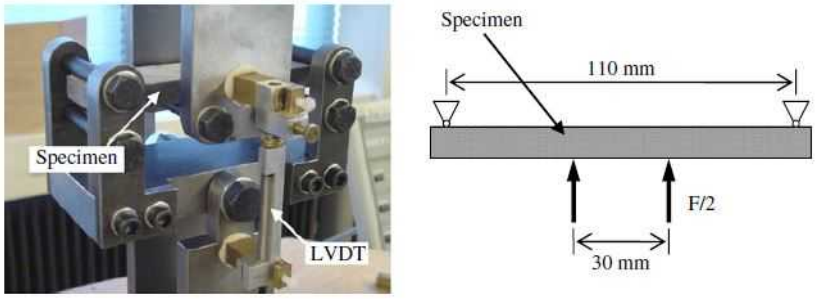

Figure 2.15: Four-point bending test set-up [41].

For the compressive tests, prisms specimens are sawn into three cubes with the dimensions of 40 x 40 x 40 mm^3. For each mixture, three experiments are performed.

From the experimental results, it is concluded that all mixtures examined showed multiple-cracking behaviour under four-point bending and uniaxial tensile load. The last mixture (M6) shows the best flexural and tensile properties. M6 has the lowest cement content of all the mixtures tested. However, this amount is more or less equal to the cement content of normal concrete (15% of powder materials by weight). The flexural deflection capacity and tensile strain capacity of mixture M6 are calculated by averaging the results of the three four-point bending measurements and the four uniaxial tensile measurements. These are 3.9 mm and 3.3% respectively, see Figure (2.19) and (2.24).

The results of the four-point bending test and the uniaxial test indicates a linear correlation between the flexural deflection capacity and the tensile strain capacity. It is concluded that the decrease in PC/BFS ratio results in the increase in the flexural deflection capacity and in the increase in the tensile strain capacity.

Table 2.2: Flexural deflection capacity and tensile strain capacity of M6 at 28 days [41].

Mixture	M6	Unit
Flexural Deflection Capacity	3.9 ± 0.3	mm
Tensile Strain Capacity	3.3 ± 0.2	%

Besides positive material characteristics, like flexural and tensile capacity, the durability of these type of materials is of high interest. The loaded crack width of the ECC determines the transport properties in the loaded state, and therefore it is a crucial parameter for the durability of ECC. All mixtures show a loaded crack width smaller than 100 μm. Mixture M6 showed a very low crack width of 57 μm. This is due to the increase of limestone powder and BFS content.

2.5.2. Fibers

Different types of fibres have been used in the past. However, SHCC reinforced with PVA fibres has attractive characteristics in terms of cost, processing, mechanical properties, and durability and represents the most practical SHCC application for field application to date [40]. Generally, a fibre volume equal to 2% is used.

This polyvinyl alcohol (PVA) fibre generally has a diameter of 39 μm and a length of 6-12 mm [41]. This type of fibre shows slip-hardening behaviour. The behaviour of these fibres is described in more detail in [40]. Obtaining the required tensile strain-hardening material properties of the SHCC mixture is done via tailoring the material microstructure, including this fibre-bridging behaviour. This reference proposes a constitutive law for this fibre-bridging behaviour. The overall importance of these fibres in the SHCC mixture is discussed here. The exact formulation of the proposed constitutive law for this phenomenon is out of the scope of this thesis.

2.5.3. Surface Preparation SHCC

In standard concrete repair, surface preparation of the substrate concrete is considered critical in achieving a durable repair [22]. In this reference, different base concrete surfaces are examined (i.e. smooth surface, lubricated smooth surface, and a rough surface). The different specimens are tested via 4-point bending tests. The specimens are designed to induce a defect in the SHCC-concrete interface. This is achieved via an additional notch and joint created in the concrete substrate. Both of these imperfections are created via the application of smooth tape on the base concrete before casting the SHCC repair material. An overview of the test set-up is shown in Figure (2.17).

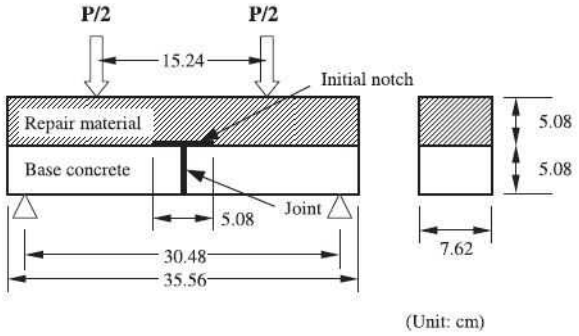

Figure 2.16: Four-point bending test set-up [22].

An SHCC repaired specimen shows, as expected, much larger ductility than a concrete repair system. The SHCC overlay failed without spalling or delamination from the interface. For the system with the rough surface, no interface crack propagation is seen in the SHCC overlay system. The SHCC mixture with a W/C ratio (water-cement ratio) equal to 0.28 shows two macro cracks at both of the initial notches in the overlay. For the specimen with a higher W/C ratio (0.6) only one macro crack, at the centre of the overlay system is observed. See Figure (2.17a) and (2.17b), respectively. In the smooth surface specimen, however, the kink-crack is arrested when the energetics favours interface defect to propagate along the interface. This preference is due to the lower interface toughness associated with the smooth surface of the base material. Hence smooth surface specimen is able to redistribute the load and utilize more material of the SHCC repair system than a rough surface specimen to resist the final failure loading. Also, the crack width belonging to the smooth surface specimen is much smaller compared to the rough surface specimen at peak resistance. This is an important parameter concerning the durability of the repaired structure.

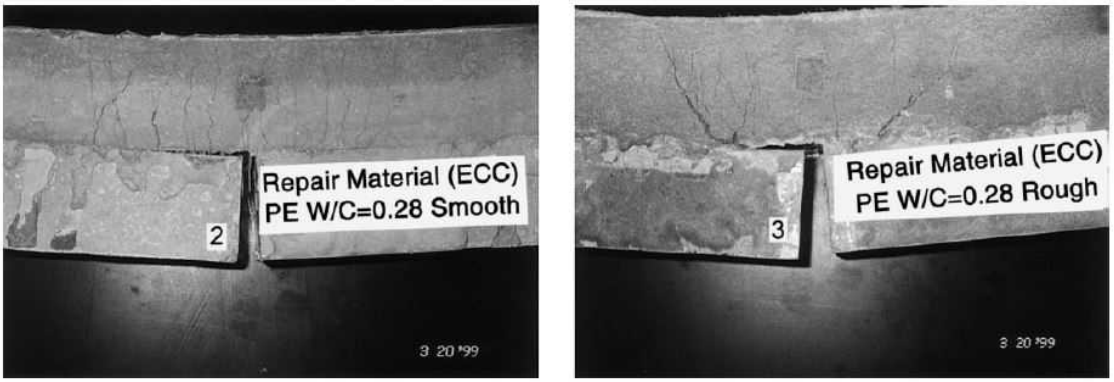

(a) Smooth (b) Rough

(a) Crack patterns of the ECC (W/C = 0.28) overlay system: (a) Smooth; (b) Rough.

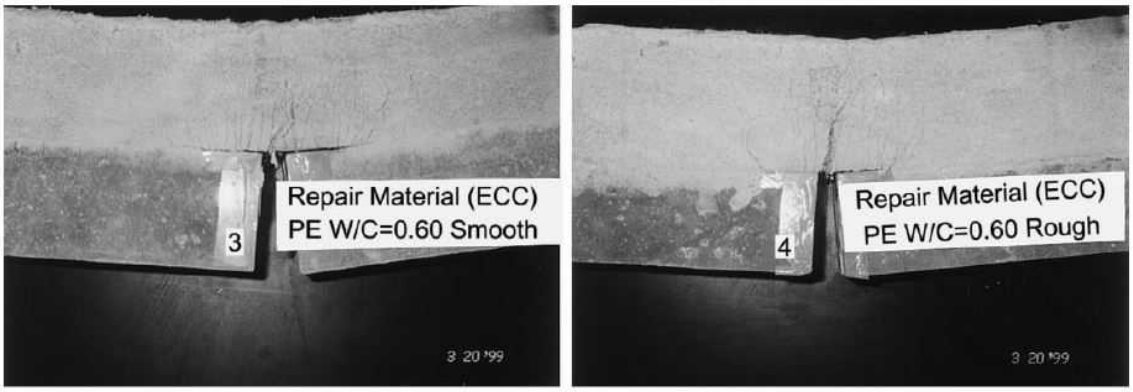

(a) Smooth (b) Rough

(b) Crack patterns of the ECC (W/C = 0.6) overlay system: (a) Smooth; (b) Rough.

Figure 2.17: Crack patterns four-point bending tests. Different W/C ratios examined. Both smooth and rought interfaces [22].

The interface crack trapping mechanism is described in [22]. This mechanism depends on several parameters of the repair system, the substrate material, and the interface properties between these two materials. Different failure modes can be described with the proposed concept of the trapping mechanism. Brittle failure can occur if a crack in the interface between the substrate and the repair material propagates along the interface if no bridging or interlocking along the interface, between the substrate and the repair material, occur. Another possibility for brittle failure to occur is a so-called surface spall. This could happen if an interface crack kinks out into the repair material and this repair material is too brittle to stop this kinked crack. However, also more ductile failure mechanisms are possible if the repair material has rapidly rising fracture resistance, the kinked crack can be stopped or 'trapped' in the repair material. There is no more crack propagation in the repair material when the driving force of the kinked crack equals the increasing fracture resistance of this material. This is possible if the repair material possesses a hardening characteristic, for example, due to the fibres bridging a matrix crack if the repair material is fibre reinforced. Multiple kinked cracks are possible until the full interface is exhausted or other failure modes take over. This mechanism is depicted in the figure below.

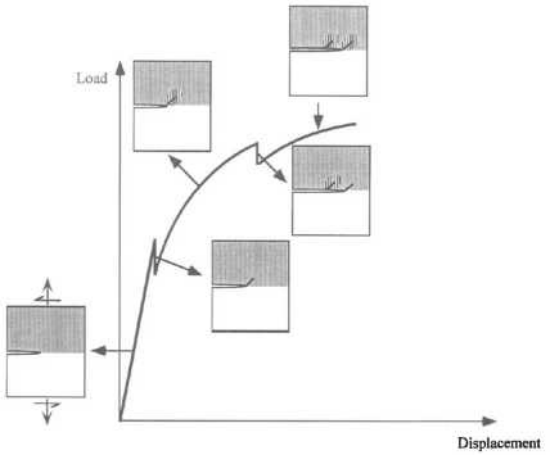

Figure 2.18: Trapping mechanism in a bimaterial interface system [22].

This trapping mechanism is discovered via theoretical considerations and experimental observations. The SHCC material examined in literature is found to produce the special characteristics of trapping as described. The low initial toughness of the SHCC material allows for repeated kink-trapping rather than delamination.

2.5.4. Tensile Behaviour

In Figure (2.19) a typical stress-strain diagram of SHCC is shown. The tight crack width of the material under these loading conditions is also depicted.

After the first cracking SHCC shows a metal-like property, this differs with respect to plain concrete and ordinary fibre reinforced concrete. This unique tensile strain-hardening behaviour results from an intensive design procedure of the material at the micro-mechanical level. In this design approach, the interactions between the fibres, matrix and the fibre-matrix interface are considered. This fibre-matrix interface plays a very important role in the tensile strain-hardening behaviour of the SHCC [41].

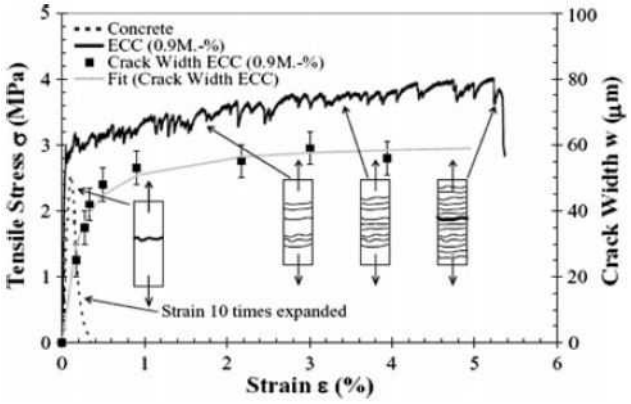

Figure 2.19: Tensile stress-strain curve and tight crack width control of SHCC [41].

When the SHCC is loaded in tension, the matrix starts to crack at its weakest cross-section. The fibres will bridge this initiated crack and take over the tensile load, just like steel reinforcement in ordinary reinforced concrete. The fibres show a slip-hardening behaviour which results in the increased load capacity of the SHCC. This behaviour of the fibres gives rise to the possibility of new cracks to develop in other locations of the SHCC cross-section. Repeating this process will generate a multiple-cracking behaviour of the SHCC mix and, therefore, strain-hardening behaviour. In [2] this characteristic is referred to as 'steady-state cracking' because the increase in tensile load will not induce significant widening of the existing cracks, but new micro-cracks will form.

Many research is available with respect to the tensile behaviour of SHCC mixtures, see the literature mentioned. The mixture for this thesis is based on mixture M6, as described in [41]. This mixture is designed at Delft University of Technology. The tensile behaviour of this specific mixture is also examined via uniaxial tensile tests. More than four samples are tested for every single mixture designed. Mixture M6, however, showed the best flexural and tensile properties. The tensile-strain curves of the M6 mixture are shown below in Figure (2.20).

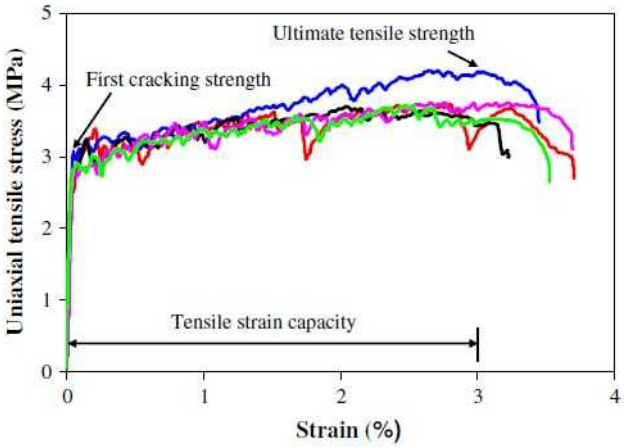

Figure 2.20: Tensile stress-strain curves of M6 with an average tensile strain capacity of 3.3% [41].

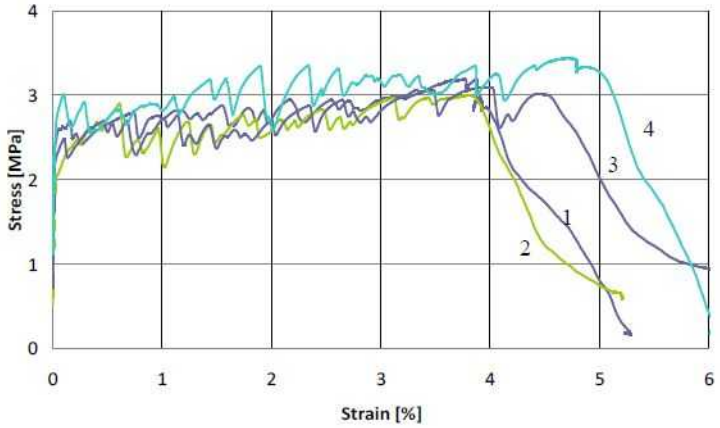

Figure 2.21: Typical direct tensile responses, with an average strain determined from LVDT measurement over the 80 mm gauge length [2].

Additional research, with respect to the crack formation under different loading regimes, is described in [2]. With the help of digital photo images, the crack formation is determined accurately. This reference also provides diagrams with respect to the results of a typical tensile response of SHCC, which was developed at Stellenbosch University earlier. Figure (2.21) shows good correspondence with Figure (2.20). However, for the experimental campaign [2] both monotonic and cyclic loading regimes are tested. This resulted in different observations for the crack patterns. For the monolithic tests, it is concluded that no significant loading rate dependence acts for the ultimate tensile resistance of the SHCC material. However, an increased first cracking stress is observed with increasing loading rate. A slight reduction in ductility with the increase of loading rate is observed. Nevertheless, the ultimate tensile strain remains greater than 3%, see Figure (2.22).

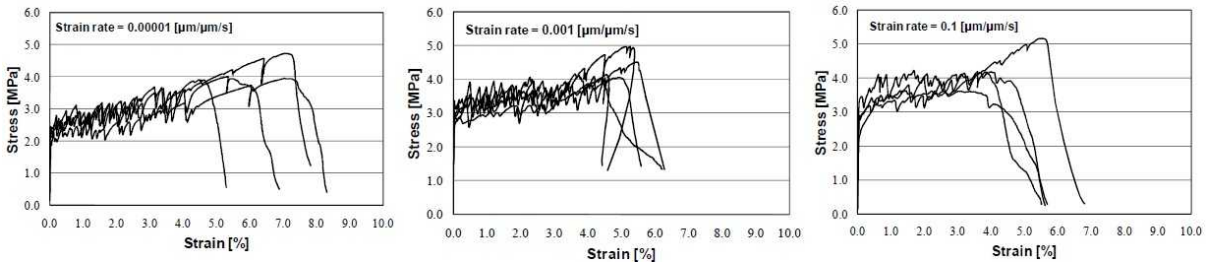

Figure 2.22: Stress-strain responses at three different loading rates [2].

The crack width evolution remains typical for all loading rates. Two different cyclic tests are performed, larger and smaller load cycles are examined. It is concluded that the ductility of the SHCC specimen reduced with an increased number of cycles. This result is shown in Figure (2.23) below. The average crack widths confirmed the same trends as observed for the monolithic tests. However, it is also noted more research should be done to study this phenomenon.

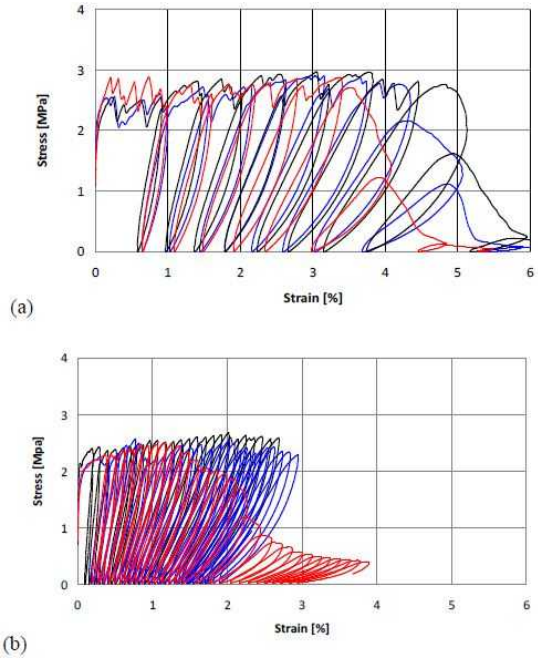

Figure 2.23: Responses to cyclic tensile tests: (a) large load cycles; (b) small load cycles [2].

2.5.5. Flexural Behaviour

The flexural strength of SHCC mixture M6 is determined via four-point bending tests, as described in [41]. All different mixtures exhibited multiple-cracking behaviour. In the figure below the obtained flexural load-deflection curve is shown. The maximum flexural stress is defined as the flexural strength, and the corresponding deflection is defined as the flexural deflection capacity. The average flexural capacity of mixture M6 equals 3.9 mm.

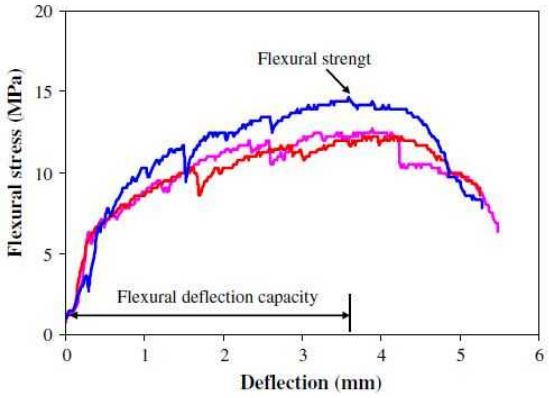

Figure 2.24: Flexural load-deflection curves of M6 with a flexural deflection capacity of 3.9 mm [41].

2.5.6. Shear Behaviour

In [36] it is investigated if this crack bridging behaviour of the fibres also occurs for pure shear cracking. An Iosipescu shear specimen, see Figure (2.25), is designed through numerical analyses to obtain perfect shear

failure. From the test results, it is concluded this designed Iosipescu shear specimen behaves as expected. Satisfying results are obtained. The cracking initiated at the notch of the specimen and in the fibre reinforced specimen these cracks are arrested. For the specimen with a fibre volume greater or equal than 2% multiple cracks arose in the notch zone, indicating inherent shear cracking control. Specimen with a lower fibre volume, i.e. smaller than 2%, showed diagonal failure. The shear cracks were not arrested in the material. It is determined that the shear strength of the SHCC exceeds the direct tensile strength up to 50%. It is argued that this behaviour is due to the ability of SHCC to maintain its tensile resistance well beyond its first cracking strain, allowing for principle stress rotation and accompanied increased orthogonal compression upon the shear loading case. For a more detailed description, the reader is referred to the literature.

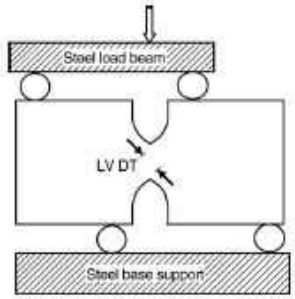

Figure 2.25: Iosipescu shear specimen [36].

2.5.7. Compressional Behaviour

As mentioned earlier, the SHCC mixture used for this thesis is similar to the M6 mixture [41]. This mixture showed a compressive strength of around 40 MPa at 28 days. This property is checked during this experimental campaign via similar experiments. Uniaxial compression tests are performed on SHCC cubes (40x40x40 mm). The 28-day average compressional strength equals 38.5 Mpa, which is coinciding with the results presented in the literature. For the results one is referred to Appendix A.

2.6. Unreinforced Masonry Retrofitted with Strain Hardening Cementitious Composites

To decide which types of experiments should be conducted during this experimental campaign, much time is devoted to the investigation of previously executed experiments and their results. Derivation of the material properties with the help of experiments is well documented. Also, up to some extent, the numerical modelling of the material itself is being researched [14]. A more in detail description, with respect to the numerical modelling, is presented in the following section.

Many literature is present with respect to research in the retrofitting of URM structures by means of a SHCC overlay. Casted, as well as sprayed, overlays are considered [9, 14, 38]. The experimental results provided in these references show a significant positive influence of the SHCC overlay for URM structures. Several types of experiments are performed in the presented literature. Most commonly shear triplet tests are performed to determine the improved performance of the retrofitted specimen under shear loading conditions. Additionally, the in-plane shear resistance of retrofitted masonry wallets is investigated [37]. Besides the shear strength experiments also out-of-plane bending tests on retrofitted masonry beams are performed [9, 14].

2.6.1. Shear Behaviour - Material Level

Investigating the shear strength properties of SHCC-masonry systems are currently being investigated. Research in South Africa [38] performed different experiments (i.e. shear triplet tests and enlarged shear triplet tests) on SHCC retrofitted masonry specimen with masonry bricks having both a smooth-faced surface and a grooved face. The grooved face of the bricks have five, 5 mm thick and 12 mm wide, grooves. For these tests, the SHCC is applied on both sides of the masonry specimen, i.e. to both on the smooth face and the grooved face a SHCC layer is applied. For this research, a sprayable version of the SHCC mixture is investigated. This mixture showed lower performance compared to the original mixture, however, still sufficient to be applied for retrofitting purposes. Two different thicknesses are investigated in this experimental campaign. The thicker,

30 mm overlay, showed brittle failure via complete delamination of the SHCC material.

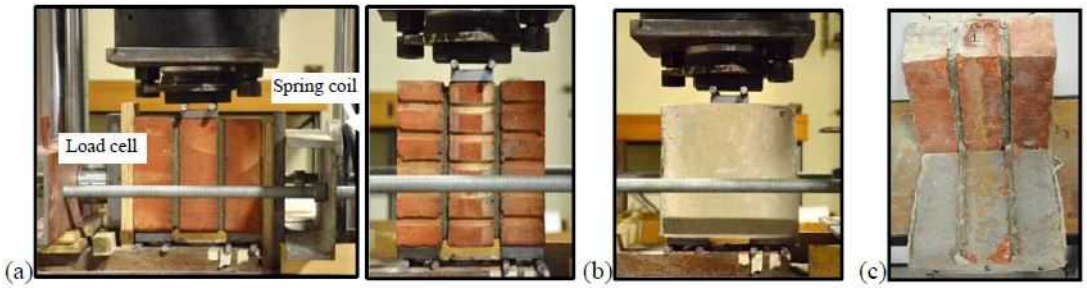

Figure 2.26: Triplet test configuration for triplet specimen: (a) smooth and grooved face; (b) SHCC overlay applied; (c) debonded SHCC overlay [38].

The different thicknesses are examined to obtain two different failure modes. See Figure (2.27). A thin layer of SHCC will induce a ductile like failure with a fine crack pattern spread over a relatively wide area (Mode 1 failure). However, a thick layer will introduce brittle failure behaviour. Debonding of the SHCC layer and the masonry underneath is observed by different researchers and is referred to as Mode 2 failure. In [38] equations are proposed from which the critical overlay thickness can be determined.

$$F_{Mode,1} = 4 \cdot \tau_s \cdot h_b \cdot t_s + 2 \cdot h_b \cdot t_b \cdot (c_j - \Phi\sigma) \tag{2.3}$$

$$F_{Mode,2} = 2 \cdot \tau_b \cdot h_b \cdot d_b + 2 \cdot h_b \cdot t_b \cdot (c_j - \Phi\sigma) \tag{2.4}$$

Where:

τ_s: SHCC shear resistance (assumption that the ultimate shear resistance is 50% more than the ultimate tensile resistance of the sprayed SHCC [38].
τ_b: Masonry-SHCC interface bond strength
h_b: brick element height (222 mm)
t_b: brick element thickness (105 mm)
d_b: brick element thickness (70 mm)

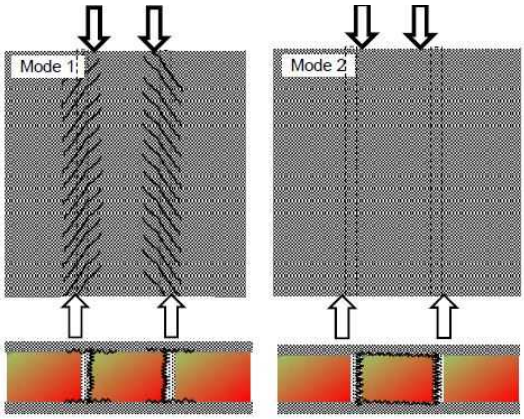

Figure 2.27: Failure modes corresponding to retrofitted masonry triplets [38].

The shear bond strength of the SHCC-masonry interface is determined to be equal to 2.3 N/mm^2, see mentioned reference. The figure shown below shows the experimental results related to the determination of this interfacial bond strength. The results shown are related to the experiments performed on masonry triplets with a 30 mm thick SHCC overlay applied to both sides (both smooth and grooved surface). It is shown, by the

coloured curves, that the retrofitted specimen shows a significant increase in strength over the plain masonry specimen (T0-110-0-1). This increase in strength is contributed to the interfacial shear strength of the SHCC overlay alone, i.e. τ_b equals the peak loading divided by shear areas central masonry unit. However, the value mentioned represents the average value of all experiments, thus also taking into account both the smooth and grooved interfaces. These curves are obtained directly from the author of the mentioned reference and are not present in the reference itself.

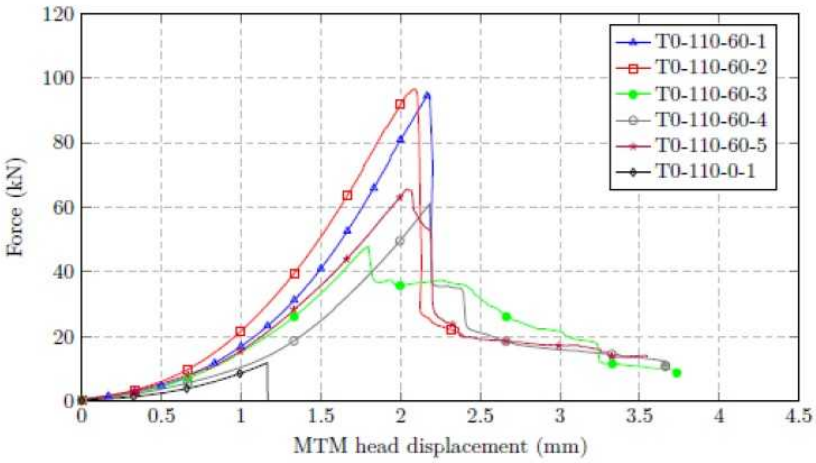

Figure 2.28: Experimental results shear strength masonry triplets retrofitted with a 30 mm thick sprayed SHCC overlay, applied on both sides. Experimental results obtained via Prof. G. P.A.G. van Zijl.

The same reference also tested enlarged retrofitted triplets. These specimen consists out of 9 clay units and 8 mortar joints. For these experiments, the SHCC overlay material is, again, applied at both sides of the specimen (i.e. the smooth and the grooved face) by spraying. Failure patterns of these specimen are shown below.

Figure 2.29: (a) Large triplet test setup of control and overlayed specimens, showing (b) de-bonding along the masonry-overlay interface for 30 mm overlays and (c) (from left to right) multiple shear crack formation in 10 mm overlays, localisation and larger de-bonded region on the (rear) smooth brick face than on the (front) grooved brick face. [38].

In [9] a vertically applied (troweled) SHCC layer on top of the masonry triplets. The thickness of the SHCC overlay is controlled via a wooden frame around the masonry specimen. The influence of the layer thickness is well shown in the figure below. A more stable post-peak regime is achieved with the thinnest overlay (i.e. 5 mm). It is mentioned that the development of cracks, and therefore achieving a good ductile behaviour, depends on the thickness to area ratio of the overlay. It is also mentioned that additional performed experiments, on masonry triplets retrofitted by a 20 mm thick overlay, exhibited a rather brittle behaviour characterized by the limited shear failure of the bricks and debonding of the overlay material. Thus, confirming the results of the other reference.

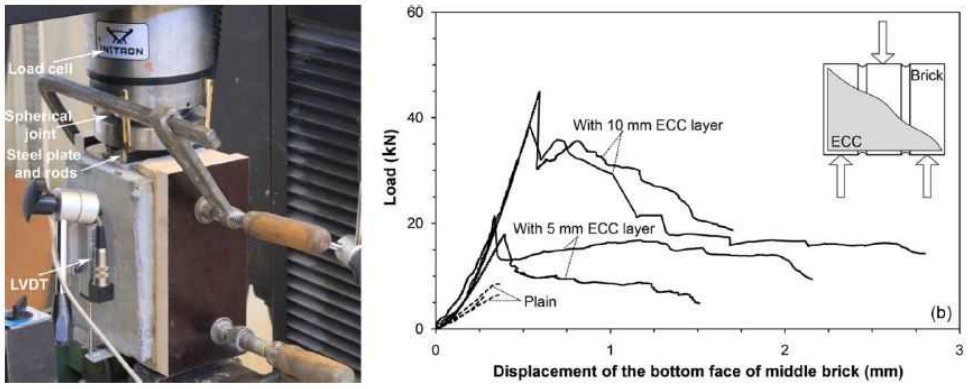

Figure 2.30: (a)Triplet test setup (b) Load-displacement curves obtained from the triplet tests [9].

Failure of the specimen, as described in [9], is due to the collapse of one of the mortar joints. Hereafter, the shear load is transferred to the SHCC overlay, and a sudden loss in strength occurred (see the first drop in Figure (2.30)). After this initial damage, the specimen shows a ductile behaviour up to failure. This ductile

behaviour is characterized by the initiation of cracks in the overlay material around the collapsed joint, by the increase of deformation. Debonding of the overlay started from this initial location. At higher loads, the width of these initial cracks increased. In the end, the specimen failed due to the collapse of the second mortar joint.

The experimental setups used for both [9, 38] is of interest since no pre-compression is applied to any of the specimen tested. This is in contradiction to the earlier described experiments related to the shear strength of URM. The Coulomb criteria does not hold for these presented results. When comparing the experimental results of the experimental campaign corresponding to this report, this fact is taken into account.

2.6.2. Shear Behaviour - Component Level

Besides performing shear triplet tests (on both normal and enlarged triplets) also small masonry wallets are tested. These wall specimens have a dimension: 935 x 1150 mm (hxw). In total, three walls are tested. Two walls are control specimen, the first a single leaf masonry wall of 110 mm thick, and the second one a double-leaf masonry wall of 220 mm thick. The third, and final, specimen is a single leaf masonry wall of 110 mm thickness onto which a 30 mm thick SHCC layer is sprayed. For this experiment, the overlay is applied to only one side of the specimen.

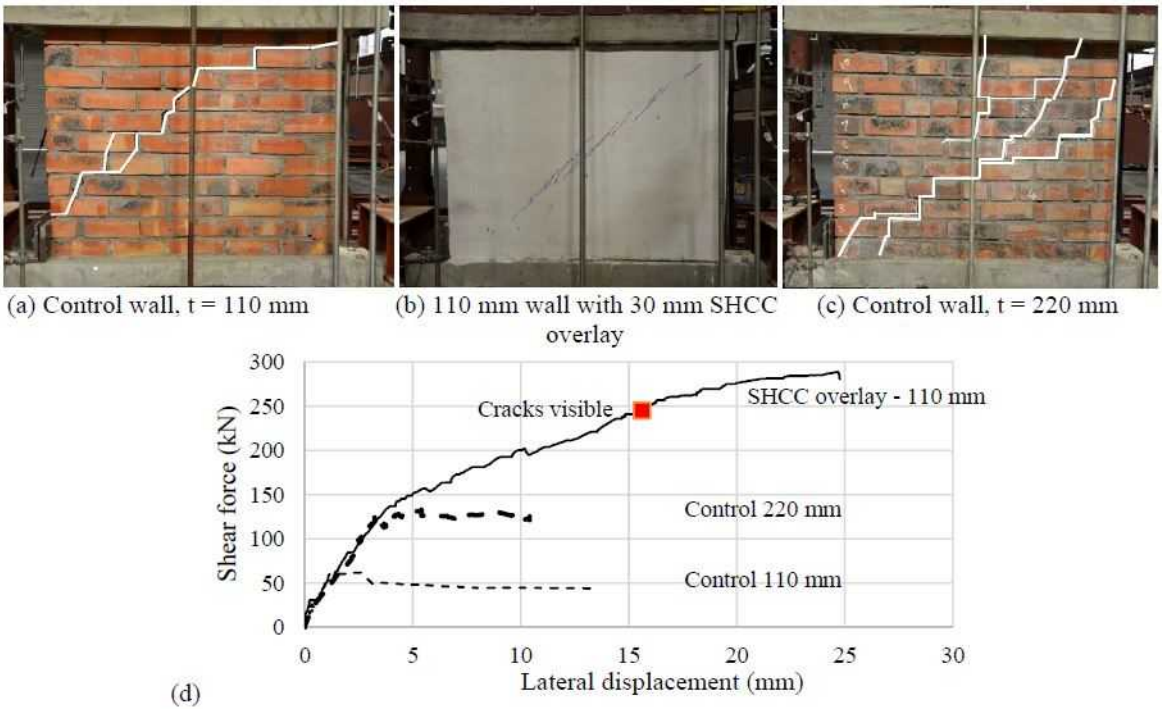

Figure 2.31: Failure patterns after the shear tests drawn in white on (a) single leaf (110 mm thick) reference wall, (b) single leaf with 30 mm SHCC overlay and (c) double leaf (220 mm thick) reference wall, as well as (d) the corresponding shear force – displacement responses [38].

Diagonal cracks occurred in all the specimen. Multiple cracks are successfully induced in the SHCC overlay material. In this reference, it is mentioned that further research will be conducted to investigate the influence of the application of debonding strips along the diagonal where the cracks occurred. The results of this additional research are presented in [39]. The application of debonded strips should prevent the reflective cracking from the masonry substrate into the SHCC overlay. In the presence of these debonded areas, kinked-crack trapping is suppressed, as described earlier. Multiple cracks in the overlay material occur in a wide region to restore the deformation compatibility with the masonry substrate that contains a localized crack. See Figures (2.32) and (2.33).

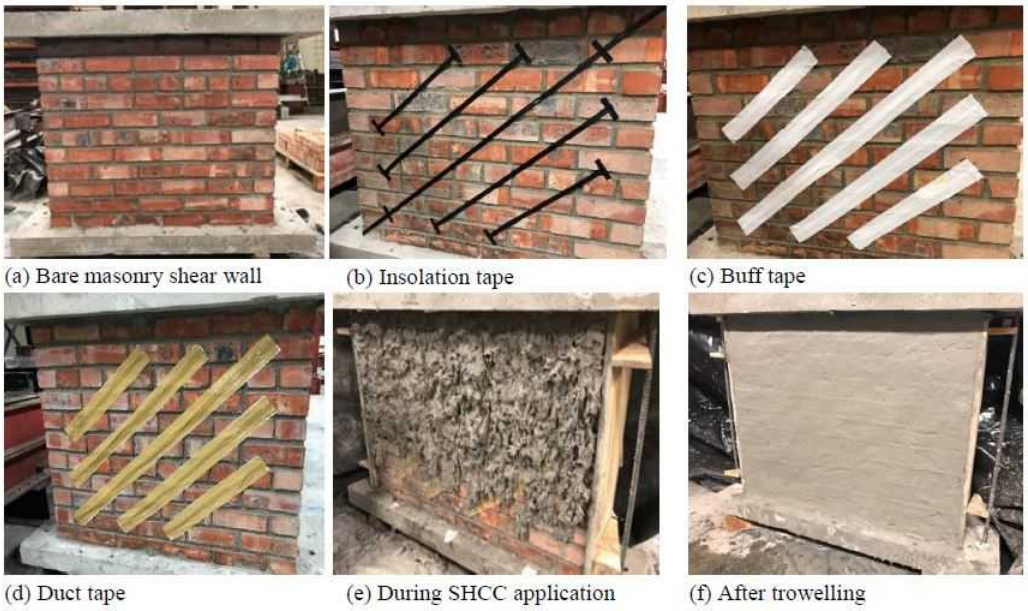

Figure 2.32: Manufacturing of masonry walls with debonded strips [39].

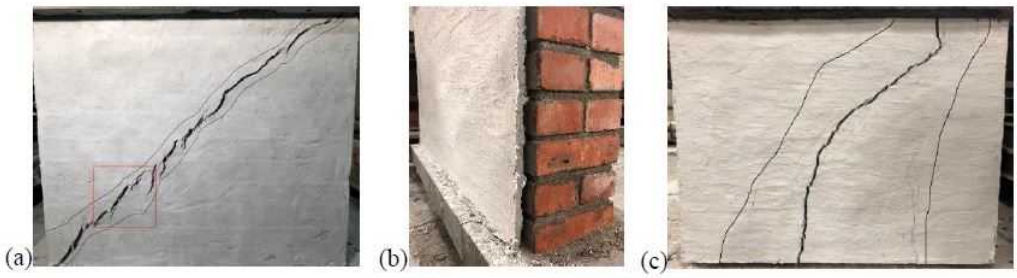

Figure 2.33: (a) Diagonal crack pattern in SW-220-15-Reference wall, (b) delamination of the overlay of SW-100-200-01, and (c) wide crack distribution in SW-100-200-02 [39].

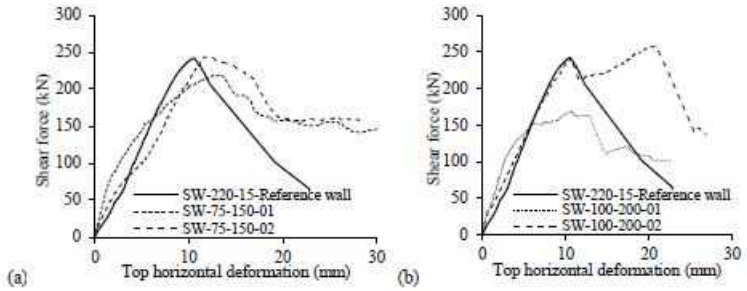

Figure 2.34: Shear walls with (a) 75 mm debonded strips, and (b) 100 mm debonded strips compared with the reference wall with fully bonded overlay [39].

It is concluded that the debonded strips cause a slight reduction in stiffness, insignificant change in shear resistance, but significantly increased the ductility. However, from Figure (2.34), it is also shown that the experimental results show a large amount of scatter. This can be influenced by a lot of different factors, e.g. surface preparation.

2.6.3. Flexural Behaviour - Material Level

To determine the out-of-plane flexural strength of the retrofitted masonry four-point bending tests will be performed on masonry beams like described in [9, 14]. The latter performed four-point bending tests on a retrofitted masonry beam consisting out of eleven clay masonry bricks with 20 mm thick mortar joints in between. A stacked bond pattern is considered, see Figure (2.35). The beams are constructed horizontally, in a prefabricated formwork, the joints are casted in between the unit bricks, which are placed inside the horizontal formwork. These joints are partially removed over a depth of 20 mm. This is done to create an increased thickness of the SHCC above the mortar joints. One day after casting the low strength mortar (LSM), the beam is cured for 7 days. In total, four strengthened masonry beams are examined. Two different layer thicknesses are examined, 15 mm and 20 mm, respectively (2 specimens per layer thickness). This SHCC overlay is applied 7 days later, thus 14 days after the LSM was first cast. This SHCC layer is screed up to the designed level of the formwork and is externally vibrated to remove trapped air bubbles in the mixture. Again, after 24 hours of the application of the SHCC overlay, the beam is cured for 7 days. Now under wet towels. The flexural tests are performed 13 days after the casting of the SHCC. The LSM and SHCC overlay had cured for 27 and 13 days, respectively.

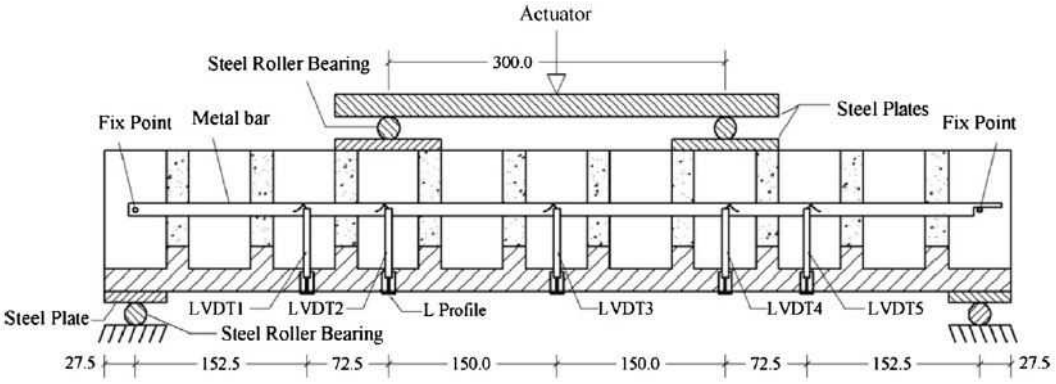

Figure 2.35: Four-point beam bending test setup (all dimensions are in mm) [14].

Due to the brittle behaviour of the plain masonry specimen, the reference specimen failed during its demoulding process. This is due to the very low bond strength between the units and the mortar. It is imagined this low bond strength resulted from the building procedure used (i.e. the horizontal casting). In this way minor (or no) adhesion is too be expected in between the masonry units and the mortar material. Also, the used mortar joint thickness is double the normal thickness (i.e. 10 mm). Both of these factors are taken into account during this experimental campaign.

The low strength of the reference beam led to the conclusion that any increase in terms of both strength and ductility is solely related to the SHCC overlay applied [14]. The two masonry beams strengthened with a 15 mm thick SHCC overlay (B15-1 and B15-2) showed a quite similar load-deflection curve, see Figure (2.36), with almost linear-elastic behaviour up to a load level of approximately 3.3 kN and a corresponding deflection of 0.4 mm. This linear-elastic phase is followed by nonlinear behaviour due to the formation of a diffuse crack pattern in the SHCC. These cracks mainly developed in the constant bending moment region. These specimen, in the end, failed due to the formation of a macro-crack, which progressed from the SHCC layer into the mortar joints in between the units. The masonry beams strengthened by means of a 20 mm thick SHCC layer (B20-1 and B20-2) showed a more heterogeneous behaviour in terms of the force-displacement relationship, see Figure (2.36). This is due to the larger irregularities in the SHCC layer along the length of the specimen, which are caused by the irregular height of the units used for these beams. However, for both specimen, a more or less similar maximum load (F=12.89 kN) is obtained. The deflection at failure is different for both specimens. Similar to the specimen with the 15 mm thick overlay also these specimen failed due to crack localization in the SHCC overlay and its propagation into the SHCC-unit and unit-mortar interfaces. The more brittle behaviour of specimen B20-2 (second specimen with 20 mm thick overlay) is justified by the higher brittleness of the shear crack propagation through the brick element, instead of the unit-mortar interface.

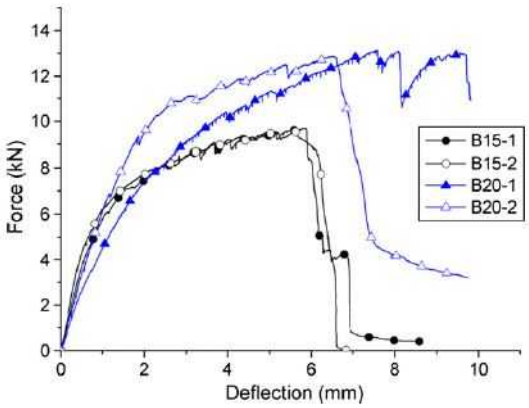

Figure 2.36: Force versus mid-span deflection curves for the beams strengthened with SHCC [14]. B15 = specimen retrofitted by means of 15 mm thick SHCC overlay. B20 = specimen retrofitted by means of 20 mm thick SHCC overlay.

[9] also examined the structural behaviour of small scale masonry elements which were retrofitted via a SHCC overlay. One part of the study relates to the four-point bending experiments on masonry beams. The set-up used is shown in Figure (2.37). These tests will give the performance of the SHCC retrofitted URM beams on the flexural strength, out-of-plane behaviour, and these tests can show the direct tensile behaviour of the SHCC material in the tensile zone of the loaded specimen. A total of nine specimens are built, each one consisting out of ten unit bricks and nine 10 mm thick mortar joints. All the specimen are built in a vertical orientation. Three of these specimen function as reference material. The other six specimens are strengthened via a 20 mm thick overlay, which is applied at one side of the specimen. On three of the retrofitted specimen, an adhesive is applied to examine the influence of the bond between the SHCC overlay and the masonry beams.

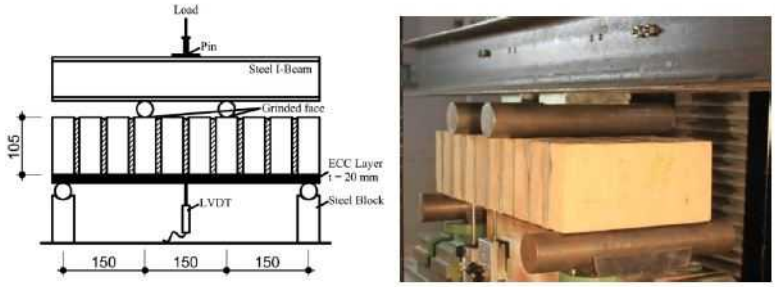

Figure 2.37: Left: Four-point bending test schematic view and dimensions; Right: test setup and instrumentation [9].

It is concluded that both the strength and the ductility of the retrofitted specimen are increased drastically. The reference specimen revealed an approximately linear-elastic behaviour up to the ultimate load and an abrupt failure at 0.2 mm midspan deflection. This failure originated in a crack which occurred inside one of the mortar joints between the units. In contrast, the retrofitted specimen exhibited the first crack at a load almost five times greater than the ultimate bearing load of the reference specimen. Also, the formation of multiple cracking in the overlay material is observed. The ductility of the retrofitted specimen increased by a factor of 25 to 30, and all retrofitted specimen showed strain-hardening behaviour. Non-brittle failure governed the experiments of the retrofitted specimen. The retrofitted specimen with an additional bonding agent showed a more constant behaviour in the inelastic branch, which resulted from a more constant tensile stress distribution in the overlay material. However, Figure (2.38), also shows that the specimen with the bonding agent applied showed a lower strength (see dotted curves). It is argued that this resulted from the penetration of the wet bonding agent into the SHCC material, leading to a change in the mechanical characteristics of this overlay.

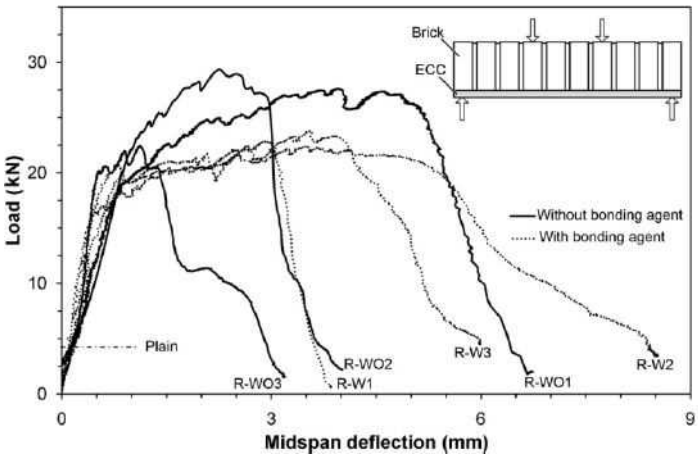

Figure 2.38: Flexural response of the (retrofitted) masonry beams [9]. Thickness SHCC overlay = 20 mm for all retrofitted specimen.

2.6.4. Restrained Drying Shrinkage SHCC Overlay

The restrained shrinkage of the SHCC overlay material is of interest for the practical application of this retrofitting approach. In [38] the free and restrained drying shrinkage of the SHCC overlay material is measured. For the retrofitted shear triplet experiments the specimen are wrapped into plastic foil after application of the SHCC overlay, which prevents (i.e. limits) the occurrence of drying shrinkage. However, for practical applications, this curing method is not possible (i.e. wrapping a whole structure or structural components in foil).

Free shrinkage is measured from specimens with the size 100 mm x 100 mm and length 500 mm. After 24 hours these specimens are demoulded, and Demac targets are attached at a 100 mm gauge length. The specimens are left unsealed hereafter in a climate room at 24±2°C at 65±5%. In total four samples are used with 2 measurement instruments on each sample.

The restrained drying shrinkage is measured from the bonded SHCC, on top of the masonry substrate, which serves as a restraint to the drying overlay material. Two different masonry layouts are tested to investigate the influence of mortar joints on the restraint drying of the overlay. The dimensions of these different specimen are 1030 mm by 220 mm. The masonry specimens are left to cure for 7 days under laboratory conditions. A 30 mm thick SHCC layer is sprayed onto one side of the masonry substrates and left to harden for 24 hours. Hereafter the strain gauges are placed on top of the SHCC overlay material. The strain gauge length equals 500 mm. These specimens are left in similar conditions as the free shrinkage specimen. Over a period of 56 days, both the free and the restrained drying shrinkage are investigated.

It is concluded that restrained drying shrinkage leads to micro-crack formation in the SHCC overlay. However, no crack localization is observed, which is ascribed to the great tensile capacity of the sprayed SHCC (roughly 2%) with respect to the maximum observed shrinkage strain (0.068% at 56 days).

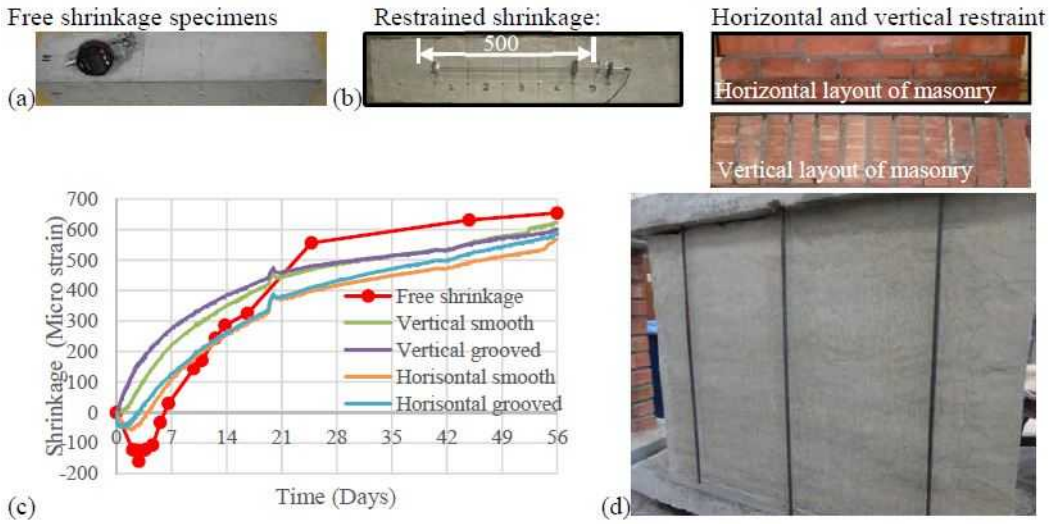

Figure 2.39: Drying shrinkage measurement on (a) free shrinking SHCC specimens (b) restrained SHCC overlays (c) shrinkage development in time (d) fine shrinkage cracks on the large shear wall overlay [38].

From the figure above, it is shown that the restrained shrinkage, measured on top of the vertical masonry layout, is smaller compared to the results corresponding to the horizontal masonry layout investigated. Shrinkage perpendicular to the masonry bed joints is less restraint. Also, it must be noted that no differences are observed between the smooth and grooved surfaces of the masonry bricks. The free shrinkage is slightly larger, compared to the restrained shrinkage. However, this free shrinkage measurement shows a negative value in the first 7 days.

Additionally, the direct comparison, between the free and restrained shrinkage specimen, is questionable due to the boundary conditions of both specimens. The SHCC specimen used to determine the free drying shrinkage is much thicker (i.e. 100x100x500 mm^3) compared to the overlay thickness used for the restrained drying shrinkage (i.e. 30 mm). Also, the free shrinkage specimen is able to dry out from all sides. However, this is not similar to the restrained overlay on top of the masonry substrate, which is only in direct contact with air at the sides and top surface.

2.7. Numerical Modelling

Numerical modelling, to validate the obtained experimental results, is commonly used. Additionally, by means of numerical simulations, extra information, into the failure mechanisms observed in the experiments, can be obtained. This is off course when the numerical model is able to describe the material behaviour in a detailed manner, i.e. material models containing multiple parameters are present. In this part of the study, only certain specific information is provided with respect to the numerical models used for this thesis. It is assumed by the author that the reader of this report has a basic understanding of the numerical modelling approaches currently present and the procedures of these numerical approaches (e.g. iteration schemes).

Different modelling approaches are described in the literature. For this research, only small scale experiments will be modelled. Therefore, only this scale of finite element analyses (FEA) is discussed in this section. However, if one requires a global overview of the different scales of numerical models, the reader is referred to, for example, [1, 23, 27].

2.7.1. URM - Simplified Micro-Scale Numerical Model

Masonry is a composite material consisting out of unit bricks and mortar joints. Its behaviour is strongly influenced by the presence of vertical and horizontal mortar joints, which are weak elements along which shear failure usually occurs. In [16] different factors, which might influence this shear failure, are investigated via numerical simulations of masonry shear triplet experiments. In this reference, calcium silicate bricks are used. A simplified micro-modelling strategy is adopted. For this type of model, the unit bricks and the mortar joints are individually taken into account [24]. For this type of approach, the mortar joints are modelled as zero-thickness interface elements with expanded geometry, to maintain the overall dimensions of the specimen.

In this modelling approach, it is assumed that all non-linear behaviour is expected at the zero thickness mortar-unit interfaces. Please note that in Figure (2.40) also an interface is presented at the centre of the masonry unit, representing a possible crack inside of the masonry unit.

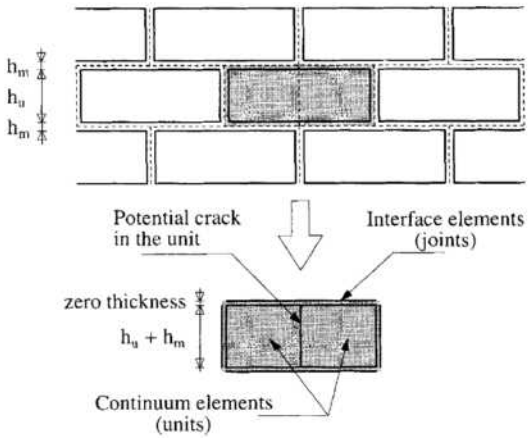

Figure 2.40: Suggested simplified micro-modelling technique. Units, modellied by continuum elements, are expanded in both directions by the mortar joint thickness. Mortar joints and potential cracks are modelled with zero-thickness interface elements [24].

By means of this simplified micro-scale model, the shear strength experiments, performed with masonry triplets, is validated. This method of modelling is assumed to be satisfactory for the strived for results (capturing the shear behaviour from the experiments). In [16], this simplified micro-modelling approach is used to validate the experimental results of shear triplet tests performed on calcium silicate masonry triplets. Different influence factors that could affect the shear-sliding behaviour (i.e. boundary conditions and dilatancy) are investigated. In this literature review, the numerical modelling approach is of main interest, for a more in detail description regarding the experimental setup the reader will be referred to the literature.

For this simplified micro-model, the elastic stiffness parameters of the unit-mortar interface are determined based on the actual dimensions of the units and mortar joints and their mechanical properties [24]. The following equations are used.

$$k_n = \frac{E_b E_m}{t_m(E_b - E_m)} \tag{2.5}$$

$$k_t = \frac{G_b G_m}{t_m(G_b - G_m)} \tag{2.6}$$

Where E_b and G_b are the elastic and shear modulus of the bricks, E_m and G_m are the same quantities for the mortar, t_m is the mortar joint thickness. The constitutive behaviour of these interface elements, in the linear elastic range, equals:

$$\begin{bmatrix} \sigma \\ \tau \end{bmatrix} = \begin{bmatrix} k_n & 0 \\ 0 & k_t \end{bmatrix} \cdot \begin{bmatrix} \Delta u \\ \Delta v \end{bmatrix} \tag{2.7}$$

Sliding failure is expected to occur along the bed joint of the masonry triplets. Therefore, the nonlinear behaviour is only assigned to this failure plane. The multisurface interface model proposed in [24] is used. The (expanded) masonry units are modelled via linear elastic continuum elements. This is a valid assumption since no failure of these elements is observed during the experiments [16].

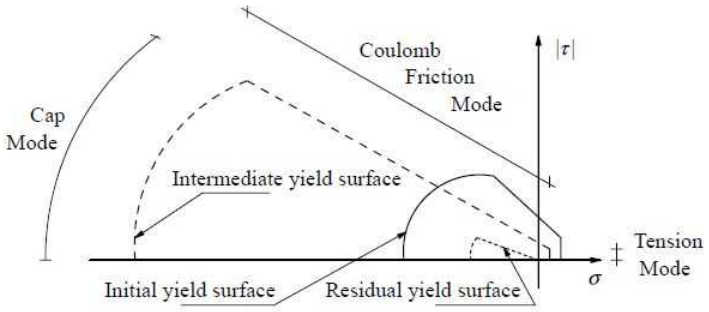

Figure 2.41: Composite interface model for nonlinear unit-mortar interface elements [24].

This interface model is described in more detail in [23]. This model assumes exponential softening for both the tensile and shear failure modes (mode-I and mode-II failure types). For the compressive behaviour, a hardening/softening law is used. For a detailed description regarding the yielding potentials etc. the reader is referred to the literature [23, 24]

As mentioned in section 2.2 uplift upon shearing (i.e. dilatancy) is present during the experiments. This is taken into account via a variable formulation proposed by [35]:

$$\tan(\Psi) = \tan(\Psi_0) \left\{ 1 - \frac{\sigma}{\sigma_u} \right\} e^{-\delta v_p} \tag{2.8}$$

Where:

v_p : plastic shear displacement
Ψ_0: dilatancy angle at zero confining stress and shear slip
σ_u: the pre-compression level at which the dilatancy goes to zero
δ: the dilatancy shear-slip degradation coefficient

In this formulation, the dilatancy angle is considered as a function of the plastic relative shear displacement and the normal confining pressure. The parameters are obtained by least-square fitting the experimental data. As mentioned earlier, this phenomenon must be taken into account to obtain realistic numerical results.

Additional to the modelling of the linear calcium silicate units and the non-linear unit-mortar interfaces also the steel loading and supporting plates of the experimental campaign are taken into account via linear elastic continuum elements [16]. By means of these steel plates, the loads (and reaction forces) are better distributed through the masonry specimen.

Part of the numerical simulations showed good coincidence with the experimental results. The shear stress versus tangential displacement diagram shows good agreement between both cases. However, in the experimental results, multiple peaks are present which are not shown from the numerical results, see Figure (2.42a).

It is assumed this is due to the fact that symmetry is used for the modelling procedure. Using symmetry assumes that both mortar joints will fail simultaneously or, at least, no distinction can be made anymore between different failure instants of these individual mortar joints. However, it is noted by the author of this report a full-scale modelling approach will not cause different results if both unit-mortar interfaces are provided with the same material properties. This will also result in only symmetric failure of the numerical model.

Comparing the normal displacements to the tangential displacements in Figure (2.42b) it is seen that for higher pre-compression levels (i.e. $0.6\,N/mm^2$ and $1.2\,N/mm^2$) the experimental curves show a negative normal displacement which is not captured by the numerical model. Two possible influences are mentioned, namely, the implemented boundary conditions the use of a simplified micro-model. It is noted that a detailed micro-model might result in better performance in this case, since for this modelling approach also the mortar material itself is taken into account in the model.

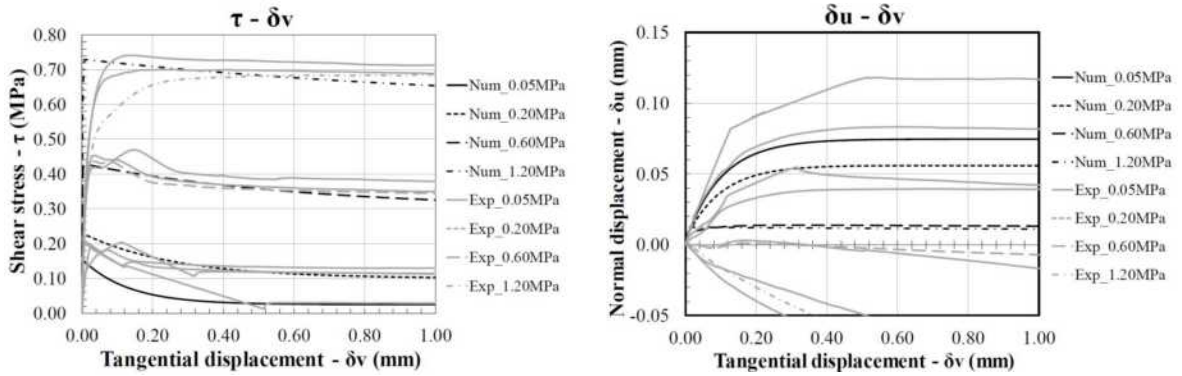

(a) Shear stress versus tangential displacement, triplet tests [16].

(b) Normal displacement versus tangential displacement, triplet tests [16].

Figure 2.42: Results standard triplet tests, initial simulations [16].

It is concluded from the numerical analysis that both the normal- and shear stress distributions along the nonlinear interface are non-uniform. Also, peak stresses are observed at the joint extremities.

By means of a parametric study, the influence of several parameters is examined. For more information, the reader is referred to the literature. By means of this research, a better understanding of the sliding failure in calcium silicate masonry triplets is obtained. More information, related to a detailed micro-modelling approach, is found in [3].

2.7.2. URM - SHCC Systems

A numerical model of the retrofitted URM material is, by the knowledge of the author, not widely investigated. However, a small amount of literature is present with respect to the modelling approaches considered [7, 14]. The first reference describes a FEM model using the FE program FEMIX 4.0 for modelling the four-point out-of-plane bending experiments performed on retrofitted masonry beams. A multi-directional fixed smeared crack model is used to simulate the crack formation in the SHCC overlay. Also for the mortar joints and masonry units, this material model is assumed.

In [7] it is verified if the shear strength experiments, performed on small (retrofitted) masonry wallets, can be modelled in DIANA using the available material models. Here the masonry wallets are modelled as one single continuum, no micro-modelling approach is considered. For the interface between the SHCC overlay and the masonry wallet, a Coulomb-friction model is assumed to be sufficient. The interfacial bond strength and friction angle coefficient are determined via the experimental results corresponding to the retrofitted masonry triplets, as described in section 2.6.

For this research, DIANA version 10.3 is used. Only the shear triplet experiments are investigated via a numerical modelling approach. Information about the mentioned literature is taken into account. The numerical analyses are discussed in Chapter (5).

3

Experimental Setups

3.1. Introduction

This chapter, provides a detailed description related to the different specimen considered, construction processes of these specimen, and finally, discusses the experimental setups used. A great amount of detail is incorporated here to enable a basis for future research.

The different specimen investigated are discussed first. This part of the report contains a detailed description of all the different geometries, building procedures, curing methods, and surface preparation of the masonry substrate. Additionally, the multiple parameters investigated during this experimental campaign are discussed. Finally, the used testing setups are shown. For the results of this experimental campaign, the reader is referred to the next chapter.

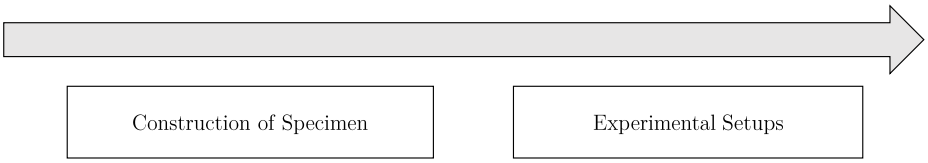

3.2. Materials

This experimental campaign examines only solid clay masonry specimen. For all specimen, general-purpose mortar is used. The material properties of both the mortar and masonry units are well documented at the TU Delft. The solid clay masonry units have a dimension of (210x100x50 mm). The normalized compressive strength of these units is determined to be equal to 28.31 N/mm^2, the elastic modulus is 8049 N/mm^2, and the flexural strength equals 6.31 N/mm^2. The former two parameters are determined to conform EN 772-1:2000. The flexural strength is based on tests following EN 6790:2015.

For all specimen, a mortar joint thickness equal to 10 mm is used. Both the compressive and flexural strength of this general-purpose mortar are determined to conform EN 1015-11:1999. The compressional strength is equal to 4.65 N/mm^2. The flexural strength is determined to be equal to 2.17 N/mm^2.

3.3. Construction of Specimen

This section describes the different steps of specimen construction. The following steps are considered and discussed in detail. Figures of the different stages are provided.

Two different types of specimens are built (i.e. masonry triplets and masonry beams), to examine the influence of a retrofitting overlay, on both the shear and flexural behaviour of masonry. Both in-plane and out-of-plane experiments are performed, i.e. shear triplet and four-point bending tests. The construction process of these different specimens is discussed hereafter. For all the specimens, the same clay bricks (210x100x50

mm) and mortar are used. It should be noted that the mortar used was of low strength quality. This type of mortar is used for the different experimental campaigns performed at the TU Delft to characterize the material properties, of different types of masonry, coinciding with existing building stock in Groningen.

A 'front' and 'back' side is created for the different specimen (i.e. the surface facing the mason during the production of the specimen), because of the construction process. The front side contains equally filled mortar joints. This is not the case for the rear of the specimen. This backside of the specimen is similar to the inside of a masonry cavity wall. The SHCC overlay is applied at the front side of the specimen only. This side is representative of the outside surface area of actual masonry buildings.

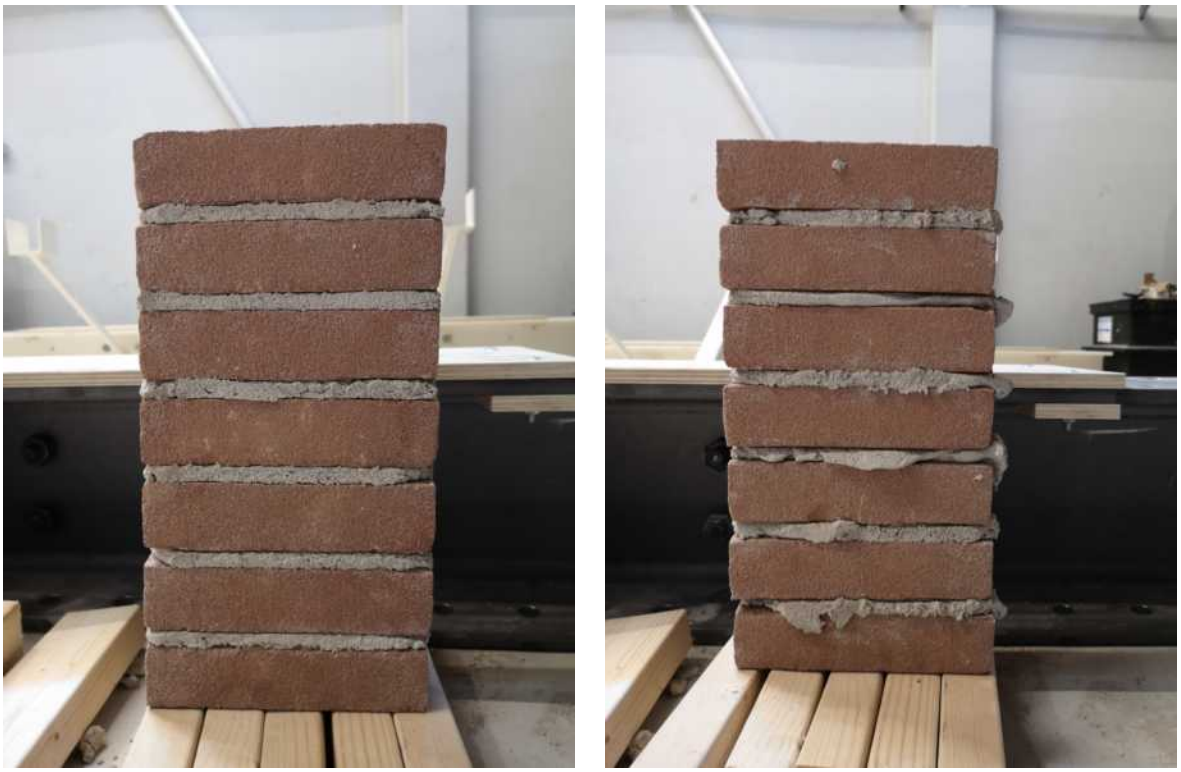

(a) Front side specimen

(b) Back side specimen

Figure 3.1: Front and back side of masonry specimen.

Below, the different steps of specimen construction are provided. The individual steps are described in more detail in the following sections of this report.

1. Building masonry specimen (both triplets and beamsl), see paragraph 3.3.1 and 3.3.2.
2. Preparation of masonry specimen for casting SHCC (masonry specimen at least 28 days old):
    - (For masonry beams only): apply steel transporting frame and place the specimen on a horizontal surface;
    - Brush of excess sand particles with steel brush;
    - Application of plastic mould;
        (a) Apply double-sided sticking tape to the masonry;
        (b) Apply plastic strips (size depending on SHCC thickness);
        (c) Apply ducttape on top of the plastic strips to ensure tight seal with masonry underneath.
    - Depending on the interface surface preperation: apply 25 mm wide sticking tape on top of the mortar joints;
3. Casting of the SHCC overlay, see paragraph 3.3.4.

- Mixing ingredients M6 [41] mixture;
- (Light) Wetting of masonry surface, just before casting, with wet towels to ensure qualitative bond with the SHCC;
- Casting SHCC overlay on masonry specimen and SHCC prisms (40x40x160 mm);
- Apply several layers of plastic foil over the fresly casted SHCC layer and fix the plastic foil by means of ductape.

4. Curing process (sealed and non-sealed curing conditions), see paragraph 3.3.4.
    - Non-sealed curing: remove plastic foil 24 hours after casting SHCC overlay. Leaving the plastic moulding on the sides;
    - Apply strain gauges on both SHCC prisms (free shrinkage) and masonry-SHCC specimen (restrained shrinkage);
    - Checking shrinkage strain gauges daily (first days two times per day).
5. Performing experiments (SHCC 28 ± 1 days old).

3.3.1. Masonry triplets

To investigate the in-plane shear strength of both the plain and retrofitted masonry triplet specimens are constructed. The experiments performed are coinciding with the following code NEN-EN 1052-3. Following this code, type A specimen is constructed. The masonry triplets consist out of three clay masonry unit bricks (210x100x50 mm) with two 10 mm thick mortar joints in between. The units are placed in a stacked bond pattern. The overall size of one masonry triplet equals (210x100x170 mm). After construction, one additional clay unit is placed on top of the triplet specimen (without mortar joint) to ensure a distributed vertical force is present in the new specimen, as prescribed by the stated norm.

(a) Front view masonry triplet.

(b) Overview multiple masonry triplet specimen.

Figure 3.2: Overview constructed masonry triplet specimen.

3.3.2. Masonry beams

Besides masonry triplets also masonry 'beams' are constructed for the out-of-plane flexural tests. These specimens are built with the same materials as the masonry triplets.

The dimensions of these specimen are related to literature [14, 33] and initial performed analytical calculations. This analytical calculation requires the flexural failure to be governing. It is concluded that a specimen consisting out of seven masonry units has sufficient length to ensure flexural failure. The total specimen consists out of seven clay masonry bricks and six 10 mm thick mortar joints. Again, a stacked bond pattern is used. The total length of one specimen equals 410 mm. An overview of this type of specimen is provided above, see Figure (3.1). During construction, vertical timber is used as support to obtain an as straight as possible specimen. The specimens are placed on timber supports, instead of directly placing them on the floor.

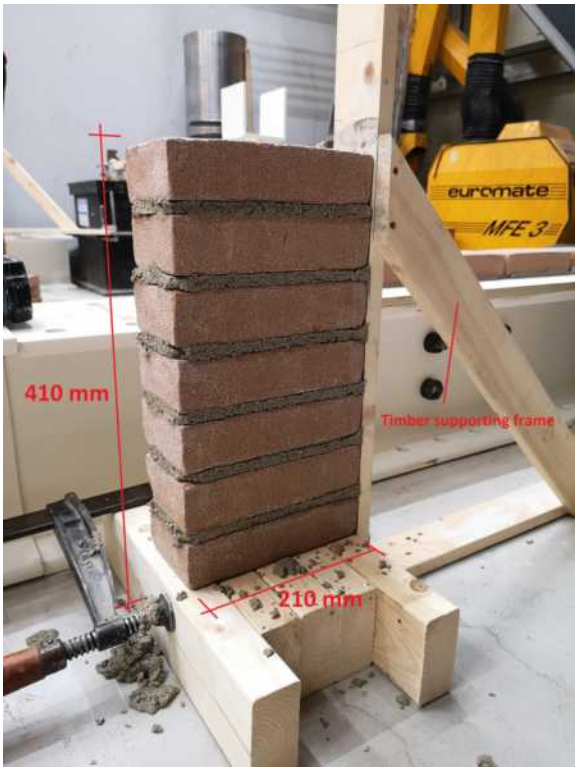

(a) Front view masonry beam specimen in vertical orientation.

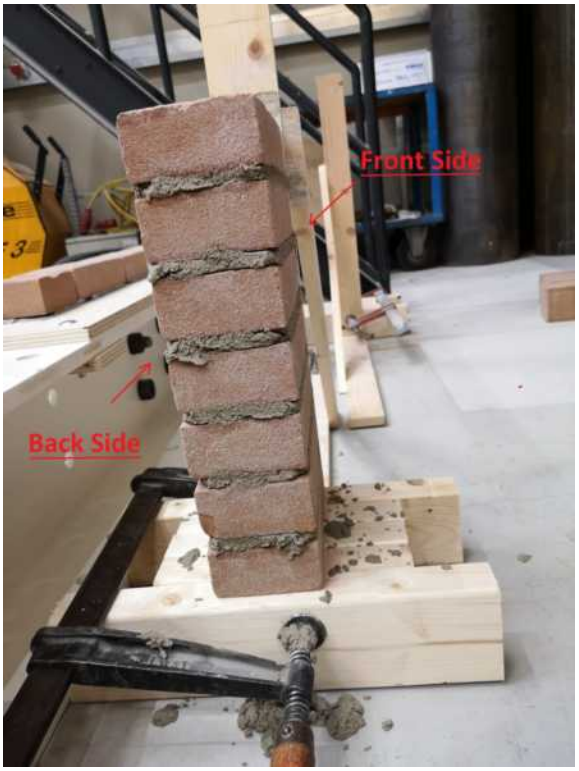

(b) Side view masonry beam specimen in vertical orientation

Figure 3.3: Building masonry beam specimen.

The casting of the SHCC overlay requires the specimen to be placed horizontally. Transporting these specimen from their vertical to their horizontal position is done with the help of steel supporting frames, see Figure (3.4a). A slight pre-compressive force is applied to the specimen by tightening the top bolts of this steel frame. The bolts were only hand tightened to avoid possible influences of the compressive force on the specimen. This frame is purely designed for a more stable transportation process.

(a) Masonry beam in steel supporting frame.

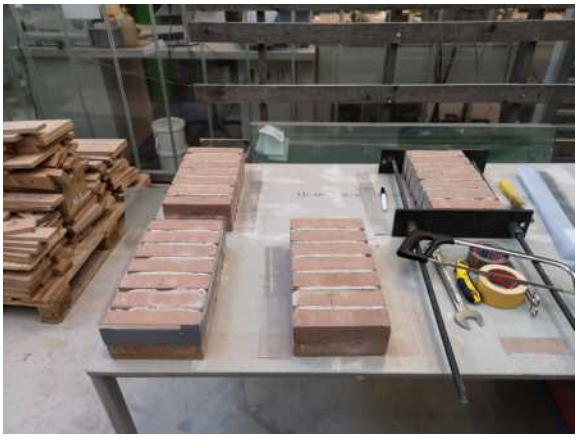

(b) Multiple masonry beams on table.

Figure 3.4: Transport process vertical to horizontal orientation masonry beams.

Initially, one single steel frame was constructed. The individual masonry beams were transported one by one via cart, see Figure (3.4a). However, for one specimen after removal of this steel frame, debonding of one masonry units from the mortar joint is observed. Debonding is assumingly because of the non-perfect vertical nature of these specimen and the horizontal tabletop onto which the specimens were placed. Another possible influence of the observed delaminations is the vibrations induced from the cart during transportation. Below a few figures show these observed failures. The failed joint has been glued. This debonding is only observed at the outside unit. In the designed four-point-bending setup, this joint is not in the constant bending moment region and, therefore, assumingly glueing of this failed interface does not influence the experimental results.

Figure 3.5: Delaminated masonry unit, masonry beam specimen

Soft foam panels are placed underneath the specimen, and steel frames are constructed for all ten specimens to avoid failure of the other masonry beam specimen. Additionally, the specimens were lifted by hand between the two locations to avoid possible vibrations from the previously used cart. Figure (3.6) shows the final location of the masonry beams specimen.

Figure 3.6: Final configuration masonry beams before casting SHCC overlay.

3.3.3. Parametric study

Based on the literature study, different parameters of interest are derived. For example, the thickness of the SHCC overlay determines the type of failure (i.e. ductile or brittle) under shear loading conditions, corresponding to [38] and [9]. Also, the surface preparation of the substrate material influences the behaviour of the SHCC overlay, see [21] and [22]. Finally, the influence of the curing conditions (i.e. sealed or unsealed curing) is examined, since curing in perfect laboratory conditions is not realistic for a practical application of a SHCC overlay. The following sections discuss the different parameters investigated in this experimental campaign.

Overlay thickness

In this research two different overlay thicknesses are examined. Based on the equations provided in [38] the required overlay thickness is determined. However, it must be noted that the equations provided in the reference are based on the double-sided application of the SHCC overlay on top of the masonry substrate. This is taken into account by adjusting the provided equations. The following equations are used and correspond to a single-sided overlay retrofitting approach:

$$F_{Mode,1} = 2 \cdot \tau_s \cdot h_b \cdot t_s + 2 \cdot h_b \cdot w_b \cdot (c_j - \Phi\sigma) \tag{3.1}$$

$$F_{Mode,2} = \tau_b \cdot h_b \cdot t_b + 2 \cdot h_b \cdot w_b \cdot (c_j - \Phi\sigma) \tag{3.2}$$

Where:

τ_s: SHCC shear resistance, taken equal to $6.9\,\mathrm{N/mm^2}$, by the assumption that the ultimate shear resistance is 50% more than the ultimate tensile resistance of the applied SHCC material ($4.60\,\mathrm{N/mm^2}$) [41].
τ_b: Masonry-SHCC interface bond strength, taken equal to $2.33\,\mathrm{N/mm^2}$ [38].
h_b: brick element height [mm], for this experimental campaign equal to 210 mm.
w_b: brick element width [mm], for this experimental campaign equal to 100 mm.
t_b: brick element thickness [mm], for this experimental campaign equal to 50 mm.

Rewriting the above equations to serve as a limit function for the overlay thickness:

$$t_s \leq \frac{t_b \cdot \tau_b}{2 \cdot \tau_s} \tag{3.3}$$

Which, is precisely similar to the one as used in literature. Thus, one-sided or two-sided application of the SHCC overlay does not influence this threshold.

Using the values stated above the critical thickness of the overlay equals 8.4 mm. A thickness smaller than this value is required to obtain the ductile Mode-I failure.

Unfortunately, in the calculation above a mistake has been made by the author of this report. The tensile strength of the SHCC material from [38] is taken into account (i.e. $2.1\,\mathrm{N/mm^2}$). However, this is not correct, since this value does not correspond to the actual mixture used (M6). The ultimate tensile resistance of this latter mixture equals $4.6\,\mathrm{N/mm^2}$. By this mistake the shear resistance of the overlay material is falsely determined to be equal to $3.2\,\mathrm{N/mm^2}$, which is much lower compared to the actual shear resistance of the mixture used, i.e. $6.9\,\mathrm{N/mm^2}$. Due to this error, the critical overlay thickness is wrongly determined to be equal to 17 mm, instead of the previously mentioned 8.4 mm. Based on the (wrong) critical thickness, two overlay thicknesses are investigated in this experimental campaign (10 and 30 mm). Both of these are higher compared to the correct critical thickness calculated, and therefore, based on equation (3.3), both thicknesses investigated are prone to brittle failure.

However, one might also question the validity of the shear bond strength determined in the literature (τ_b). This value is determined via the experimental results of masonry triplets with a 30 mm thick sprayed SHCC overlay on both sides. Since these specimen failed in a completely brittle manner, i.e. debonding of the applied overlays, and the shear strength of these retrofitted specimen is far higher compared to plain masonry triplets, the total shear strength is attributed to only the sliding interfaces of these two overlays. However, the

backside of the masonry triplets contained grooves, profoundly influencing the shear bond strength of the SHCC-masonry interface. From equation (3.3) it is clear this interfacial bond strength is of strong influence for the critical thickness of the overlay material.

From this critical thinking, it becomes clear that both the material properties of the overlay material and the interfacial bond strength between this overlay and the masonry substrate are of high interest. A high value of the SHCC shear strength results in a low critical thickness, as shown earlier. However, if a low interfacial shear strength is present, this same critical thickness is reduced drastically. This idea is treated further in the discussion of the experimental and numerical results.

Surface preperation

From the literature review, it is concluded that the surface preparation of the substrate material is of high importance for the performance of the retrofitted system. This surface preparation influences mechanisms like kink-crack trapping. The masonry specimen assumingly will start cracking in the mortar joints, in between the masonry bricks. This initial crack reflects into the SHCC overlay. Creating a debonded area above the initial crack location is showed to influence the results, see section (2.4.7). Therefore, the influence of a debonded area above the mortar joints is investigated. With the help of sticking tape a 25 mm wide strip is debonded at the location of the mortar joints, see Figure (3.7). With a mortar joint thickness equal to 10 mm only 15 mm (7.5 mm on each side of the mortar joint) of SHCC-masonry interface is debonded on top of each single mortar joint. The chosen width is not based on literature but expert judgement. From the authors' perspective, using even wider strips of sticking tape would have created specimens with not enough bond between the SHCC overlay and the masonry substrate. Assumingly, this induces a primary failure mechanism equal to delamination of the SHCC overlay, which is not strived for.

Figure 3.7: Applied tape on top of the mortar joints for several specimen (both masonry triplets and beams).

It must be noted that two layers of tape are used. For the first (bottom) layer duct tape is considerd because this showed good sticking properties to the masonry units. On top of this duct tape, a more smooth packing tape is applied to create an even more smooth surface onto which the SHCC overlay does not stick.

3.3.4. Application SHCC overlay

This section discusses the different steps related to the application of the SHCC overlay onto the different masonry specimen. See steps two and three, as mentioned in paragraph (3.3).

Before casting the SHCC, the masonry specimen are prepared. Below the different steps for both the masonry beams and triplets are mentioned. The only difference between the two types of the specimen is that the masonry beams required a steel supporting frame for transport, as discussed earlier.

2. Preparation of masonry specimen for casting SHCC (masonry specimen at least 28 days old):

- (For masonry beams only): apply steel supporting frame and place the specimen on a horizontal surface;
- Brush of excess sand particles with steel brush;
- Application of plastic mould;
  (a) Apply double-sided sticking tape to the masonry;
  (b) Apply plastic strips (height depending on SHCC thickness);
  (c) Apply ducttape on top of the plastic strips to ensure tight seal with masonry underneath.
- Depending on the interface surface preperation: apply 25 mm wide sticking tape on top of the mortar joints;

3. Casting of the SHCC overlay:

   - Mixing ingredients M6 mixture;
   - (Light) Wetting of masonry surface to ensure qualitative bond with the SHCC;
   - Cast SHCC mixture by hand. Casting SHCC overlay on masorny specimen and SHCC prisms (40x40x160 mm);
   - Apply several layers of plastic foil on top of the fresly casted SHCC layer and fix this plastic foil by means of ductape.

(a) Mixing ingredients SHCC mixture.

(b) Mixing bowl with all solid particles SHCC mixture.

(c) Final SHCC mixture.

Figure 3.8: Mixing procedure SHCC mixture.

Before casting the SHCC, the masonry was wetted to create a better bond between the SHCC and the masonry [9]. During an earlier performed small-scale trial casting, it is observed wetting of the clay unit bricks was required to ensure a bond between the two materials. Dry masonry sucks up the moisture from the SHCC, leaving a dry paste on top without any bond to the masonry substrate. The SHCC mixture used behaves more like a clay due to the fibres, see Figure (3.8c). Therefore, the SHCC is applied by hand, pasting it onto the masonry. The SHCC is lightly pressed onto the masonry.

(a) Application double-sided sticking tape.

(b) Application plastic mould.

(c) Fixation plastic mould by means of ducttape.

(d) Application of debonding strips (NOTE: not for all specimen).

(e) Pre-wetting masonry and application SHCC overlay by hand.

(f) Initial plastic foil layer.

Figure 3.9: Overview general casting procedure SHCC overlay.

For the masonry beam specimen, it is noted that during the casting process, the plastic mould slightly deflected over the long sides of the specimen. Through clamping wooden planks to these sides of the masonry specimens, this issue is fixed. Below additional pictures are provided related to the different steps of the SHCC application. The additional clamps are also shown.

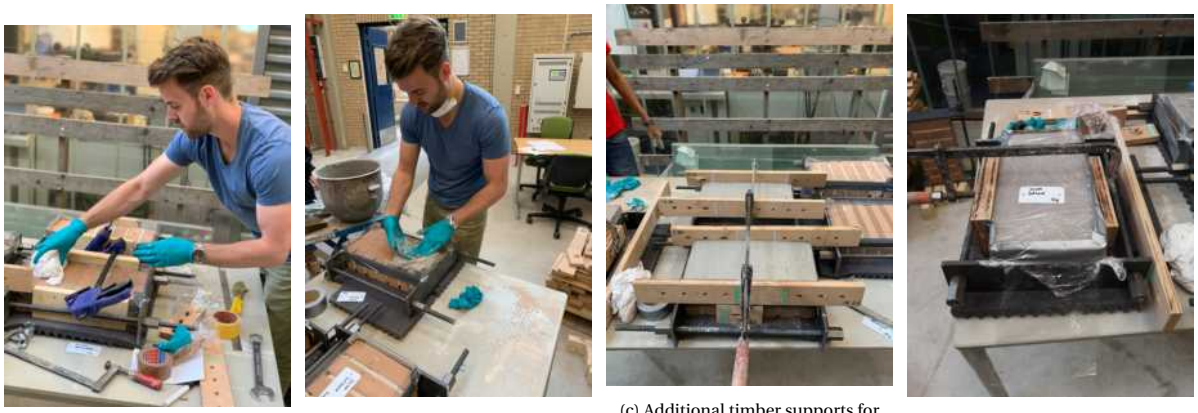

(a) Pre-wetting of the masonry.

(b) Application of SHCC mixture by hand.

(c) Additional timber supports for plastic mould (NOTE: only used for the masonry beam specimen).

(d) Retrofitted masonry beam in final stage.

Figure 3.10: Additional figures overview general casting procedure SHCC overlay.

It must be pointed out that the working procedure is similar for both types of specimen. Thus, pictures related to the triplet specimen are of equal importance for the masonry beam specimen. The only difference between the two types of specimen, for the casting procedure of the SHCC overlay, is the use of additional timber planks for the masonry beam specimen to avoid bulging of the plastic mould.

Curing conditions

The third and final parameter examined is the influence of the curing process (i.e. sealed or non-sealed curing). Non-sealed curing causes an increase in the drying shrinkage of the specimen which, if restrained, can lead to high tensile stresses in the SHCC overlay and, depending on the magnitude of these stresses, even cracking. The SHCC is restricted to shrink by its bond to the masonry substrate. Both free- and restrained shrinkage of the non-sealed specimen is examined. The free shrinkage is measured on prism specimen with equal thicknesses of the SHCC overlay applied to the masonry (i.e. 10 mm and 30 mm). These prisms are cut to size (40x10x160 and 40x30x160 mm) from the standard size prisms (40x40x160 mm), 24 hours after casting the SHCC. All edges and bottom of the prisms are sealed with tape to ensure similar drying conditions with the retrofitted specimen, which contain a plastic mould on the sides of the SHCC overlay, see Figure (3.11).

4. Curing process (sealed and non-sealed curing conditions):
    - Non-sealed curing: remove plastic foil 24 hours after casting SHCC overlay. Leaving the plastic moulding on the sides;
    - Apply strain gauges on both SHCC prisms (free shrinkage) and masonry-SHCC specimen (restrained shrinkage);
    - Checking shrinkage strain gauges daily (first days two times per day).

After casting off the SHCC overlay, all the specimen are wrapped in foil. After one day the foil is removed from the specimen used for the investigation in the non-sealed curing conditions. Analog strain gauges are glued to the surface of these masonry-SHCC specimen and the SHCC prisms. The restrained shrinkage is measured directly from the retrofitted masonry specimen on two locations, i.e. the centre and edge of the specimen, see Figure (3.11a). Only specimens with full-bond conditions between the overlay and the masonry substrate are used for this experiment. Thus, the influence of debonded areas above the mortar joints is not examined.

The retrofitted masonry beams were kept in laboratory conditions. However, the temperature inside this particular part of the laboratory is not constant. One set of SHCC prisms is placed inside a climate-controlled room (i.e. constant temperature and relative humidity), to investigate the influence of these possible temperature changes, see Figure (3.11c).

(a) Strain gauges restrained shrinkage masonry beams, laboratory conditions.

(b) Strain gauges free shrinkage SHCC prisms, laboratory conditions.

(c) Strain gauges free shrinkage SHCC prisms, controlled conditions.

Figure 3.11: Free and restrained shrinkage measurements SHCC overlay.

Figure 3.12: Boundary conditions free shrinkage specimen.

Initially, all the steel frames, used for transporting the masonry beams, are kept in place. However, one week after casting the SHCC, these frames are removed.

3.4. Experimental Setups

In the previous paragraphs, the different parameters of interest and building methods are described. In this section, the experimental setups used are discussed. In total, two types of experiments are conducted, i.e. shear triplet tests and four-point out-of-plane bending tests. The shear triplet tests are based on NEN-EN 1052-3:2002. The four-point out-of-plane bending tests are usually performed on wallets (i.e. small masonry wall specimen), as described in NEN-EN 1052-2:2015. However, in this experimental campaign, masonry beams are used to determine the flexural performance of the plain and retrofitted masonry. Determination of the flexural strength of unreinforced masonry, using beam like specimen, is discussed in [33]. A similar configuration is used for this research.

All the different specimen examined are summarized in the Tables (3.1) and (3.2). The different specimen numbers are provided in between brackets. These numbers are used throughout this report.

Table 3.1: Overview specimen shear strength; retrofitted masonry triplets.

	Bond (SHCC-Masonry)	Thickness Overlay	Pre-compression level	Amount of Specimen (Specimen no.)	Curing Conditions
Shear Triplet Tests	Full Bond	10 mm	$0.2\,N/mm^2$ $0.6\,N/mm^2$ $1.0\,N/mm^2$	3 (1-3) 3 (4-6) 3 (7-9)	Sealed Curing
		30 mm	$0.2\,N/mm^2$ $0.6\,N/mm^2$ $1.0\,N/mm^2$	3 (10-12) 3 (13-15) 3 (16-18)	
		Safety		6 (34-36/37-39)	
	Debonded	10 mm	$0.2\,N/mm^2$ $0.6\,N/mm^2$ $1.0\,N/mm^2$	3 (19-21) 3 (22-24) 3 (25-27)	
		30 mm	$1.0\,N/mm^2$	3 (28-30)	
		Safety		4 (40-42/43)	
	Full Bond	10 mm	$1.0\,N/mm^2$	3 (31-33)	Non-Sealed Curing
		Safety		1 (44)	

Table 3.2: Overview specimen flexural strength- masonry beams.

Four-Point Bending Tests	Bond (SHCC-Masonry)	Thickness Overlay	Amount of Specimen (Specimen no.)	Curing Conditions
	Reference Specimen	-	3 (1-3)	-
	Full Bond	10 mm 30 mm	2 (4-5) 2 (6-7)	Sealed Curing
	Debonded	10 mm 30 mm	2 (8-9) 2 (10-11)	
	Full bond	10 mm 30 mm	1 (12) 1 (13)	Non-Sealed Curing

It is strived for to perform all experiments after 28 days of casting the SHCC overlay. The exact ages of both the masonry and the SHCC are provided in the following chapter. The masonry material was already 28 days old when the SHCC overlay was applied. Thus, at the moment of testing the masonry substrate was older than the, by the norms prescribed, 28 days. However, assumingly this age is realistic for the actual structures in Groningen, for which this experimental campaign is performed. In this campaign, the age of the overlay material is governing.

3.4.1. Shear Triplet Test Setup

The setup used to determine the shear strength capacity of the retrofitted masonry triplets is based on the mentioned norm (NEN-EN 1052-3:2002). A setup designed by the TU Delft is used for this experimental campaign. This setup is already used for multiple research programs for the investigation of the material properties of both clay and calcium silicate masonry specimen under shear loading conditions. Therefore, the reliability of this setup is known to be sufficient. Below a global overview of the setup used is provided.

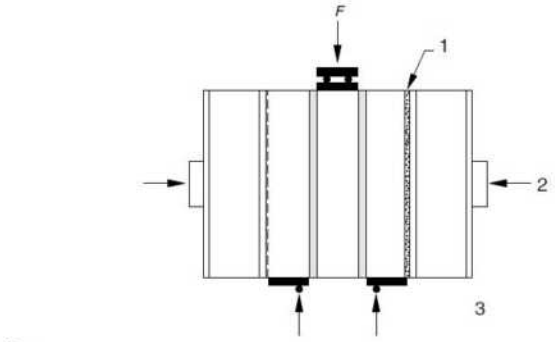

(a) Loading conditions shear triplet specimen (NEN-EN 1052-3:2002).

(b) Picture actual experimental setup at TU Delft [26].

Figure 3.13: Overview experimental setup used for shear strength experiments.

Figure (3.13) shows a gypsum plaster or other type of material used between the system which applies the pre-compression and the triplet specimen. For this experimental campaign, a gypsum plaster is used. For the retrofitted specimen the gypsum is applied to both the masonry and the SHCC overlay.

In total three different pre-compression levels are applied (i.e. 0.2 N/mm^2, 0.6 N/mm^2, and 1.0 N/mm^2). These load levels are based on the compressive strength of the units, which, in this case, is greater than 10 N/mm^2. For each pre-compression level at least three specimens are tested.

For both the shear and pre-compressive load, an independently operating jack is used. The shear loading in the vertical direction is applied through an apparatus with a capacity of 100 kN. This shear loading is

applied through a spherical joint onto the steel loading plate, which is placed on top of the central masonry unit. This jack operates in a displacement controlled manner with a loading rate equal to 0.005 mm/s. The pre-compressive loading is applied through a manually operated hydraulic jack. By this jack, it is possible to ensure that the pre-compressive loading remained between the ± 2% margin. This pre-compressive loading is applied in a loading controlled manner.

Additionally, three Linear Variable Differential Transformers (LVDTs) are attached to one side of the specimen. Two vertical LVDTs measure the relative vertical displacement of the middle masonry unit. One horizontal LVDT measured the horizontal displacement of the two exterior bricks, i.e. the dilatant behaviour of the masonry triplet, see Figure (3.14).

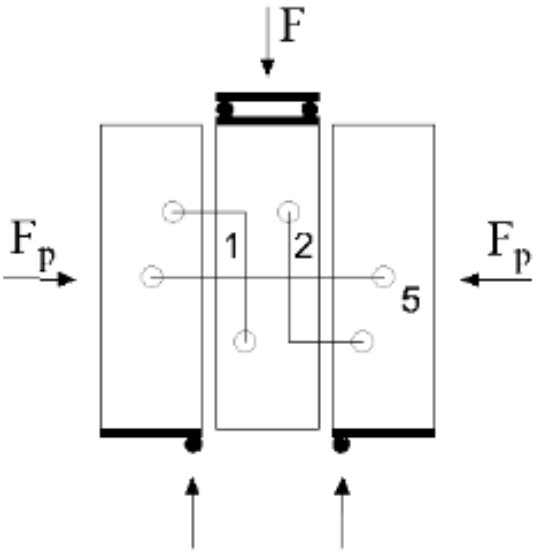

(a) Schematical view LVDT locations masonry triplet specimen.

(b) Picture LVDT locations masonry triplet specimen.

Figure 3.14: Overview setup LVDTs used for shear strength experiments.

Additionally, to examine the crack pattern in the different retrofitted specimen, a Digital Image Correlation (DIC) technique is used. This technique provides additional information into the failure mechanisms observed.

Properties of plain masonry triplets are well documented at the university and, therefore, no experiments are performed on these reference type of specimen. All the experimental results are discussed in the next chapter.

3.4.2. Four Point Out-of-Plane Bending Test Setup

The experimental setup used for the flexural tests is based on the literature review performed. Initially, it is planned to test both plain and retrofitted specimens. The retrofitted masonry beams are tested in a four-point out-of-plane bending setup. Additionally, the standard NEN-EN 1052-5:2015 is also used to determine requirements for the setup.

Due to the brittle nature of these specimen (as observed during the construction phase) steel transport frames are used for installing the different specimen into the testing setup. These frames are removed after the full setup is ready to perform the test to avoid premature failures.

The support and loading positions are based on the requirement stated in the previously mentioned standard (i.e. a minimum of two-bed joints must be present within the constant bending moment region). In Figure (3.15), a global overview of the testing setup is shown.

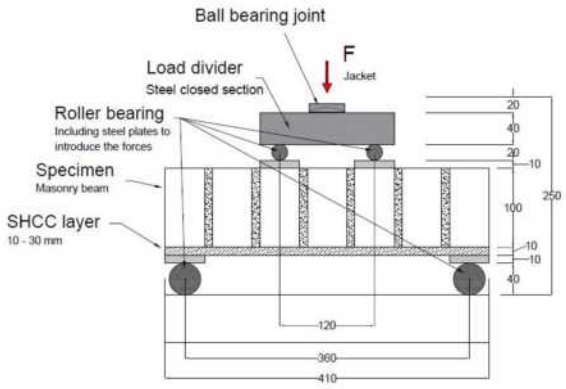

(a) Overview flexural setup including geometry.

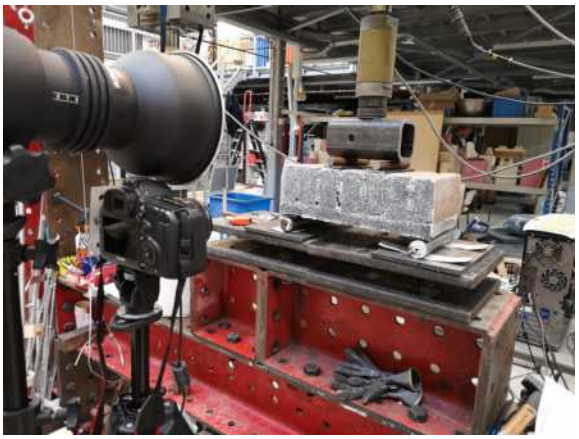

(b) Front view retrofitted masonry beam with the DIC pattern applied.

Figure 3.15: Overview experimental setup four-point out-of-plane bending tests.

One single apparatus, with a capacity of 100 kN, is used for this test. All the tests are performed in a displacement controlled manner. Different load speeds (e.g. 0.0005 mm/s and 0.005 mm/s) are considered. Initially, the slowest loading speed is used. For later tests, this loading speed is increased, as it is noticed this does not change the obtained results. The hydraulic jack transfers its load via a ball bearing onto a steel closed section which, in turn, divides the total load to the two loading points on top of the specimen. This ball bearing is used to overcome any imperfections of the specimen, which will induce eccentricities of the loading positions. As for the loading positions, the two supports underneath the specimen consist out of roller bearings. These supporting rollers are of the same length as the depth of the specimen (210 mm). Additionally, to avoid stress concentrations, steel plates are used in between the specimen and the rollers.

It should be noted that Figure (3.15b) shows that a pattern is applied to the retrofitted masonry specimen. This pattern is used for the Digital Image Correlation (DIC). Using this DIC, a more in-depth understanding of the observed failure mechanisms is obtained. The results of the DIC are presented alongside the other testing results.

In total, four LVDTs are applied to each (retrofitted) masonry beam to measure different deflections. Three LVDTs measured the horizontal deflection of both the masonry bricks itself and the SHCC overlay (cracking). One LVDT is applied vertically to measure the vertical deflection of the total specimen.

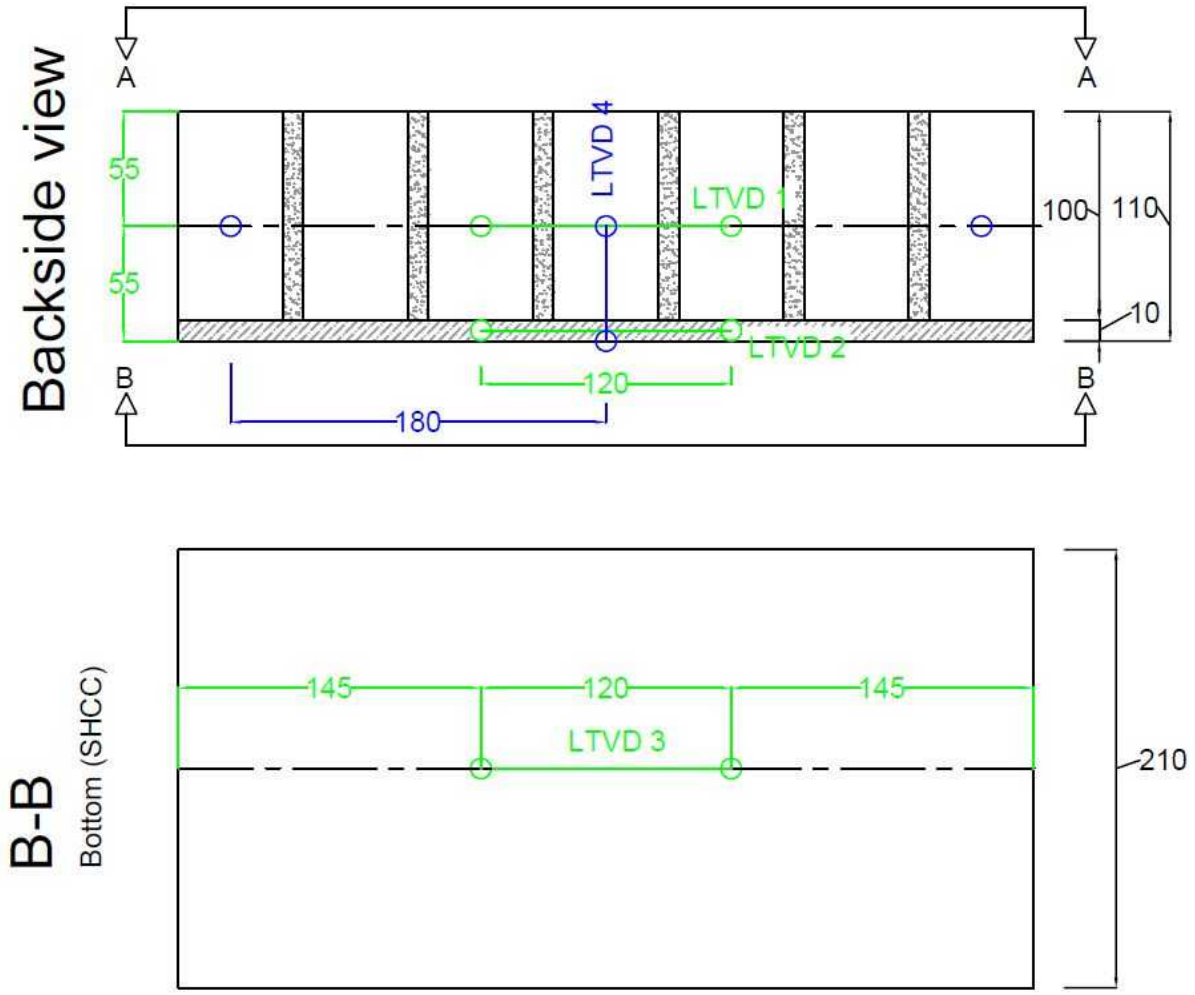

Figure 3.16: LVDT setup flexural test.

3.4.3. Digital Image Correlation (DIC)

Nowadays, the use of Digital Image Correlation (DIC) techniques becomes 'normalized'. In different fields of operation, this technique is employed, and the accuracy is tested and compared to other, more conventional, ways of measuring. For example, [5] uses this technique to investigate the accuracy of this method in the determination of the failure mechanisms related to landslides. However, in [29] the usability of DIC in utilizing this technique for observing the development in cracks in reinforced concrete beams is investigated. For these type of experiments, usually, strain gauge measurements are performed. However, these (conventional) techniques have several drawbacks, e.g. these traditional strain measurement techniques rely on direct contact between the instrument and the specimen surface. However, DIC is a non-contact measuring technique, thus not depending on any surface conditions of the specimen examined.

In this report, the DIC technique is used to obtain more detailed information related to the failure mechanisms of the different (retrofitted) masonry specimen tested in the experimental campaign. For this technique to work, a non-uniformly distributed pattern needs to be applied to the surface of interest. Via this stochastic pattern, the DIC method can compare the initial stage to the deformed stages of the specimen. Through the analysis of these different stages, the program can determine different outputs, e.g. normal strain, shear strain, and von Mises strain fields. [29] states that if the specimen examined is loaded past its linear elastic stage, the von Mises strain field must be considered. The propagation of cracks is estimated with higher precision, using this strain field.

For this research, a two-dimensional DIC method is applied. In Figure (3.17), a schematic overview of this

2D DIC technique is shown. The program analyses the pictures by sub-structuring these into so-called subsets [5]. These subsets are defined by their stochastic pattern, applied to the surface of interest. Because of the randomly applied pattern, no double subsets are assumed to be present.

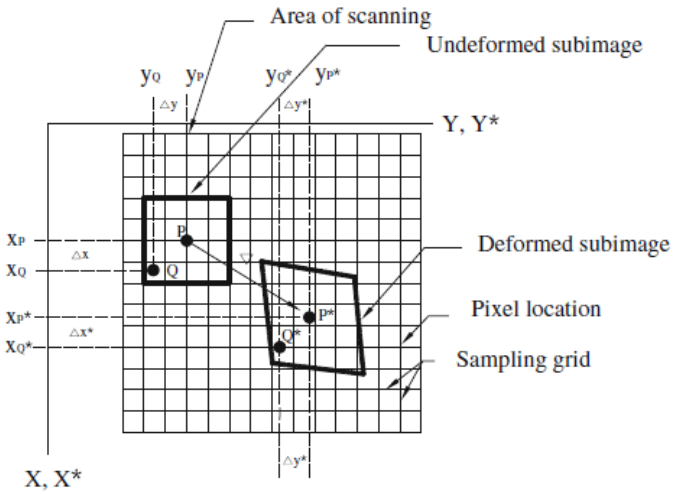

Figure 3.17: Schematic overview initial and deformed subimages on surface of interest [29].

The centre of each subset (or sub-image) P is determined and after the event (e.g. loading of the specimen) this central point must have moved if deformations of the specimen are present. P* denotes the new location of this centre point. By measuring the incremental displacement of this centre point, the strain field is determined.

Both of the mentioned references provide a more in-depth description of the DIC technique applied. It is not in the scope of this report to provide the reader with all the equations, related to the derivation of strain fields etc. The use of DIC is well-known at the Stevin Laboratory of TU Delft. For this experimental campaign, a SLR camera is used for taking the pictures of the different specimen, onto which a random pattern is applied. The camera used has a high resolution of 50 megapixels. For every experiment (shear or flexural), the camera is positioned at the same height and distance from the specimen. Additionally, to ensure the camera can catch every detail, during all experiments, a studio light is used to ensure the proper lighting for the photos.

The stochastic pattern is applied in two steps. First, a layer of white paint is applied to the masonry (or SHCC overlay) surface to serve as a good basis for the pattern. Secondly, after drying of the first layer of paint, an additional (thin) layer of white paint is applied to the same surface. However, immediately after this second layer is applied, black sand is sprayed onto this wet paint layer. This sand is applied via a paint sprayer, loaded with this black sand instead of paint. During this experimental campaign, it is always strived to obtain a qualitative pattern containing equal amounts of sand at every spot of the surface of interest. Before performing the experiments, the specimens are left to dry.

4

Experimental Results

4.1. Introduction

This chapter presents the experimental results. The following order is used:

1. Shrinkage measurements;
2. Shear strength - shear triplet tests;
3. Flexural strength - masonry beam tests.

Initially, a global overview of the results is presented using graphs, tables, and pictures. With this global overview, a general understanding of the failure modes observed and of the influence of the different parameters examined are strived to obtain (e.g. SHCC thickness).

This global overview is followed by a more in-depth analysis of the experimental results, i.e. combining the DIC results with the earlier presented results to obtain a more detailed understanding into the actual failure mechanisms of the specimen.

Finally, different parameters required for the numerical modelling of the experiments are derived from the experimental results. The numerical models, however, are discussed in the next chapter.

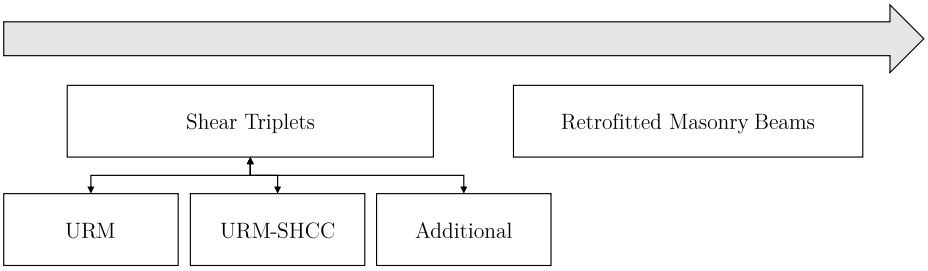

4.2. Shrinkage

Both free and restrained shrinkage of the SHCC overlay material is investigated. Recall Figures (3.11) and (3.12). Due to the high cement content in the SHCC material high values of shrinkage are expected.

The masonry substrate, onto which the SHCC overlay is applied, restrains the free deformation of the overlay material due to the interfacial bond between the two materials. This initiates additional stresses in the retrofitted cross-section. Also, sufficient strength of the interface is required to prevent complete delamination of the overlay from the masonry.

The following parameters are investigated:

- Free and restrained shrinkage;
- Thickness SHCC layer (10 and 30 mm);
- Climate conditions; and
- Influence of the direction of the bed joints for the shrinkage of the overlay material

As mentioned above, two different directions of restrained shrinkage are measured, i.e. parallel and perpendicular to the mortar joints. [38] states that the direction of the mortar joints influences the shrinkage measurements. In Figure (4.1) the different shrinkage measurement setups are shown.

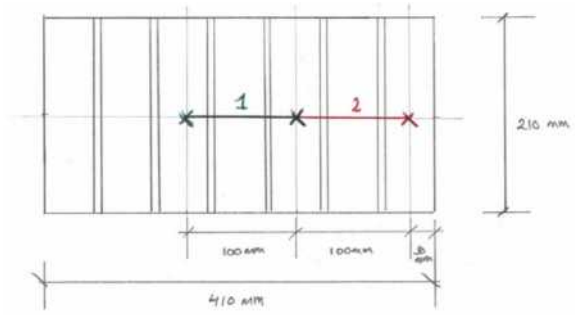

(a) Direction of shrinkage measurement SHCC overlay on masonry beam specimen.

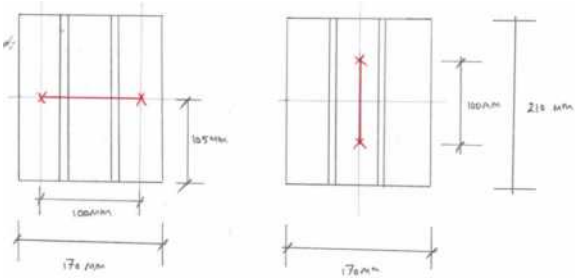

(b) Direction of shrinkage measurements SHCC overlay on masonry triplet specimen. Left: perpendicular to mortar joints, right: parallel to mortar joints.

Figure 4.1: Directions of shrinkage measurements SHCC overlay different specimen.

In the following figures, the experimental results are depicted for all the different specimen. Measurement data up to 28 days of age are included. The strain gauge value, represented in terms of 0.01 mm, is plotted against the age of the SHCC material. It should be noted that once a day, the measurements are performed. However, for both the free shrinkage and masonry beam specimen, two measurements are performed for the first couple of days (first one early in the morning and the second one in the late afternoon). This is shown by the jumps in measured shrinkage on the same day. Positive values, as shown in the following figures, corresponds to a shortening of the specimen (i.e. shrinkage).

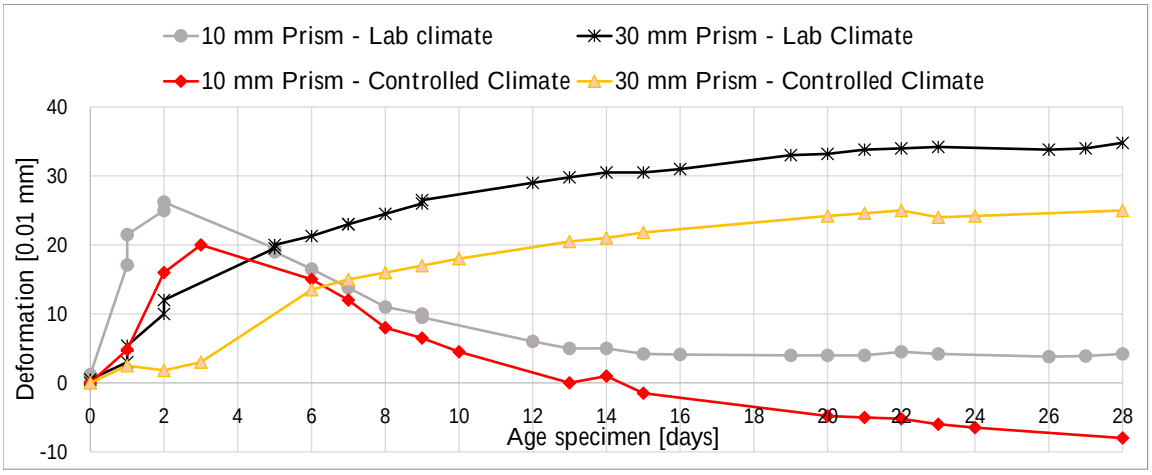

Figure 4.2: Measured shrinkage - Free shrinkage, SHCC prisms. Both 10 and 30 mm thickness investigated.

In Figure (4.2), the results of all the free shrinkage specimen are provided. It is clearly shown that the thinner 10 mm specimen has a quicker increase in shrinkage during the first couple of days, compared to the 30 mm SHCC specimen. The difference in exposed surface to total volume ratio of the specimen explains this shrinkage. The thin prisms have, compared to their total volume, a large amount of surface area exposed to the outside environment, causing it to dry out faster.

However, an additional explanation of this result is also possible. The SHCC prisms are exposed to drying of their top surface, see Figure (4.3). For the thinner, 10 mm thick, SHCC prisms this might induce curvature of the total specimen, leading to higher values of the measured shrinkage because the points of measurement move together. This fact is substantiated by the shown influence of strain gauge measurement with respect to an applied curvature.

Far after the 28 day measurement period, the influence of a possible curvature of the thin SHCC prism on the strain gauge is investigated. By applying a small pressure on the outer ends of the specimen, just by 'bending' the specimen with two hands, large influences in the value depicted by the strain gauge are observed, satisfying the earlier statement made.

Besides the rate of shrinkage measured, also the magnitude of total deformation differs between the different specimen. The peak value of the 10 mm thick prism cured in the laboratory equals ±0.26 mm. After this peak, the contraction of the specimen reduced back to ±0.04 mm. This reduction is obtained by thoroughly drying out of the thin specimen, causing the possible curvature of the specimen to diminish. Both 30 mm SHCC prisms do not show this type of behaviour during the 28 days of measurement. However, after a longer period, these thicker specimens do show the same trend. This trend is seen from the specimen in the climate-controlled room. These specimens are kept here long after the initial testing phase.

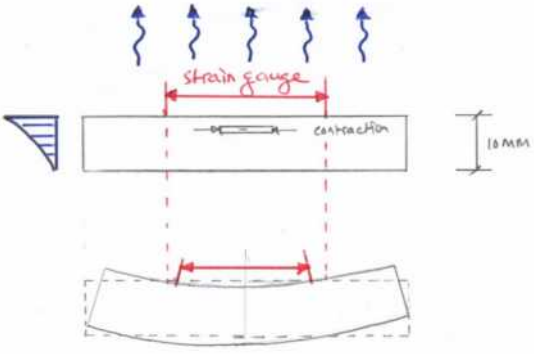

Figure 4.3: Influence measurement data shrinkage 10 mm SHCC prisms. Sides and bottom of specimen sealed off. Drying of top surface only possible.

Additionally, it is shown in Figure (4.2) that for both the 10 and 30 mm thick SHCC prisms a difference is present between the specimen cured in lab climate conditions and the specimen cured in temperature-

controlled conditions. The specimen cured in controlled conditions show overall lower values of deformation compared to the specimen cured in laboratory conditions. The curing conditions in the laboratory are less stable, compared to the controlled conditions. Airflow due to, for example, opened cargo doors profoundly influences the shrinkage of the specimen.

Figure (4.4) presents the shrinkage, as measured from the masonry beam specimen. Two different locations on the SHCC overlay are used to investigate the restrained shrinkage of this overlay on top of the masonry substrate, as was previously shown in Figure (4.1). Beforehand, it is thought that the strain gauge placed in the centre of the specimen measures smaller values of shrinkage, due to the higher level of restraint of the overlay. This is best shown for the thicker, 30 mm SHCC overlay. Initially, this is also true for the 10 mm overlay. However, after ±15 days, the central strain gauge provides higher measurement results, compared to the edge of the specimen.

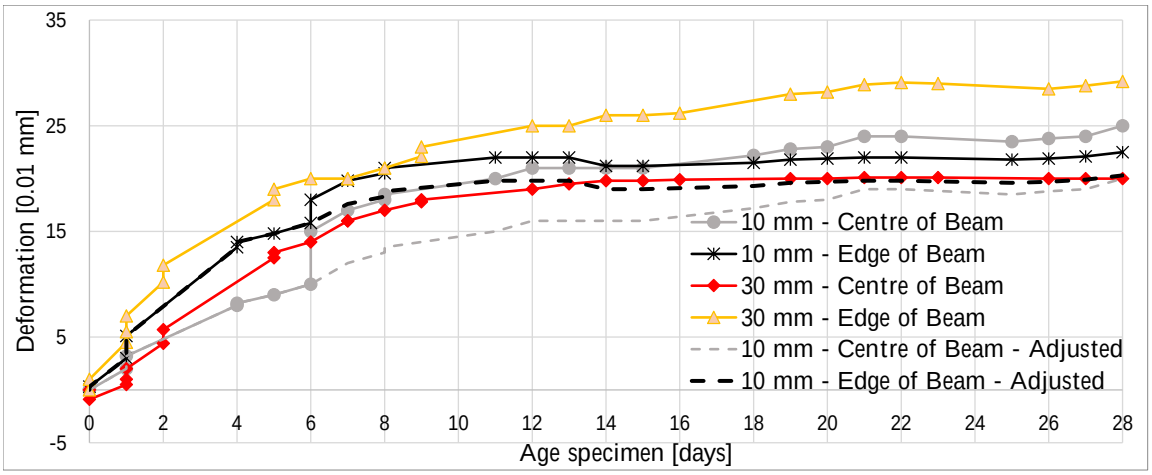

Figure 4.4: Measured shrinkage - Restrained shrinkage, masonry beams. Shrinkage measured perpendicular to the mortar joints.

As mentioned in the previous chapter, steel supporting frames are used during the construction phase of the masonry beam specimen. These frames are kept in place during the first seven days after casting of the SHCC. Removal of these frames resulted in a significant jump of the strain gauge values for the 10 mm thick SHCC overlay specimen, see Figure (4.4). It is thought that the steel supporting frame created a light curvature in the masonry beam, before casting the SHCC. After the steel frame was removed, also the prescribed deformation of the masonry substrate was removed, causing extra deformation at the top of the SHCC overlay. The specimen with a 30 mm thick overlay was not (noticeable) affected by the removal of the steel frames. This, again, shows the strong influence of strain measurements of the 10 mm thick specimen, with respect to curvatures of the specimen.

Taking into account the sudden increase in deformation, due to the removal of the steel supporting frame for the 10 mm overlay specimen, more comparable results, with respect to the 30 mm overlay specimen, are obtained. Figure (4.4) represents the adjusted results by the dotted curves. With these adjusted results, it is shown that the edges of the overlay are less constraint during drying and therefore show a higher amount of deformation. In the following sections and figures, only the adjusted results are presented.

The same figure also shows that the edge location of the beam with a 30 mm thick SHCC overlay shows to be less restrained compared to its 10 mm thick overlay counterpart. A higher level of shrinkage deformation is observed for the masonry beam with a thicker overlay.

As mentioned, the influence of the bed joint direction, with respect to the measured shrinkage, is investigated. The experimental data is shown in Figure (4.5). It is shown that the direction of the masonry bed joint influences the restrained shrinkage of the SHCC overlay. Shrinkage measured parallel to the mortar joints

shows to be more restrained, compared to the direction perpendicular to the mortar joints. Thus, the ratio between the SHCC-unit and SHCC-mortar area highly influences the level of restrained. This corresponds to the findings presented in [38].

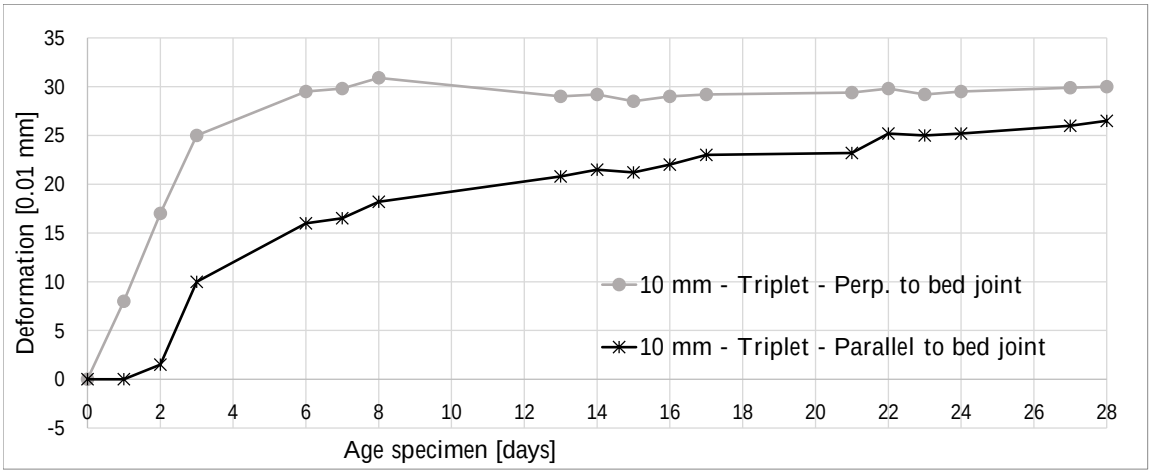

Figure 4.5: Measured shrinkage - Restrained shrinkage, masonry triplets.

The results coinciding with the triplets are compared to the data of the masonry beams in Figure (4.6). For this comparison, the 'perpendicular to the bed joints' data of the masonry triplets are used, since this direction of the bed joints corresponds with the masonry beams. A blue curve represents the data of the triplet. From this figure, it is concluded that the shrinkage of the masonry triplet progressed more quickly, compared to the beam specimen. Multiple reasons can be thought of for this observed difference, e.g. less constraint of the SHCC overlay due to a smaller amount of mortar joints for the triplet specimen. At the 28 day mark, the measured deformation of the triplet specimen is equal to the data collected from the edge position of the beam specimen with a 30 mm thick overlay. This can be explained by looking back at Figure (4.1). The edge location of the masonry beams contains an equal amount of mortar joints as for the triplet, creating similar boundary conditions.

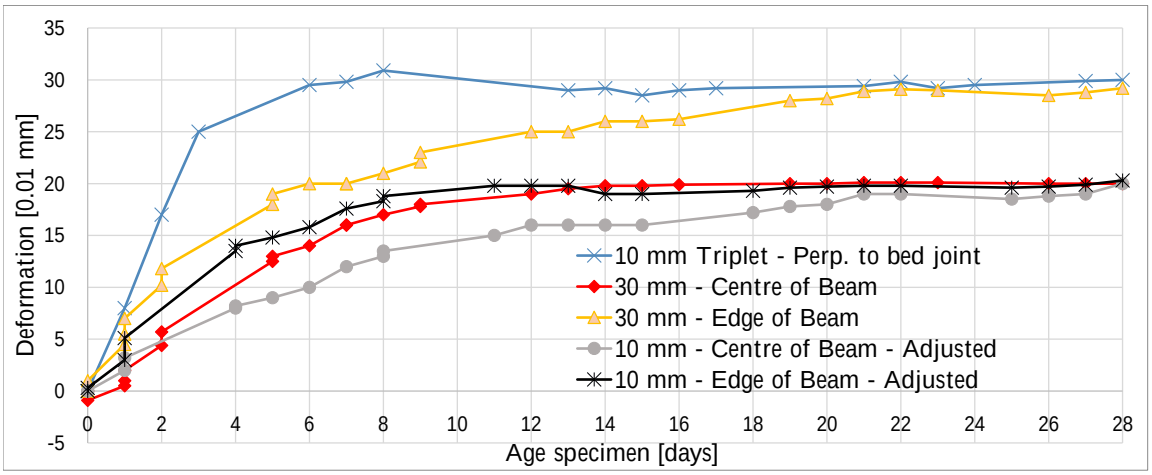

Figure 4.6: Measured shrinkage - Restrained shrinkage, masonry beams versus triplet.

Comparing all the specimen with an 10 mm and 30 mm thick SHCC overlay, respectively, generates results as shown in Figure (4.7) and (4.8). In the first figure, the specimen with a 10 mm thick overlay are compared. It is shown that the peak value of the non-restrained SHCC prism (red curve) equals the measured shrinkage of

the SHCC overlay on top of the masonry beam specimen. The restrained shrinkage is of comparable magnitude with the free shrinkage measurements. Delamination of the overlay is not observed after demolding the specimens. Thus, the only possibility of these comparable results is the development of cracks in the overlay material, causing an increase in deformation. However, these cracks are not visible with the naked eye, but during the shear strength experiments, cracks parallel to the mortar joints are observed, see paragraph 4.3.3. The direction of these cracks corresponds to the measured shrinkage perpendicular to the bed joints.

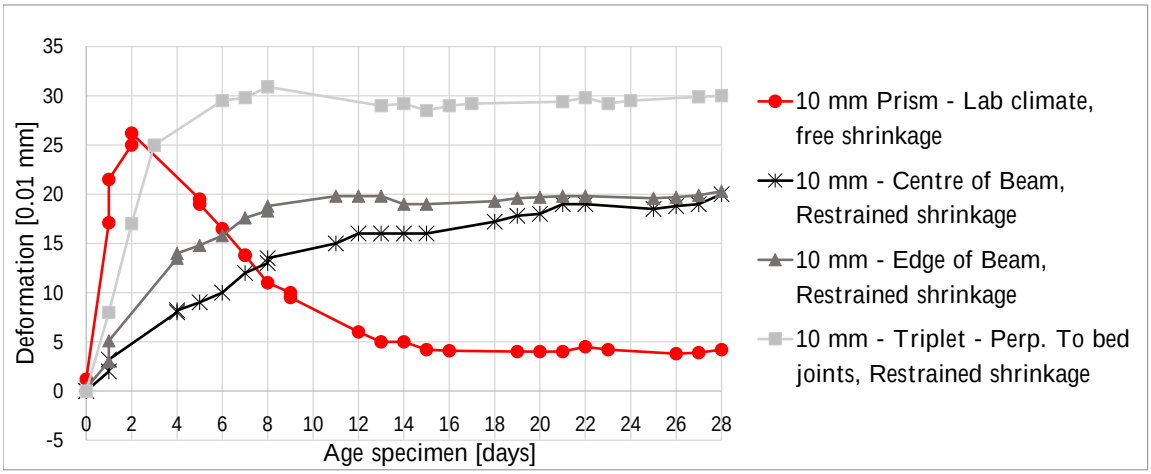

Figure 4.7: Measured shrinkage - All specimen with an 10 mm thick SHCC overlay. Both free and restrained shrinkage. Shrinkage measured perpendicular to the mortar joints.

The specimen with a 30 mm thick overlay shows a higher level of constraint, compared to the specimen with a 10 mm thick overlay, see Figure (4.8). This is more in line with the findings of [38], i.e. larger free shrinkage compared to restrained shrinkage. Again, no formation of cracks is observed.

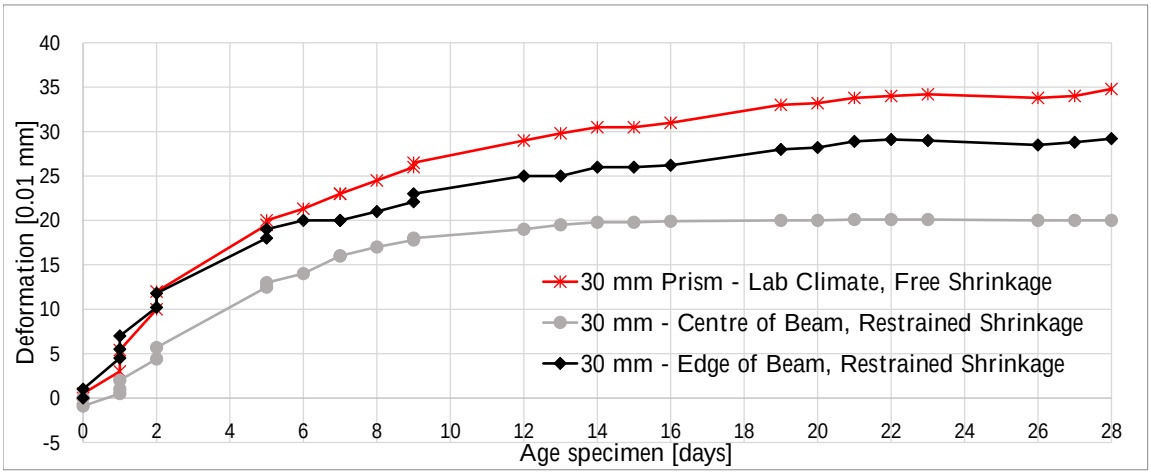

Figure 4.8: Measured shrinkage - All specimen with an 30 mm thick SHCC overlay. Both free and restrained shrinkage. Restrained shrinkage measured perpendicular to the mortar joints.

4.2.1. Analtyical approach tensile stresses due to restrained shrinkage

Using simple analytical calculations, the amount of stresses in the retrofitted cross-section, due to the restrained shrinkage, is investigated. These calculations are based on [42] and are used to gain a conservative estimation of the stress distribution in the specimen. This reference proposes an analytical tool to determine different stresses in and at the interface of, the repair material. It is investigated if SHCC is a good material to use for concrete repairs. Assumingly, this analytical tool is also valid for masonry retrofitting purposes.

Because of the strain-hardening behaviour of the retrofitting material, a different approach is used to determine the stresses in the overlay material. Usually, for conventional concrete overlays (i.e. brittle materials), a method as described in [32] can be used. However, the described method in this reference assumes only one elastic modulus of the material, i.e. the linear elastic stiffness, up to failure. Using this method causes a significant overestimation of the tensile stresses in the overlay. The difference in these methods is shown in Figure (4.9).

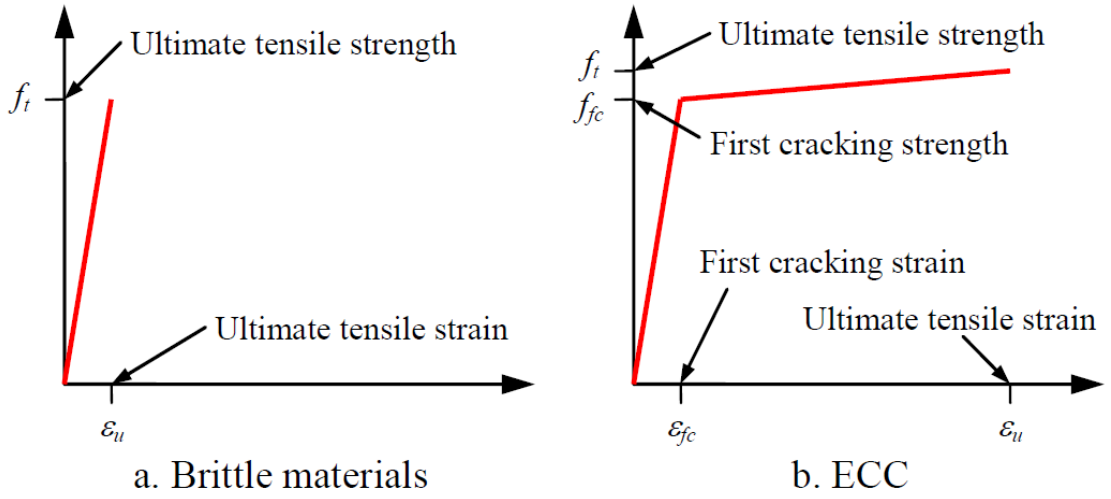

Figure 4.9: Tensile stress-strain curves of (a) brittle materials and (B) SHCC (ECC) [42].

In [42] equations are proposed to determine the tensile stresses in the overlay material initiated by this restrained shrinkage. These equations are shown below.

$$\sigma_{xx}^{precr} = \frac{E_{precr}\varepsilon_{fc}}{\frac{E_{precr}h_r}{E_s h_s}+1}\cdot\left(1-\frac{2}{e^{\lambda_{precr}\frac{L}{2}}+e^{-\lambda_{precr}\frac{L}{2}}}\right) \tag{4.1}$$

$$\sigma_{xx}^{postcr} = \frac{E_{postcr}\left(\varepsilon_{sh}-\varepsilon_{fc}\right)}{\frac{E_{postcr}h_r}{E_s h_s}+1}\cdot\left(1-\frac{2}{e^{\lambda_{postcr}\frac{L}{2}}+e^{-\lambda_{postcr}\frac{L}{2}}}\right) \tag{4.2}$$

Where:

$$\lambda_{precr} = \sqrt{\frac{K}{E_{precr}h_r}+\frac{K}{E_s h_s}} \tag{4.3}$$

$$\lambda_{postcr} = \sqrt{\frac{K}{E_{postcr}h_r}+\frac{K}{E_s h_s}} \tag{4.4}$$

In which:

E_{precr}	:	Young's modulus before first cracking
E_{postcr}	:	Young's modulus after first cracking
E_s	:	Young's modulus substrate material
h_r	:	thickness overlay material
h_s	:	thickness substrate material
ε_{fc}	:	first cracking strain overlay material
ε_{sh}	:	differential shrinkage strain overlay material
K	:	interfacial shear striffness
L	:	length of specimen

By superimposing the stresses calculated for both stages of the stress-strain curve, the total stresses in the SHCC overlay material induced by restrained drying shrinkage is determined:

$$\sigma_{xx} = \sigma_{xx}^{precr} + \sigma_{xx}^{postcr} \tag{4.5}$$

All mentioned quantities mentioned are known, except the interfacial shear stiffness K of the SHCC-masonry interface. However, with analytical analyses, it is determined that this quantity does not influence the tensile stresses in the interface significantly. For this analysis, this quantity is set to equal $10\,\mathrm{N/mm^3}$, similarly as in the literature.

For these calculations, the experimental results corresponding to the masonry triplets, in the parallel to the masonry joint direction, are taken into account. In Table (4.1) the mechanical properties of the SHCC overlay material used are summarized. The mentioned shrinkage is determined in this experimental campaign. All the other properties are derived from the mentioned reference.

Table 4.1: Mechanical properties SHCC overlay material [42].

Age [days]	Shrinkage ε_{sh} [$\cdot 10^{-6}$]	First cracking strength f_{fc} [N/mm^2]	Ultimate tensile strength f_t [N/mm^2]	Young's modulus before first cracking E_{precr} [N/mm^2]	Young's modulus after first cracking E_{postcr} [N/mm^2]
3	1000	2.45	3.68	9940	24
7	1650	3.12	4.23	14850	31
28	2650	3.58	4.59	18500	32

By using the shown equations and the mechanical properties mentioned above, the tensile stresses in the SHCC overlay are calculated. The resulting tensile stresses are summarized in Table (4.2). It can be seen that these values are similar to those mentioned in [42]. The same overlay material is considered in this experimental campaign.

Table 4.2: Calculated critical stresses in the SHCC overlay.

Age [days]	Tensile stress in SHCC [N/mm^2]
3	2.46
7	3.16
28	3.66

It is shown that, for all ages, the tensile stresses are just above the first cracking strength f_{fc}. Thus, by the use of the analytical tool proposed in the literature, it is determined that cracks in the overlay are present. However, these cracks are minor because the tensile stresses in the overlay are just above the first cracking strength.

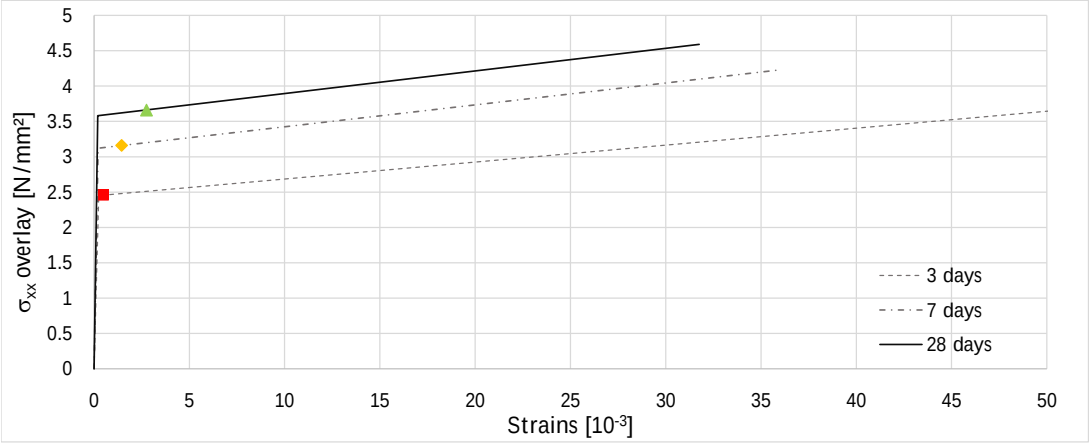

Figure 4.10: Tensile stresses overlay material due to restrained drying shrinkage. Stresses plotted in stress-strain diagram. Three ages of overlay material considered.

4.3. Shear Triplets

This paragraph presents and discusses the experimental results of the performed shear triplet tests. Furthermore, tables with the summarized results are presented. Firstly, the experimental results related to the non-retrofitted masonry triplets are presented.

The shear tests performed are focussed on retrofitted masonry specimen, i.e. masonry triplets with a single-sided SHCC overlay applied. No experiments are executed on plain masonry triplets. Experimental results of these non-retrofitted specimen are present at the faculty. Experiments on the plain triplets are conducted in the same period as the retrofitted specimen, however, performed by another researcher. Both types of specimens (i.e. plain and retrofitted) are built in the same period, with the same materials, and by the same masons. No differences in material- and or construction properties are assumed to be present.

Because a displacement controlled experiment is performed, the post-peak behaviour is determined. For each initial pre-compression level, after the specimen has reached its residual strength, two additional increments ($0.2\,\mathrm{N/mm^2}$) of pre-compression are applied to the same specimen. By means of this second stage of loading more information, related to the residual strength of the specimen, is obtained. Thus, each specimen is loaded by one initial level of pre-compression, followed by two incremental increases.

For the retrofitted specimen, only the peak shear force from the force-displacement curves can be directly compared to the plain (non-retrofitted) specimen. Determination of both the cohesion c_0 and mode-II fracture energy G_f^{II} is not possible for the retrofitted specimen, at least not in the same manner as used for the plain masonry triplets. The cohesion is based on the Coulomb criterion. However, the interface between the SHCC overlay and the masonry is not loaded in pre-compression, making it not possible to apply the linear regression technique employed for the plain masonry. The same is true for the mode-II fracture energy.

In this section, all the experimental results of the masonry triplet, both plain and retrofitted, are discussed. The failure modes of the non-retrofitted masonry triplets are investigated with the help of DIC. These experimental results are provided in Appendix B. Using detailed analyses with the help of DIC, a better description of the failure modes is presented. Additionally, the accuracy of the DIC is checked via verification with the experimental results. The results of this latter analysis are provided in Appendix C.

Results of the retrofitted specimen are presented in terms of force-displacement curves and tables. Again, DIC results are shown for these type of specimen as well, see paragraph 4.3.3.

4.3.1. Material properties plain masonry

The experimental results corresponding to the non-retrofitted masonry specimen are depicted through tables and figures. Additionally, a more in detail description of the observed failure mechanisms, using digital image correlation, is provided.

In this section, multiple different parameters related to these type of experiments are used and mentioned. To create a general understanding of these different parameters, these are briefly discussed below.

- The shear strength of the specimen is determined as:

$$f_v = \frac{F_{max}}{2 \cdot A_{mortar}} \tag{4.6}$$

  This equation is provided in EN 1052-3:2002. The total surface area of one mortar joint equals: $21.000\,\mathrm{mm^2}$ ($210 \cdot 100\,\mathrm{mm}$);

- Cohesion ($\tau = c$), i.e the initial shear strength of the specimen without the application of pre-compression ($\sigma_p = 0$). This parameter is determined via a linear regression of the experimental results by the application of the Coulomb criterion. The shear strength of each specimen, versus its corresponding pre-compression level, are plotted in the $\tau - \sigma$ plane. A linear relationship, between the shear and normal stresses, is assumed:

$$\tau = c_0 - \sigma \cdot \tan\left(\phi_0\right) \tag{4.7}$$

- Mode-II fracture energy G_f^{II} is also determined for the three different pre-compression levels. The fracture energy at zero pre-compression (G_{f0}^{II}) is, again, determined based on a linear regression of the results corresponding to the other three pre-compression levels:

$$G_f^{II} = a \cdot \sigma + b \tag{4.8}$$

- Dilatancy of the masonry units ψ is measured via multiple LVDTs, glued to each specimen. The horizontal LVDTs measures the so-called uplift of the masonry units and the vertical (relative) displacement of the central unit is measured via two vertically placed LVDTs. For the determination of the dilatancy, only the plastic deformations of the specimen are considered. The relationship below, between the plastic shear and normal displacements (v_s and v_n, respectively), result in the so-called dilatancy:

$$\psi = \arctan\left(\frac{v_n}{v_s}\right) \tag{4.9}$$

Table (4.3) provides the general results of the different masonry specimen. The shear strength is determined via equation (4.6). The total cross-sectional area used in this equation equals $42,000\,\text{mm}^2$ ($2 \cdot 210\,\text{mm} \cdot 100\,\text{mm}$). The mode-II fracture energy G_f^{II} is calculated. It is important to note that the latter is based on the average vertical displacement of the central masonry unit, as measured by the two vertical LVDTs. The vertical displacement of the jacket is only used for graphical purposes. No material properties are derived using this measurement data.

Please note the specimen numbers used in this table. These are not coinciding with literature and are only used in this report. Averaged values are provided for each quantity. The values presented in between brackets represent the Coefficient of Variation (C.o.V).

Table 4.3: Experimental results plain masonry triplets.

Specimen number	Pre-compression (N/mm^2)	Shear Strength (N/mm^2)	G_f^{II} (N/mm)
100	0.2	0.365	0.1148
101		0.278	0.1043
102		0.319	0.0569
	Average:	**0.320 (0.11)**	**0.092 (0.27)**
110	0.6	0.646	0.0677
111		0.743	0.2457
112		0.659	0.1712
	Average:	**0.683 (0.06)**	**0.1615 (0.45)**
120	1.0	0.977	0.1505
121		0.939	0.2319
122		0.860	0.0452
	Average:	**0.925 (0.05)**	**0.1425 (0.54)**

In Figure (4.11) the force-displacement curves of the different specimen, for the different levels of pre-compression levels, are depicted. As noted in Chapter (3), a displacement controlled experiment is performed, enabling the possibility to determine the post-peak behaviour at increased pre-compressive levels. Please note that the shear stresses at the unit-mortar interfaces are plotted, instead of the total shear force.

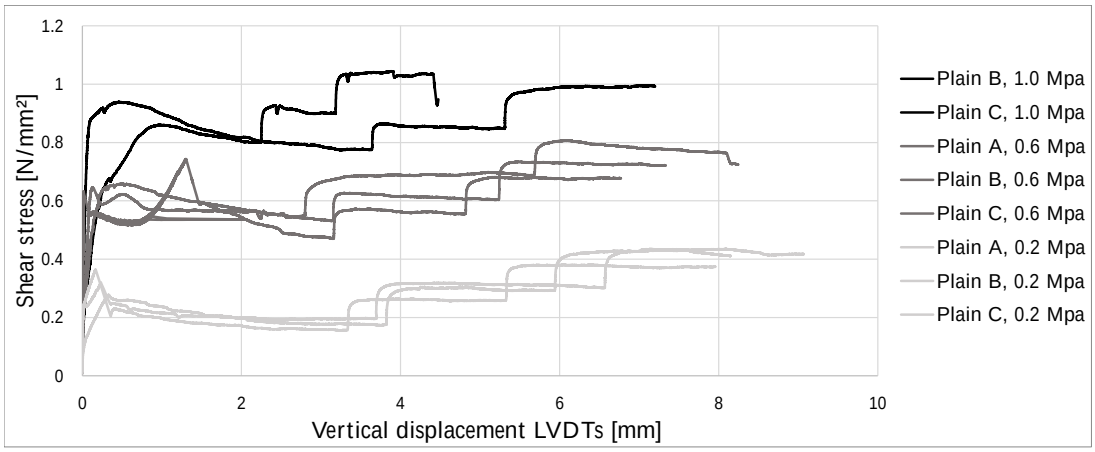

Figure 4.11: Stress-displacement curve (non-retrofitted) masonry triplet, averaged vertical displacement LVDTs. All levels of pre-compression.

The shear strength of each specimen is plotted in Figure (4.12) versus the corresponding pre-compression level. Via a linear regression of this data, the cohesion c_0 and friction angle coefficient Φ are determined, i.e. $0.1892\,\mathrm{N/mm^2}$ and 0.7562 respectively. Better results of the residual stage are obtained by performing an additional phase in the test, as mentioned earlier. In Figure (4.13) the experimental results related to this post-peak behaviour is presented. Again, via a linear regression, the residual friction angle coefficient Φ_{res} is determined to be equal to 0.6926. Finally, the mode-II fracture energy G_f^{II} is calculated for all specimen and plotted versus the pre-compression levels in Figure (4.14). In all figures, the linear regression lines are plotted with the corresponding linear equation and coefficient of determination. Additionally, figure (4.15) shows that the dilatancy angle ψ decreases down to zero with higher pre-compression levels, as noted in [33].

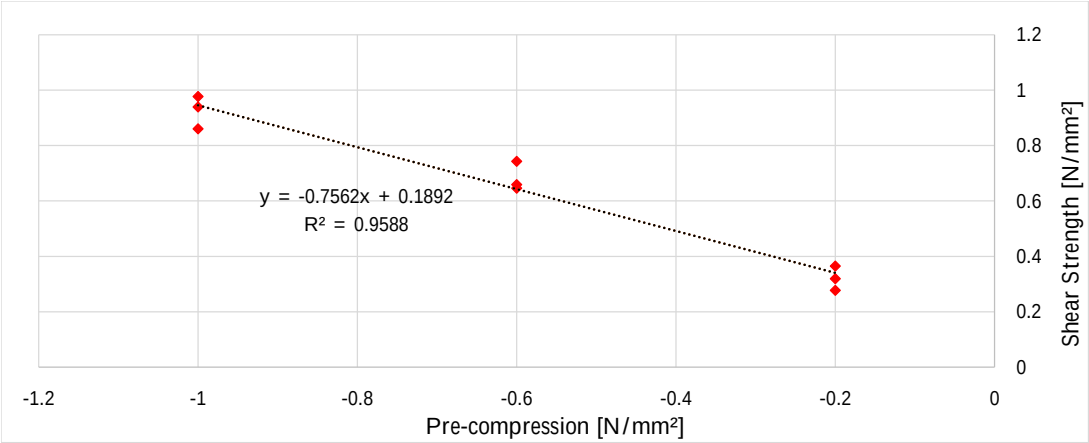

Figure 4.12: Shear strength versus pre-compression levels, intial phase testing.

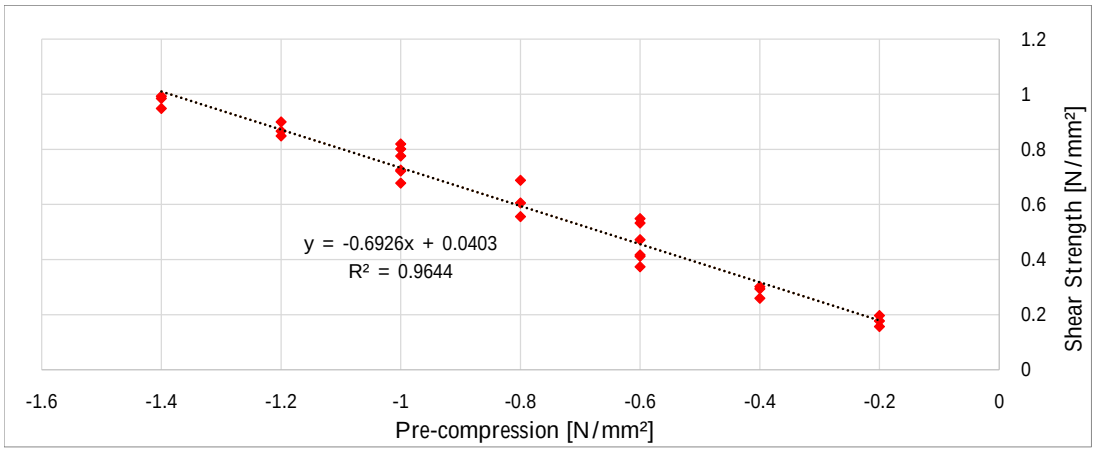

Figure 4.13: Residual shear strength versus pre-compression levels, second phase testing.

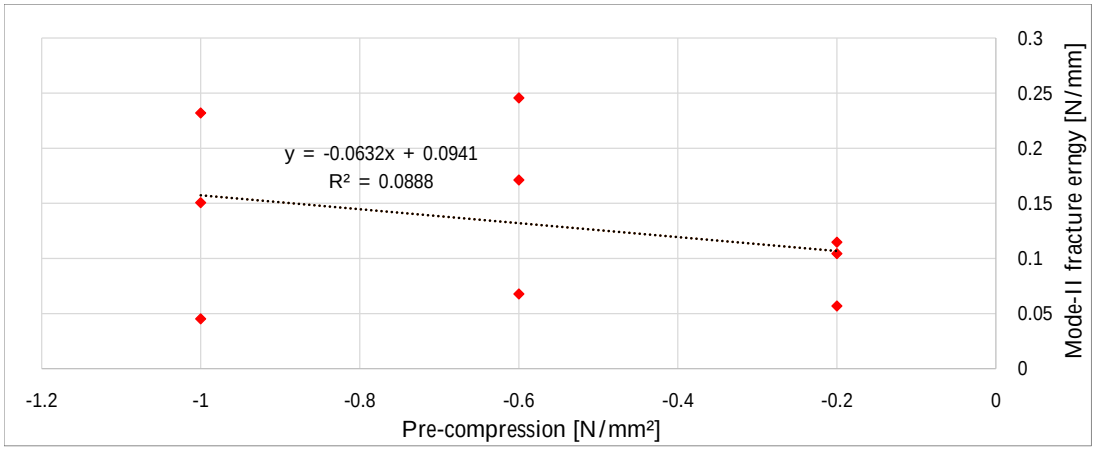

Figure 4.14: Mode-II fracture energy versus pre-compression levels.

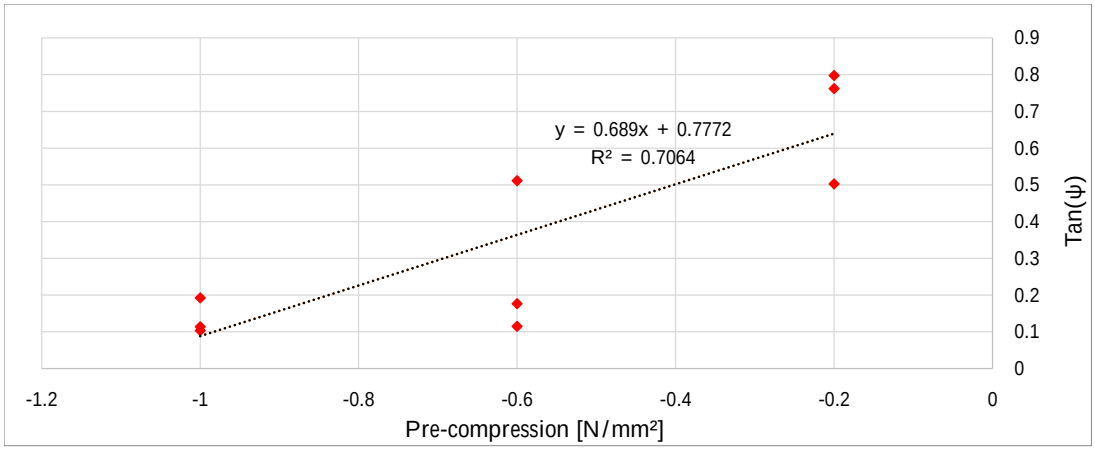

Figure 4.15: Tangent dilatancy angle versus pre-compression levels.

In the table below, the different parameters derived are summarized.

Table 4.4: Shear properties of solid (non-retrofitted) clay brick masonry.

Property	Symbol	Unit	Value
Number of specimen			9
Initial shear strength	f_{v0}	N/mm^2	0.1892
Initial friction angle coefficient	Φ		0.7562
Residual shear strength	$f_{v0,res}$	N/mm^2	0.0403
Residual friction angle coefficient	Φ_{res}		0.6926

The failure modes of the non-retrofitted masonry triplets are investigated in more detail with the help of DIC. It is concluded that sliding shear failure of the unit-mortar interfaces is governing for lower levels of pre-compression. Crushing of the mortar joints is observed for higher levels of pre-compression. These results are not part of the scope of this research and are therefore provided in Appendix B.

4.3.2. General conclusions - Plain masonry triplets

In this section, some of the more general conclusions drawn, related to the experimental results of the non-retrofitted masonry triplets, are provided.

- The vertical displacements, as obtained directly from the hydraulic jack, are overestimated. One explanation is the deformation of the frame in which the hydraulic jack is mounted. During loading, mainly in the linear elastic stage of the specimen (high stiffness specimen), the vertical deformations differ the most. This is also observed via the rigid body motions captured by the DIC, which are only present during the pre-peak stage, see Appendix C;
- The averaged value of the vertical LVDT measurements provide a better representation of the actual relative displacement. If material properties are derived these measurements should be used for input;
- The relative vertical displacement of the central masonry unit is well estimated via the DIC. However, one should take into account the corresponding locations of the vertical LVDTs of the experimental setup;
- For both the lowest and highest pre-compression levels (i.e. $0.2\,N/mm^2$ and $1.0\,N/mm^2$) the DIC well represents the total stress-displacement curves. However, this curve is not exact around peak resistance for a pre-compression level equal to $0.6\,N/mm^2$. Using more pictures in the DIC analysis will solve this issue. For this analysis, every 10^{th} picture is taken into account. Decreasing this interval enables the DIC analysis to better approximate the actual stress-displacement behaviour;
- The DIC does not represent as well the horizontal (tangential) displacements of the masonry units. One might consider using a greater amount of pictures to solve this inaccuracy;
- Overall, the DIC is a valid tool to determine the relative displacements of the masonry triplet specimen. Additionally, extra information is obtained with respect to the actual failure mechanisms of the specimen. Also, since the glue, used to connect the LVDTs to the specimen, sometimes fails, there always remains a possibility for the researcher ending up without useable data.

4.3.3. Results retrofitted masonry

The experimental results of the retrofitted masonry triplets are presented in this section. Just as in the previous section, the results are presented in tables and figures. The results of the retrofitted specimen are compared to their non-retrofitted counterpart.

In the tables below the experimental results of the different type of retrofitted masonry, triplets are depicted. Again, the averaged values and coefficient of variation (C.o.V.) are mentioned. The differences between the averaged values of the retrofitted and plain specimen are noted by means of percentages. A positive value equals a positive increase for the retrofitted specimen.

Please note that the maximum shear force is provided, instead of the shear strength. For the retrofitted masonry specimen, this latter quantity cannot be determined similarly as for the plain masonry specimen.

Table 4.5: Experimental results retrofitted masonry triplets, full bonded 10 mm thick SHCC overlay. Coefficient of variation provided in between brackets. Average difference with plain masonry specimen given in %.

Specimen number	Overlay Thickness (mm)	Bond	Curing	Pre-compression (N/mm^2)	Max shear force (kN)	Residual shear force (kN)
1 2 3 4	10	Full Bond	Sealed	0.2	9.84 11.86 17.96 9.14	6.01 6.87 8.10 7.76
				Average:	**12.20 (0.28), -9.36**%	**7.19 (0.11), -3.21**%
5 6 7 8	10	Full Bond	Sealed	0.6	24.36 20.33 23.82 24.11	20.49 19.74 19.81 22.52
				Average:	**23.15 (0.07), -19.25**%	**20.64 (0.05), -5.07**%
9 10 11 12	10	Full Bond	Sealed	1.0	36.30 42.56 40.46 36.17	33.62 30.37 36.14 33.55
				Average:	**38.87 (0.07), +0.0**%	**33.42 (0.06), -0.44**%

Table 4.6: Experimental results retrofitted masonry triplets, full bonded 30 mm thick SHCC overlay. Coefficient of variation provided in between brackets. Average difference with plain masonry specimen given in %.

Specimen number	Overlay Thickness (mm)	Bond	Curing	Pre-compression (N/mm^2)	Max shear force (kN)	Residual shear force (kN)
13 14 15 16	30	Full Bond	Sealed	0.2	11.26 18.17 17.03 9.84	7.41 10.42 8.91 9.51
				Average:	**14.70 (0.20), +9.24**%	**9.06 (0.12), +22.08**%
17 18 19 20	30	Full Bond	Sealed	0.6	18.84 25.35 32.35 29.06	18.32 22.96 21.03 25.64
				Average:	**26.40 (0.19), -7.94**%	**21.99 (0.12), +1.10**%
21 22 23 24	30	Full Bond	Sealed	1.0	46.63 52.88 54.33 41.04	35.03 36.40 31.20 30.84
				Average:	**48.72 (0.11), +25.34**%	**33.37 (0.07), -0.60**%

Table 4.7: Experimental results retrofitted masonry triplets, debonded 10 and 30 mm thick SHCC overlay. Coefficient of variation provided in between brackets. Average difference with plain masonry specimen given in %.

Specimen number	Overlay Thickness (mm)	Bond	Curing	Pre-compression (N/mm^2)	Max shear force (kN)	Residual shear force (kN)
33	10	Debonded	Sealed	0.2	12.05	7.18
34					10.28	8.30
35					10.25	8.95
36					14.93	8.82
				Average:	**11.88 (0.16), -2.63%**	**8.31 (0.08), +11.95%**
29	10	Debonded	Sealed	0.6	30.15	24.50
30					33.33	27.10
31					23.65	20.13
32					29.41	24.40
				Average:	**29.14 (0.12), +25.84%**	**24.03 (0.10), +10.52%**
25	10	Debonded	Sealed	1.0	39.51	31.12
26					42.77	37.85
27					33.33	32.28
28					36.84	23.25
				Average:	**38.11 (0.09), -1.95%**	**31.17 (0.17), -7.14%**
37	30	Debonded	Sealed	1.0	44.04	36.80
38					47.22	31.49
				Average:	**45.63 (0.03), +17.39%**	**34.14 (0.08), +1.71%**

Table 4.8: Experimental results retrofitted masonry triplets, 10 mm full bond, non-sealed curing. Coefficient of variation provided in between brackets. Average difference with plain masonry specimen given in %.

Specimen number	Overlay Thickness (mm)	Bond	Curing	Pre-compression (N/mm^2)	Max shear force (kN)	Residual shear force (kN)
41	10	Full bond	Non-sealed	1.0	40.28	24.70
42					32.59	27.43
43					39.52	31.29
44					38.53	32.87
				Average:	**37.73 (0.08), -2.92%**	**29.08 (0.11), -13.39%**

Peak Resistance

First, the differences between the retrofitted and plain masonry triplets, in terms of peak resistance, are addressed. From the summarized results in Tables (4.5), (4.6), (4.7), and (4.8) it is concluded that different results are obtained for all the retrofitted specimen. The experimental results in Table (4.5) clearly show no increase in strength by the application of a 10 mm thick SHCC overlay with full bond to the masonry substrate. Even lower maximum shear forces, compared to the non-retrofitted masonry triplets, are observed during the experiments. Especially for the intermediate pre-compression level, this negative difference is noticeable. Overall, in terms of maximum shear force, the retrofitted specimen with a 30 mm thick SHCC overlay applied performed best, both for the bonded as debonded SHCC-masonry interface. Overall, the increase in resistance due to the SHCC overlay is not as expected.

The similarity in experimental results is visible in the force-displacement curves, as shown below. The

retrofitted and plain specimen are represented using blue and red curves, respectively. The vertical displacement used corresponds to the averaged value of the two vertical LVDTs.

When investigating these figures, one might notice some specimen are not represented, e.g. experimental results URM triplet A for the highest pre-compression level. This is due to the lack of experimental results. It is possible that the glue of one of the vertical LVDTs did not hold during the experiment, causing deformations measured which are not related to the experiment itself.

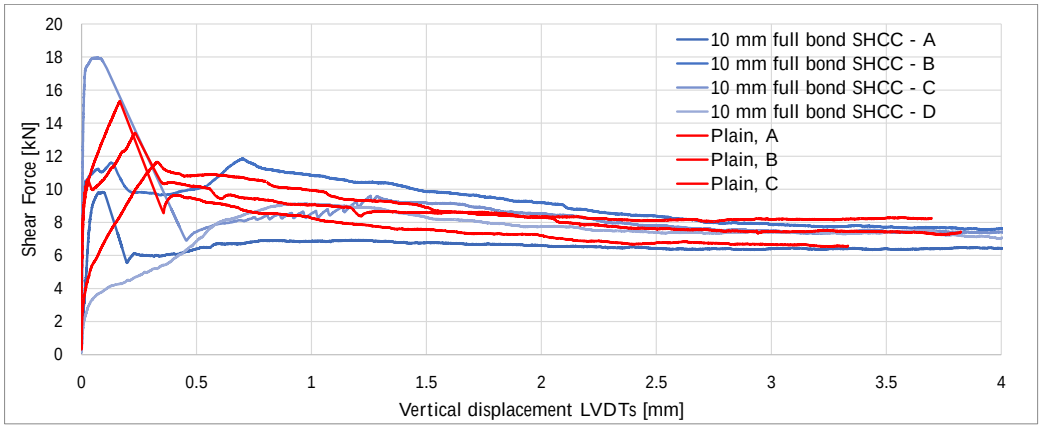

(a) Force-displacement curve (non-)retrofitted specimen, 10 mm full bonded. Pre-compression level = 0.2 Mpa.

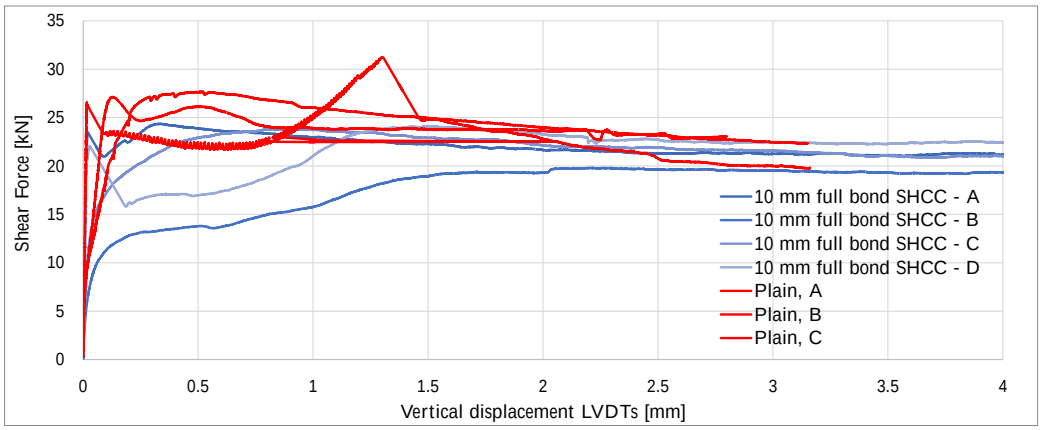

(b) Force-displacement curve (non-)retrofitted specimen, 10 mm full bonded. Pre-compression level = 0.6 Mpa.

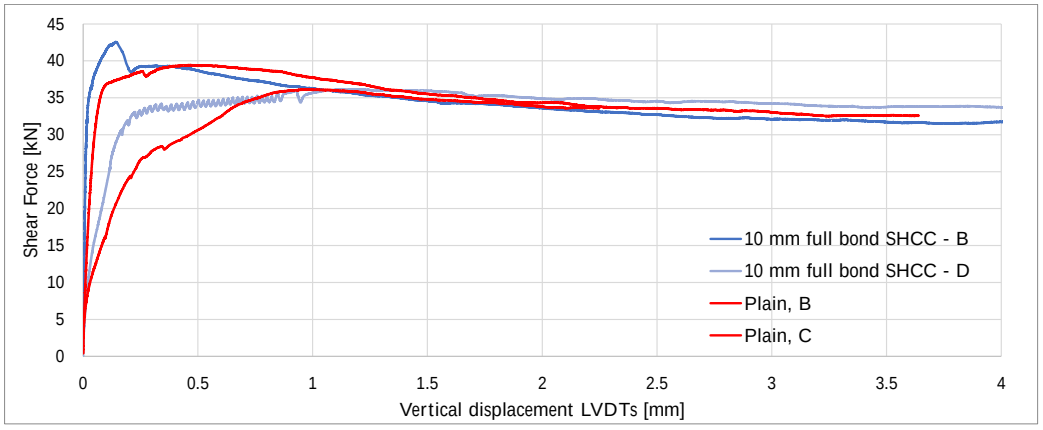

(c) Force-displacement curve (non-)retrofitted specimen, 10 mm full bonded. Pre-compression level = 1.0 Mpa.

Figure 4.16: Force-displacement curves. Plain masonry triplets versus 10 mm full bonded SHCC specimen. All three levels of pre-compression.

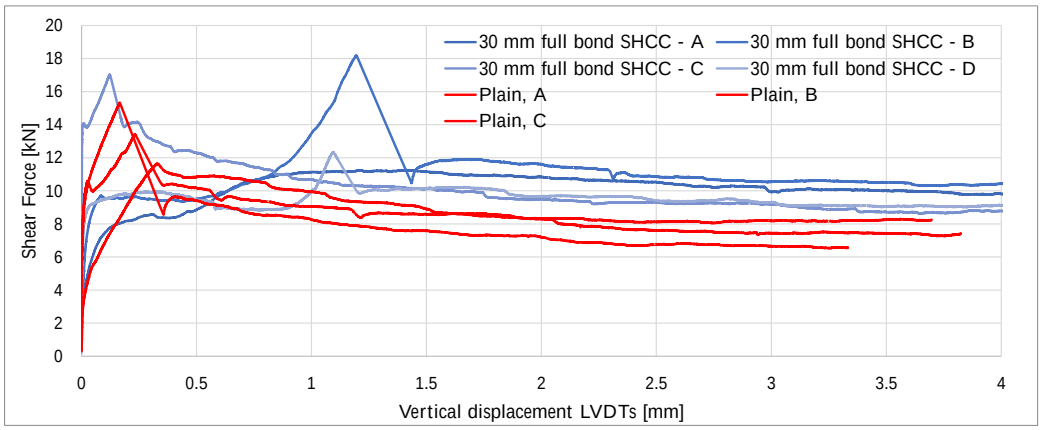

(a) Force-displacement curve (non-)retrofitted specimen, 30 mm full bonded. Pre-compression level = 0.2 Mpa.

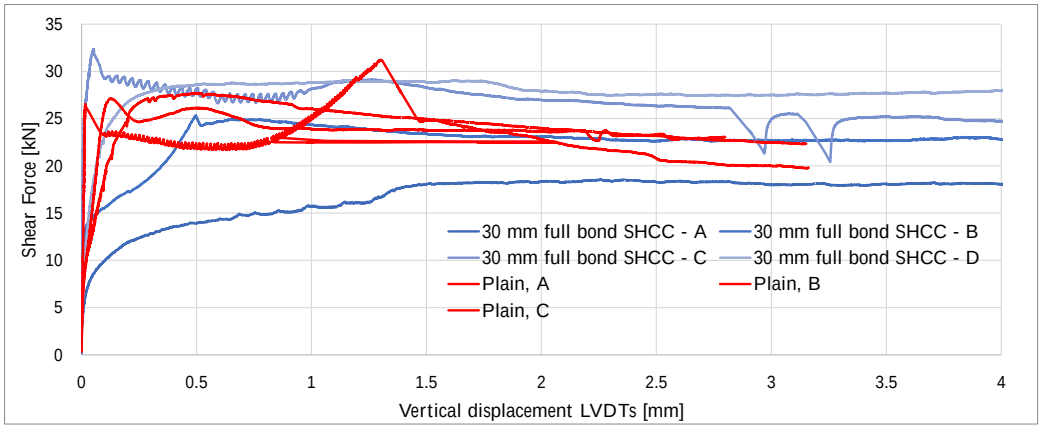

(b) Force-displacement curve (non-)retrofitted specimen, 30 mm full bonded. Pre-compression level = 0.6 Mpa.

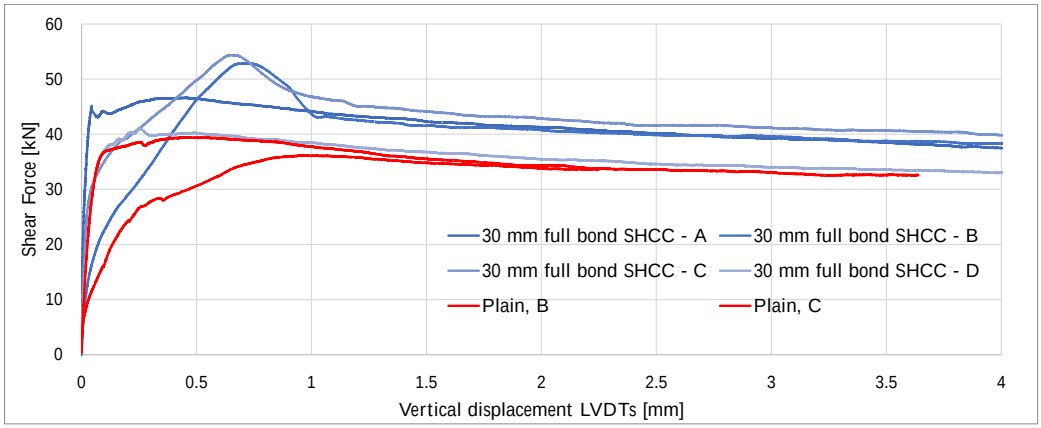

(c) Force-displacement curve (non-)retrofitted specimen, 30 mm full bonded. Pre-compression level = 1.0 Mpa.

Figure 4.17: Force-displacement curves. Plain masonry triplets versus 30 mm full bonded SHCC specimen. All three levels of pre-compression.

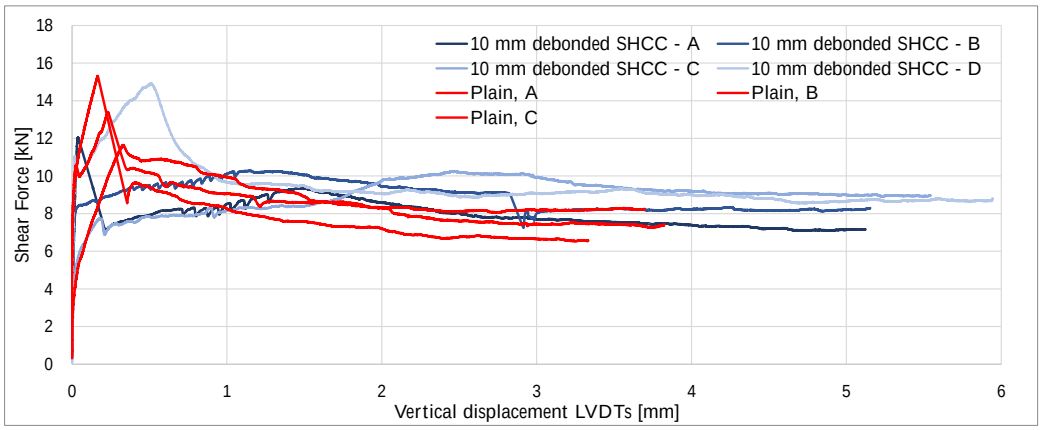

(a) Force-displacement curve (non-)retrofitted specimen, 10 mm debonded. Pre-compression level = 0.2 Mpa.

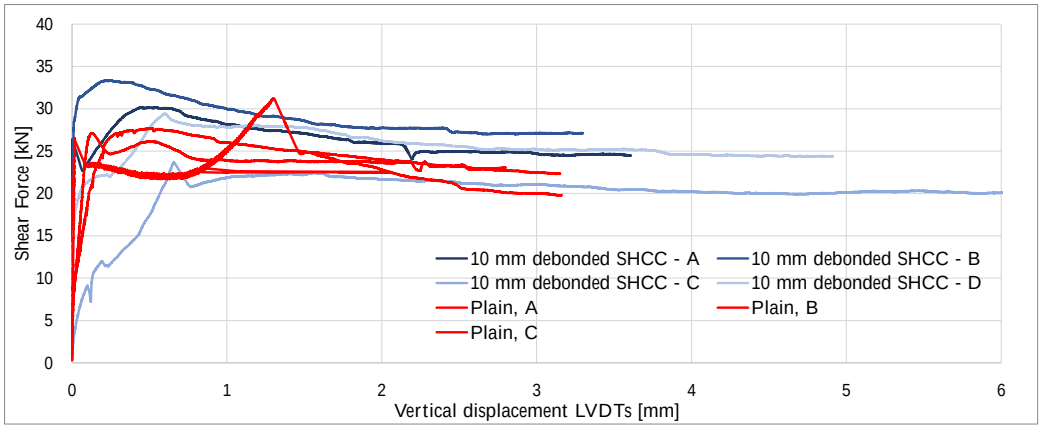

(b) Force-displacement curve (non-)retrofitted specimen, 10 mm debonded. Pre-compression level = 0.6 Mpa.

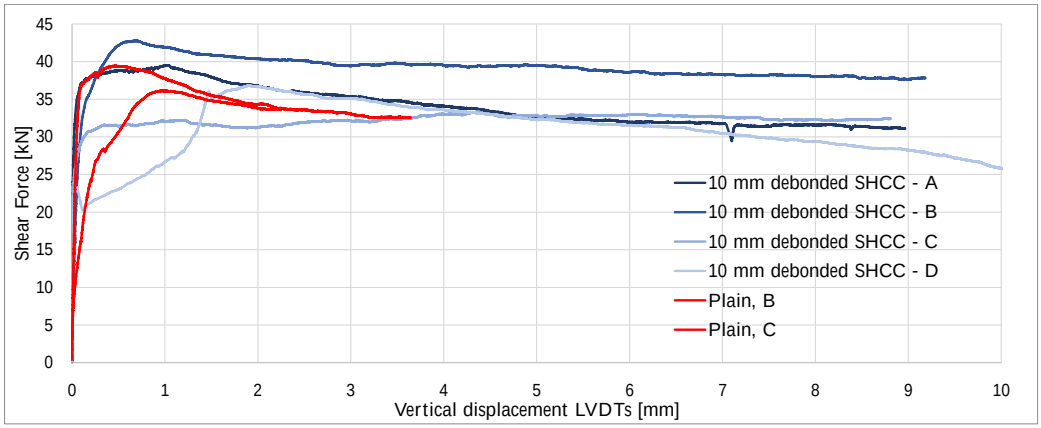

(c) Force-displacement curve (non-)retrofitted specimen, 10 mm debonded. Pre-compression level = 1.0 Mpa.

Figure 4.18: Force-displacement curves. Plain masonry triplets versus 10 mm debonded SHCC specimen. All three levels of pre-compression.

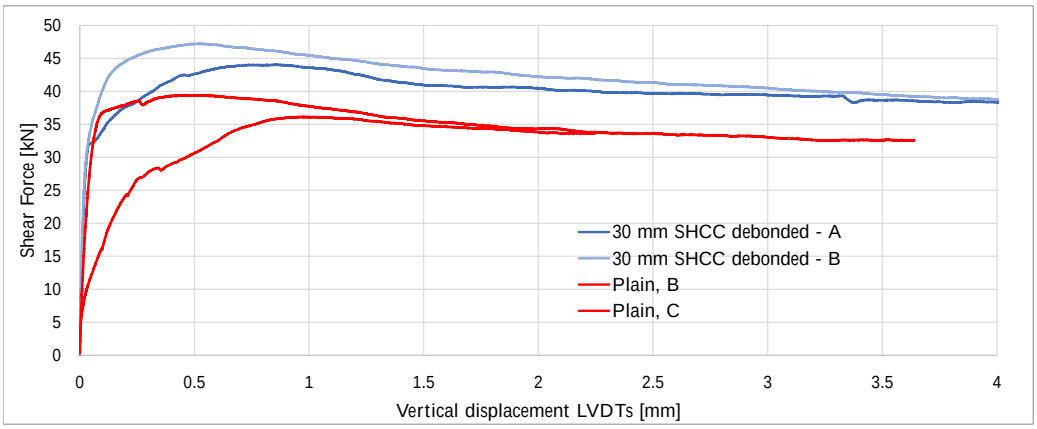

Figure 4.19: Force-displacement curves. Plain masonry triplets versus 30 mm debonded. Pre-compression level = 1.0 N/mm^2.

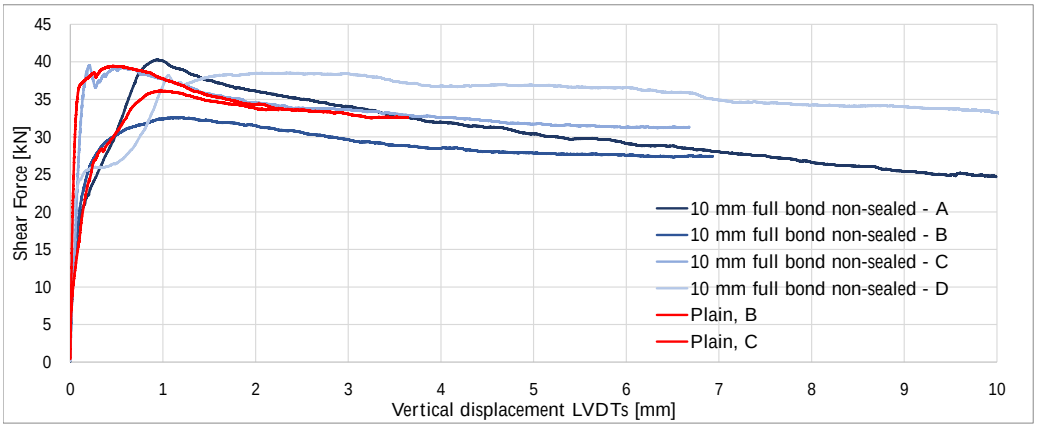

Figure 4.20: Force-displacement curves. Plain masonry triplets versus 10 mm full bonded, non-sealed curing coditions, SHCC specimen. Pre-compression level = 1.0 N/mm^2.

The figures above show that the peak resistance does not differ (significantly), between the retrofitted and plain specimen. Without looking to other experimental results, it can be (prematurely) concluded that the applied SHCC overlay does not influence the peak resistance. For some groups of specimen even lower results, with respect to the plain masonry triplets are depicted, see, for example, Figure (4.16b). This is not as expected, and therefore the validity of the experimental results is questioned by the author for the following reasoning: the addition of a reinforcing overlay to the URM must lead to a higher resistance compared to the non-retrofitted specimen. Because of these unexpected results, multiple possible influencing factors are thought of (e.g. experimental setup used). These are discussed in Chapter 6 and 7.

However, looking to the averaged results presented in Table (4.6) and the corresponding force-displacement curves in Figure (4.17), it must be noted that the retrofitted specimen with a 30 mm thick overlay does show some increase in resistance over the plain specimen, especially for the highest level of pre-compression.

The application of debonded areas at the SHCC-masonry interface shows similar results to the fully bonded specimen, i.e. no noticeable strength improvements over the plain specimen. Again, for the specimen with a partial debonded 10 mm thick overlay, no real trend is observed from which it can be concluded that this type of interface preparation is beneficial for the retrofitting of URM. The specimen with a 30 mm thick overlay shows the same trend as their fully bonded counterparts, i.e. a slight increase in strength. Thus, without any bond between the SHCC and the mortar material similar (or higher) results are obtained for the retrofitted specimen.

Comparing the curves from Figure (4.16c) and (4.20) it is shown that the curing conditions of the 10 mm SHCC overlay do not show differences in results. Both the pre- and post-peak behaviour are similar for both type of specimen.

All the specimen showed complete delamination of the SHCC overlay. In the figures below some pictures of a tested specimen are provided. The pictures shown correspond to specimen number 4 (i.e. 10 mm full bonded overlay) which is tested at the highest level of pre-compression. It must be noted that these type of pictures are present for all the different specimen. However, all these pictures show similar results. Combining Figure (4.21a) and (4.21e) it is shown that sliding of the masonry units occurred along its smooth surface. This is characteristic for these type of masonry bricks used and coinciding with other experimental results present at the TU Delft. Different figures show that the overlay is completely delaminated from the masonry substrate. Special attention for Figure (4.21d) is required. This figure clearly shows that mortar material is present on the inside of the SHCC overlay, generating the thought that the bond between the SHCC overlay and the mortar joints is greater than the strength of the SHCC-unit interface. Of course, the mortar joints are not as smooth as a face of the masonry units, increasing the surface area present for the SHCC overlay to bond to. Similar results are known from [38]. However, looking at the results of the specimen with a partial debonded overlay, see Figure (4.18) and (4.19), the opposite seems to be true. The specimen with the partial debonded overlay show similar, or even better results, for the higher two levels of pre-compression, compared to the specimen with a fully bonded overlay.

(a) Backside view specimen after testing.

(b) Top view specimen after testing.

(c) Front view specimen after testing, delaminated SHCC overlay on the left.

(d) Delaminated SHCC overlay.

(e) Tested specimen showing all interfaces.

Figure 4.21: Overview failure pattern tested retrofitted specimen. Example = specimen number 4 (10 mm full bond) pre-compression = $1.0 \mathrm{N/mm^2}$.

4.3.4. DIC Analysis

By using the DIC analysis, additional information into the failure mechanisms of the retrofitted specimen is obtained. This report mentions only the outliers. Based on the force-displacement curves, the examined specimen are chosen. For all specimen tested, total delamination of the SHCC overlay is observed. With the help of the DIC analysis, it is concluded no shearing capacity of the SHCC is activated, i.e. no cracks are observed in the overlay.

Only for one of the specimen cracks in the overlay are observed, see Figure (4.22). This specimen has a 10 mm thick overlay, fully bonded to the masonry substrate. The overlay material is cured in non-sealed curing conditions. Restrained shrinkage of this overlay might have resulted in the cracks observed with the help of DIC. No increase in shear strength is shown for this specimen, see Figure (4.20). The cracks in the overlay are not related to the activation of the SHCC material during the shear test.

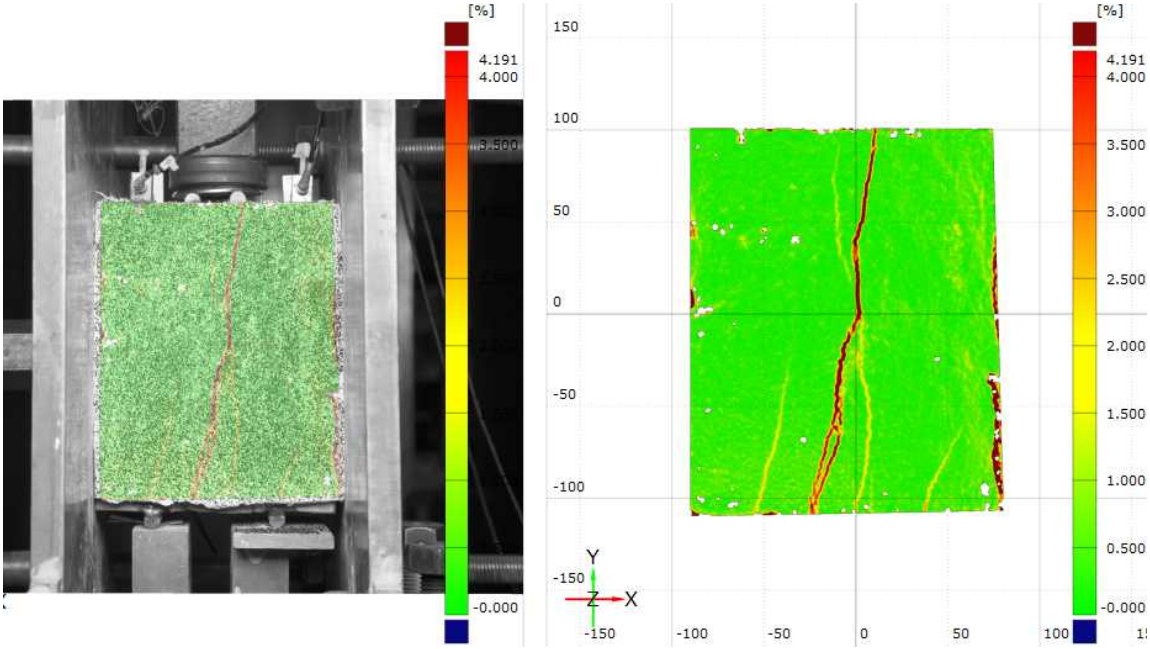

Figure 4.22: Post-peak state SHCC overlay. Specimen number 42, 10 mm full bonded SHCC, non-sealed curing conditions. Pre-compression level = 1.0 Mpa.

For all specimen, this DIC analysis is performed. No cracks in the overlay are observed for most of the

specimen. The corresponding DIC pictures are provided in Appendix D. From these results, it is concluded that the overlay material is not activated for the different specimen.

Some of the retrofitted specimens showed some marginal improvement over the plain specimen. For example, sample '30 mm SHCC debonded - B' in Figure (4.19). This specimen shows an increased peak shear force equal to $\pm 10\,\text{kN}$. This increase is not as significant as presented in literature [9, 38]. No activation of the SHCC overlay is shown from the DIC results.

4.4. Flexural Tests

In this paragraph, all the experimental results corresponding to the flexural tests are discussed. In Table (4.9) an overview is presented with all the values of interest of the different specimen. For specimen number 9 (10 mm overlay with partial debonding) no values are presented. Due to technical problems, the data file corresponding to this specific specimen got corrupted causing it to be impossible to extract the data from the experimental setup (i.e. exporting the data file containing the experimental result to an Excel format). However, the type of failure observed is known, but, numerical values for the peak loading and corresponding vertical displacements are unknown.

Just as for the shear strength experiments, no plain masonry specimen are tested. The capacity of these non-retrofitted masonry beams is not sufficient to be able to place the specimen in the testing setup. It is therefore assumed that all capacity captured in these experiments is related to the applied SHCC overlay. The different beam specimen is built in the same period, and with the same materials, as the masonry triplets.

In the following sections, the experimental results are discussed with the help of force-displacement curves and DIC analyses. As for the shear strength experiments, the difference in vertical displacement, as measured by the vertical hydraulic jacket and the LVDT, is taken into account. In the following figures, the vertical displacement provided by both instruments is plotted. The vertical displacements of the vertical hydraulic jacket are shown in brown.

Table 4.9: Overview Experimental Results Flexural Tests

Specimen nr.	**4**	**5**	**6**	**7**	**8**	**9**	**10**	**11**	**12**	**13**	Units
Thickness SHCC	10	10	30	30	10	10	30	30	10	30	-
Bonding	Full bond	Full bond	Full bond	Full bond	De-bonded	De-bonded	De-bonded	De-bonded	Full bond	Full bond	-
Curing	Sealed	Sealed	Sealed	Sealed	Sealed	Sealed	Sealed	Sealed	Non-sealed	Non-sealed	-
Date built masonry	21-2-19	21-2-19	21-2-19	21-2-19	21-2-19	21-2-19	21-2-19	21-2-19	21-2-19	21-2-19	-
Date casting SHCC	24-4-19	24-4-19	23-4-19	23-4-19	24-4-19	24-4-19	23-4-19	23-4-19	24-4-19	23-4-19	-
Age masonry at casting SHCC	62	62	61	61	62	62	61	61	62	61	days
Date un-moulding											-
Date testing	27-5-19	29-5-19	22-5-19	23-5-19	28-5-19	29-5-19	23-5-19	24-5-19	29-5-19	27-5-19	-
Age masonry at test	95	96	90	91	96	97	91	92	97	95	days
Age SHCC at test	33	34	29	30	34	35	30	31	35	34	days
Type of failure observed	Shear	Flexural	Flexural	Shear	Shear	Shear	Shear	Shear	Shear	Shear	-
Peak loading	7.37	6.53	19.91	12.32	6.55	-	8.46	6.58	8.63	10.29	kN
Deflection jacket	0.32	0.42	1.51	1.78	1.49	-	0.57	0.33	0.51	1.03	mm
Deflection LVDT04	0.32	0.73	1.74	1.73	3.66	-	1.38	0.93	0.91	3.35	mm

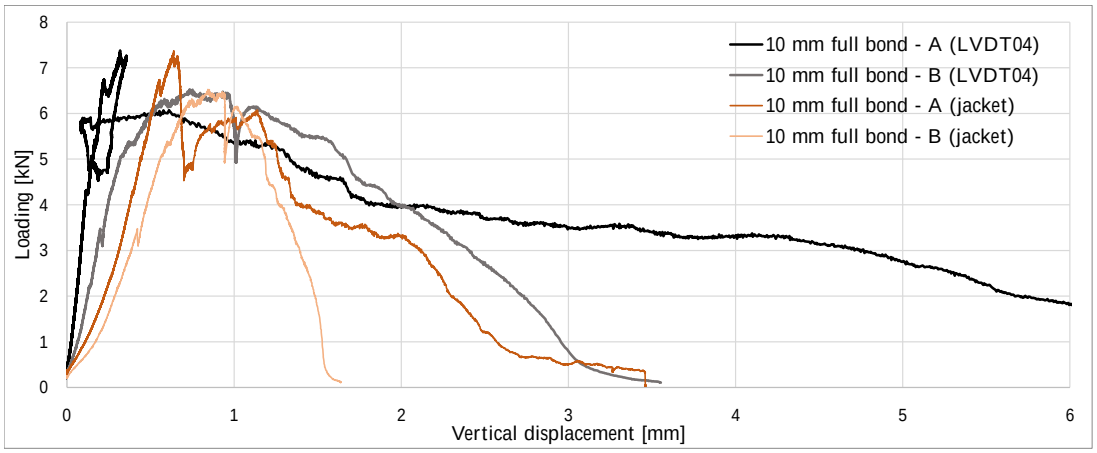

(a) Force-displacement curve retrofitted masonry beams with an 10 mm full bonded SHCC overlay.

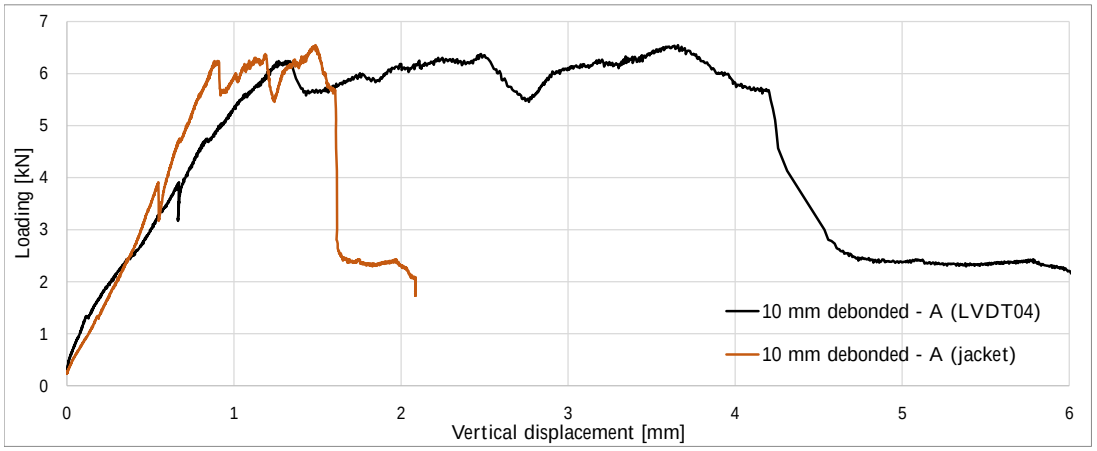

(b) Force-displacement curve retrofitted masonry beams with an 10 mm partial debonded SHCC overlay.

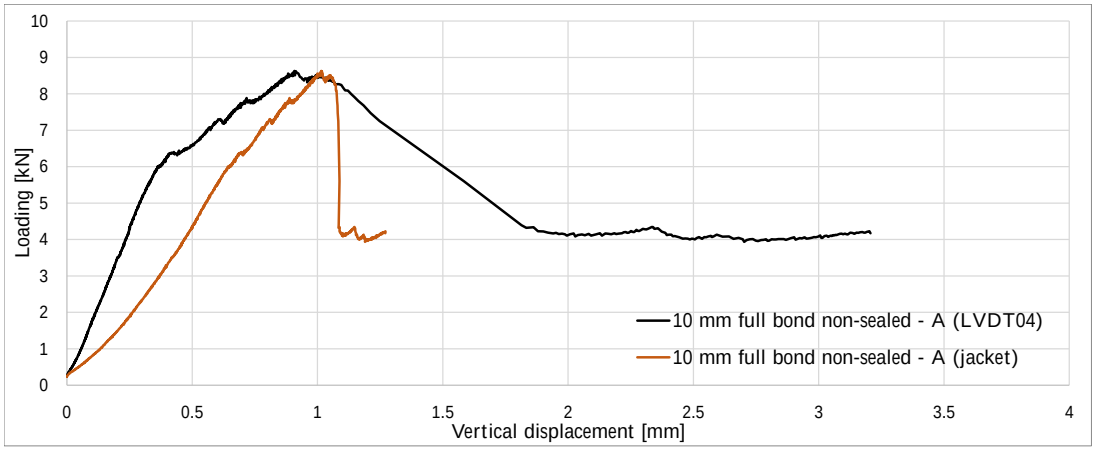

(c) Force-displacement curve retrofitted masonry beams with an 10 mm full bonded (non-sealed curing) SHCC overlay.

Figure 4.23: Force-displacement curves all retrofitted masonry beams with an 10 mm thick SHCC overlay.

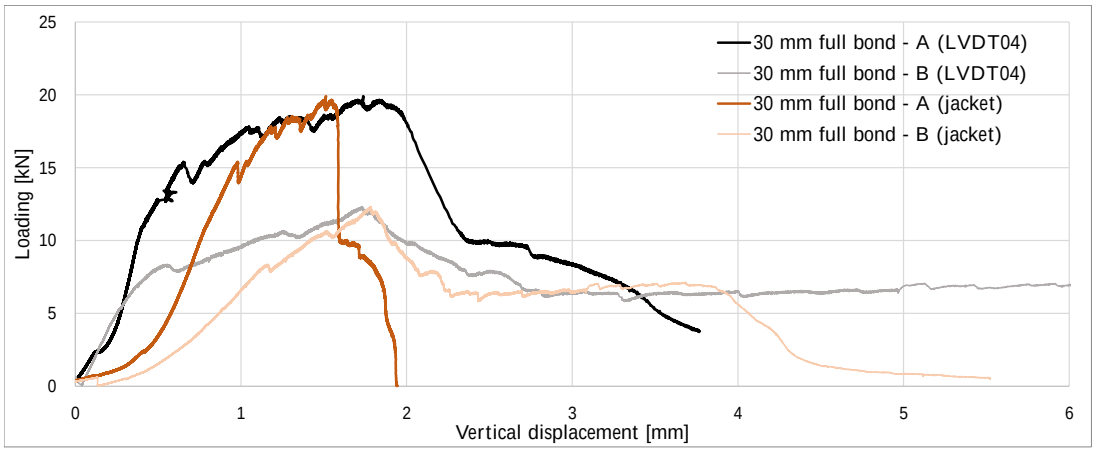

(a) Force-displacement curve retrofitted masonry beams with an 30 mm full bonded SHCC overlay.

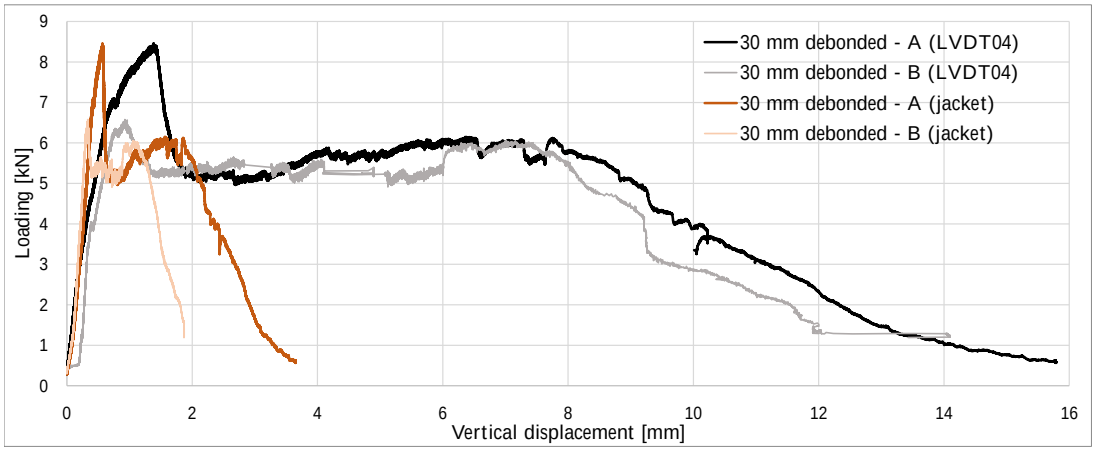

(b) Force-displacement curve retrofitted masonry beams with an 30 mm partial debonded SHCC overlay.

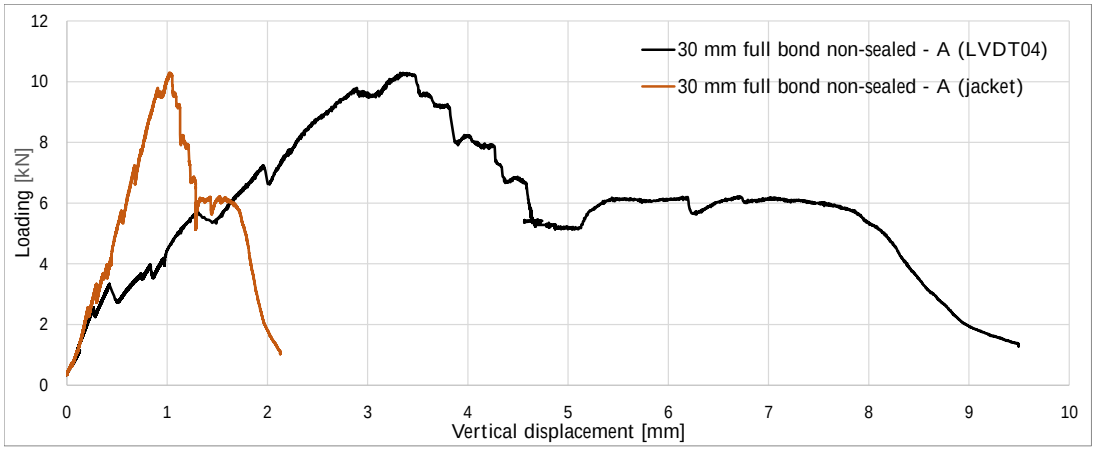

(c) Force-displacement curve retrofitted masonry beams with an 30 mm full bonded (non-sealed curing) SHCC overlay.

Figure 4.24: Force-displacement curves all retrofitted masonry beams with an 30 mm thick SHCC overlay.

From the force-displacement curves shown, several conclusions are drawn. Firstly, the measured vertical displacement requires attention. It is shown that the vertical displacements measured by the vertical hydraulic jacket are significantly smaller, compared to the output of the vertical LVDT (LVDT04). This is in contradiction

with the earlier presented results, related to the masonry triplet experiments. However, considering the experimental setup used for these flexural tests, this is as expected. A different, stiffer, steel frame is used. Additionally, the vertical applied LVDT is strongly dependent on the vertical motions of the outside two masonry units, to which it is connected, recall Figure (3.16). From the failure modes observed it is concluded these assumed 'fixed in place' connection points for LVDT04 (i.e. the outside masonry units) are not a rigid base to use. In many cases one, or multiple, of these outside masonry units debonded from the SHCC overlay, disabling the ability of accurate measurements via this instrument.

Debonding of the outer units depends on the type of failure observed. Two different types of failure governed this part of the experimental campaign: flexural failure and shear failure. Only two out of ten specimens failed in the first type of failure. The other specimen are governed by the debonding of the masonry units from the SHCC overlay. Both failure modes are depicted in Figure (4.25). The uplift of the outer units is shown in Figure (4.25c), see the right-hand side masonry units.

(a) Front view flexural failure (specimen number 6).

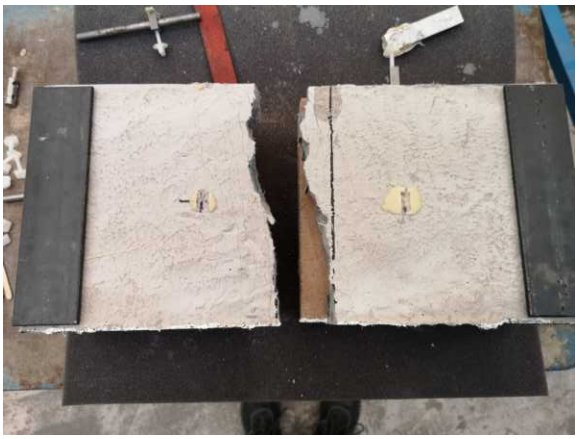

(b) Bottom view flexural failure (specimen number 6)

(c) Front view shear failure (specimen number 7).

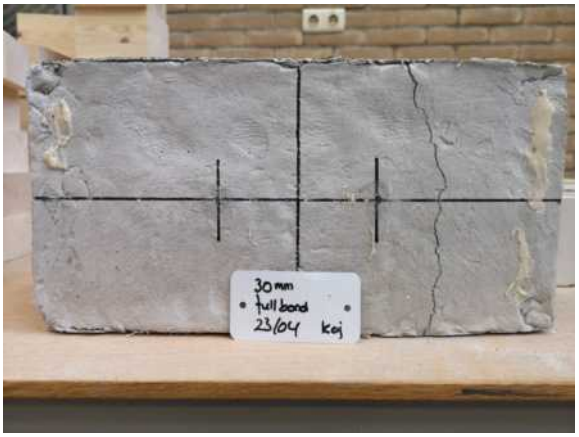

(d) Bottom view shear failure (specimen number 7).

Figure 4.25: Flexural and 'shear type' failure masonry beams.

Below the different conclusions drawn from the experimental results are summarized. Additionally, in Figure (4.26) the different specimen, with the same investigated parameters, are plotted.

- From Table (4.9) and Figure (4.26a) it is concluded that the specimen with the thicker 30 mm overlay resulted in higher resistance. This is corresponding to the basic understanding of mechanics since a thicker overlay results in a higher bending moment resistance due to the larger internal lever arm. The vertical displacement corresponding to the peak resistance is greater for the specimen with the thicker overlay;
- For the specimen with a partial debonded overlay not as significantly different resistances are obtained, between the two investigated overlay thicknesses. However, in the linear elastic stage, a significantly

lower stiffness for the specimen with a 10 mm thick overlay is observed. This is different compared to the specimen with a fully bonded overlay; and

- From Figure (4.26c) it is concluded that no remarkable differences in results are observed for the specimen of which the overlay was cured in non-sealed conditions. Initially, the shear strength of the specimen with a 30 mm thick overlay seemed to be reduced drastically due to the non-sealed curing, compare Figure (4.26a) and (4.26c). However, this direct comparison is not valid since the failure mechanism differs between the individual specimen. Specimen number 6 (30 mm full bond - A) showed flexural failure. All the retrofitted beams with the non-sealed curing conditions failed by debonding of the masonry units.

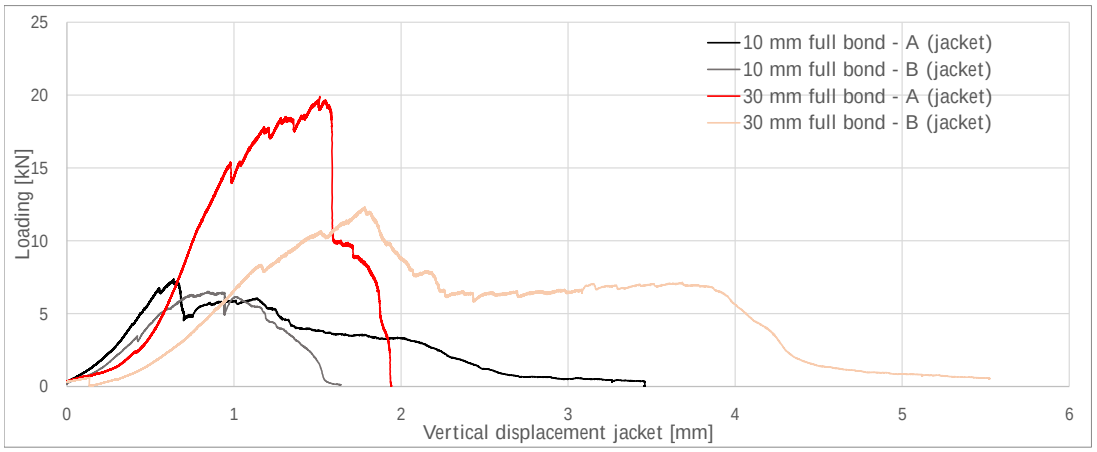

(a) Force-displacement curve retrofitted masonry beams with 10 and 30 mm full bonded SHCC overlay.

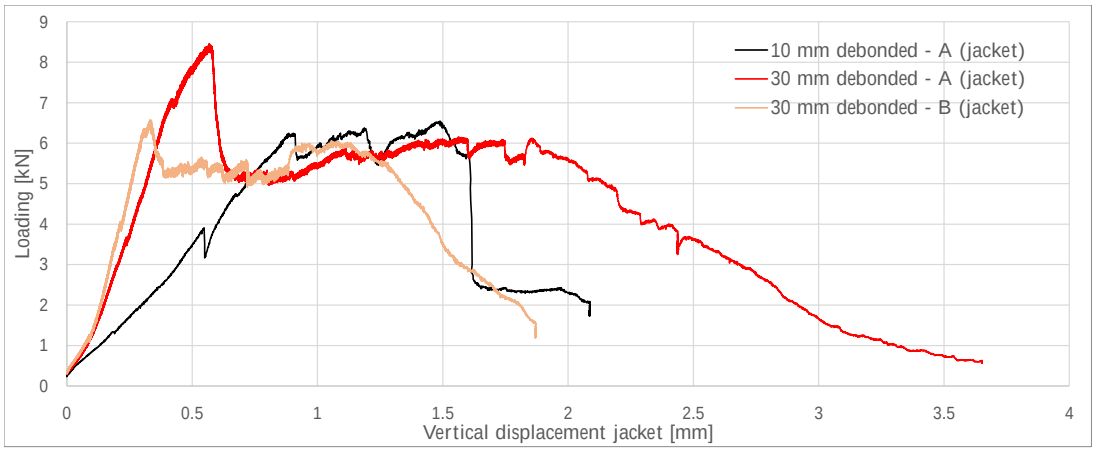

(b) Force-displacement curve retrofitted masonry beams with 10 and 30 mm partial debonded SHCC overlay.

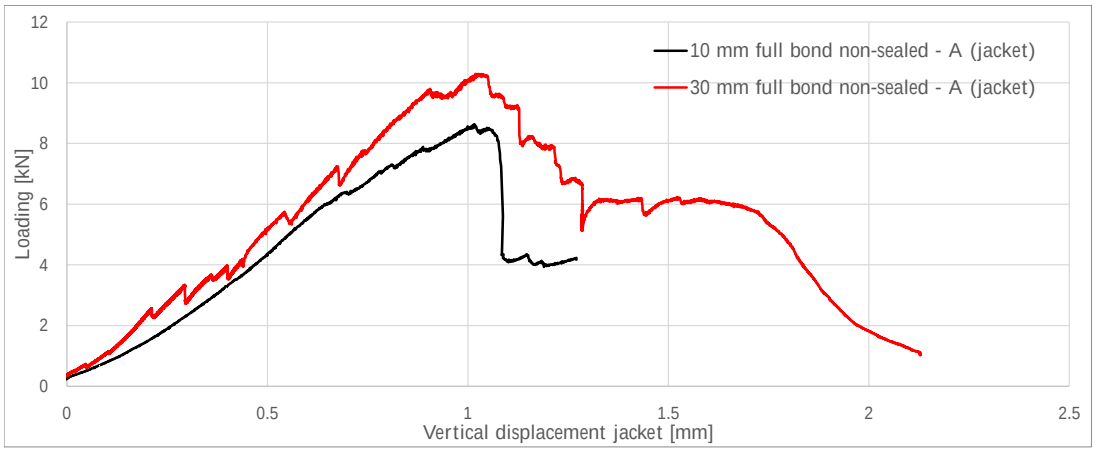

(c) Force-displacement curve retrofitted masonry beams with 10 and 30 mm full bonded (non-sealed curing) SHCC overlay.

Figure 4.26: Force-displacement curves all retrofitted masonry beams with an 10 and 30 mm thick SHCC overlay.

4.4.1. DIC Analysis

Digital Image Correlation is used to investigate the failure mechanisms of the retrofitted masonry beams in more detail. The photos analysed are coupled to the corresponding f-u curve. In this report, only two specimens are investigated, i.e. specimen number 4 and 6. These two specimens represent the two failure mechanisms observed.

Additionally, the accuracy of the used DIC is examined. The possibility to use the DIC to estimate the vertical deformations of the retrofitted masonry beams is investigated. These results are presented in Appendix C.

Specimen number 4 - 10 mm full bond - Shear failure

Specimen number 4 is retrofitted with a 10 mm full bonded overlay. This specimen failed by debonding of the masonry units. As mentioned in Table (4.9), most of the masonry beams failed in shear. With the help of this single specimen, the global failure mechanism is described.

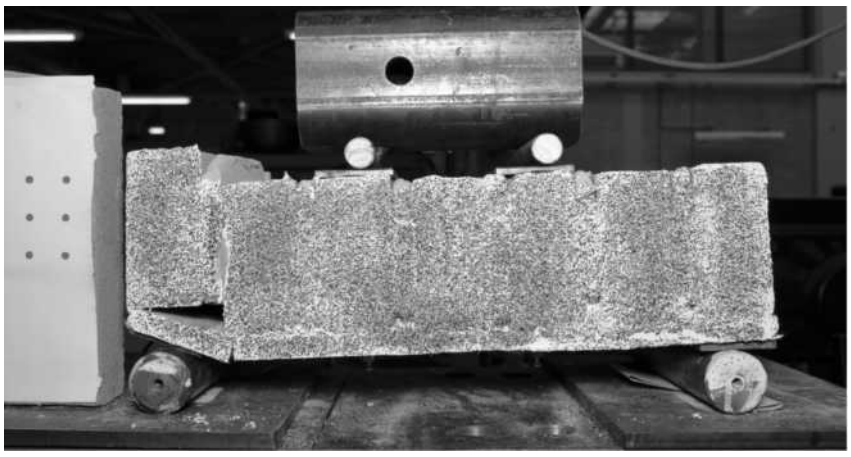

(a) Front view.

(b) Bottom view.

Figure 4.27: Failure pattern specimen number 4; 10 mm full bond - A.

In Figure (4.28a) the corresponding force-displacement curve is presented. Multiple points of interest (A-F) are selected. With the help of the DIC, the deformed shapes of this specimen are determined for these six points. The von Mises strain field is calculated.

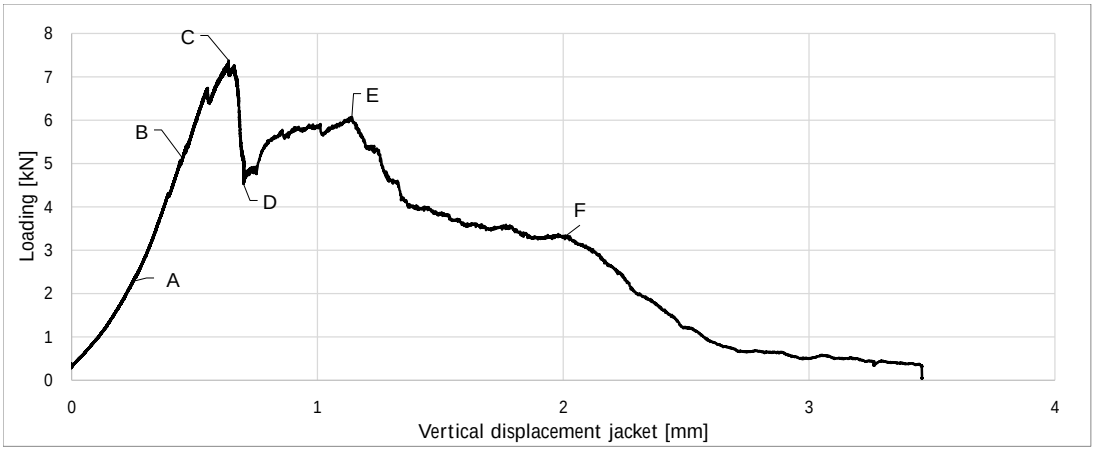

(a) Force-displacement curve with points of interest.

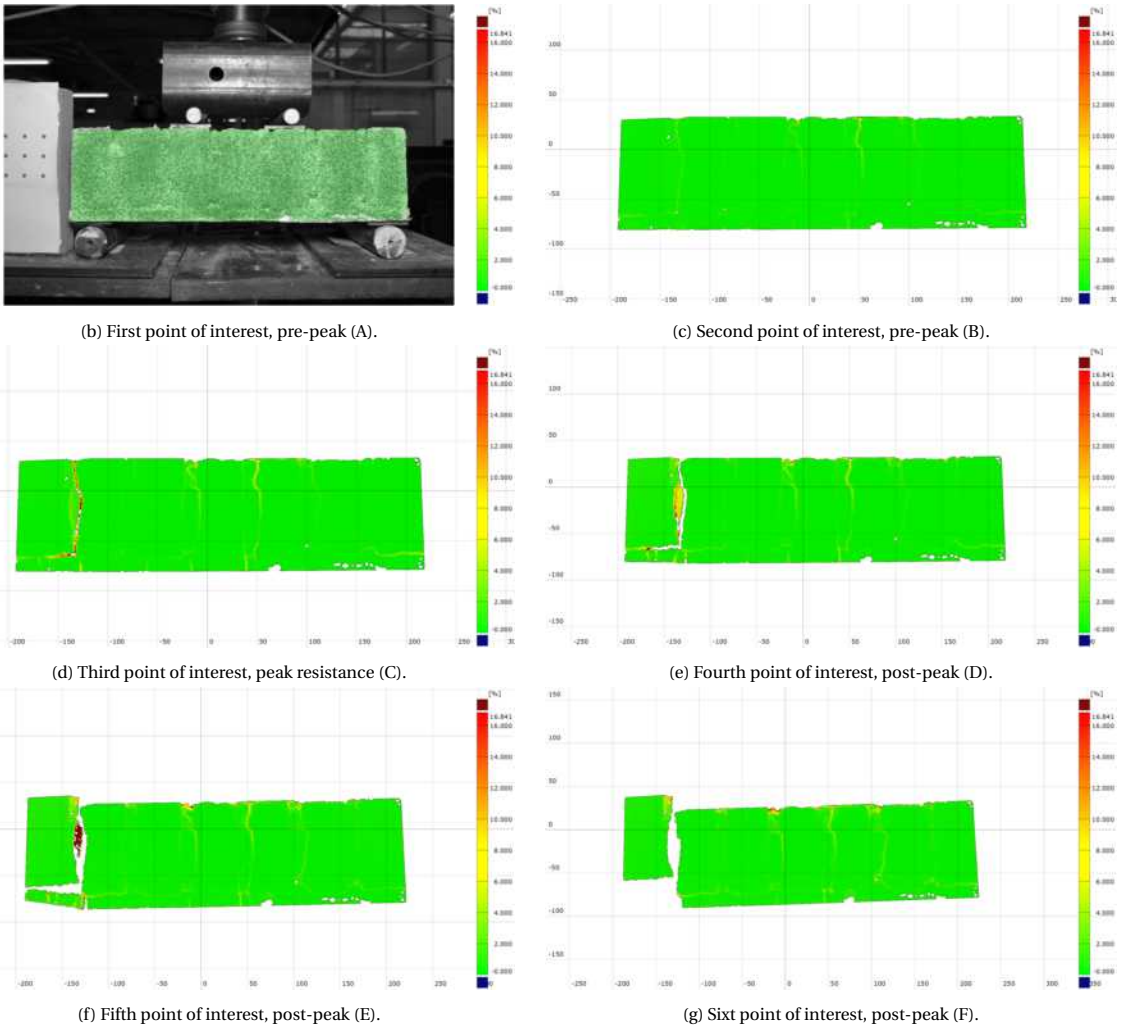

(b) First point of interest, pre-peak (A).

(c) Second point of interest, pre-peak (B).

(d) Third point of interest, peak resistance (C).

(e) Fourth point of interest, post-peak (D).

(f) Fifth point of interest, post-peak (E).

(g) Sixt point of interest, post-peak (F).

Figure 4.28: Mises equivalent strains pre- and post-peak. Specimen number 4.

With the help of Figure (4.28) the 'shear-type' failure of the retrofitted masonry beams becomes clear. The strains are concentrated around the left outside masonry unit. Cracks in the overlay are only present underneath this debonding masonry unit. No cracks in the constant bending moment region are present. This coincides with the crack pattern found on the actual specimen, see Figure (4.27b).

As stated before, the possible movement of the masonry units at the edges of the specimen influences the measurement data of the vertically aligned LVDT. The black curve shows the influence of this movement in Figure (4.23a). It can be seen that the LVDT data is incorrect since the measured vertical deformation reduces after peak resistance. This is because of the vertical movement of the left-hand side masonry unit.

Specimen number 6 - 30 mm full bond - Flexural failure

The first tested specimen with a fully bonded 30 mm SHCC overlay failed in a completely different manner compared to the previously discussed specimen. This specimen failed in a flexural manner, recognized by the crack pattern in the SHCC overlay material in the constant bending moment region. Similar to the previously discussed specimen first, the strain field is investigated for multiple points on the force-displacement curve. In Figure (4.29) the final failure of this specimen is depicted.

Figure 4.29: Failure pattern specimen number 6; 30 mm full bond - A.

As for the previous specimen discussed, multiple points of interest are chosen and analysed from the governing force-displacement curve. A clear difference in failure mechanism is shown for this specimen. For load step A the strains are located at the left unit-mortar interface of the central masonry unit of the masonry beam. No high strains are present at the SHCC-masonry interface, at any location. Increased loading results in even higher strains around this central masonry unit. Additionally, cracks in the SHCC overlay start to develop in the constant bending moment region. At the left-hand side of the specimen, high strains are present at the SHCC-masonry interface, see Figure (4.30c). At even higher loads, the strains/cracks increase at the centre of the specimen. The strains in the SHCC-masonry interface, at the left side of the specimen, do not increase significantly. Figure (4.30e) shows the strains at peak resistance. Over the full width of the constant bending moment region, cracks in the overlay material are present. After peak loading, one discrete crack opens up in the SHCC. This initiates large curvatures of the specimen, resulting in the debonding of the central masonry unit with its neighbouring elements.

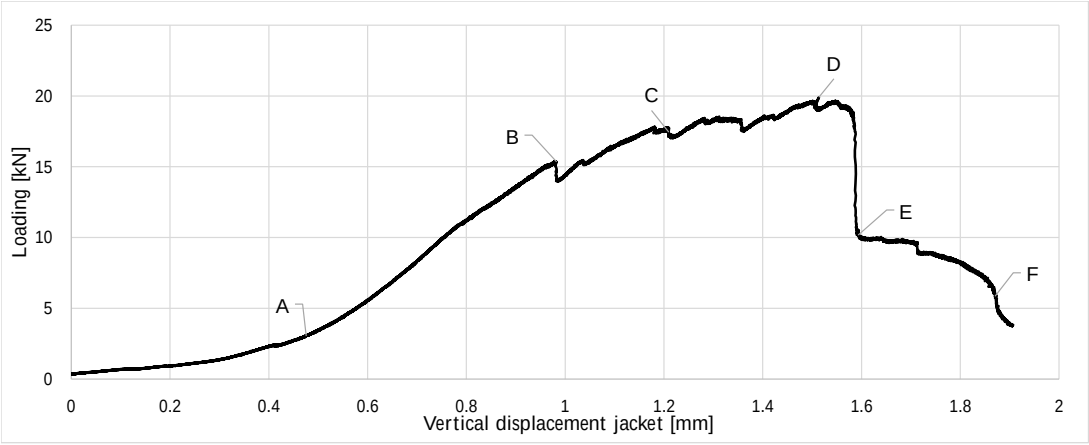

(a) Force-displacement curve with points of interest.

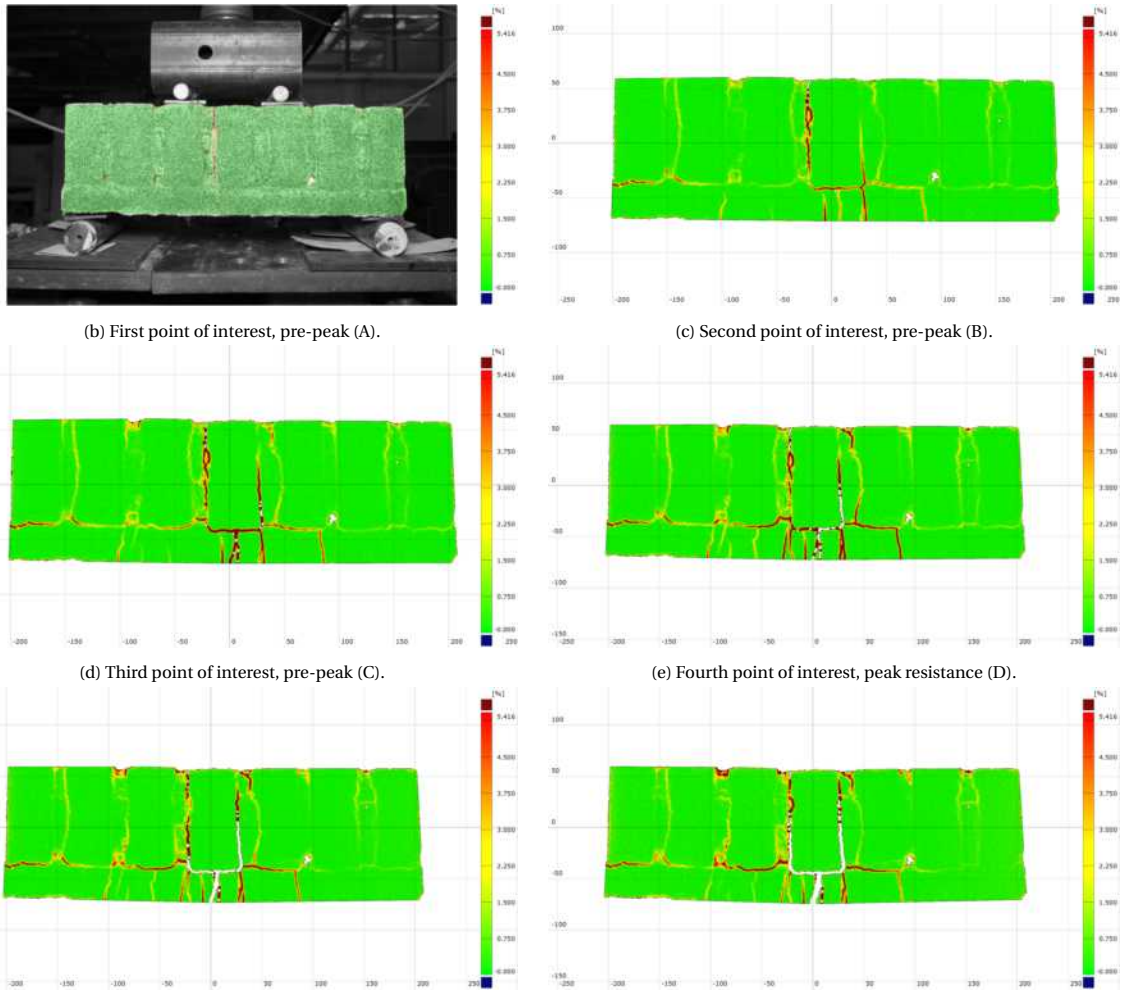

(b) First point of interest, pre-peak (A).

(c) Second point of interest, pre-peak (B).

(d) Third point of interest, pre-peak (C).

(e) Fourth point of interest, peak resistance (D).

(f) Fifth point of interest, post-peak (E).

(g) Sixt point of interest, post-peak (F).

Figure 4.30: Mises equivalent strains pre- and post-peak. Specimen number 6.

5

Numerical Analysis

5.1. Introduction

For this research, numerical analyses are used to investigate possible influence parameters which resulted in the failure mechanisms observed during the experimental campaign. If the numerical model is accurate in describing the global failure mechanisms of the examined specimen, it might, in the best-case scenario, also be possible to derive more local and more in-depth failure mechanisms which are not well captured in the experiments. Currently, much investigation is performed in the application of FEM onto masonry samples, both small- and larger scale.

For this numerical research program, the main focal point is to investigate the ability to use known material- and interface models to describe the general failure mechanisms, as observed in the experimental campaign. Only shear tests are modelled in DIANA version 10.3. Additionally, the influence of multiple parameters is considered and discussed, see Chapter 7.

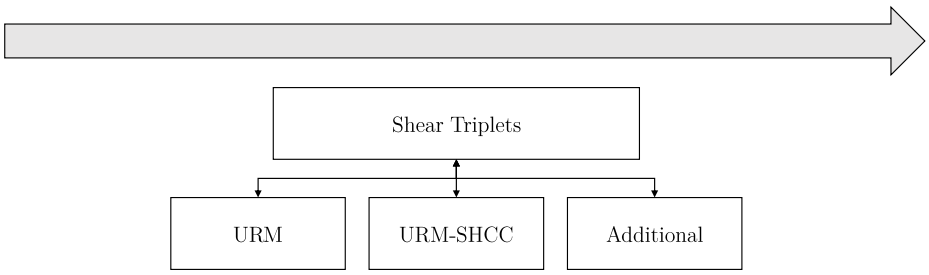

In this chapter, the numerical models examined for both the non-retrofitted masonry as well as the retrofitted masonry triplets are discussed. Modelling of the plain masonry triplets is done to investigate the accuracy of the used material and interface models, compared to the experimental results. Since this model forms the basis of the final retrofitted specimen, limitations of the numerical model considered must be known.

5.2. Non-retrofitted clay masonry triplets

The masonry specimen used for the shear strength experiments consist out of three clay masonry units, which are bonded to each other by two mortar joints. The size of the clay masonry units is equal to 210x100x50 mm. The mortar joints are 10 mm thick.

From the literature review, it is known that two micro-modelling approaches are well documented, i.e. the simplified- and detailed micro-models. In this numerical campaign, a simplified micro-model is considered.

All the non-linear behaviour is contributed to the unit-unit interfaces. Both 2D and 3D models are considered. In Figure (5.1) an overview of these models is provided. Additional information, with respect to the support and loading conditions is provided in Figure (5.1a). Also, the different interfaces present in these models are shown. In Figure (5.1b) the symmetric boundary conditions for the 2D numerical model are depicted. For the 3D models similar to supporting, symmetry, and loading conditions are used. For the 3D models, the different interfaces are modelled as 3D planes instead of 2D line interfaces.

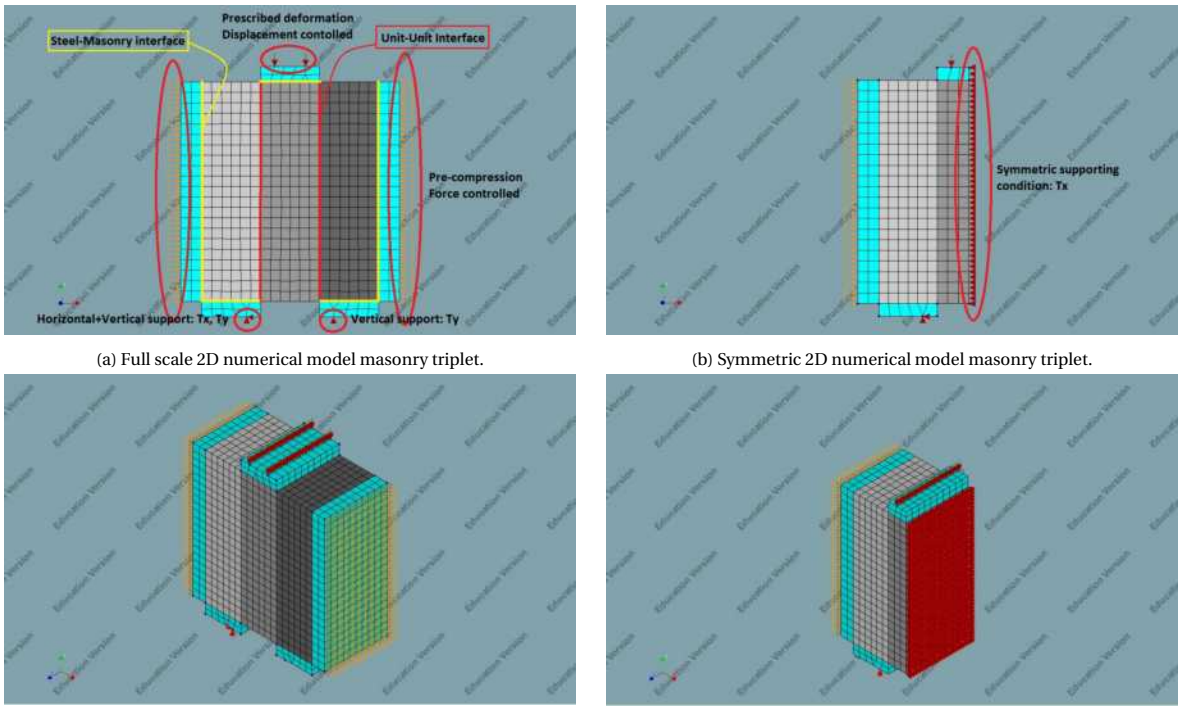

(a) Full scale 2D numerical model masonry triplet.

(b) Symmetric 2D numerical model masonry triplet.

(c) Full scale 3D numerical model masonry triplet.

(d) Symmetric 3D numerical model masonry triplet.

Figure 5.1: Numerical models non-retrofitted masonry triplets, 2D and 3D, full scale and symmetric.

In Figure (5.1 it is shown that not only the masonry units are modelled (grey elements). To simulate the actual experiment in more detail the steel plates, used for supporting and loading the specimen, are also taken into account (blue elements). The dimensions of the steel elements modelled coincide with the dimensions of the actual steel plates used in the experiments, which provides more realistic results.

In Table (5.1) and (5.2) additional information related to both the 2D and 3D numerical models is provided. For all analyses the finite element program DIANA version 10.3 is used. For more detailed information about this software, the reader is referred to [10]. For all analyses, quadratic elements are used.

Table 5.1: General information 2D numerical models, non-retrofitted masonry triplet.

Parameter	
Scale of model	2D
Type of loading	Shear displacement: displacement controlled Pre-compression: force controlled
Finite element types	Eight-noded quadrilateral isoparametric plane stress elements (CQ16M) Six-noded triangular isoparametric plane stress elements (CT12M) Six-noded line interface elements (CL12I)
Stress state	Plane stress state
Interpolation scheme	Quadratic
Integration scheme	CQ16M - 2x2 Gaussian integration CT12M - 3-point integration over the area CL12I - 4-point Newton-Cotes integration
Shape dimension	2D
Topology dimension	2D
Stress components	Plane stress elements: σ_{xx} / σ_{yy} / σ_{xy} Interface elements: t_{nx} / t_{sy}
Element size	10x10 mm
DOF per node	Plane stress elements: u_x / u_y Interface elements: Δu_{nx} / Δu_{sy}

Table 5.2: General information 3D numerical models, non-retrofitted masonry triplet.

Parameter	
Scale of model	3D
Type of loading	Shear displacement: displacement controlled Pre-compression: force controlled
Finite element types	Twenty-noded isoparametric solid brick elements (CHX60) Thirtheen-noded isoparametric solid pyramid elements (CPY39) Ten-noded isoparametric solid tetrahedron elements (CTE30) Fifteen-noded isoparametric solid wedge elements (CTP45) Sixteen-noded plane interface elements (CQ48I)
Stress state	Three-dimensional stress state
Interpolation scheme	Quadratic
Integration scheme	CHX60 - 3x3x3 Gaussian integration CPY39 - 13-point integration over the volume CTE30 - 4-point integration over the volume CTP45 - 3x2 integration scheme CQ48I - 4x4 Newton-Cotes integration
Shape dimension	3D
Topology dimension	3D
Stress components	Solid elements: σ_{xx} / σ_{yy} / σ_{zz} / σ_{xy} / σ_{yz} / σ_{zx} Interface elements: t_{nx} / t_{sy} / t_{sz}
Element size	10x10x10 mm
DOF per node	Solid elements: u_x / u_y / u_z Interface elements: u_{nx} / u_{ny} / u_{nz}

For all analyses, it is assumed that the masonry units and steel plates remain in their linear elastic stage. All the non-linear behaviour is assumed to be present at the interfaces between the clay masonry units (unit-unit interface). This coincides with the experimental results. No failure of the masonry units is observed. For the unit-unit interfaces, a combined cracking-shearing-crushing interface model is used. The interfaces between

the steel plates and the masonry specimen are modelled by discrete cracking interfaces. No bonding between the steel and masonry is present. This modelling approach is similar as documented in [16] and is proven to provide satisfactory results for calcium silicate masonry triplets. The different material and interface properties are tabularized below, see Tables (5.3), (5.4), and (5.5). The stress-strain (traction-relative displacement) relationship of the two interface models are shown in Figure (5.2).

Table 5.3: General information material models, non-retrofitted masonry triplets.

Material	Symbol	Clay masonry units	Unit
Class		Concrete and masonry	
Material model		Linear elastic isotropic	
Linear material properties			
Young's modulus	E_m	8049	N/mm^2
Poisson's ratio	ν	0.14	-
Material		**Steel plates**	
Class		Steel	
Material model		Linear elastic isotropic	
Linear material properties			
Young's modulus	E_s	210000	N/mm^2
Poisson's ratio	ν	0.3	-

Table 5.4: General information steel-masonry interface model.

Material	Symbol	Steel-Masonry interface	Unit
Class		Interface elements	
Material model		Discrete cracking	
Linear material properties [a]			
Type		2D line interface	
Normal stiffness modulus	k_n	634800	N/mm^3
Shear stiffness modulus	k_t	10	N/mm^3
Discrete cracking [a]			
Tensile strength	f_t	0.10	N/mm^2
Mode-I tension softening criterion		Brittle	
Mode-II shear criterion for crack development		Zero shear traction	

[a] Properties derived from [16].

Table 5.5: General information simplified unit-unit interface model.

Material	Symbol	Unit-Unit interface	Unit
Class		Interface elements	
Material model		Combined cracking-shearing-crushing	
Linear material properties			
Type		2D line interface	
Normal stiffness modulus	k_n	125.8	N/mm^3
Shear stiffness modulus	k_s	52.1	N/mm^3
Cracking			
Tensile strength[a]	f_{t0}	0.0667	N/mm^2
Fracture energy	G_f^I	0.01	N/mm
Shearing			
Cohesion	c_0	0.1892	N/mm^2
Friction angle	ϕ	0.647	rad
Dilatancy angle[b]	Ψ	0.647	rad
Residual friction angle	ϕ_r	0.60574	rad
Confining normal stress[c]	σ_u	-0.56	N/mm^2
Exponential degradation coefficient[c]	δ	9.63	-
Mode-II fracture energy	G_f^{II}		
Parameter a		-0.0632	mm
Parameter b		0.0941	N/mm
Crushing			
Compressive strength	f_c	13.11	N/mm^2
Factor Cs[c]		9	-
Compressive inelastic law			
Compressive fracture energy	G_{f_c}	35.06	N/mm
Equivalent plastic relative displacement		0.0058	mm

[a] Determined via the following assumption: $f_{t0} = 1.5 \cdot f_w$ in which f_w equals to the flexural bond strength (0.10 N/mm^2) of the clay masonry [33].
[b] Taken equal to friction angle. First assumption.
[c] Taken as proposed in [16].

The tables above show numerical values based on literature [16] and experimental results. The mentioned reference relates to the numerical modelling of calcium silicate masonry triplets under shear load conditions, i.e. same experiment different masonry material. Because of this similarity in the modelling approach, this reference forms a solid foundation for initial parameter choices. However, most of the material properties shown are derived at TU Delft via multiple experimental campaigns, making these parameters readily available for this research.

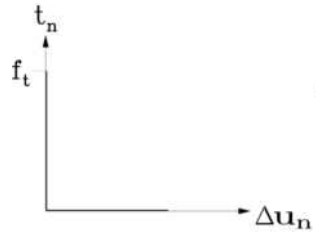

(a) Traction-slip relationship discrete cracking interface with brittle properties [10].

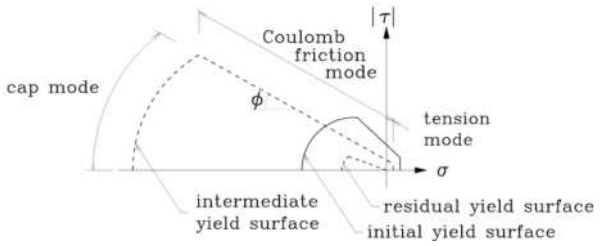

(b) Traction-slip relationship multisurface interface model, 2D. Combined cracking-shearing-crushing interface model [10].

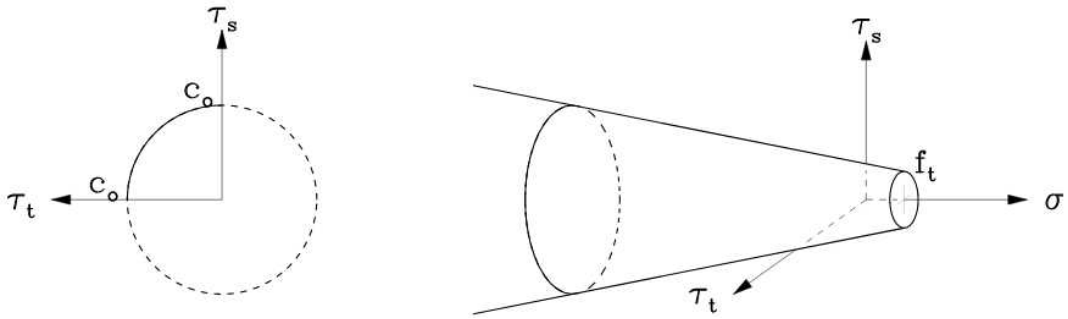

(c) Traction-slip relationship combined interface model 3D.

Figure 5.2: Stress-displacement relationships interfaces considered [10].

For both the 2D and 3D models, similar non-linear analyses are performed. The three pre-compression levels (i.e. 0.2, 0.6, and 1.0 Mpa) are all analysed. Each numerical analysis contains two different load steps. The first step represents the application of pre-compression. In the second load step, the prescribed shear deformation is applied to the model by the use of multiple load increments. All analyses (2D, 3D, full-scale, and symmetric) make use of the Full Newton-Raphson interactive procedure. Only non-linear physical behaviour is taken into account. Both the displacement and force convergence norms are used for each analysis, one of which must be satisfied for every single iteration. In Table (5.6) the different convergence norms and tolerances are summarized.

Table 5.6: General information non-linear analyses, non-retrofitted masonry triplet.

Analysis	
Nonlinear effects	Physical nonlinear
Load steps, pre-compression level = 0.2 Mpa	Pre-compression: 0.2 Mpa [(1)] Shear displacement: 1 mm [0.001(50) 0.05(25)]
Load steps, pre-compression level = 0.6 Mpa	Pre-compression: 0.6 Mpa [(1)] Shear displacement: 1 mm [0.001(100) 0.05(25)]
Load steps, pre-compression level = 1.0 Mpa	Pre-compression: 1.0 Mpa [(1)] Shear displacement: 1 mm [0.001(125) 0.05(25)]
Iterative solver	Full Newton-Raphson
Convergence norm (tolerance)	Displacement norm (10^{-7}) Force norm (10^{-4})
Max. number of iterations[a]	50

[a] This is simply used as upper limit of iterations and therefore not equal to the maximum amount of iterations required for the computational efforts.

With these material models, boundary conditions, and non-linear analysis properties considered all the different numerical models resulted in converged solutions.

Several aspects are considered in the comparison of the numerical and experimental results:

- Force-displacement relationship;
- Stress distributions; and
- Failure mechanisms.

The accuracy of both the 2D and 3D numerical models is investigated. In Figure (5.3) the force-displacement curve of the two-dimensional model is shown. The numerical results are plotted versus the experimental results.

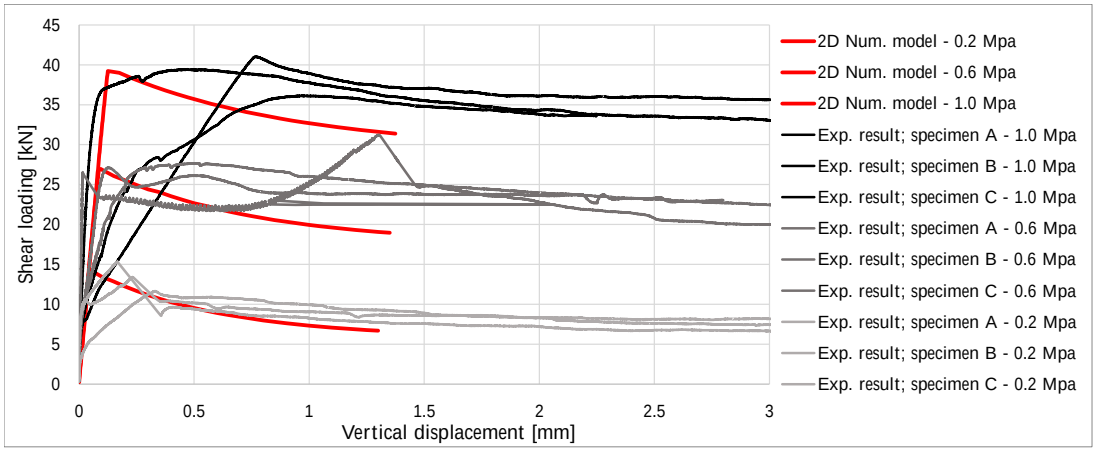

Figure 5.3: Force-displacement curve. 2D numerical simulation versus experimental results. Three pre-compression levels.

In Figure (5.4) the force-displacement relationship of both the 2D and 3D numerical model is depicted. It is clearly shown that both types of models provide similar results.

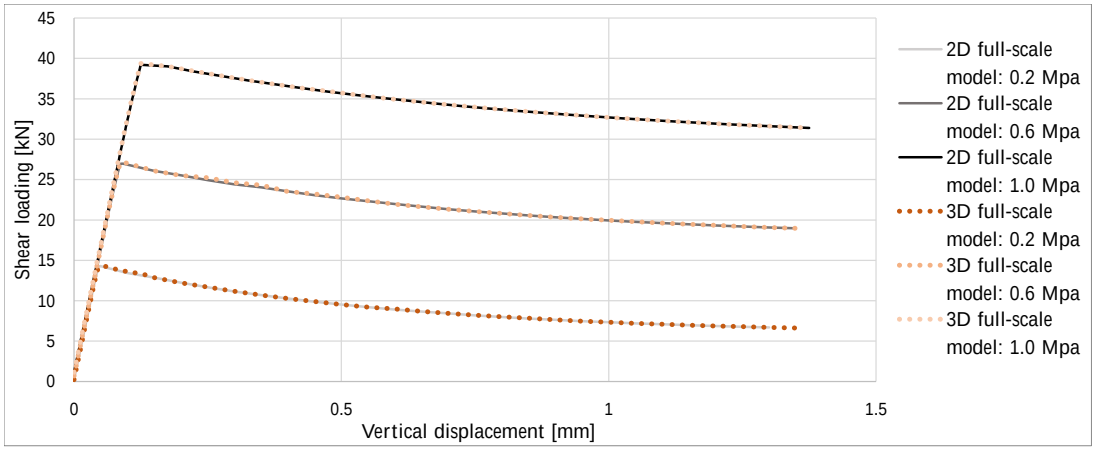

Figure 5.4: Force-displacement curves 2D versus 3D models.

More detailed analyses of these two models are performed. Tractions at the non-linear unit-unit interfaces are investigated to determine at which loading, and at which location in these interfaces, yielding starts. These additional analyses are summarized in Appendix E.

It is concluded that the global behaviour of the experimental results is represented to some extent. Better numerical results are obtained for the lowest pre-compression level. However, with the help of a parametric

study, one can create a better fit for the other two levels of pre-compression as well. Fitting the numerical model to the experimental results is not within the scope of this research. With the used finite elements, material properties, and interactive procedure convergence is always obtained for the numerical simulations.

It must also be noted that the numerical simulations are only able to capture the global behaviour of the specimen, e.g. resistance of the specimen. More detailed information, like dilatant behaviour of the masonry bricks or non-symmetric failure mechanisms, are not accurately represented. If more realistic numerical results are required, a detailed micro-modelling approach can be considered.

5.3. Retrofitted clay masonry triplets

Numerical analyses of the retrofitted masonry triplets are performed. Modelling these retrofitted specimen requires the simulation of the SHCC overlay in DIANA. The overlay is assumed to remain elastic. This is based on the experimental results. For all experiments, the overlay remained uncracked. The ability to use this type of modelling procedure for the retrofitted masonry triplets is investigated. The numerical results of the initial FE model are compared to the experimental results, as is done for the URM. Only the retrofitted specimen with a 10 mm full bonded overlay is examined.

Again, a simplified micro-model is assumed for the masonry triplet. Only 3D models (both full-scale and symmetric) are taken into account due to the out-of-plane motions of the overlay. The total numerical model is constructed with quadratic solid elements. In Figure (5.5) the mesh of these models is depicted. Just as for the non-retrofitted model, the steel plates and masonry units are coloured blue and grey, respectively. Now, the additional SHCC layer is shown with the yellow finite elements.

(a) Full scale 3D numerical model retrofitted masonry triplet, thickness SHCC equal to 10 mm.

(b) Symmetric 3D numerical model retrofitted masonry triplet, thickness SHCC equal to 10 mm.

Figure 5.5: Numerical models retrofitted masonry triplets, 3D, full scale and symmetric, thickness SHCC equal to 10 mm.

The material and interface models of the masonry units, steel plates, and the unit-unit interface are similar to the numerical simulations of the non-retrofitted masonry. Also, similar finite elements, as noted in Table (5.2), are used for these retrofitted specimen. The material properties of the SHCC are provided in Table (5.7). The interface between the SHCC overlay and the masonry triplet is also modelled with a combined shearing-cracking-crushing interface. The material properties are assumed to be equal to the unit-unit interface. This assumption is made based on the experimental results. This modelling decision is used for the first assumption. The low cohesion of the SHCC-masonry interface corresponds to the experimental results, i.e. shear strength retrofitted specimen.

Table 5.7: General information SHCC material model, retrofitted masonry triplets.

Material	SHCC	
Class	Concrete and masonry	
Material model	Linear elastic isotropic	
Linear material properties		
Young's modulus[a]	18,500	N/mm^2
Poisson's ratio	0.16	

[a] 28 days strength [42].

Again, full Newton-Raphson iterative procedures are considered. The different loading steps and convergence norms used are summarised in Table (5.8).

Table 5.8: General information non-linear analyses, retrofitted masonry triplet.

Analysis	
Nonlinear effects	Physical nonlinear
Load steps, pre-compression level = 0.2 Mpa	Pre-compression: 0.2 Mpa [(1)] Shear displacement: 1 mm [0.001(50) 0.05(65)]
Load steps, pre-compression level = 0.6 Mpa	Pre-compression: 0.6 Mpa [(1)] Shear displacement: 1 mm [0.001(75) 0.05(88)]
Load steps, pre-compression level = 1.0 Mpa	Pre-compression: 1.0 Mpa [(1)] Shear displacement: 1 mm [0.001(100) 0.05(88)]
Iterative solver	Full Newton-Raphson
Convergence norm (tolerance)	Displacement norm (10^{-7}) Force norm (10^{-4})
Max. number of iterations	50

The numerical results are compared to the experimental results of the retrofitted masonry specimen with a 10 mm thick overlay. In Figure (5.6) the force-displacement relationships of both the numerical and experimental results are depicted.

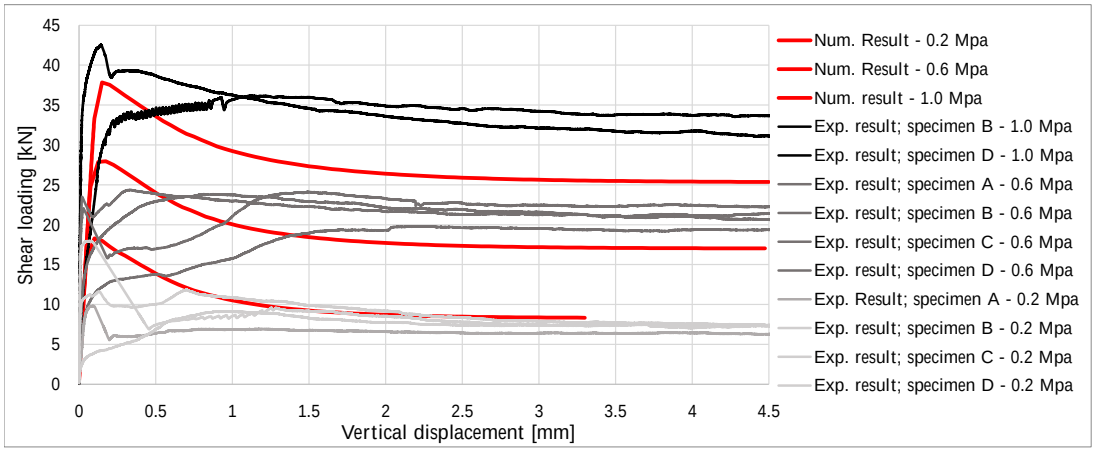

Figure 5.6: Force-displacement curve. 3D numerical simulation versus experimental results. Three pre-compression levels.

It is clearly shown that the numerical model of the retrofitted specimen overestimates the peak shear resistance, especially for the pre-compression levels equal to 0.2 and 0.6 Mpa. However, for the highest level of pre-compression, this peak resistance is well captured by the numerical model. The post-peak regime is not modelled with high accuracy. The softening in this stage is too large. This post-peak regime is also not well captured for the non-retrofitted numerical models.

A parametric study to investigate the possibility of a better fitting numerical model is not part of this research. It is shown that the resistance is lower for the retrofitted model for higher levels of pre-compression, by comparing the force-displacement curves of both the plain masonry triplet model and the retrofitted model. This is not realistic. The application of the overlay must increase resistance.

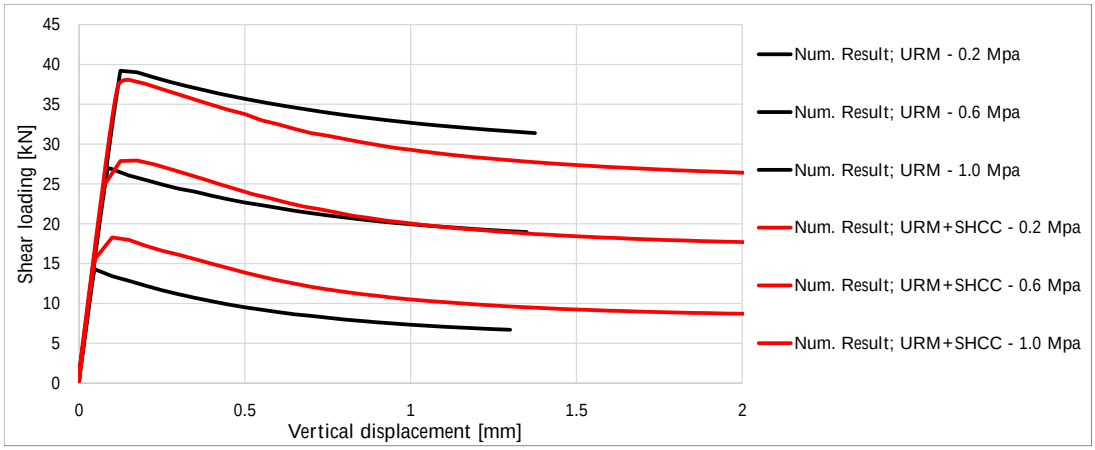

Figure 5.7: Force-displacement curves. Numerical results plain masonry triplets versus retrofitted model.

Figure (5.7) clearly shows that the idea "additional capacity due to the extra interface" is not valid for all the levels of pre-compression. For the highest pre-compression level, lower shear strength is obtained for the numerical model simulating the retrofitted specimen. Through analysing the stress distributions, at both the unit-unit and the SHCC-masonry interface, this is investigated. A total of six sections, three per type of interface, are analysed. These sections are shown in Figure (5.8).

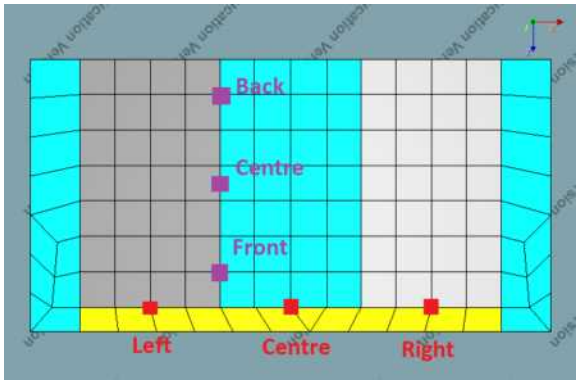

(a) Top view numerical model retrofitted masonry triplet with 10 mm SHCC overlay. Sections of interest for both unit-unit and SHCC-masonry interfaces. SHCC overlay in yellow, steel plates in blue and masonry units in grey scales. Purple = vertical sections unit-unit interface. Red = vertical sections SHCC-masonry interface.

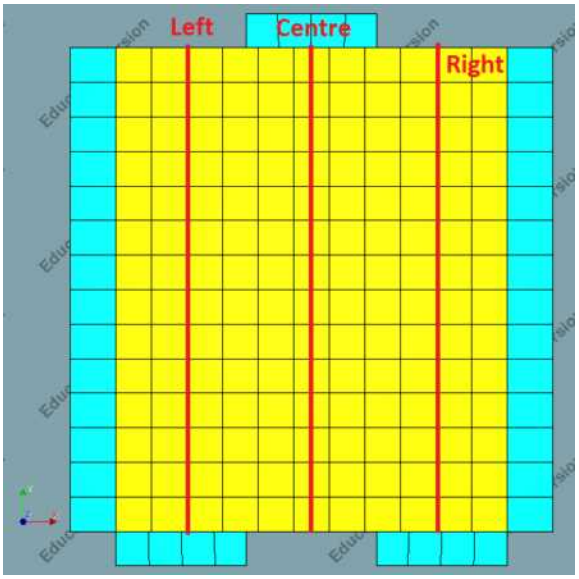

(b) Front view numerical model retrofitted masonry triplet with 10 mm SHCC overlay. Sections of interest in the SHCC-masonry interface.

Figure 5.8: Top and front view 3D FE model with the analysed sections at the unit-unit and SHCC-masonry interfaces.

The quantities analysed are the tractions and relative displacements of these two interfaces. All three pre-compression levels are considered, however, in this report, only the results corresponding to the lowest and highest pre-compression level are provided. All quantities are provided in terms of the global coordinate system used. Both the tractions and the relative displacements are determined at the integration points of the finite elements.

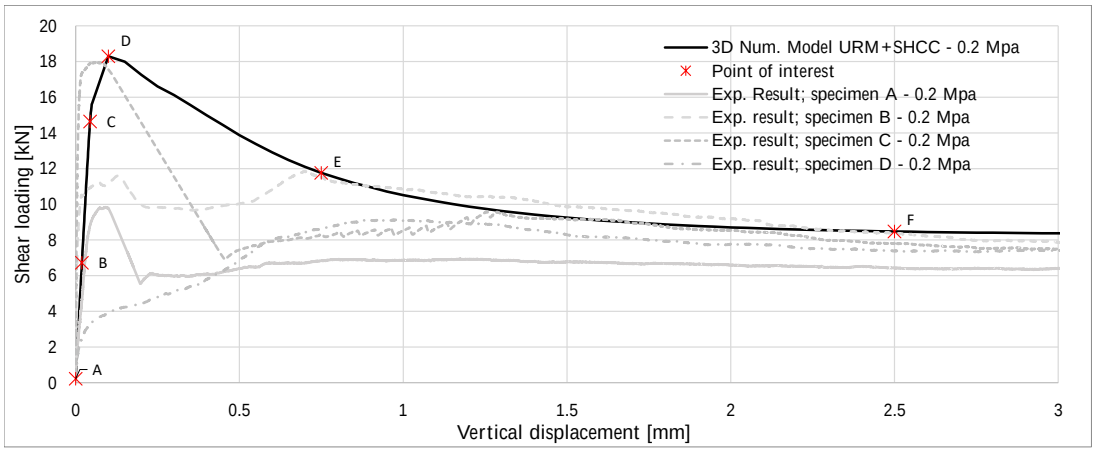

(a) Force-displacement curve experimental results and numerical model. Pre-compression level = 0.2 Mpa. Experimental curves corresponding to retrofitted masonry specimen with 10 mm full bonded overlay.

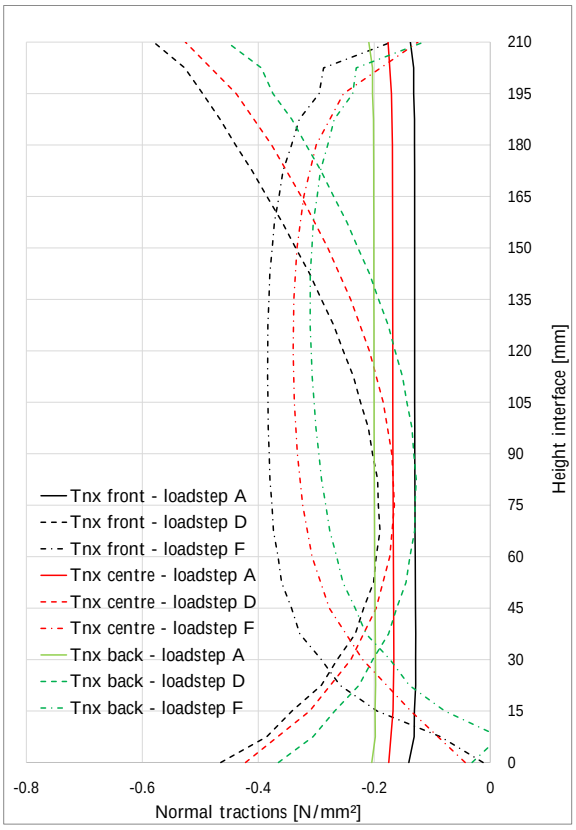

(b) Normal tractions unit-unit interface in global x-direction.

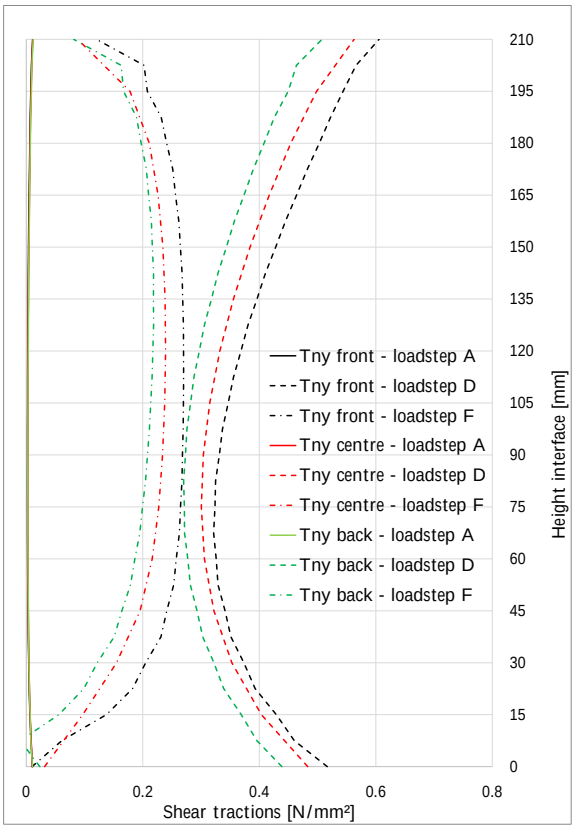

(c) Shear tractions unit-unit interface in global y-direction.

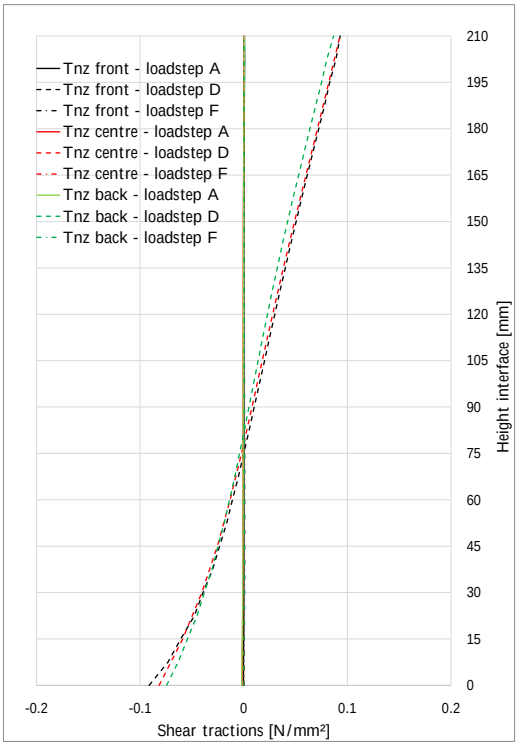

(d) Shear tractions unit-unit interface in global z-direction.

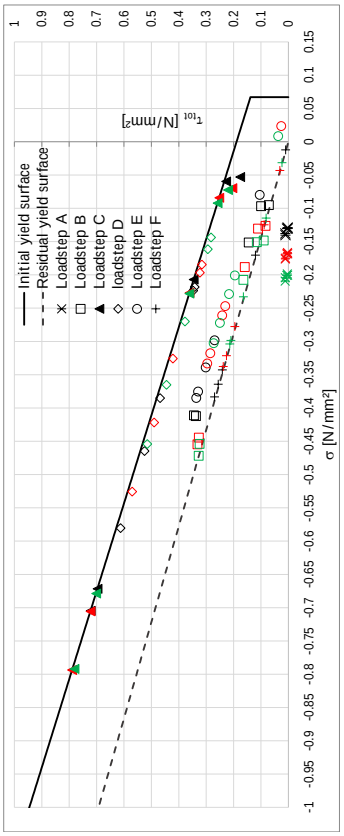

(e) $\tau - \sigma$ plane with initial and residual yield surfaces. Black markers = front section unit-unit interface, red markers = centre section, and green = back section.

Figure 5.9: Stress distribution unit-unit interface 3D numerical model retrofitted clay masonry. Pre-compression = 0.2 Mpa.

Because of the multiple sections (and load steps) taken into account, not all the numerical results are plotted. This results in unreadable graphs. In Figure (5.9b), (5.9c), and (5.9d) the tractions are plotted for only three out of six load steps. In all of these graphs, the numerical results corresponding to the 'front' section of the unit-unit interface are plotted using black curves or markers. The results of the middle section (centre) are shown in red. For the third, and final, section of interest (back) green curves are used.

As for the plain specimen, it is shown that both the normal and shear tractions are largest at the top and bottom of the specimen, up to peak resistance. In the post-peak regime, the maximum values are located at the centre of the specimen (height/2). In the legend of Figure (5.9e), only black markers are shown for simplicity. All three analysed sections use the same type of markers for the same load step of interest, however, with their corresponding colours (black, green, and red).

From the figures shown it is concluded that the pre-compression does not distribute uniformly through the unit-unit interfaces, see both Figure (5.9b) and (5.9e) load step A. This is known on beforehand since the specimen examined is inhomogeneous. Due to the application of the (stiff) SHCC overlay, the neutral axis (N.A.) of the specimen is shifted in the direction of the applied overlay. However, the resulting pre-compressional force is applied halfway the total specimen thickness, resulting in an eccentricity with the N.A. of the specimen, which, in turn, creates a curvature of the section.

Additionally, it is shown from Figure (5.9e) that yielding of the unit-unit interface occurs before the peak resistance (load step C). For all three locations, the unit-unit interface yielding occurs at the Coulomb friction plane, the compressional strength, nor the tensile strength, of the interface, is reached. From the same figure, it seems that for load step C the backside of the unit-unit interface is yielding 'more' compared to the other two locations analysed, i.e. for this location more points are located at the yield surface. However, one earlier load step (load step B) the combination of stresses determined at the front side of this same interface are closer to the yield surface. Utilizing additional analysis, the exact yielding sequence is investigated. Four additional load steps, in between the two original load steps B and C, are analysed (X1-X4). Please note that only the results of the front and back section of the unit-unit interface are plotted, since these differ the most with respect to each other, see Figure (5.10).

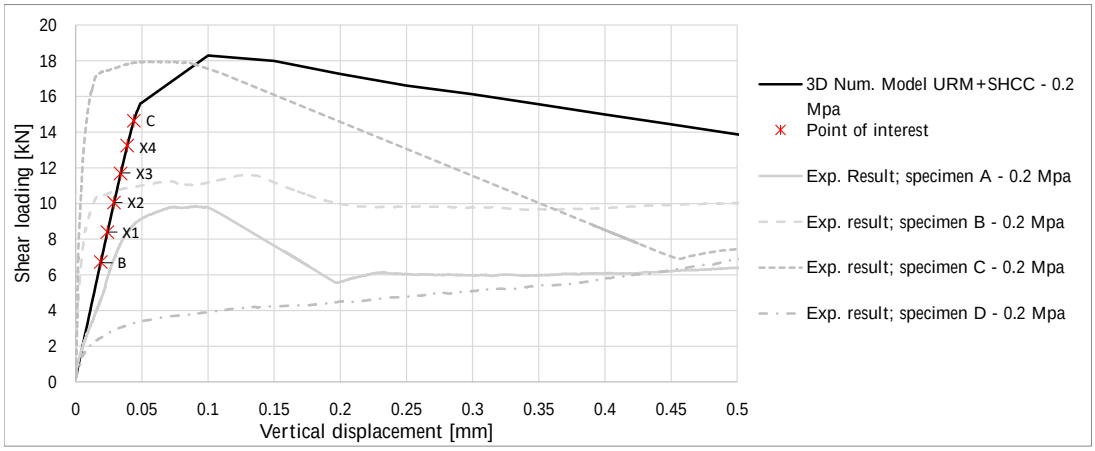

(a) Force-displacement curve experimental results and numerical model. Pre-compression level = 0.2 Mpa. Experimental curves corresponding to retrofitted masonry specimen with 10 mm full bonded overlay. Additional points of interest in the linear elastic stage.

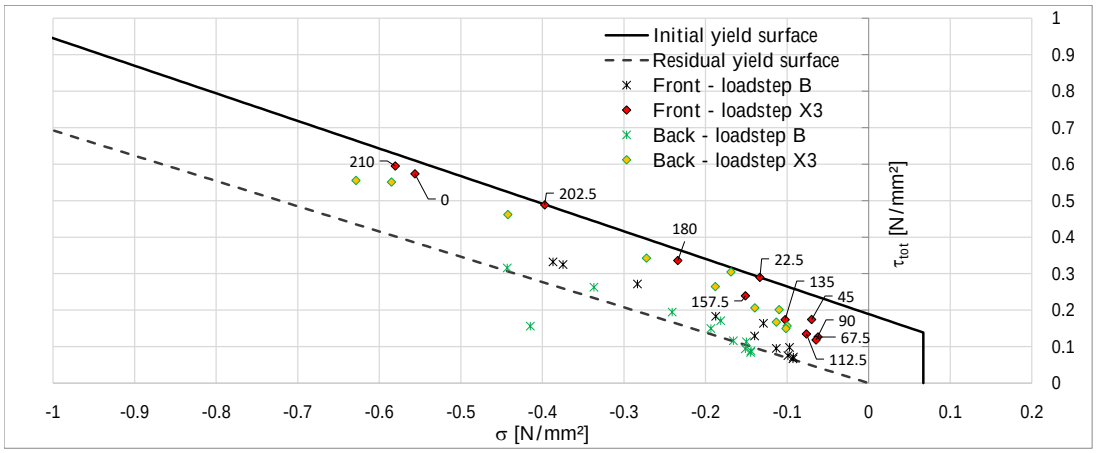

(b) $\tau - \sigma$ plane with initial and residual yield surfaces. Stress combinations for extra loading steps. Black markers = front section and green markers = back section unit-unit interface.

Figure 5.10: Stress distribution unit-unit interface 3D numerical model retrofitted clay masonry. Additional loadsteps. Pre-compression = 0.2 Mpa.

Again, for graphical reasoning, a small number of data points are plotted in the figure above. Only the first and fourth load step (B and X3) are depicted. It is shown that the tractions collected at the front section of the unit-unit interface reach the yield surface before the back section, see load step X3. However, the differences are minor.

Besides the unit-unit interface also the interface between the SHCC overlay and the masonry is analysed. The initial six loading steps (A-E), as used for the first analysis of the unit-unit interface, are considered. Besides the normal and shear tractions at this interface, also the relative displacements in global z-direction are provided. Through this latter quantity the delamination of the overlay, with respect to the masonry substrate, is investigated. Again, only the numerical results for three loading steps are presented (load step A, D, and F). In all figures, black markers (or curves) are used to visualise the results corresponding to the centre location of the SHCC-masonry interface. The red and green markers/curves are used for the left and right section, respectively.

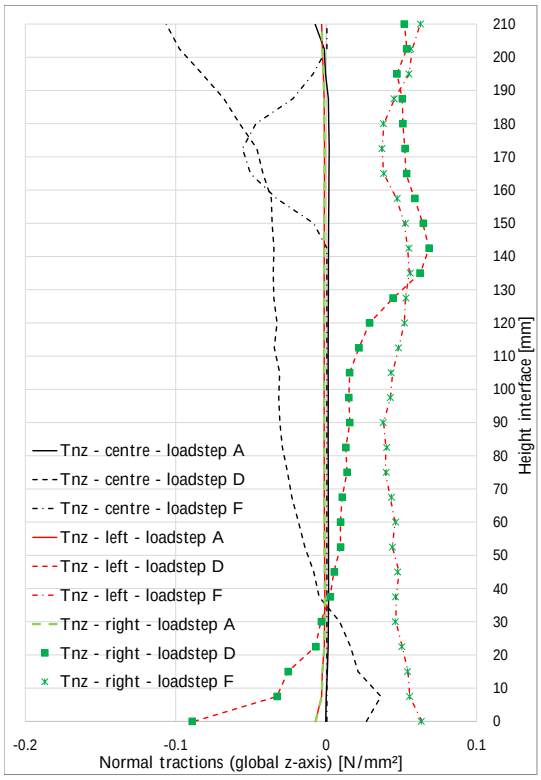

(a) Normal tractions SHCC-masonry interface in global z-direction.

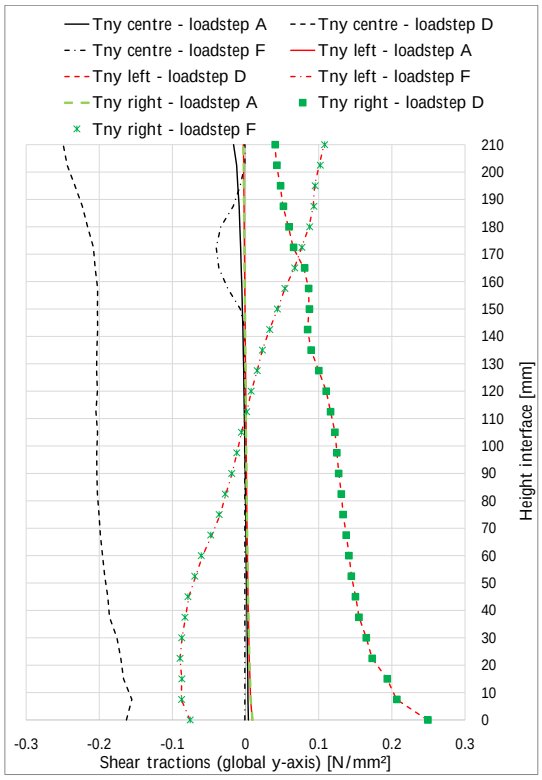

(b) Shear tractions SHCC-masonry interface in global y-direction.

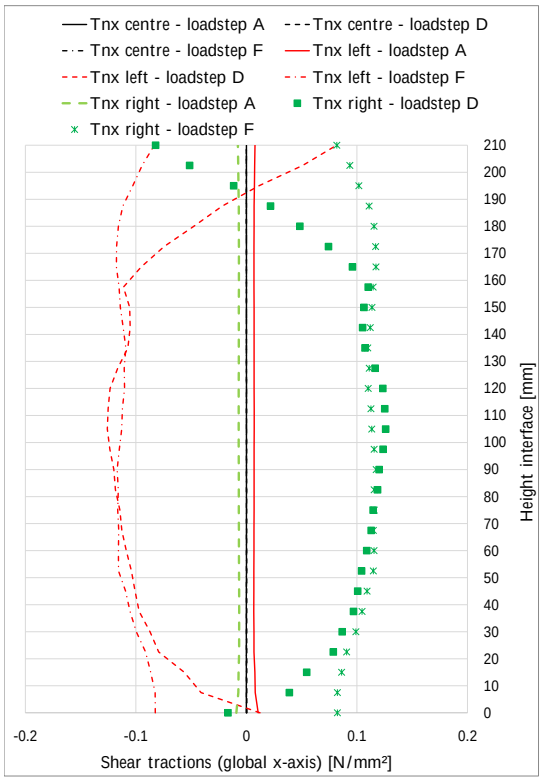

(c) Shear tractions SHCC-masonry interface in global x-direction.

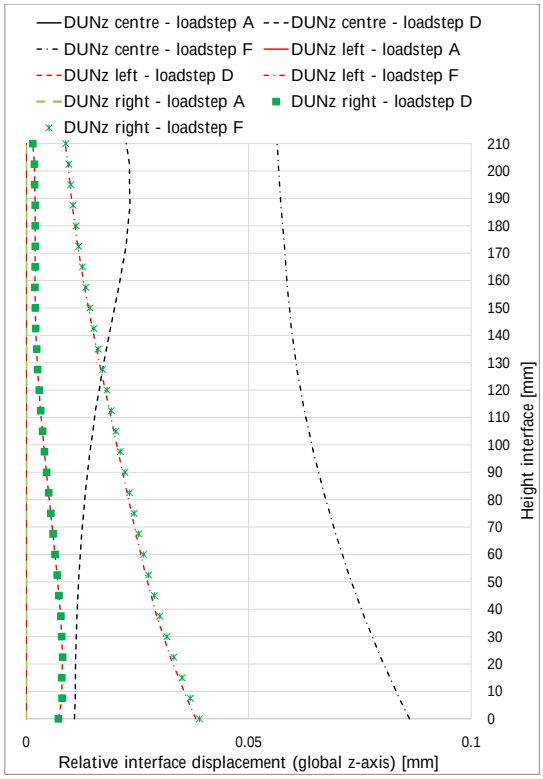

(d) Delamination SHCC overlay. Relative displacements SHCC-masonry interface.

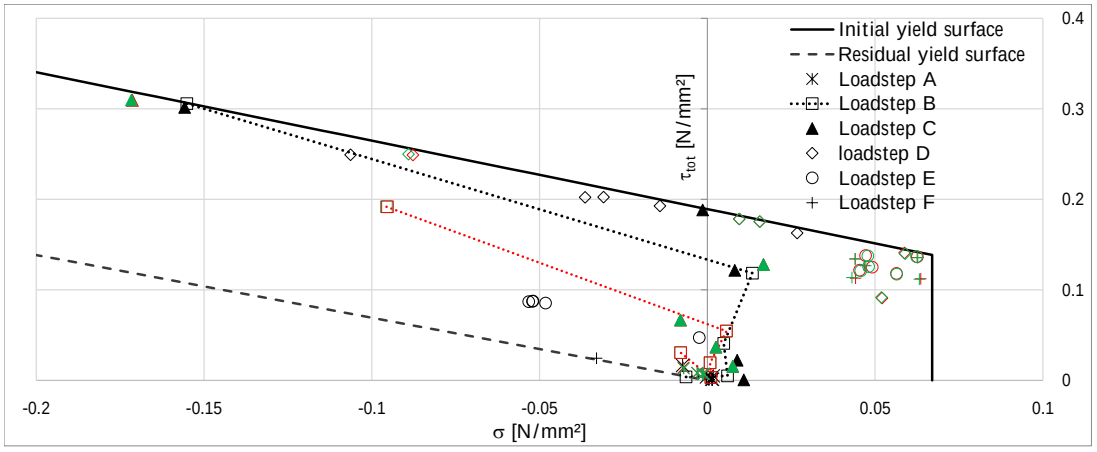

(e) $\tau - \sigma$ plane with initial and residual yield surfaces. All loadsteps shown. Black markers = centre section SHCC-masonry interface, red markers = left section, and green = right section.

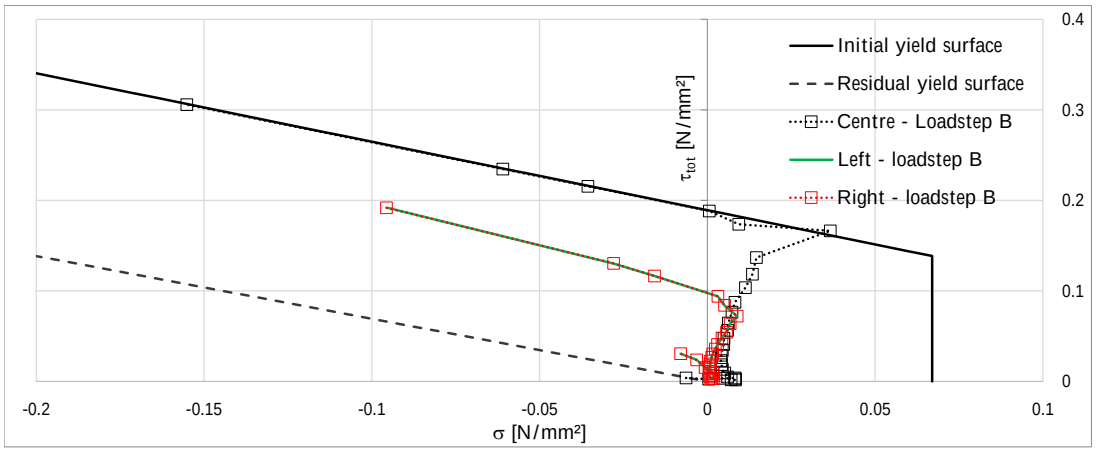

(f) $\tau - \sigma$ plane with initial and residual yield surfaces. Only loadstep B shown. Black markers = centre section SHCC-masonry interface, red markers = left section, and green = right section.

Figure 5.11: Stress distribution SHCC-masonry interface 3D numerical model retrofitted clay masonry. Pre-compression = $-0.2\,\mathrm{N/mm^2}$.

Symmetry conditions of the specimen are clearly shown. For example, in Figure (5.11b) it is shown that at peak resistance (load step D) the centre section of the SHCC-masonry interface is loaded in negative shear tractions in the global y-axis, i.e. shear tractions moving downwards. However, at both the left and right section of this interface, positive shear tractions are found, see green and red markers. This is due to the vertical supporting conditions underneath the outer masonry units. Each of these supporting locations takes into account 50% of the total shear force applied. Equilibrium in shear tractions is present between the centre section analysed, and the two outside sections, i.e. the total area under the curve equals approximately zero.

In Figure (5.11c) it is shown that only the left and right section of the analysed interface are loaded in shear tractions in global x-direction. These tractions are initiated due to the dilatant behaviour of the masonry units. Looking at the relative displacements of the interface, see Figure (5.11d), it becomes apparent that the overlay is delaminating more at the centre location. At the centre location, the tractions are very high, initiating the delamination of the overlay at this position quite early in the loading regime, see also Figure (5.11f). In this particular figure, the shear tractions are plotted versus the corresponding normal tractions for only the second load step investigated. The centre of the SHCC-masonry interface is loaded by higher shear tractions already, causing it to yield at the Coulomb friction plane.

To enable a comparison with the other levels of applied pre-compression similar output is provided for a pre-compression level equal to $1.0\,\mathrm{N/mm^2}$.

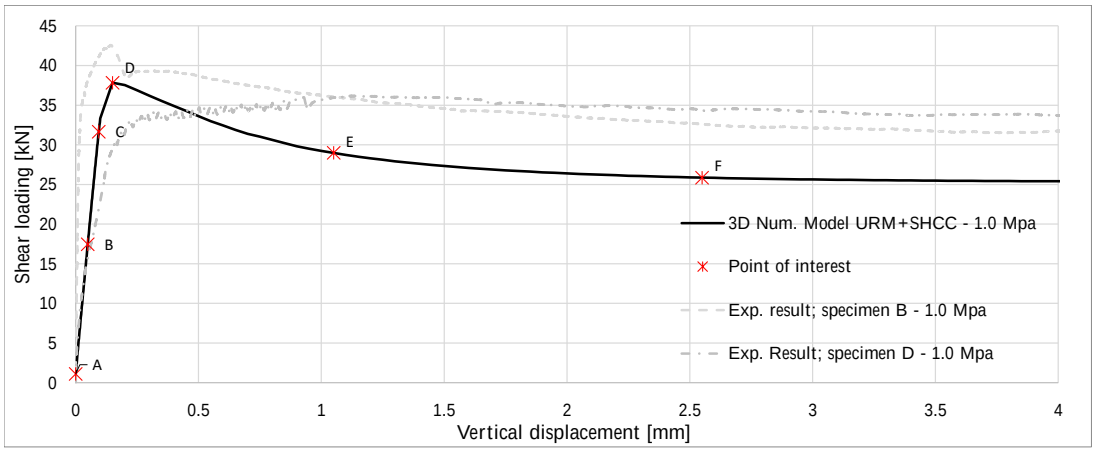

(a) Force-displacement curve experimental results and numerical model. Pre-compression level = 1.0 Mpa. Experimental curves corresponding to retrofitted masonry specimen with 10 mm full bonded overlay.

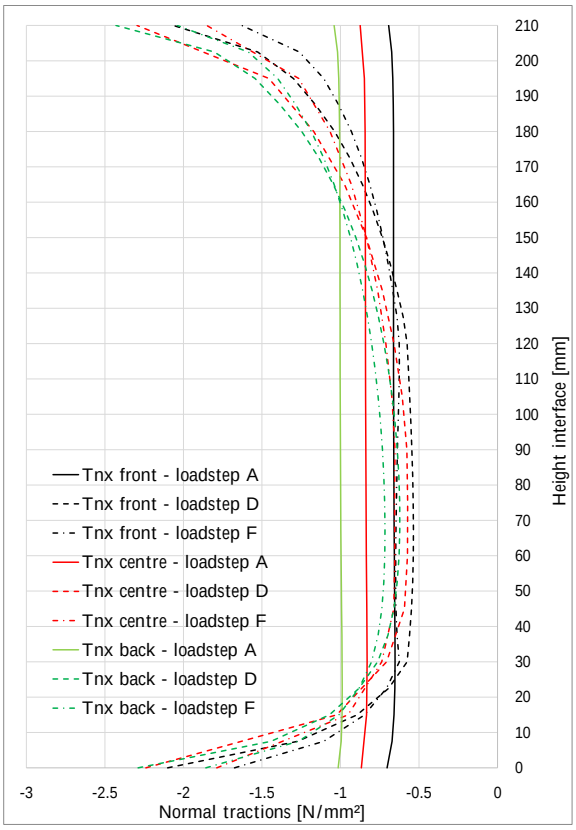

(b) Normal tractions unit-unit interface in global x-direction.

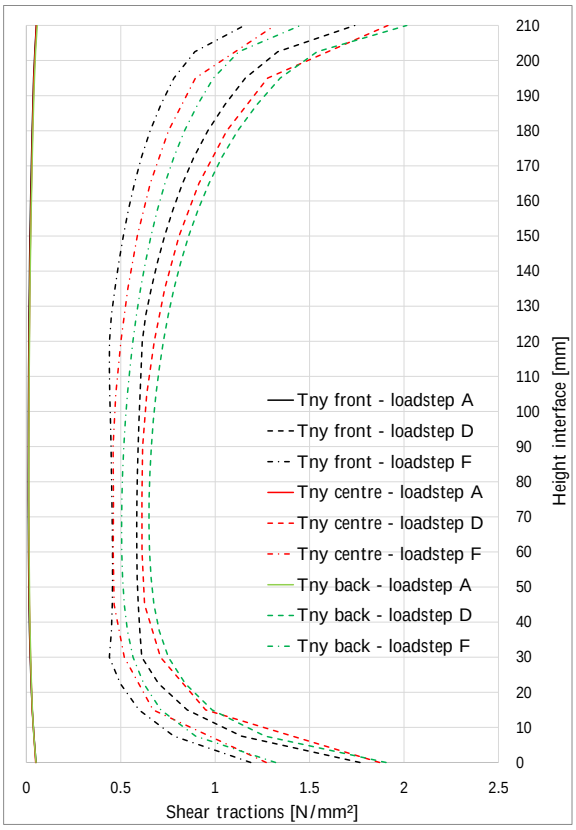

(c) Shear tractions unit-unit interface in global y-direction.

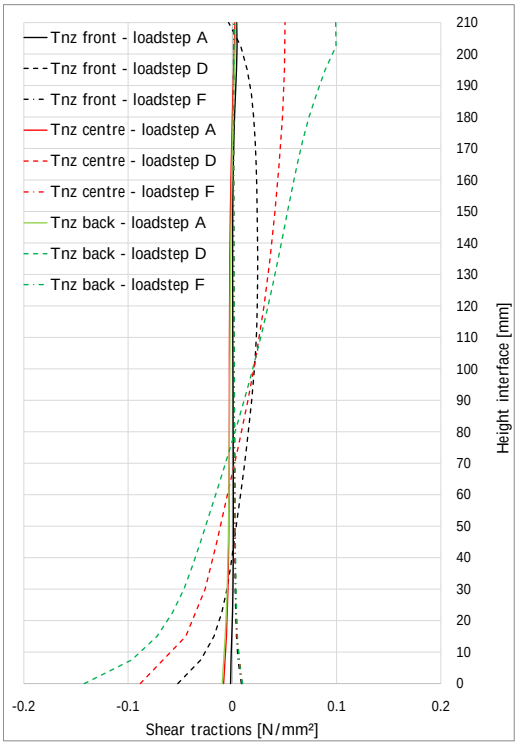

(d) Shear tractions unit-unit interface in global z-direction.

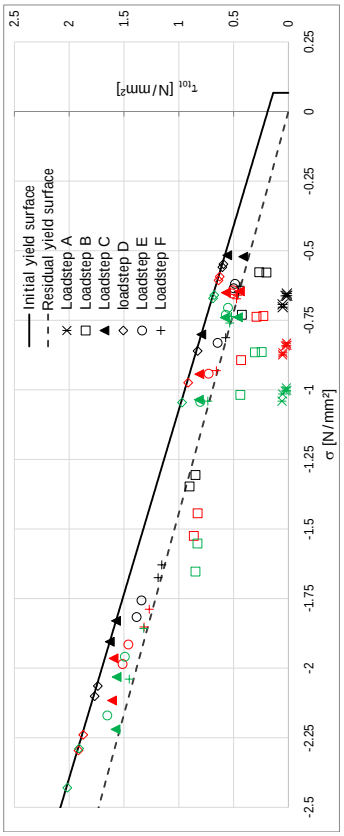

(e) $\tau - \sigma$ plane with initial and residual yield surfaces. Black markers = front section unit-unit interface, red markers = centre section, and green = back section.

Figure 5.12: Stress distribution unit-unit interface 3D numerical model retrofitted clay masonry. Pre-compression = 1.0 Mpa.

Significant differences are found in the numerical results corresponding to the highest level of pre-compression. Firstly, both the normal tractions (and shear tractions in global y-axis) at the unit-unit interface differ from the lower pre-compression level. The peak normal and shear tractions are, for this higher level of pre-compression, always located at the top and bottom of the specimen. This is different compared to the previously discussed results. For the lower pre-compression level the maximum tractions shifted from the extremities towards the centre of the specimen, with increased loading.

Besides this absent, in the shifting of the maximum tractions, the normal tractions due to the application of the pre-compression (load step A) are even less uniformly distributed over the width of the unit-unit interface, i.e. at load step A the ratio between the normal tractions at the front and the back of the unit-unit interface is greater compared to the lower, previously discussed, pre-compression level. This is because the total applied to pre-stress force is larger, causing the earlier discussed bending moment to increase as well.

From Figure (5.13e) it becomes apparent that the front section analysed already is on top of the Coulomb friction yield surface at load step C, just as for the lower pre-compression level. However, in the case of this higher pre-compression level, the yielding solely occurs in this particular section. The traction combinations of both the centre and back section are not at this yield surface. This is different from the lower level of pre-compression since, for this lower pre-compression, also the centre and back sections analysed shared points at the yield surface. Thus, the higher pre-compression level generates higher levels of non-symmetries in the failure mechanism observed. Compare Figure (5.11e) with Figure (5.13e). At peak resistance, all analysed sections of the unit-unit interface are at the shear failure yield plane.

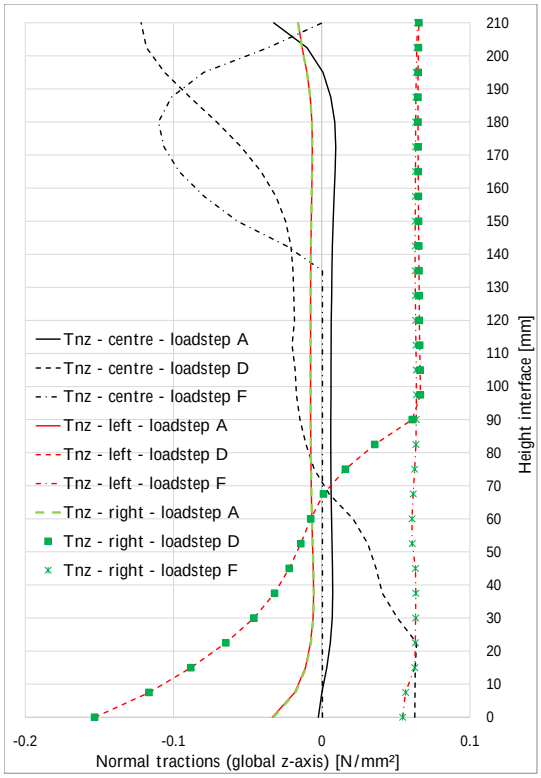

(a) Normal tractions SHCC-masonry interface in global z-direction.

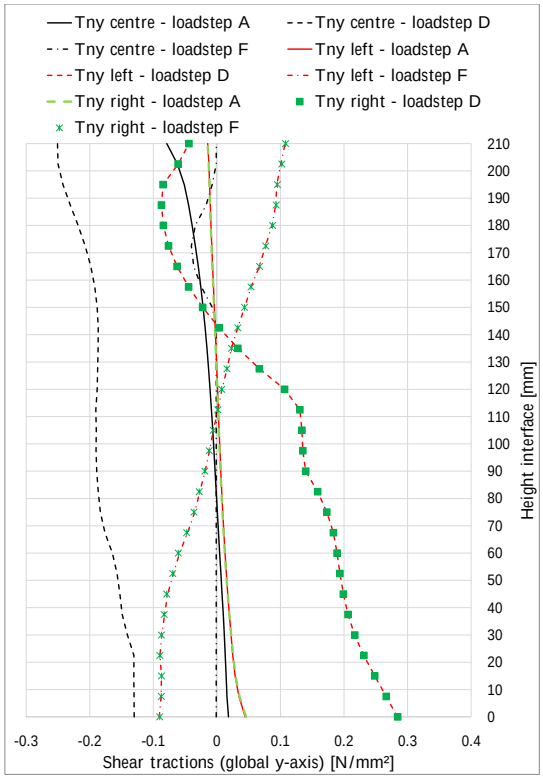

(b) Shear tractions SHCC-masonry interface in global y-direction.

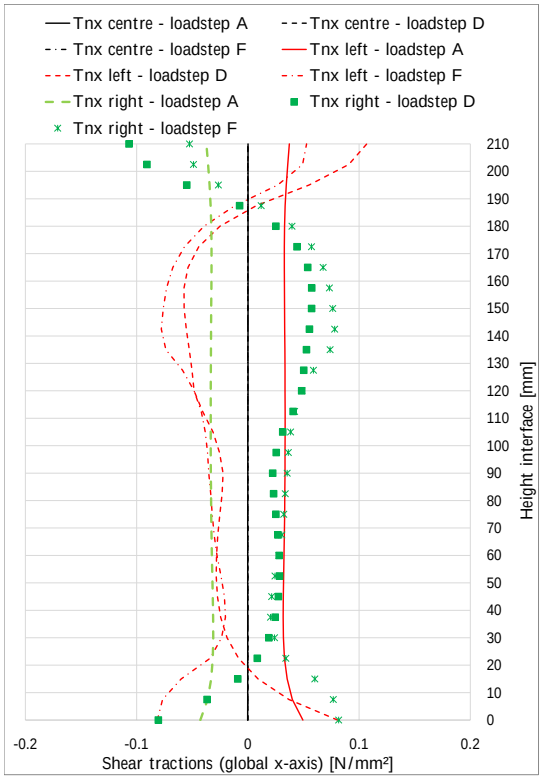

(c) Shear tractions SHCC-masorny interface in global x-direction.

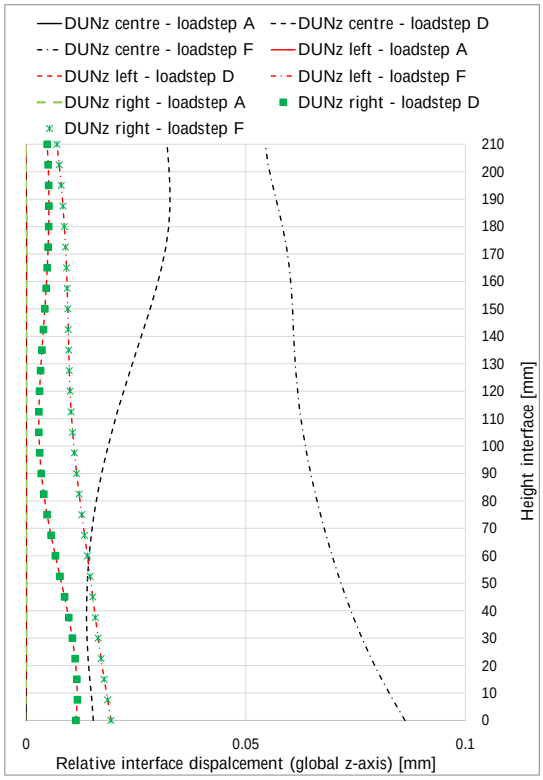

(d) Delamination SHCC overlay. Relative displacements SHCC-masonry interface.

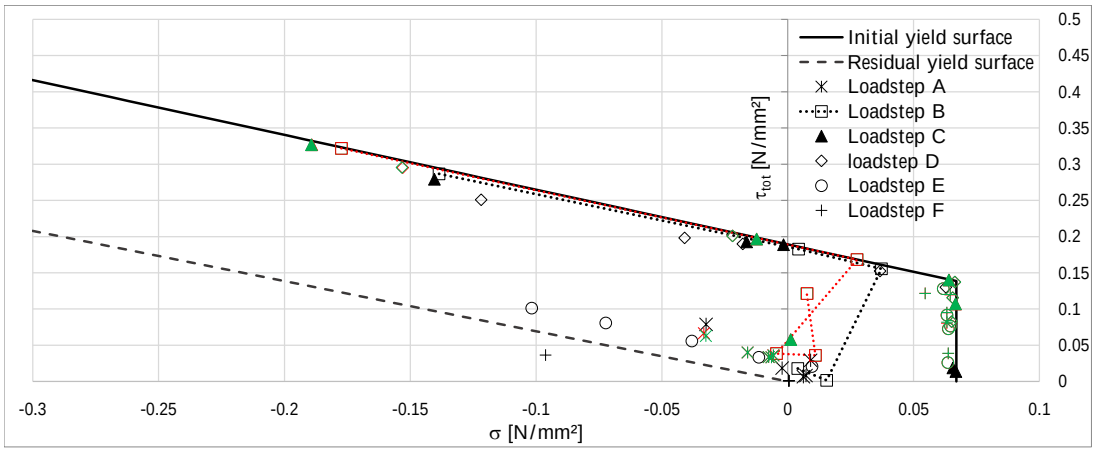

(e) $\tau - \sigma$ plane with initial and residual yield surfaces. All loadsteps shown. Black markers = centre section SHCC-masonry interface, red markers = left section, and green = right section.

Figure 5.13: Stress distribution SHCC-masonry interface 3D numerical model retrofitted clay masonry. Pre-compression = 1.0 Mpa.

Analysis of the numerical results corresponding to the SHCC-masonry interface reveals a point of interest related to the validity of the numerical modelling approach considered. From Figure (5.13c) it is determined that shear tractions, perpendicular to the shear loading direction, are already present for the first load step at the left and right section of the SHCC-masonry interface. This, however, is not realistic since, at this load step, only the pre-compression is applied to the full specimen, i.e. no shear tractions can be present in between the SHCC overlay and the masonry substrate.

From Figure (5.13e) it becomes clear that, for this numerical simulation, also the tension cut-off of the multi-surface interface model is activated. Already at load step C both the left and right section analysed share integration points which are located on this part of the yield surface. In the same figure, it is also shown that only the centre section of the SHCC-masonry interface experienced softening up to the intermediate and residual yield surface. This is not the case for the left and right section analysed. Softening in these two sections only started after load step E. Before this loading stage, all the tractions, corresponding to these two outer sections, are located on the initial yield surface. Additionally, see Figure (5.13a). It is shown that tensile stresses are present at the left and right section at higher load steps. The maximum tensile stress depicted is equal to the tensile strength of the interface ($0.667\,\mathrm{N/mm^2}$). At these two outside sections, the increase in tensile stresses, at the bottom of the SHCC-masonry interface resulted in the increase in delamination at the bottom of this interface, see Figure (5.13d).

5.3.1. Detailed analysis numerical model - Retrofitted URM

In the previous section, it is noted that shear tractions occur in the SHCC-masonry interface by the application of pre-compression. This is not realistic since, at this stage, no sliding of any of the elements is expected. A more in-depth analysis reveals a drawback of the simplified micro-modelling approach considered. By means of analytical calculations, the horizontal stress (and strain) distributions, due to the application of pre-compression, are determined. The numerical model also determines the horizontal stress and strain distribution. In Figure (5.15) both distributions are depicted. Additional information, related to the cross-section investigated, is shown in Figure (5.14).

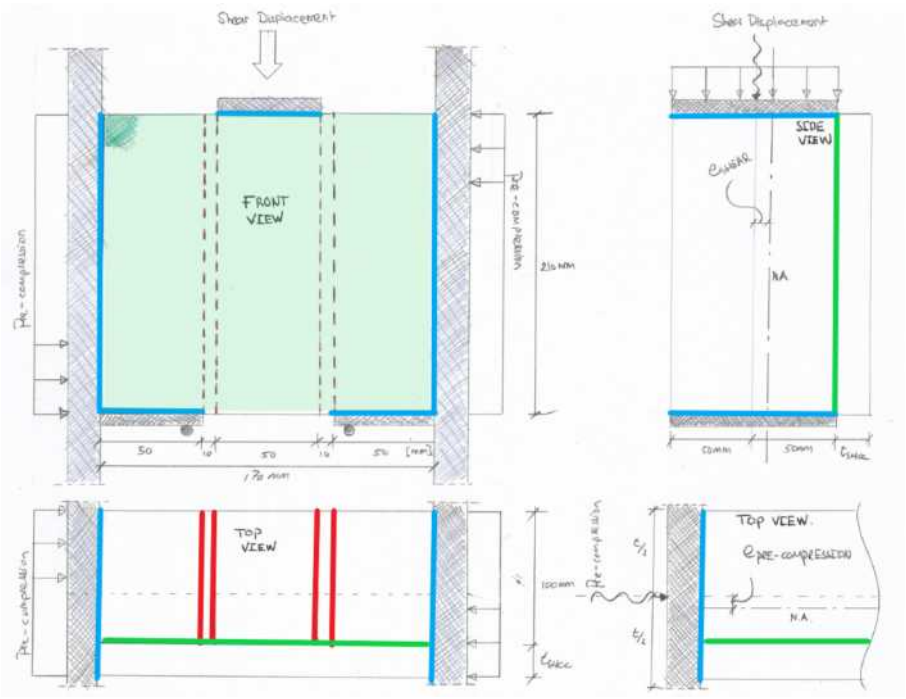

Figure 5.14: Overview different eccentricities present in the retrofitted masonry specimen. Both the shear loading and applied pre-compression do not load the specimen in its neutral axis. Blue = steel-masonry/SHCC interface, green = SHCC-masonry interface, and red = unit-mortar interfaces.

Figure (5.15) clearly shows that both the stress and strain distributions are larger in magnitude for the numerical simulations. Since the stresses are directly related to the strains, possible influences in the latter quantity are investigated. It is shown in Figure (5.15a) that the strains are not linearly distributed over the total thickness of the retrofitted specimen. A sudden increase in strains is present at the interface in between the SHCC overlay and the masonry triplet, which directly influences the stress distribution. Due to the application of pre-compression, a linearly distributed strain field must be present through the thickness of the specimen. Because of the inhomogeneous cross-section, which resulted in a shift of the neutral axis with respect to the resulting force of the pre-compression, a curvature of the cross-section is present. However, the strain distribution must not contain this sudden jump in magnitude at the SHCC-masonry interface.

This sudden increase in strains is due to low normal stiffness assigned to the unit-unit interface. As mentioned earlier, this stiffness (k_n) is based on the properties of both the masonry units and the mortar joint material. This low normal stiffness results in a 'negative volume' of this particular interface, i.e. the solid elements of the connected masonry units are pushed inside each other. The relative displacement of the structural unit-unit interface is negative. Due to this negative relative displacement of the unit-unit interface, the SHCC overlay material has to deform accordingly, to remain fixed to the masonry triplet. Increasing both the strains and stresses in the SHCC material.

In Figure (5.15) the numerical results are plotted with black curves and markers. The analytically derived stress- and strain distributions are shown with blue curves. Additionally, the SHCC-masonry interface is plot-

ted with a red dotted curve.

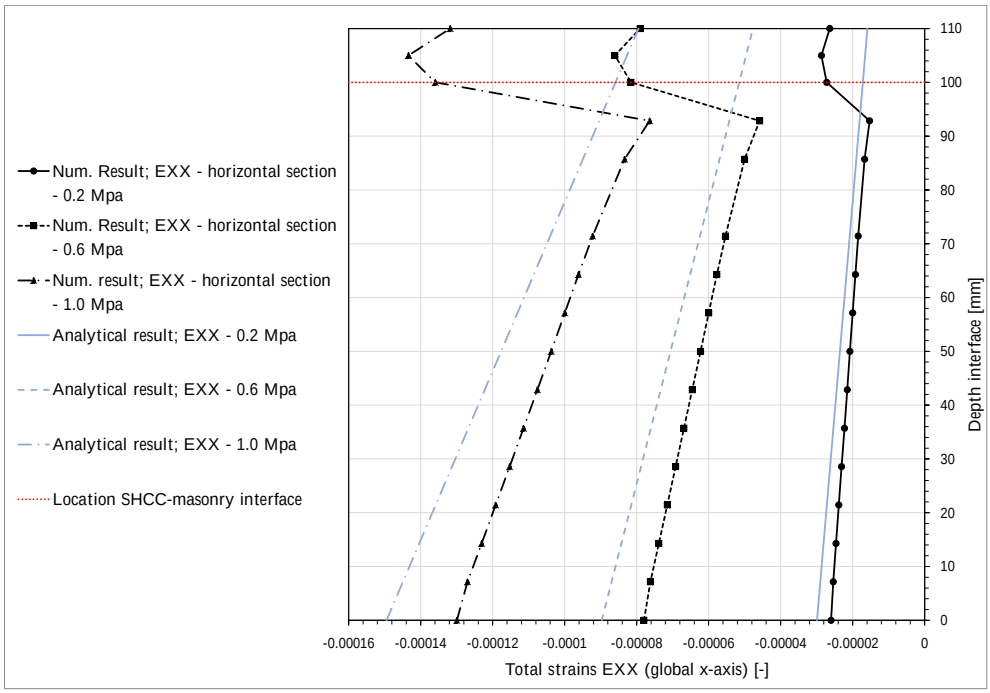

(a) Strain distribution EXX (global x-direction). All three pre-compression levels. Black curves = numerical results, blue curves = analytical calculations.

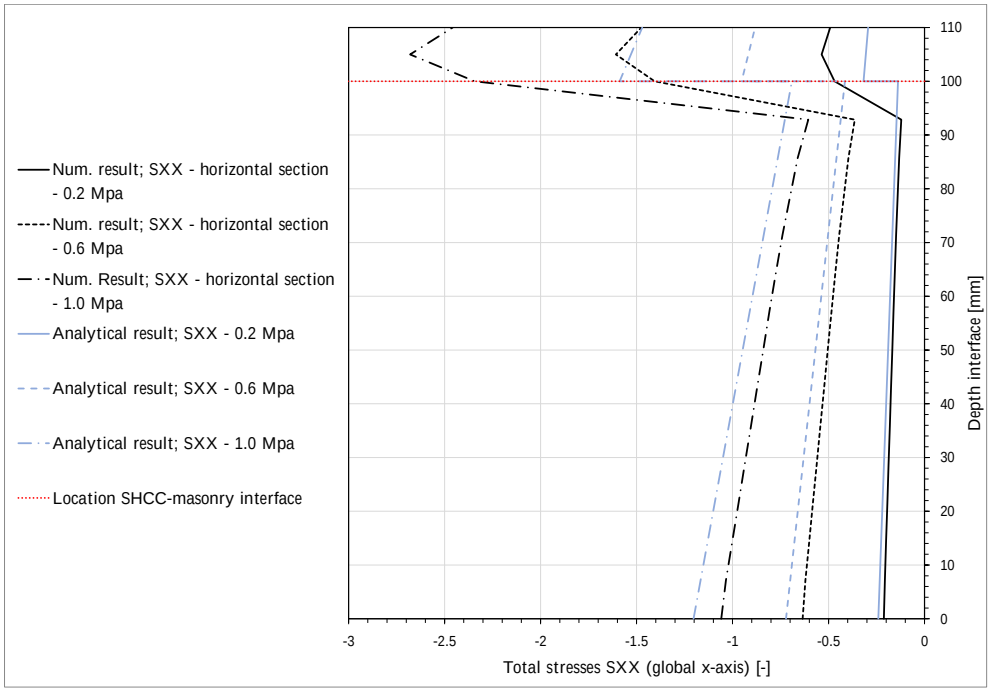

(b) Stress distribution SXX (global x-direction). All three pre-compression levels. Black curves = numerical results, blue curves = analytical calculations.

Figure 5.15: Horizontal strain and stress distributions due to application of pre-compression to total retrofitted specimen. All three pre-compression levels are represented.

The possibility of increasing the normal stiffness of the unit-unit interface is considered. This parameter is increased by a factor of 100, i.e. k_n equals 12580 N/mm^3. All the other parameters remained unchanged, see Table (5.5). Due to this increased stiffness, a different loading procedure is required to obtain convergence. In Table (5.9) the new loading procedure is provided.

Table 5.9: General information non-linear analyses, additional retrofitted masonry triplet simulations.

Analysis	
Nonlinear effects	Physical nonlinear
Load steps, pre-compression level = 0.2 Mpa	Pre-compression: 0.2 Mpa [(1)] Shear displacement: 1 mm [0.001(50) 0.05(65)]
Load steps, pre-compression level = 0.6 Mpa	Pre-compression: 0.6 Mpa [(1)] Shear displacement: 1 mm [0.001(150) 0.05(50)]
Load steps, pre-compression level = 1.0 Mpa	Pre-compression: 1.0 Mpa [(1)] Shear displacement: 1 mm [0.001(200) 0.05(88)]
Iterative solver	Full Newton-Raphson
Convergence norm (tolerance)	Displacement norm (10^{-7}) Force norm (10^{-4})
Max. number of iterations	50

Taking into account these loading procedures, converged solutions for both the pre-compression levels equal to 0.2 and 0.6 Mpa are obtained. For the highest level of pre-compression, no convergence is reached. Only the numerical results of the first two levels of pre-compression are discussed in this report. In Figure (5.16) the resulting force-displacement curves, stress, and strain distributions are provided. Additionally, the results of the initial retrofitted numerical model are shown.

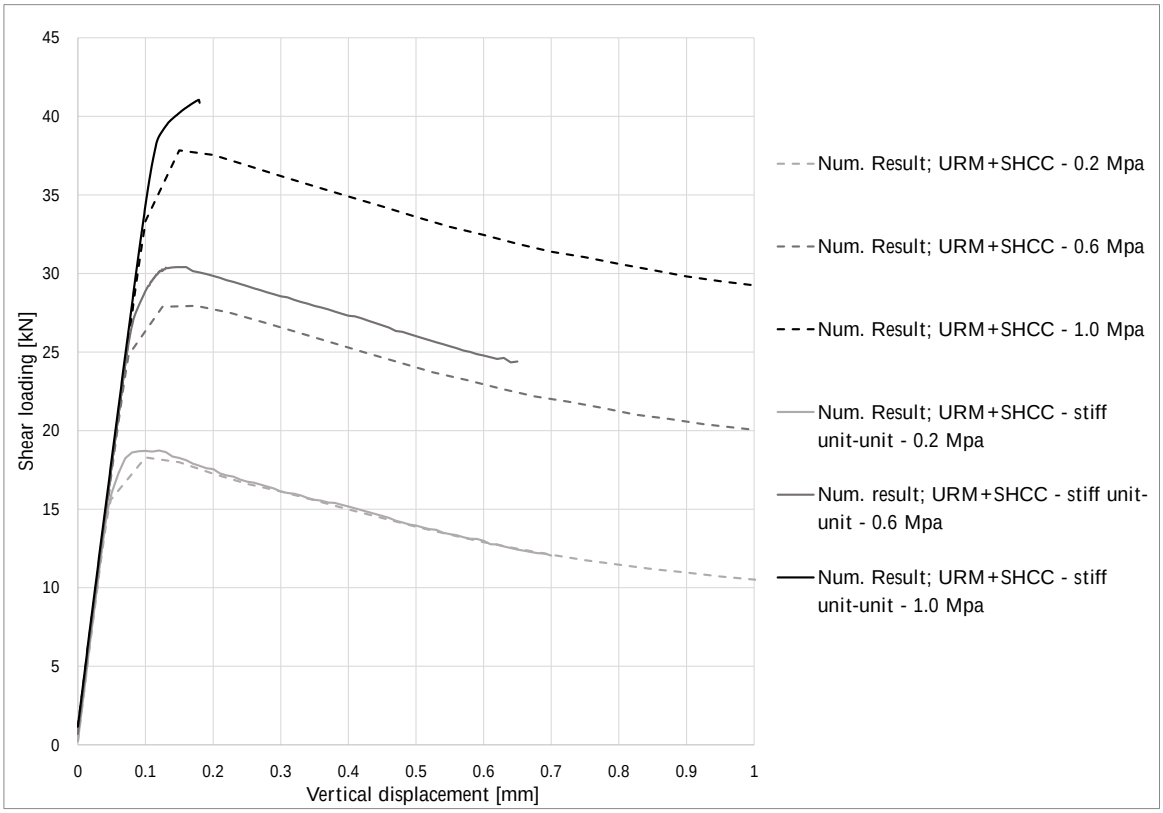

Figure 5.16: Force-displacement curves. Numerical results with increased stiffness unit-unit interface versus previous numerical results.

In Figure (5.16), it is shown that the lowest level of pre-compression is not influenced significantly with

the increased stiffness of the unit-unit interfaces. However, for the higher levels of pre-compression, this influence is clearly shown. The shear resistance of the retrofitted specimen is increased. Additionally, the difference between the peak resistance of the plain URM numerical model and the retrofitted model with increased interface stiffness are similar for all levels of pre-compression, i.e. $\pm 4\,\mathrm{kN}$. It becomes clear that the original retrofitted numerical model ($k_n = 125.8\,\mathrm{N/mm^3}$) is indeed negatively influenced by the shear tractions introduced at the SHCC-masonry interface due to pre-stressing.

6

Additional Experiments

6.1. Introduction

During the shear strength experiments, similar results are observed for the different specimen. Parallel to this part of the experimental campaign, possible influences of these results are determined:

- Low interfacial strength between the SHCC overlay and masonry substrate;
- Application of pre-compression to total specimen (both masonry and SHCC overlay);
- Thickness overlay applied; and
- Material properties overlay material.

Using additional experiments, two of these factors are examined in more detail. Most of these additional experiments are completed by using already tested specimen. However, with the use of glue or screws, these specimens are "fixed up". Only two additional experiments are performed on specimen which are not tested before. Table (6.1) summarizes different specimens and different combinations of glued interfaces, i.e. unit-unit interfaces and/or SHCC-masonry interface. However, no combinations with both screws and glue are considered. The methods used for retesting are discussed first, followed by the corresponding experimental results.

Table 6.1: Additional experiments and goals.

Measure(s) considered	Type of specimen used	Goal
Application of screws to connect the SHCC overlay to the masonry substrate	Specimen which are not tested allready and specimen which were tested before	Investigate importance bond-strength SHCC-masonry interface
Application of glue at different interfaces	Specimens which were tested before	Investigate importance of bond strength unit-mortar and SHCC-masonry interface(s)
Application of pre-compression to the masonry substrate only	Specimen with glued unit-mortar interfaces and/or SHCC-masonry interface	Investigate possible influence pre-compression applied to SHCC overlay

In Table (6.2) the results of the additional experiments are summarized. Before the experimental results are discussed in detail, the methods of building these specimen are described.

Table 6.2: Information specimen additional experiments shear triplets.

Old specimen number	Type	New retrofitting	Overlay Thickness [mm]	Pre-compression [N/mm^2]	Max shear force [kN]
39 [a]	30 mm debonded	80 mm screws, 70 mm edge distance	30	-1.0	43.54
40 [a]	30 mm debonded	80 mm screws, 25 mm edge distance	30	-1.0	61.54
18	30 mm full bond	80 mm screws, 25 mm edge distance	30	-1.0	35.21
8	10 mm full bond	60 mm screws, 25 mm edge distance	10	-1.0	41.84
12	10 mm full bond	60 mm screws, 25 mm edge distance	10	-1.0	32.65
6	10 mm full bond	All interfaces glued	10	-0.6	54.29
10	10 mm full bond	All interfaces glued	10	-0.6	31.75
3	10 mm full bond	All interfaces glued	10	-1.0	38.04
17	30 mm full bond	All interfaces glued	30	-0.6	41.69
4	10 mm full bond, non-sealed curing	SHCC-masonry glued	10	-1.0	33.37
42	10 mm full bond, non-sealed curing	SHCC-masonry glued, no pre-compression SHCC	10	-1.0	33.99
13	30 mm full bond	All interfaces glued	30	-1.0	55.82
14	30 mm full bond	All interfaces glued, no pre-compression SHCC	30	-1.0	55.15

[a] These specimen are not tested before.

6.2. Interfacial Bond Strength SHCC-Masonry Interface

6.2.1. Application of Screws

Screws are drilled into the retrofitted specimen to investigate the importance of the SHCC-masonry interface. In total five different specimens are tested. Three specimens with a 30 mm thick SHCC overlay are investigated, two of which are non-tested specimen with a partially debonded SHCC-masonry interface. The third specimen with a 30 mm overlay is made from an already tested specimen. Besides the 30 mm thick SHCC overlay specimen, also two specimens with a 10 mm thick overlay are investigated. Both are pre-tested specimens.

The installation procedure of the screws is as follows:

1. Apply F-shaped clamps;
2. Drill a total of six holes, two each per masonry unit. Clean up these holes by removing the dust with a vacuum cleaner and/or pressurized air;
3. Fill the drilled holes with two-component glue and put it the selected screws;
4. Clean off excess glue around the screws;
5. Re-apply the DIC pattern.

For the specimen with the 30 mm thick SHCC overlay 80 mm long screws are used. The specimen with a 10 mm thick overlay used 60 mm long screws. These dimensions of the screws ensured all screws to be installed up to half the thickness of the masonry units. In Figure (6.1) two different stages of the installation process are shown.

(a) Drilled holes for installation of screws, 70 mm edge distance.

(b) Installed screws, 30 mm SHCC overlay, 25 mm edge distance.

Figure 6.1: Installation process screws. Shown is an 30 mm thick SHCC overlay.

Initially, the intermediate and edge distances of the screws are taken equidistant (70 mm), see Figure (6.1a). However, during testing of this first specimen, large rotations of the central masonry unit are observed. Due to this observation, the screws are moved outward, towards the edge of the specimen, leaving a 25 mm eccentricity, as shown in Figure (6.1b). This larger internal lever-arm in between the two lines of screws ensures a

higher moment capacity of this retrofitting approach.

In Figure (6.2) the experimental results of all specimen with applied screws are plotted. All these specimens are tested with the highest level of pre-compression. For the specimen with a 10 mm thick overlay, no influence in peak shear force is obtained. However, this is as expected since no bond is present at any of the interfaces. The resistance of the masonry is governed by its residual shear strength (dry friction coefficient). No peak in shear force is obtained for these additional specimen. The maximum shear force equals the residual shear strength of the initial retrofitted specimen. It is concluded that the applied screws govern the post-peak ductility of the specimen. No debonding of the overlay is observed for any of these specimens.

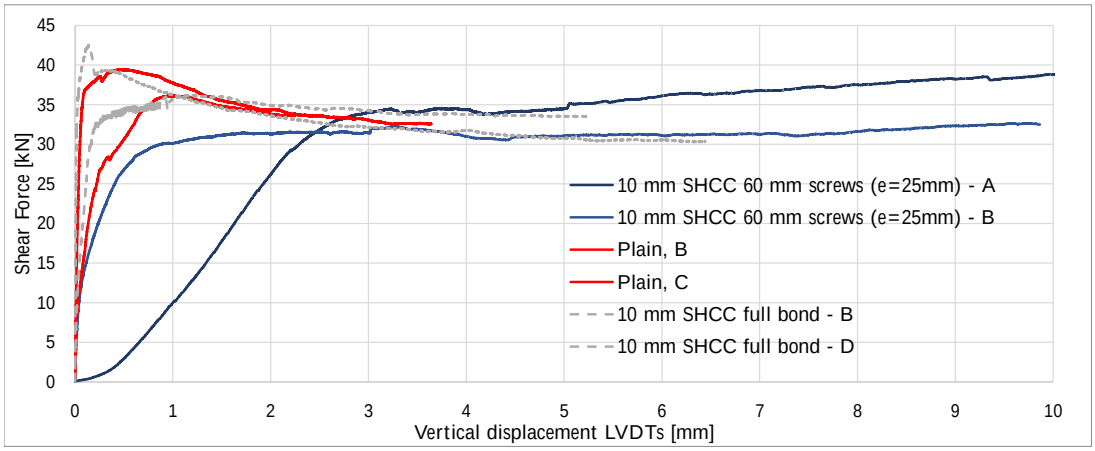

(a) Force-displacement curves additional experiments; 10 mm SHCC overlay plus screws. Pre-compression level = 1.0 N/mm^2.

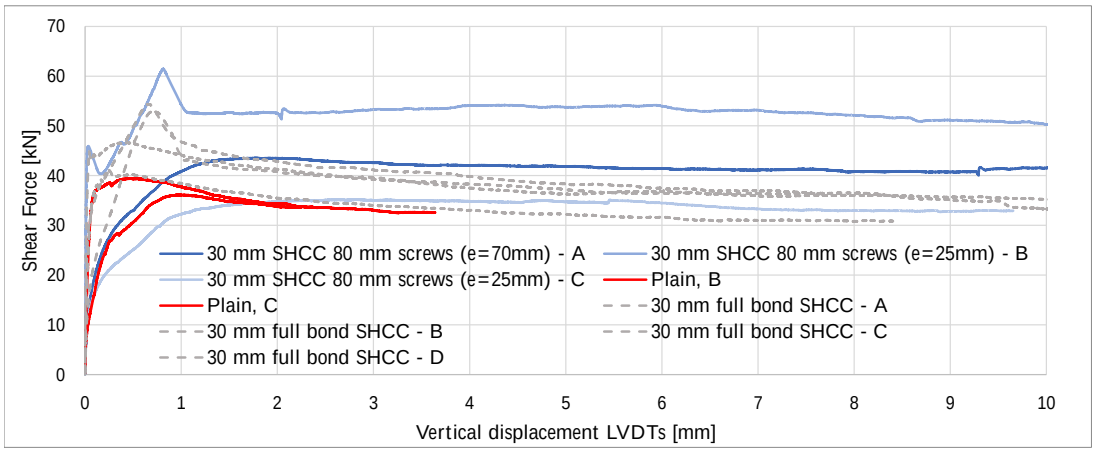

(b) Force-displacement curves additional experiments; 30 mm SHCC overlay plus screws. Pre-compression level = 1.0 N/mm^2.

Figure 6.2: Force-displacement curves additional experiments; 10 and 30 mm SHCC with screws.

For the specimen with the 30 mm thick overlay, similar results are found. The specimen with the screws placed with a larger edge distance (70 mm) shows minimal improvements of the regular specimen. One of the additional specimen resulted in increased resistance, see specimen B in Figure (6.2b). This specimen is one of the two specimens which is not tested before. Thus, the initial bond strength at all interfaces is still present, which shows by the peak in the f-u curve. Also for this specimen, the post-peak behaviour is governed by the ductility of the screws.

In Figure (6.3) and (6.4) different views of the tested specimen are shown. The earlier mentioned observed rotations of the central masonry unit are shown in Figure (6.4a). It can also be seen that, due to these large rotations, no cracking in the SHCC overlay occurred. The specimen using smaller edge distances do show ac-

tivation of the overlay material, see the diagonal cracks around the central bottom screw. The specimen which showed the higher amount of resistance (10 mm specimen A and 30 mm specimen B) also show a different crack pattern in the SHCC overlay, see both Figure (6.3b) and (6.4d). The cracking in the SHCC overlay starts for all specimen at the bottom middle screw, however, for these two specific specimens this crack propagated in a more horizontal direction, resulting in a greater area of the overlay to be activated. The other specimen shows a diagonal crack pattern around the bottom central screw. The cracks propagate in an almost perfect 45° angle downwards.

(a) Failure pattern 10 mm SHCC specimen with screws; specimen A.

(b) Failure pattern 10 mm SHCC specimen with screws; specimen B.

Figure 6.3: Failure patterns 10 mm thick SHCC overlay specimen with screws installed.

(a) Top view rotation of central unit; specimen A.

(b) Failure pattern 30 mm SHCC specimen with screws; specimen A.

(c) Failure pattern 30 mm SHCC specimen with screws; specimen B.

(d) Failure pattern 30 mm SHCC specimen with screws; specimen C.

Figure 6.4: Failure patterns 30 mm thick SHCC overlay specimen with screws installed.

6.2.2. Application of Glue

By the application of glue, the importance of high bond strength is investigated. Before retesting the specimen, a combination of interfaces is glued. Two different interfaces are distinguished, i.e. the unit-mortar interface and the SHCC-masonry interface, see Figure (6.5).

The unit-mortar interface represents the shear-sliding surface along which the masonry units slide during the shear strength experiment. The masonry triplet fails at two of the four unit-mortar interfaces, recall Figure (4.21a), leaving the other two interfaces (visually) unharmed. Therefore, glueing the two failed interfaces introduces the possibility of retesting the same specimen and allowing it to fail at the other two (still intact) interfaces. If none of these interfaces are glued, the specimen provides resistance equal to its dry friction strength ($f_{v0,res}$).

Besides the unit-mortar interfaces also the SHCC-masonry interface is restored by the application of glue. Through this glued interface the importance of interfacial capacity, related to the SHCC-masonry interface, is investigated even further. It is assumed that a glued interface has higher interfacial strength compared to the 'regular' retrofitted specimen.

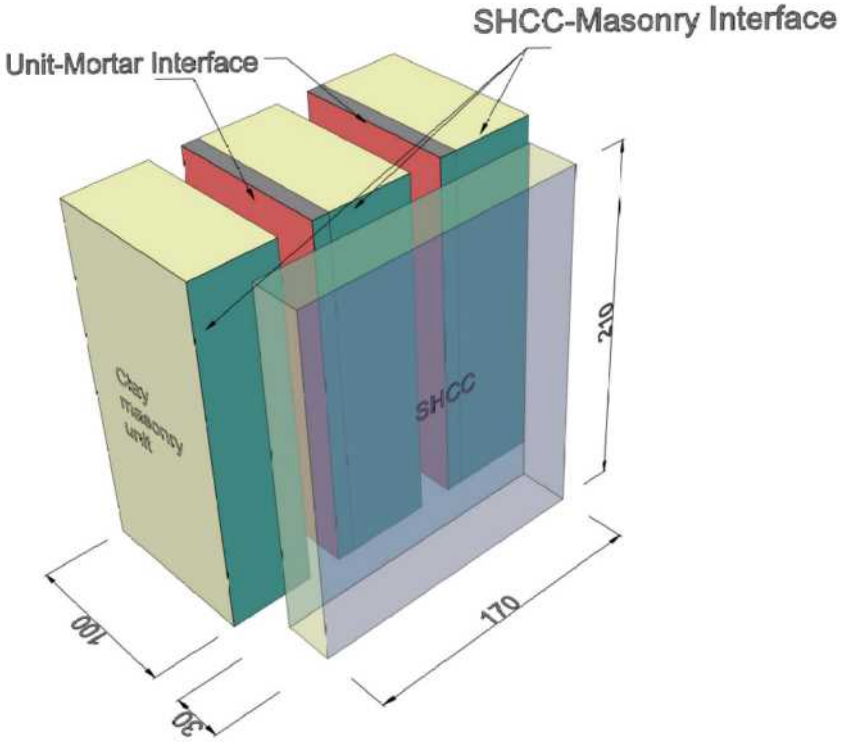

Figure 6.5: Considered interfaces for the application of glue.

It is benificial for the reader to note that cleaning of the, to-be glued, surfaces was of high interest in this additional experimental campaign. With the help of soft and hard brushes, aceton, and clean cloths it is strived for to obtain an as clean as possible surface before application of the glue is considered. This is done for all the surfaces, both unit-mortar and SHCC-masonry interfaces.

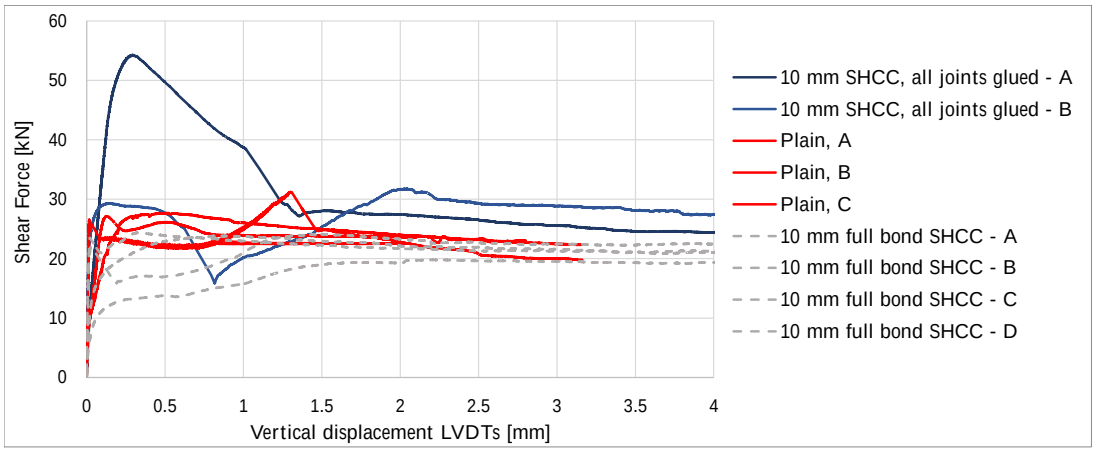

(a) Force-displacement curves additional experiments; 10 mm SHCC overlay with glued interface(s), pre-compression = 0.6 N/mm^2.

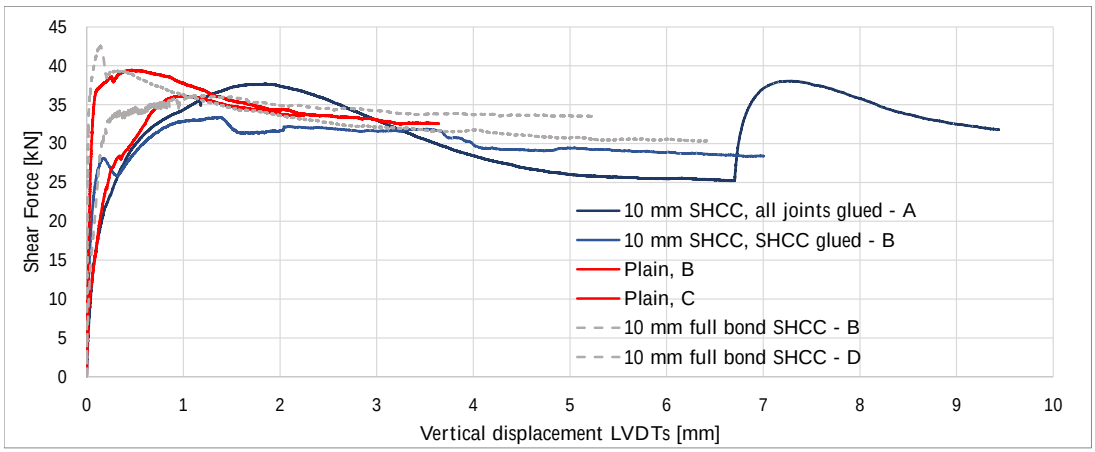

(b) Force-displacement curves additional experiments; 10 mm SHCC overlay with glued interface(s), pre-compression = 1.0 N/mm^2.

Figure 6.6: Force-displacement curves additional experiments; 10 mm specimen with glued interface(s). Two different levels of pre-compression.

From the experimental results it is concluded that, overall, no higher shear resistances are obtained by the application of glue. However, for the pre-compression level equal to 0.6 N/mm^2 remarkable results are obtained, see specimen A for both overlay thicknesses, see Figure (6.6a) and (6.9a). Especially the shear strength of the specimen with an 10 mm thick overlay is of interest. For this specimen both the unit-mortar and the SHCC-masonry interfaces are glued.

With the help of DIC it is concluded that this particular specimen did show cracking of the glued overlay. In Figure (6.7) the von Mises strain field is depicted. It is concluded that because of the high interfacial bond strength the overlay material is activated and higher shear strengths are obtained.

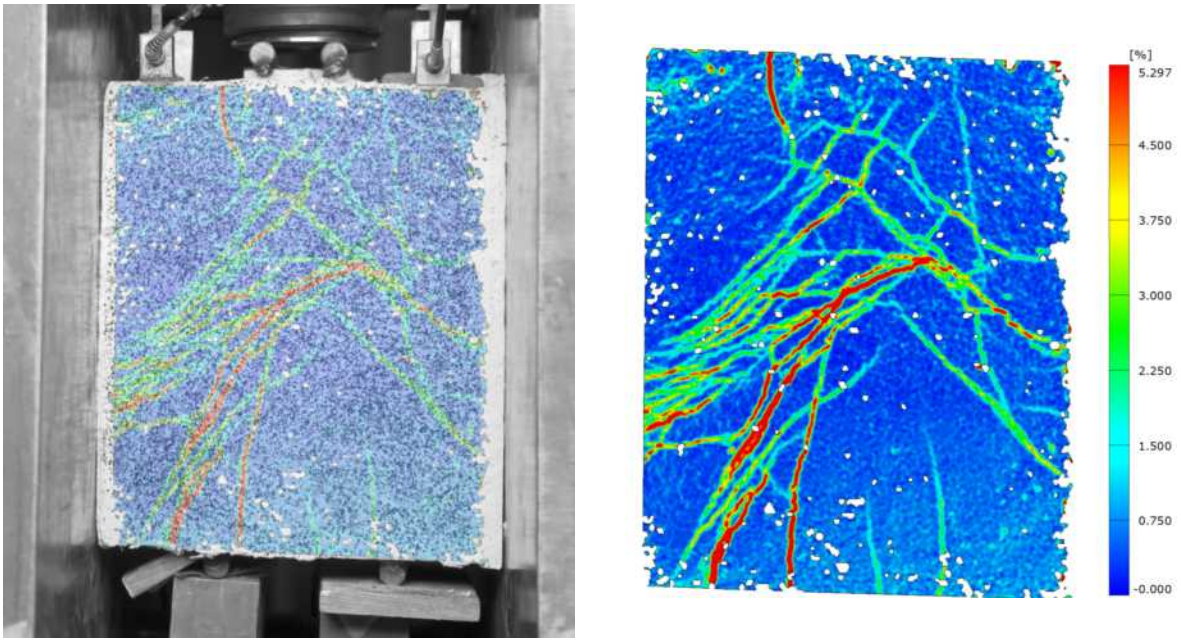

Figure 6.7: Von Mises strain field calculated with DIC. Cracking of glued, 10 mm thick, overlay shown. Pre-compression = 0.6 Mpa.

In Figure (6.8a) it is shown that, as intented, the non-glued unit-mortar interfaces failed. It is therefore assumed that these two interfaces show shear resistance equal to plain masonry triplets. Thus, the additional capacity is obtained via the SHCC-masonry interface. In the same figure it is also shown that a significant amount of brick material is stuck to the glued overlay, indicating high interface strength. This is not observed for the initial (non-glued) tested specimen.

(a) Failed interfaces specimen A, 10 mm SHCC overlay.

(b) Failed interfaces specimen A, 30 mm SHCC overlay.

Figure 6.8: Overview failed specimen all interfaces glued. Both overlay thicknesses. Pre-compression = 0.6 Mpa.

Similar results are obtained for the specimen with the 30 mm thick overlay. Only one of these specimen shows an increase in shear resistance, see Figure (6.9a).

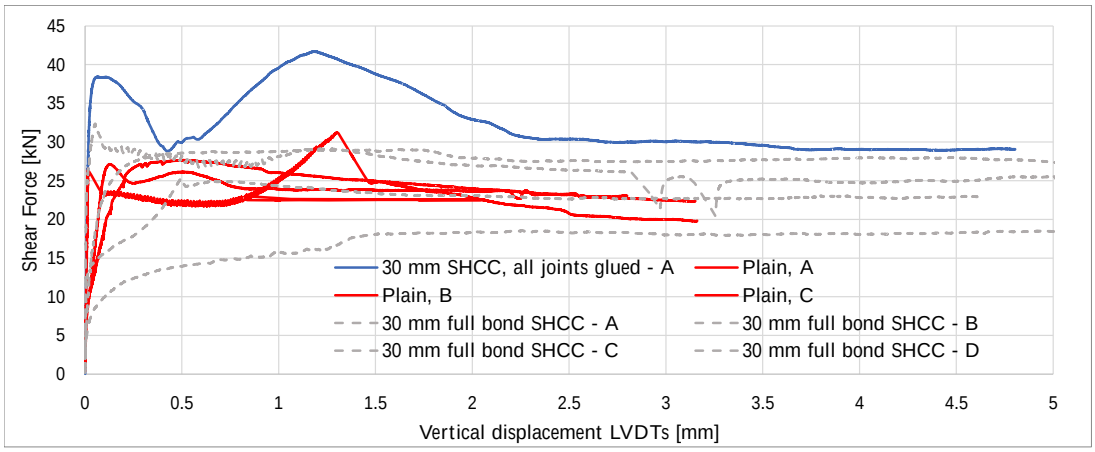

(a) Force-displacement curves additional experiments; 30 mm SHCC overlay with glued interface(s), pre-compression = 0.6 Mpa.

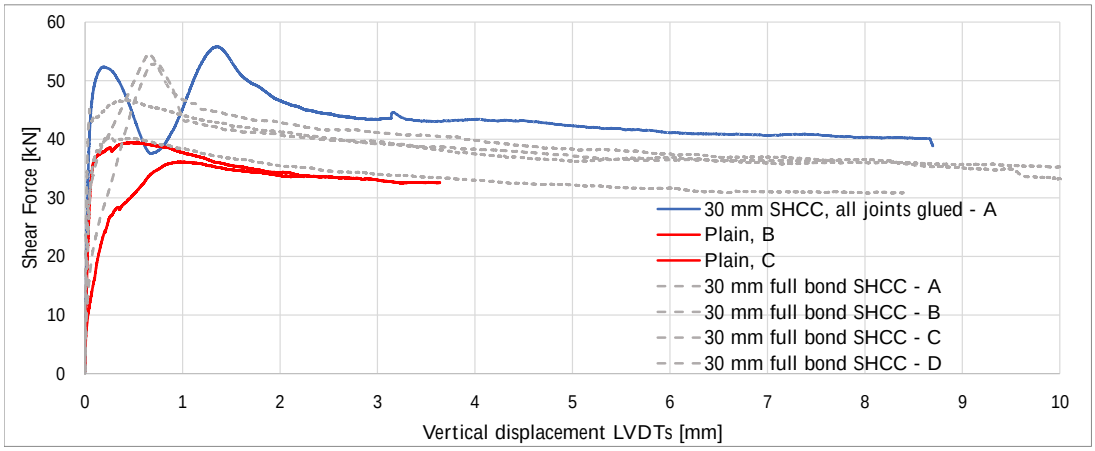

(b) Force-displacement curves additional experiments; 30 mm SHCC overlay with glued interface(s), pre-compression = 1.0 Mpa.

Figure 6.9: Force-displacement curves additional experiments; 30 mm specimen with glued interface(s)

As mentioned, for some of the specimen only the SHCC-masonry interface is glued. None of these specimen show an increase in shear resistance, see Figure (6.6b). However, these specimen do show a different failure pattern. It is shown in Figure (6.10) that considerable amounts of brick material are stuck to the SHCC overlay. Failure of the masonry units is observed as well.

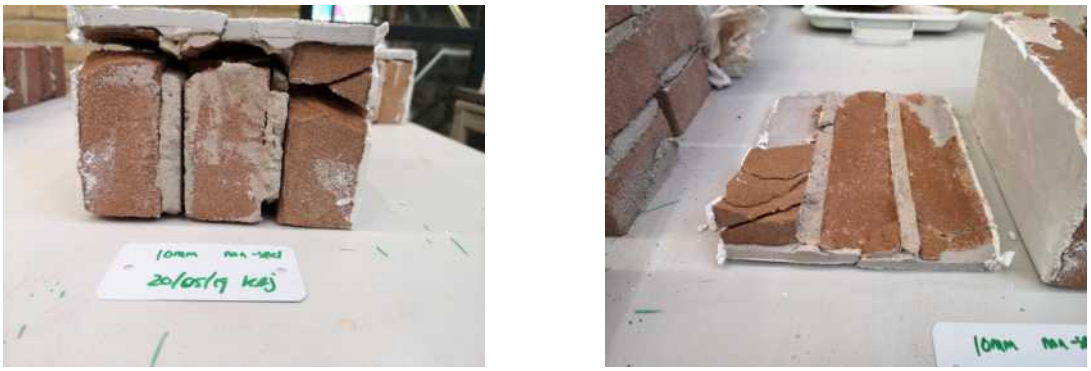

Figure 6.10: Overview failed specimen only SHCC-masonry interface glued. Overlay thickness = 10 mm, specimen B. Pre-compression = 1.0 Mpa.

Only specimen for which both the unit-mortar and SHCC-masonry interface is restored show increased shear resistance. Glueing only the latter results in failure of the masonry units itself. From additional experiments, it is concluded that both interfaces require some strength to activate higher shear resistance. The high strength of the SHCC-masonry interface is governing. The requirements for these interfaces are investigated in more detail via numerical simulations, see Chapter 7.

6.3. Application of Pre-Compression

Throughout this experimental campaign, the pre-compression is applied to the total specimen, i.e. both the SHCC overlay and the masonry is prestressed. As mentioned earlier, this is different from literature. In the previous experiments, a layer of gypsum is applied to the full side area of the specimen. By removing this gypsum layer from the side of the SHCC overlay, the prestressing is only applied to the masonry part of the retrofitted specimen. However, due to the inhomogeneous nature of the specimen, still, compressive stresses in the SHCC overlay are present. Investigation of this boundary condition is thought to be informative. Two specimens are considered, one with a 10 mm thick SHCC overlay and one with a 30 mm thick overlay, to investigate the possible influence of this loading condition. Both of these specimens are tested before. Only the SHCC-masonry interface is glued for the specimen with the 10 mm thick SHCC overlay in order to retest these specimen. For the specimen with the 30 mm thick overlay, all the interfaces are glued, i.e. unit-mortar and SHCC-masonry interfaces.

(a) Gypsum layer only applied to masonry material.

(b) Specimen inside the experimental setup clearly shows no contact between the steel plate and the overlay material.

Figure 6.11: Additional experiments only pre-compression applied to the masonry material.

In Figure (6.12) the obtained force-displacement curves are shown. Again, the influence of glueing the unit-mortar interfaces is shown. For the specimen with the thinner overlay, only the SHCC-masonry interface is glued. Because of this, no distinct peak in shear strength is observed. The peak observed for the specimen with a 30 mm thick overlay coincides with the initial experimental results of specimens with a full bonded 30 mm thick SHCC overlay.

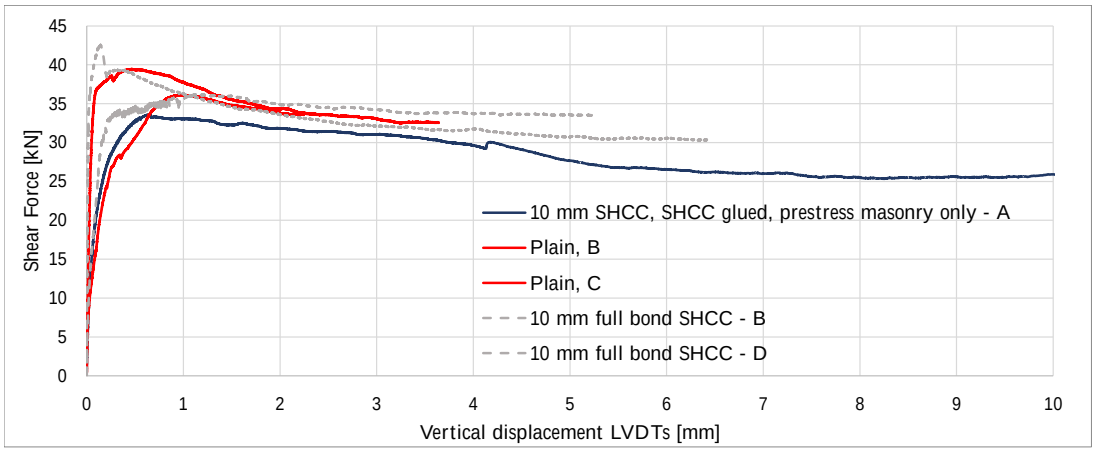

(a) Force-displacement curves additional experiments; 10 mm SHCC overlay with glued interface SHCC-masonry interface, pre-compression only at masonry surface, pre-compression = 1.0 Mpa.

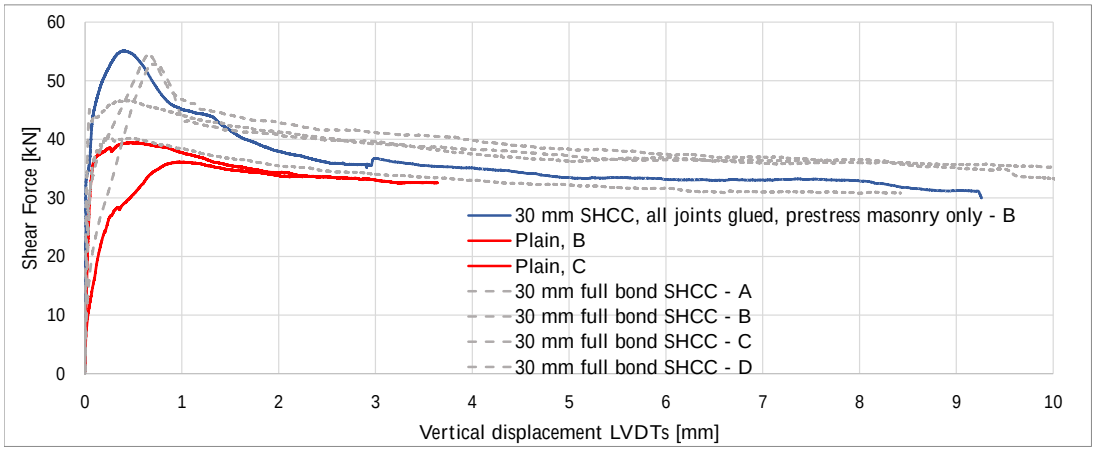

(b) Force-displacement curves additional experiments; 30 mm SHCC overlay with all interfaces glued, pre-compression only at masonry surface, pre-compression = 1.0 Mpa.

Figure 6.12: Force-displacement curves additional experiments; influence application of pre-compression.

The application of pre-compression to only the masonry triplet does not seem to influence any of the results in the force-displacement domain. However, the failure pattern of the specimen with the glued 10 mm thick overlay differs from previous results, see Figure (6.14). This figure shows the results of the DIC analyses, in which the cracking of the SHCC overlay is observed. However, two things are noted. Firstly, no additional capacity of the specimen is noticed in the force-displacement curve, initiating the thought that the cracking of the overlay for this specimen did not provide any additional resistance. Secondly, the specimen shown is tested before, see specimen number 42. This specimen is one of the four specimens cured in non-sealed conditions, i.e. possible drying cracks are present. This particular specimen already showed cracking of the SHCC overlay during its initial testing, see Figure (6.13).

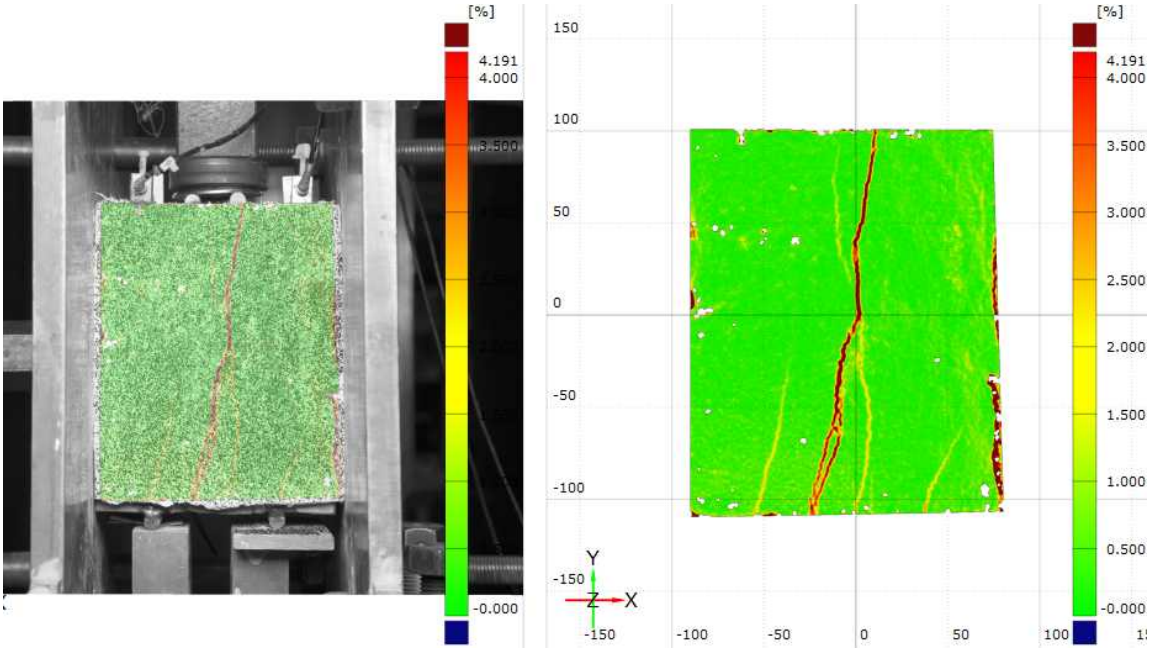

Figure 6.13: Vertical cracking present in SHCC overlay after initial testing phase. Retrofitted specimen with 10 mm full bonded overlay (non-sealed curing conditions).

These cracks might have initiated the final failure of the glued SHCC overlay. Figure (6.14d) shows that the failure of the glued specimen is initiated by vertical propagating cracks in the SHCC overlay. As shown, this crack orientation was already present from the initial testing phase. The horizontal crack propagated from one of these vertical cracks. Also, the horizontal crack is initiated because the bottom part of the SHCC overlay was stuck to the central masonry brick, moving down. The top part of this overlay was bonded to the outside units, remaining in place, see Figure (6.14f).

Different loading conditions did not result in the expected results. Due to the inhomogeneous cross-section pre-compressive stresses are introduced in the overlay material. Possible influences of the applied pre-compression are investigated in more detail via numerical analysis, see Chapter 7.

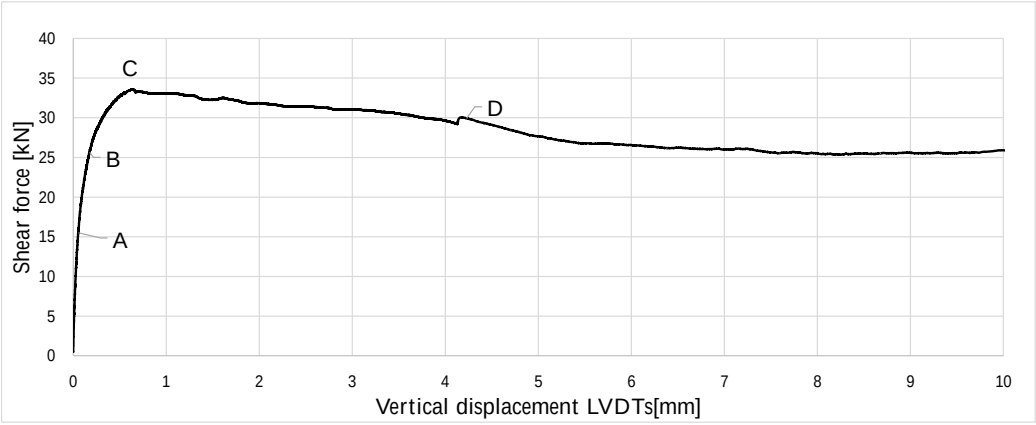

(a) Force-displacement curve with points of interest.

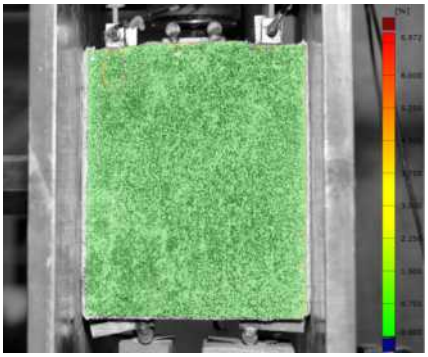

(b) First point of interest, pre-peak (A).

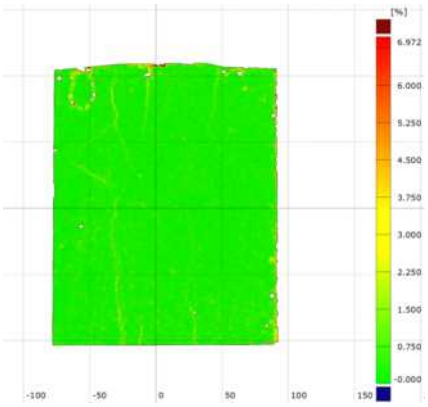

(c) Second point of interest, pre-peak (B).

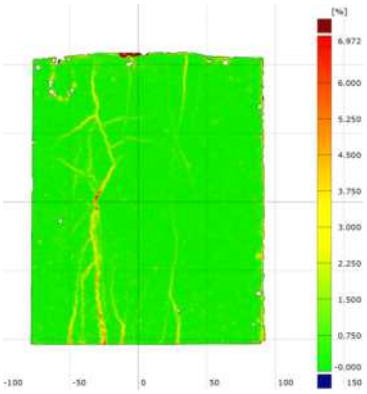

(d) Third point of interest, peak-resistance (C). Vertical crack coinciding with the crack found during initial phase of testing.

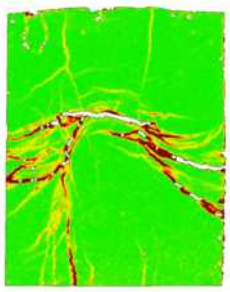

(e) Fourth point of interest, post-peak (D).

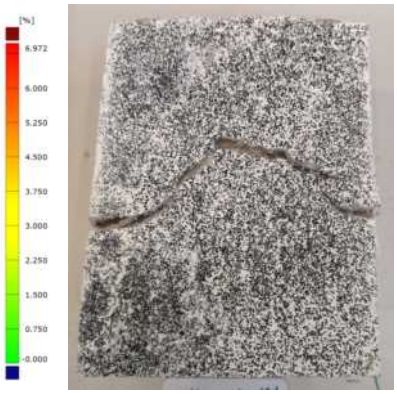

(f) Failed overlay.

Figure 6.14: Mises equivalent strains pre- and post-peak. Pre-compression equal to 1.0 N/mm^2. Pre-compression only applied to masonry surface.

7

Additional Numerical Analyses

7.1. Introduction

From the earlier studies it is known that multiple factors might have influenced the results of the experimental campaign. With the help of additional experiments two of the possible influence factors are investigated. Via additional numerical analyses the following parameters are investigated:

- Influence of the applied pre-compression to the full retrofitted specimen, see paragraph 7.3;
  - For realistic applications the used experimental setup is not representative. In this experimental campaign the pre-compression is applied to the full specimen, i.e. both the masonry substrate and the overlay material. However, in actual structures this pre-compressive force is only present in the existing (loadbearing) masonry wall, onto which the overlay material is applied. No pre-compressive stresses are present in the retrofitting overlay; and
  - The used experimental setup introduced a loading eccentricity for the applied pre-compressive force. The possible influence of this factor is investigated.
- Influence of interfacial bond strength SHCC-masonry interface, see paragraph 7.4;
- Influence of material properties SHCC overlay material, see paragraph 7.5;
- Influence of overlay thickness, see paragraph 7.6; and
- Influence of the vertical eccentricity with the hydraulic jacket, loading the specimen in shear, see paragraph 7.7.

In the previous analyses the combined shearing-cracking-crushing interface model is used for both the unit-unit and SHCC-masonry interfaces. For this part of the research the interface between the SHCC overlay and the masonry triplet is modelled by means of a Coulomb friction model. This latter model is considered because of the fewer parameters it requires, making it easier to examine the different parameters. Additionally, a brittle gapping model is included.

In Figure (7.1) the force-displacement curves of both type of models are depicted. The solid curves correspond to the numerical results of the model using the Coulomb friction model for the SHCC-masonry interface. The dotted curves represent the numerical results corresponding to the models examined earlier in Chapter 5. For both models the unit-unit interface has an increased normal stiffness. These material properties are summarized in Table (5.5). For both models the bond strength of the SHCC-masonry interface is taken equal to the cohesion of the masonry material, i.e. $0.1892\,\mathrm{N/mm^2}$.

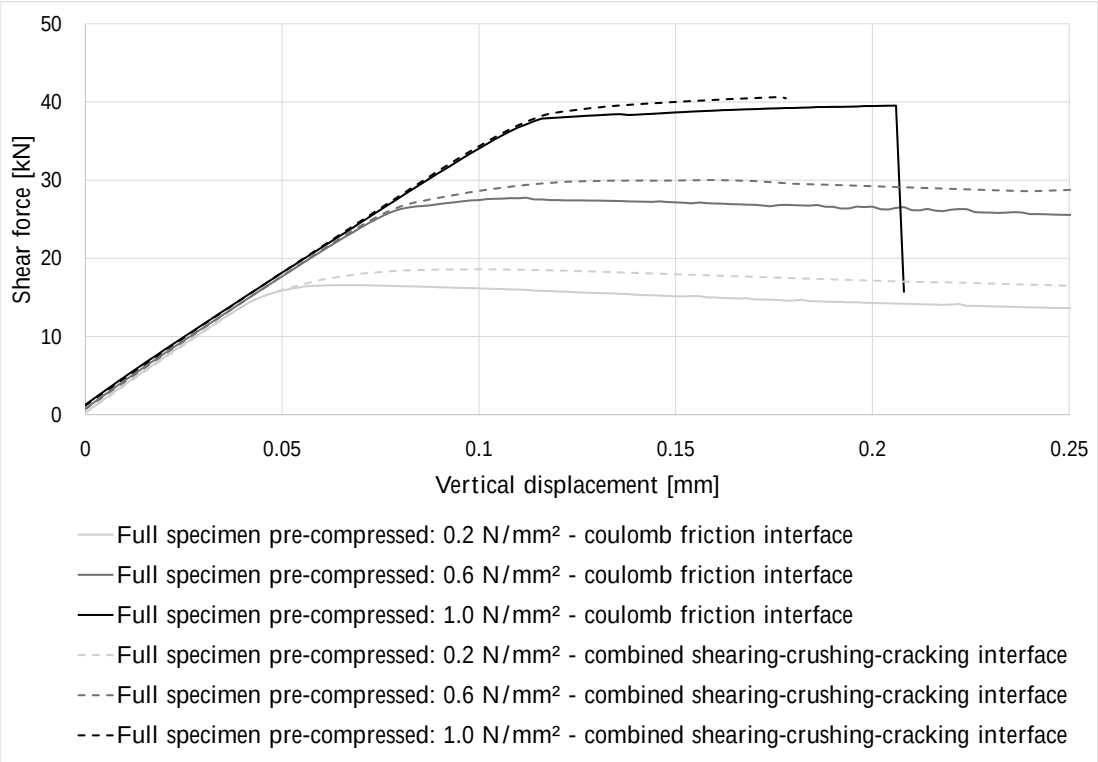

Figure 7.1: Force-displacement relationship numerical models. Solid curves = numerical model with Coulomb friction model for SHCC-masonry interface. Dotted curves = numerical results model with combined shearing-cracking-crushing model for all interfaces.

It is shown that both models result in similar force-displacement relationships. However, if the coulomb friction model is considered, even for the highest level of pre-compression a fully converged solution is obtained. This is not possible for the earlier discussed model. The numerical simulation with the combined interface model shows fractional higher shear strength capacities. This difference occurs because the combined shearing-cracking-crushing interface model contains softening for all three modes (shearing-cracking-crushing). No softening is considered in the Coulomb friction model.

7.2. Reproduction experimental results literature

Initially, reproduction of the experimental results as shown in literature is strived for. In [9, 38] retrofitting of the masonry material with an SHCC overlay is considered. Both show improved shear capacity over the plain masonry material. In this paragraph the experimental results corresponding to [38] are reproduced with the help of numerical simulations.

In Figure (7.2) the experimental results of multiple retrofitted masonry triplets are depicted. The coloured curves are representing the retrofitted specimen. These specimen are retrofitted with a double-sided 30 mm thick SHCC overlay. The vertical displacement is representative of the vertical displacement of the hydraulic jacket. No data, related to the relative vertical displacement of the central masonry unit, is present.

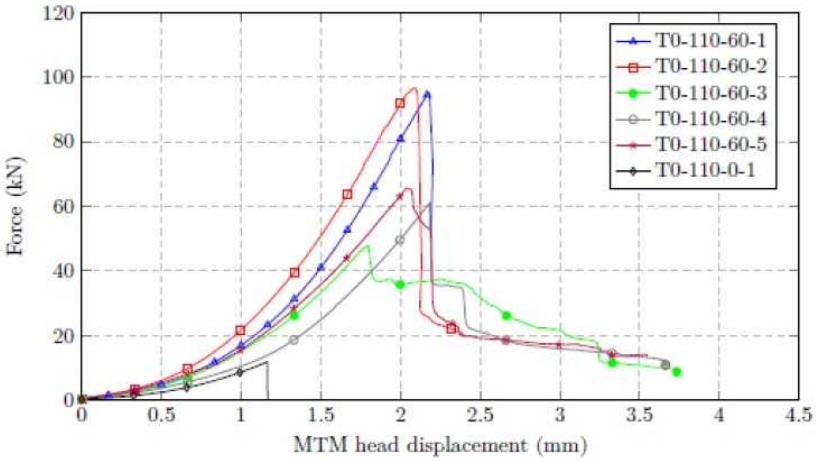

Figure 7.2: Experimental results shear strength masonry triplets retrofitted with a 30 mm thick sprayed SHCC overlay, applied on both sides. Curves T0-110-60-1 up to T0-110-60-5 represent the restrofitted specimen. T0-110-0-1 corresponds to a non-retrofitted masonry triplet. Experimental results obtained via Prof. G. P.A.G. van Zijl.

No pre-compression is applied to the retrofitted specimen. The specimen are only loaded vertically via the vertical hydaulic jacket. The shear loading is directly applied to the top surface of the central masonry unit, no direct loading of the SHCC overlays is present. Also, only the masonry units are supported vertically. The loading and supporting plates are only in contact with the masonry units. Similar boundary conditions are considered in the numerical model. In Figure (7.3) the mesh of the new numerical model is presented. Only three dimensional models are considered. For all analyses quadratic elements are used. The usage of the brittle Coulomb friction model is based on the brittle behaviour shown in the experimental results. Again, a simplified micro-model approach is considered for these analyses.

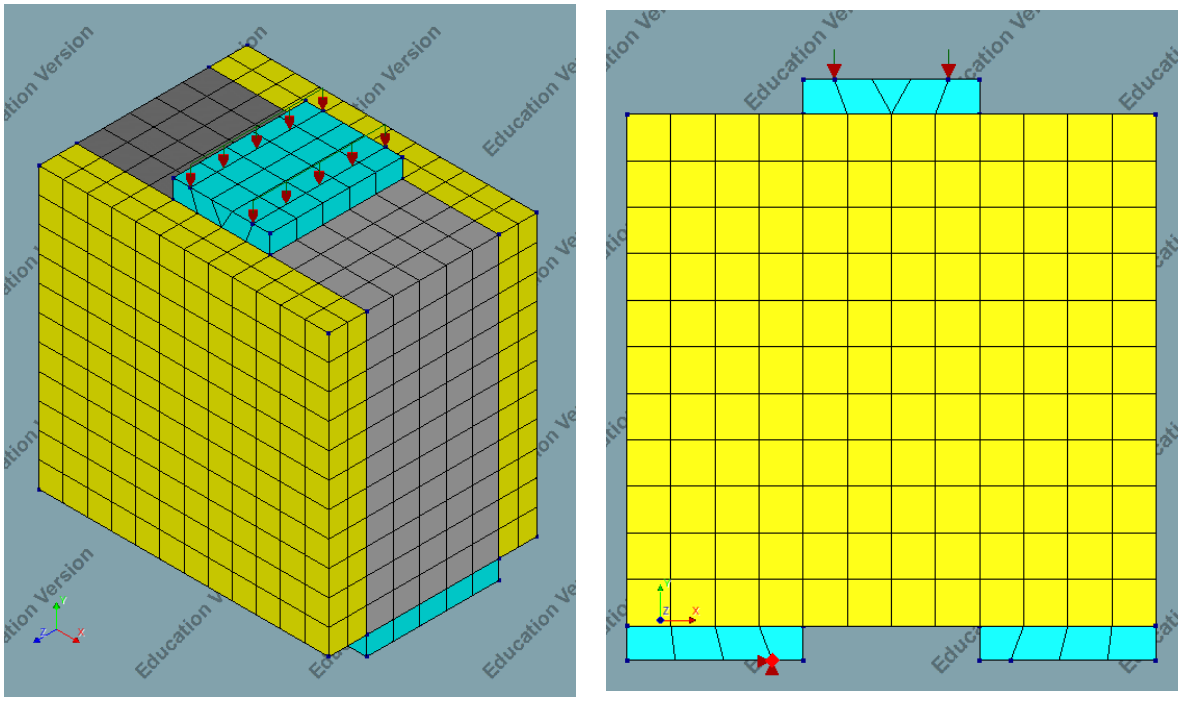

(a) Isometric view mesh numerical model.

(b) Front view mesh numerical model.

Figure 7.3: Overview mesh numerical model considered to investigate the experimental results as presented in literature. Blue = steel loading and supporting plates, grey = masonry units, and yellow = SHCC overlay.

For these additional simulations all of the known data (e.g. geometry) from the reference is considered. The following parameters are derived from [7, 38]:

- The geometry of the masonry units is determined to be equal to: 222x105x70 mm. The mortar joint thickness is equal to 10 mm;
- The cohesion corresponding to the used masonry is equal to 0.277 N/mm^2; and
- The interfacial bond strength between the SHCC and the masonry triplet is derived to be equal to 2.30 N/mm^2. This value is considered as initial value.

The material properties of both the unit-unit and SHCC-masonry interface are summarized in Table (7.1) and (7.2), respectively. The material properties of both the masonry units and steel plates are similar to earlier analyses. These latter two elements are again modelled linear elastically. The overlay material is modelled via a total strain based crack model. The tensile properties of the SHCC material are implemented via the fib fiber reinforced concrete tensile curve. The uniaxial tensile strength of the SHCC mixture is derived from [7]. The numerical values of this total strain based cracking model are summarized in Table (7.3). Not all of the input parameters shown are based on literature (e.g. stress confinement model). The influence of these parameters is not investigated. For the unit-unit interface, only the cohesion of the mentioned reference is considered. All other parameters are corresponding to the experimental results of this research.

Table 7.1: General information simplified unit-unit interface model.

Material	Symbol	Unit-Unit interface	Unit
Class		Interface elements	
Material model		Combined cracking-shearing-crushing	
Linear material properties			
Type		3D surface interface	
Normal stiffness modulus	k_n	125.8	N/mm^3
Shear stiffness modulus - x	k_{sx}	52.1	N/mm^3
Shear stiffness modulus - y	k_{sy}	52.1	N/mm^3
Cracking			
Tensile strength	f_{t0}	0.067	N/mm^2
Fracture energy	G_f^I	0.01	N/mm
Shearing			
Cohesion[a]	c_0	0.277	N/mm^2
Friction angle[b]	ϕ	0.647	rad
Dilatancy angle	Ψ	0.647	rad
Residual friction angle	ϕ_r	0.60574	rad
Confining normal stress	σ_u	-0.56	N/mm^2
Exponential degradation coefficient[c]	δ	9.63	-
Mode-II fracture energy	G_f^{II}		
Parameter a		-0.0632	mm
Parameter b		0.0941	N/mm
Crushing			
Compressive strength	f_c	13.11	N/mm^2
Factor Cs		9	-
Compressive inelastic law			
Compressive fracture energy	G_{f_c}	35.06	N/mm
Equivalent plastic relative displacement		0.0058	mm

[a] As proposed in [7].
[b] Taken equal to the experimental results of this research.

Table 7.2: General information Coulomb friction model SHCC-masonry interface.

Material	Symbol	SHCC-masonry interface	Unit
Class		Interface elements	
Material model		Coulomb friction	
Linear material properties			
Type		3D surface interface	
Normal stiffness modulus	k_n	200	N/mm^3
Shear stiffness modulus - x	k_{sx}	200	N/mm^3
Shear stiffness modulus - y	k_{sy}	200	N/mm^3
Coulomb friction			
Cohesion	c_0	2.3	N/mm^2
Friction angle[a]	ϕ	0.647	rad
Dilatancy angle	Ψ	0.647	rad
Interface opening model		Gapping model	
Tensile strength	f_t	0.68	N/mm^2
Mode-II shear			
Model for gap appearance		Brittle	

[a] Taken equal to the unit-unit interfaces.

Table 7.3: General information SHCC material model.

Material	Symbol	SHCC material model	Unit
Class		Concrete and masonry	
Material model		Total strain based crack model	
Linear material properties			
Young's modulus	E_{SHCC}	15270	N/mm^2
Poisson's ratio	ν	0.2	-
Total strain based crack model			
Crack orientation		Rotating	
Tensile behaviour			
Tensile curve		fib fiber reinforced concrete	
CMOD or strain curve		Total strain	-
Uniaxial tensile strength	fL	2.19	N/mm^2
Uniaxial residual strength	fRi	2.1925	N/mm^2
Uniaxial total strain at fRi		0.00569	-
Uniaxial residual strength	fRj	2.195	N/mm^2
Uniaxial total strain at fRj		0.01125	-
Uniaxial residual strength	fRk	2.2	N/mm^2
Uniaxial total strain at fRk		0.02236	-
Uniaxial ultimate total strain	ε_u	0.02236	-
Stress factor Fiber Reinforced Concrete model		1.0	-
Reduction model		Damaged based	
Compressive behaviour			
Compressive curve		Ideal	
Compressive strength[a]	f_c	38.5	N/mm^2
Reduction due to lateral cracking		No reduction	
Stress confinement model		Selby and Vecchio	

[a] Taken equal to the compressive strength of the mixture used in this research.

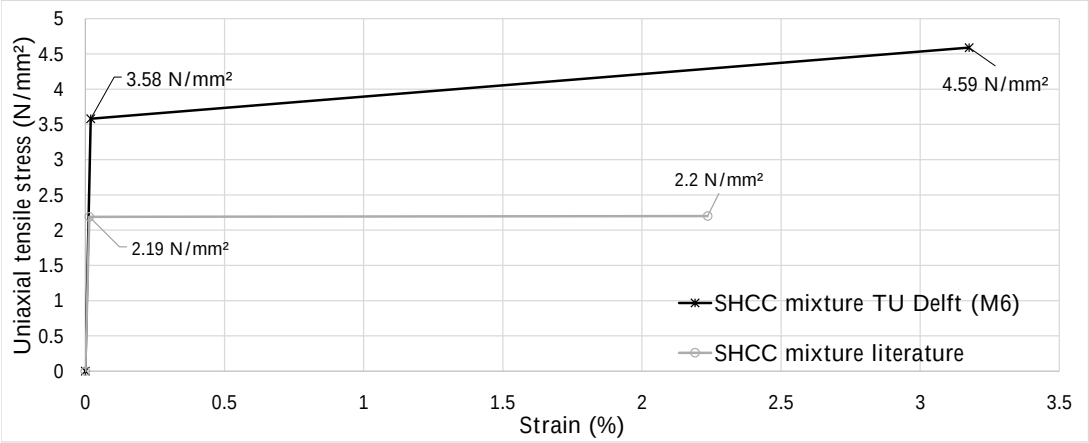

Figure 7.4: Tensile stress-strain curves M6 mixture [41] and mixture used in literature [7].

The numerical results are plotted versus the experimental results in Figure (7.5).

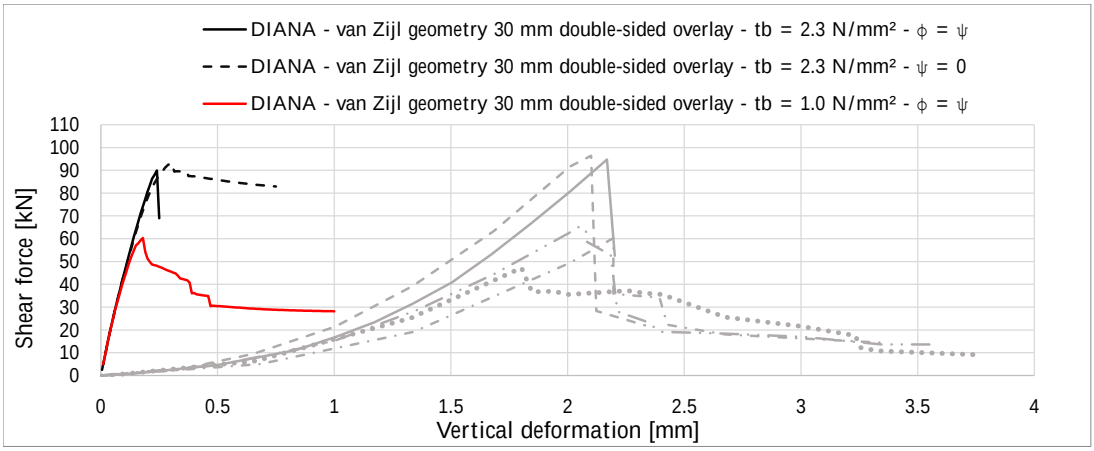

Figure 7.5: Numerical versus experimental results. Grey curves = experimental results. Solid black curve = numerical result, cohesion SHCC-masonry interface equal to 2.3 Mpa, $\Psi = \phi$. Dotted black curve = numerical result, cohesion SHCC-masonry interface equal to 2.3 Mpa, $\Psi = 0$. Red solid curve = numerical result, cohesion SHCC-masonry equal to 1.0 Mpa, $\Psi = \phi$.

The average peak shear strength derived from the experiments equals 60.6 kN. The experimental results are plotted through grey curves. The initial numerical model (see solid black curve) overestimated this strength (89.9 kN). However, a lower value of the SHCC-masonry interfacial bond strength (τ_b = 1.0 Mpa) does provide satisfying results, i.e. peak shear strength equal to 60.32 kN. Also, the brittle failure of the experiments is well represented by the sudden failure of the numerical model, resulting in divergence. This brittle behaviour is avoided when using a dilatancy angle equal to zero (see black dotted curve). From the experimental results of this research, it is known that dilatant behaviour of this overlay is present, therefore, using a zero dilatancy angle is not representative. In conclusion, the numerical model, with interfacial bond strength equal to 1.0 Mpa and a dilatancy angle equal to 0.647 rad, results in satisfying outcomes.

As reported in [38], no cracking of the overlay is observed during the experiments. From DIANA the crack strains of the overlay material do show coinciding results, i.e. no cracking of the 30 mm thick overlay, see Figure (7.6). This figure presents the cracking strains at peak resistance of the numerical model with the lowered SHCC-masonry bond strength (1.0 Mpa). Additionally, the figure shows the crack widths in a global X direction. It is clearly shown only minor crack activity is present at the bottom side of the overlay.

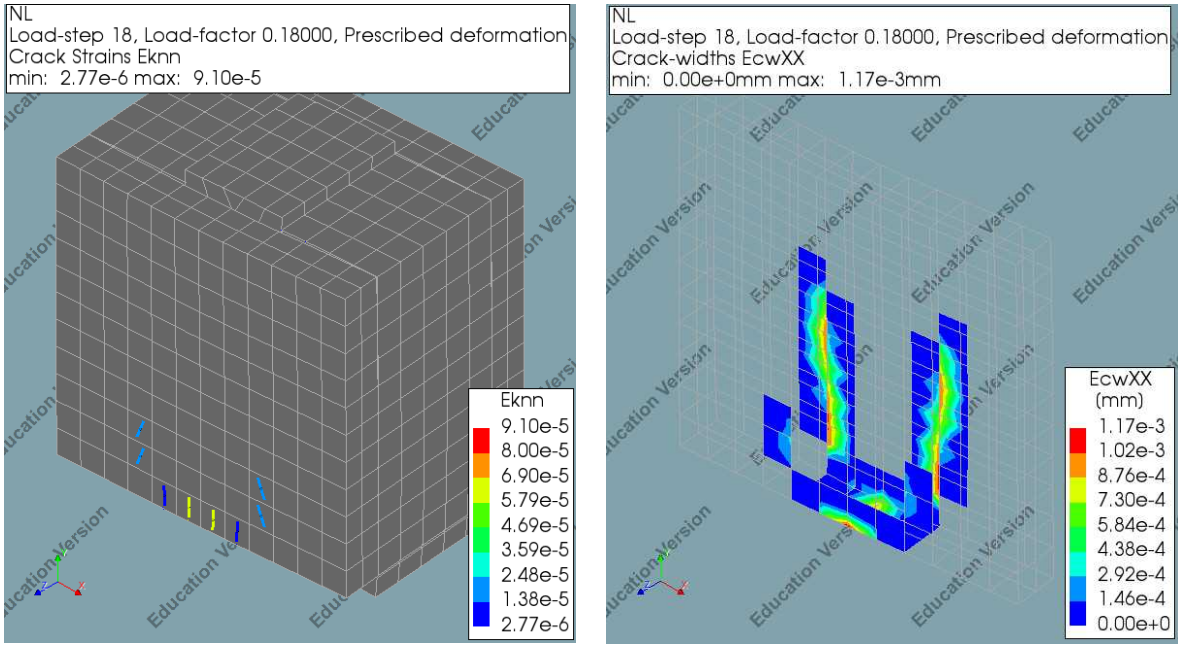

(a) Isometric view mesh full numerical model. Cracking strains Eknn shown at peak resistance.

(b) Isometric view front SHCC overlay. Crack widths EcwXX shown at peak resistance.

Figure 7.6: Cracking strains and cracks widths at peak resistance numerical model with adjusted cohesion SHCC-masonry interface ($tau_b = 1.0 \text{N/mm}^2$).

An additional numerical model with a thinner, 10 mm thick, overlay is considered to investigate the crack behaviour of the SHCC overlay. Similar material properties for all the continuum and interface elements are used, besides the adjusted cohesion of the SHCC-masonry interface. In Figure (7.7) the force-displacement curve of this new model is plotted versus the specimen with the thicker overlay. See the black and red curve, respectively. It is shown that the model with the thinner overlay does not show brittle failure.

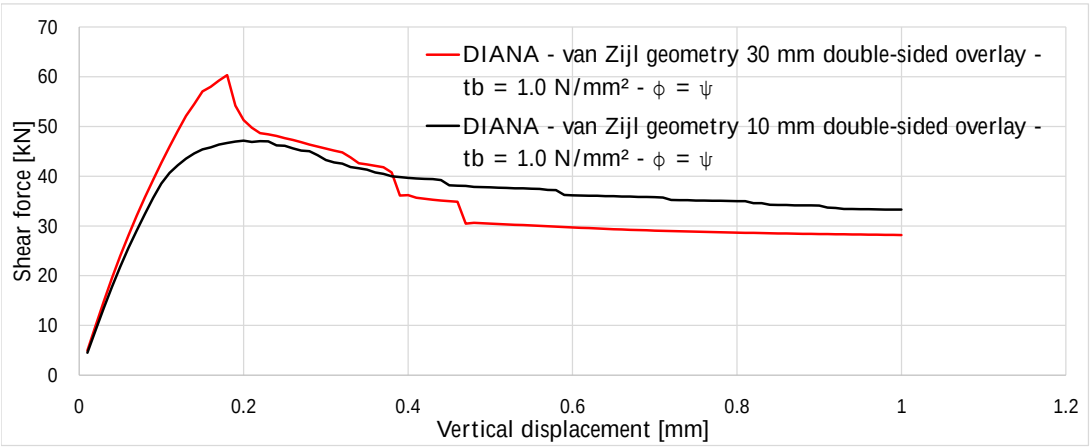

Figure 7.7: Force-displacement relationship numerical simulations. Red curve = retrofitted masonry triplet with double-sided 30 mm thick overlay. Black curve = retrofitted masonry triplet with double-sided 10 mm thick overlay. Cohesion of SHCC-masonry interface equal to 1.0 Mpa, $\Psi = \phi$.

Because of the smaller thickness, the applied overlay is less stiff. Because of this lower stiffness, the dilatant behaviour of the overlay is not resulting in sudden debonding of the complete overlay. To accommodate this

bending behaviour of the overlay cracking over the full height is present, see Figure (7.8). A top view of the deformed model, the cracking strains, and the crack widths are shown for peak resistance.

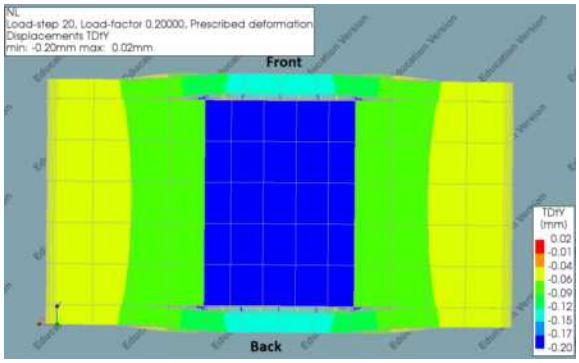

(a) Top view deformed model at peak resistance.

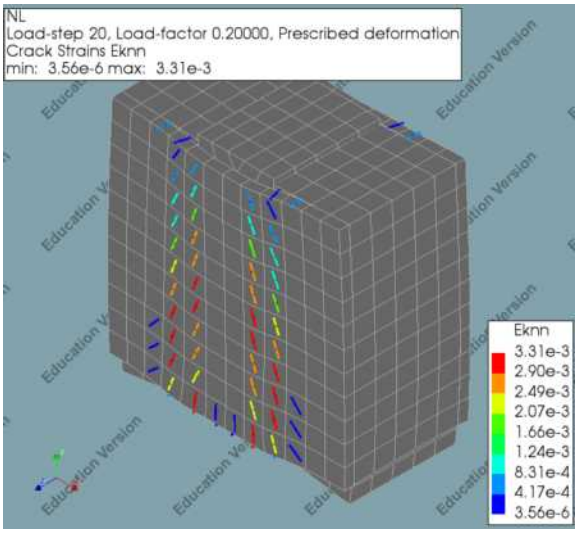

(b) Isometric view cracking strains SHCC overlay at peak resistance.

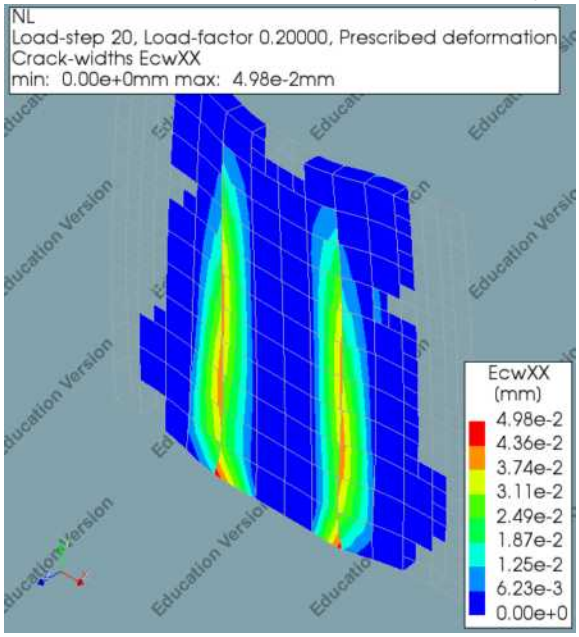

(c) Isometric view crack widths frontside SHCC overlay at peak resistance.

Figure 7.8: Deformed mesh, cracking strains and cracks widths at peak resistance. Numerical simulation retrofitted masonry triplet with a double-sided 10 mm thick overlay ($\tau_b = 1.0\,\mathrm{N/mm^2}$).

Thus, as mentioned in the literature, the thinner overlay results in a more ductile failure pattern, including a broad crack pattern in the overlay material. With the help of this numerical model, the different influence factors mentioned at the beginning of this chapter are investigated. It is shown that both brittle and ductile failure modes can be represented with the help of the Coulomb friction model for the SHCC-masonry interface.

No figures or force-displacement curves are provided in the literature to enable further investigations with respect to the correspondence of the numerical simulations.

7.3. Influence applied pre-compression

Two different investigations are performed concerning the application of the pre-compression. Firstly, the influence of the method to apply this pre-loading is investigated. Loading conditions from literature and this experimental campaign are compared. Additionally, a more realistic boundary condition, concerning actual URM structures, is modelled.

Secondly, the possible influence of the loading eccentricity of this pre-compression is investigated. The experimental setup used did not load the retrofitted specimen in its neutral axis, causing a non-uniformly distributed normal stress in the unit-mortar interfaces.

7.3.1. Application of pre-compression

One of the discussed factors that might have influenced the experimental results is the application of pre-compression, which is different in literature. Additionally, the used experimental setup is not representative of actual structural systems.

In this additional study, only specimens with a single-sided SHCC overlay are contemplated. The study considers three types of boundary conditions:

1. No pre-compression applied;
2. Pre-compression applied to full retrofitted specimen; and
3. Pre-compression is only present in the masonry substrate.

The first condition is corresponding to literature. Only vertical shear loading is present for these models. Differences in crack pattern and resistance concerning the boundary conditions considered in this experimental campaign are investigated. Finally, phased analyses are performed. With the help of these analyses, the pre-compression is only applied to the masonry substrate (first loading phase). After this first loading phase, the SHCC overlay is applied to the masonry triplet. In this way the SHCC overlay is not pre-loaded with the pre-compressive force, creating a more realistic representation of retrofitted unreinforced masonry.

For these numerical analyses the SHCC material properties as mentioned in Table 7.3 are used. In paragraph 7.5 the influences of the SHCC material properties are discussed. Figure (7.9) shows the numerical models considered for these additional analyses. In these figures, only the specimens with a 10 mm thick overlay are shown. Numerical simulations on retrofitted masonry triplets with a 30 mm thick overlay are also considered.

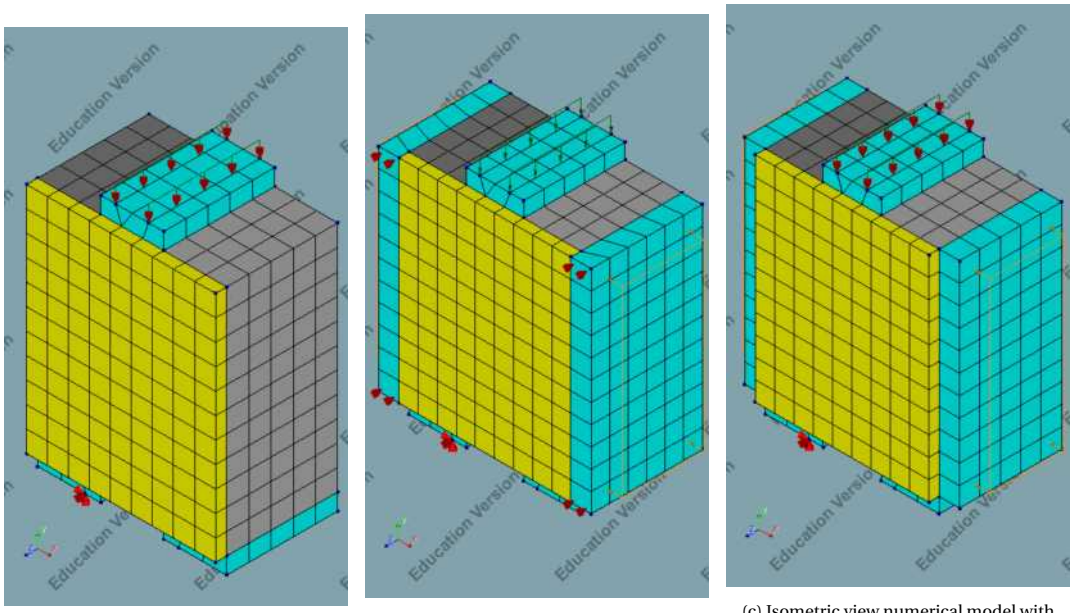

(a) Isometric view numerical model without pre-compression.

(b) Isometric view numerical model with pre-compression applied to full retrofitted specimen.

(c) Isometric view numerical model with pre-compression only applied to masonry substrate. Phased analysis, SHCC overlay applied after pre-loading.

Figure 7.9: Overview different numerical models (a) no pre-compression applied (b) full retrofitted specimen pre-compressed (c) phased analysis, only pre-compression present in masonry substrate. Blue = steel elements, yellow = SHCC overlay, and grey = masonry units.

The material properties of the unit-unit interfaces are similar to the previous analyses performed for the TU Delft masonry specimen, see Chapter (5). The cohesion of this interface is equal to $0.1892\,N/mm^2$. For the pre-compressed specimen, the normal stiffness of the unit-unit interface is increased by a factor of 100. The increase is required for a realistic strain distribution in the retrofitted specimen, as discussed in paragraph 5.3.1. For the SHCC-masonry interface, a Coulomb friction model is considered, with a cohesion equal to $2.3\,N/mm^2$. However, through multiple analyses, different numerical values for this quantity are taken into account. The results of these analyses are provided in the next paragraph (7.4).

In Figure (7.10) and (7.11) the force-displacement curves of the different specimen are shown. All of the levels of pre-compression are analysed.

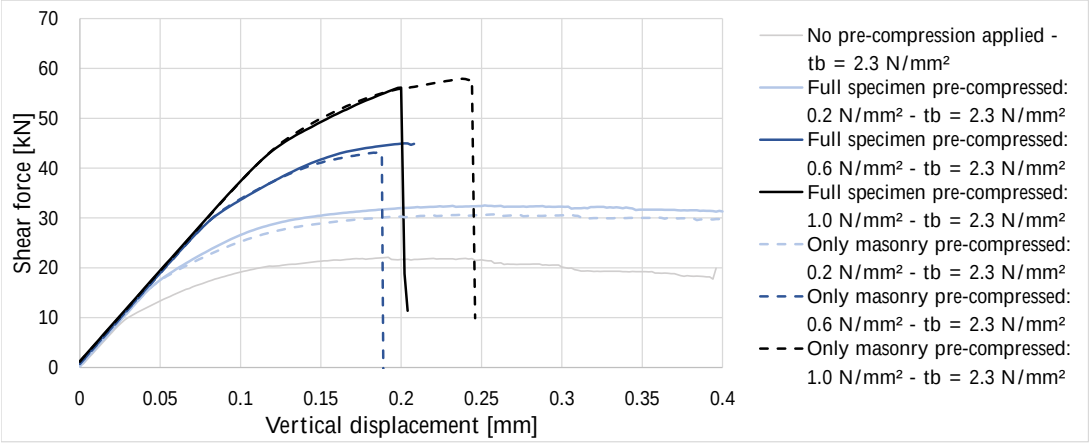

Figure 7.10: Force-displacement relationship numerical simulations. Retrofitted specimen with a single-sided 10 mm thick overlay. Grey curve = specimen without pre-compression applied. Solid curves = specimen with pre-compression applied to full cross-section. Dotted curves = specimen with pre-compression only applied to masonry triplet.

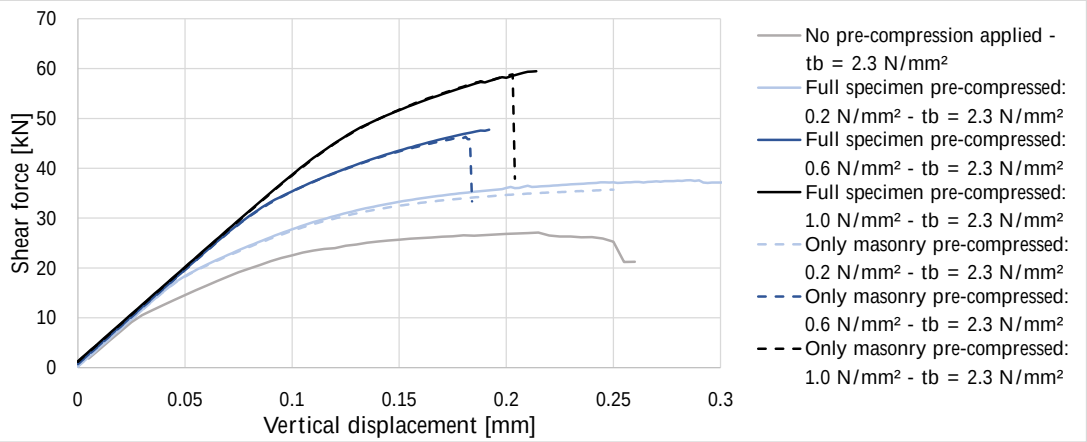

Figure 7.11: Force-displacement relationship numerical simulations. Retrofitted specimen with a single-sided 30 mm thick overlay. Grey curve = specimen without pre-compression applied. Solid curves = specimen with pre-compression applied to full cross-section. Dotted curves = specimen with pre-compression only applied to masonry triplet.

It is shown that the specimen without the application of pre-compression resulted in lower capacities of the unit-unit interfaces. Without this pre-compression, the shear strength of the masonry material is equal to the cohesion. The additional capacity is obtained because of the additional shear surface with the applied overlay. A higher level of pre-compression results in a higher level of shear resistance, which is already known from the initial numerical analyses. More importantly, it is also shown that the method of application of the pre-compression is not influencing the resistance of the different specimen. Pre-loading both the masonry and the overlay material results in similar shear strength quantities as for the phased analyses. However, differences are observed in the cracking behaviour of the overlay.

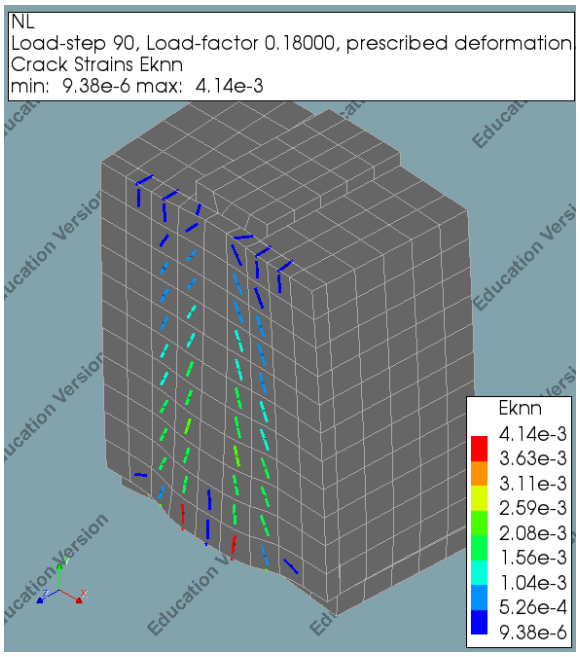

(a) Isometric view cracking strains SHCC overlay. No pre-compression applied to specimen. Overlay thickness = 10 mm.

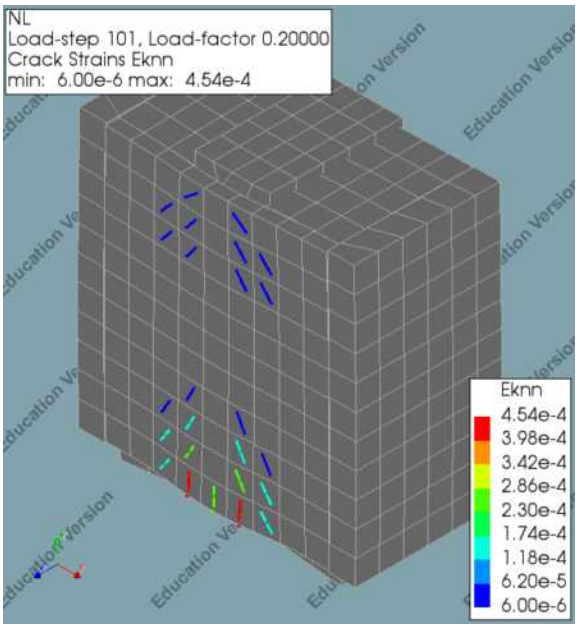

(b) Isometric view cracking strains SHCC overlay. Pre-compression applied to full retrofitted cross-section. Overlay thickness = 10 mm.

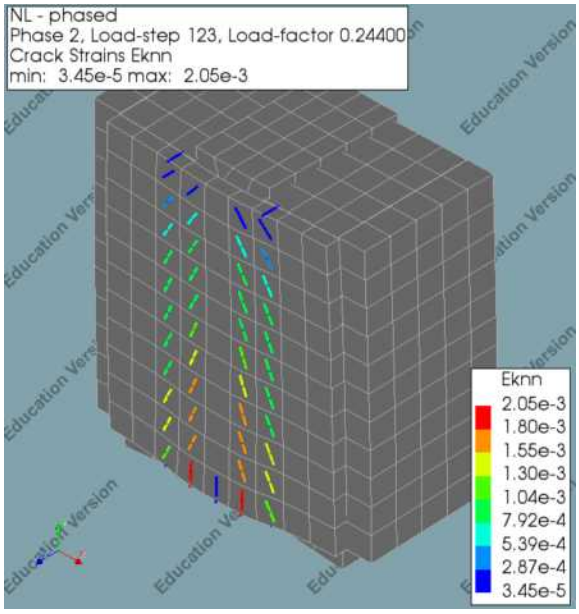

(c) Isometric view cracking strains SHCC overlay. Pre-compression only applied to masonry triplet via phased analysis. Overlay thickness = 10 mm.

Figure 7.12: Influence application of pre-compression for crack patterns SHCC overlay. Overlay thickness = 10 mm.

Figure (7.12) presents that the specimen, fully pre-compressed, show a much different crack pattern compared to the specimen with the other considered boundary conditions. Cracking of the overlay is restricted because of the applied pre-compression. The specimen with the thicker 30 mm SHCC overlay does not show any significant cracking in the overlay material.

In conclusion, from this analysis, the application method of the pre-compression does not influence the shear resistance of the retrofitted specimen. However, the crack pattern is highly influenced if the full retrofitted specimen is pre-loaded, which corresponds to the experimental results of this research.

7.3.2. Eccentricity applied pre-compression

To investigate the influence of the non-uniformly distributed pre-compression, in the unit-unit interface, additional numerical simulations are performed. This linearly distributed pre-compression might have influenced the experimental results observed.

Because the resulting force of the pre-compression is applied halfway the total height of the retrofitted triplet, an eccentricity with the neutral axis is introduced, initiating curvature of the specimen. This creates non-uniformly distributed normal stresses in the unit-mortar interfaces. These normal stresses (or tractions) are directly related to the shear resistance of this interface via the assumed Coulomb criterion. A lower pre-compression equals a lower shear resistance. Thus, the magnitude of normal stresses at this interface is of high importance.

Additional numerical simulations are performed to investigate this possible influence. The influence of this linearly distributed pre-compression is considered for the plain masonry triplets only. An additional moment is applied to the steel plates loading the specimen in pre-compression to initiate the linearly distributed normal tractions in the unit-unit interfaces. This additional moment is introduced via two surface loads. The use of solid elements makes it impossible to introduce the moment directly to the finite elements since these type of elements do not contain a rotational degree of freedom at the nodes. In Figure (7.13) the assumptions made for this modelling procedure are shown. The curvature is derived analytically for a retrofitted specimen with a 10 mm thick overlay.

These additional surface loads are applied in a force-controlled manner to the URM model to investigate the shear strength of this specimen under non-uniform pre-compressive conditions.

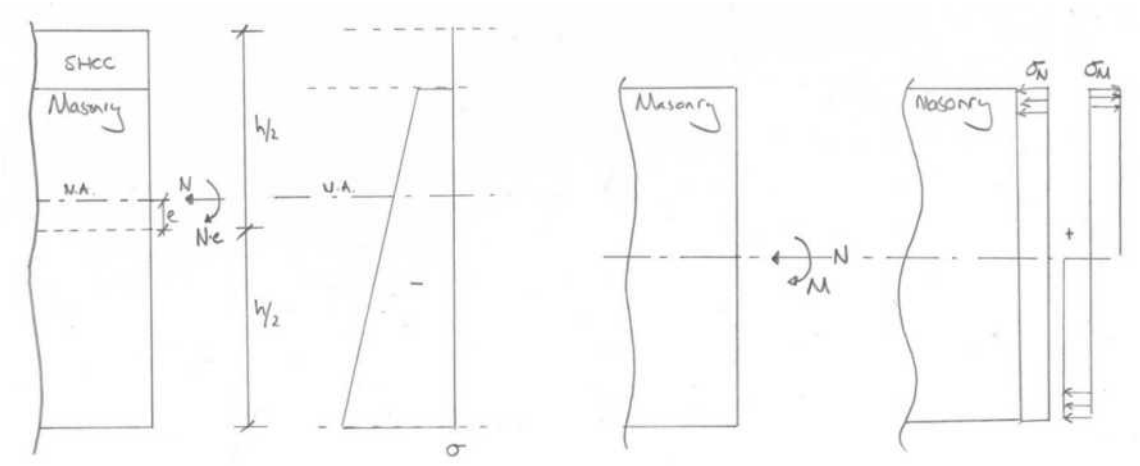

(a) Left: overview influence linear distributed normal stress masonry substrate retrofitted specimen. Right: simplified model to simulate the linear distributed normal stress in masonry triplet.

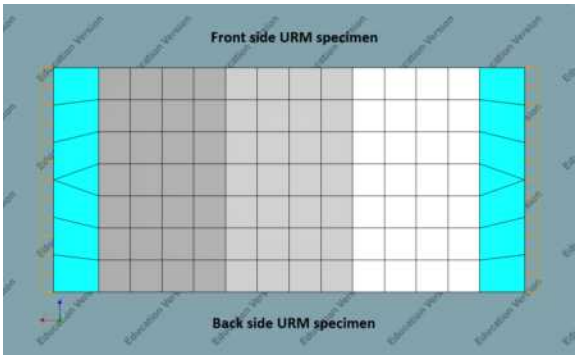

(b) Top view numerical model URM triplet with uniformly applied pre-compression.

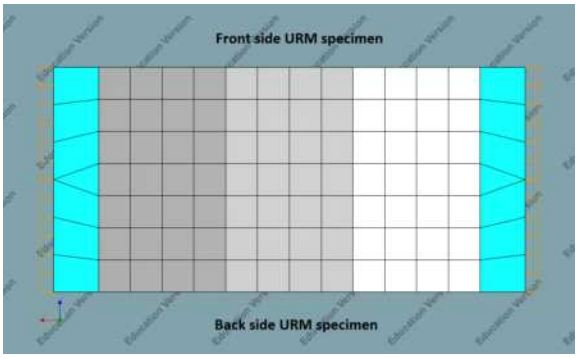

(c) Top view numerical model URM triplet with additionally applied pre-compression to simulate the bending moment occuring in the retrofitted masonry.

Figure 7.13: Overview approach considered additional numerical models. Steel plates loading the URM specimen in pre-compression are visualized by blue mesh elements.

The applied pre-compression is determined via the following calculations:

$$N = \sigma_p \cdot A_{tot} \tag{7.1}$$

$$M_e = N \cdot e_{N.A.} \tag{7.2}$$

$$M_e = \frac{t_b}{2} \cdot F_{eq} \tag{7.3}$$

$$\sigma_{eq} = \pm \frac{F_{eq}}{h_b \cdot t_b} \tag{7.4}$$

In which σ_p equals the pre-compression level analysed (e.g. 0.2 Mpa). To determine the total pre-compressive force N the surface area of the retrofitted specimen with a 10 mm overlay is considered (210 mm·110 mm). The eccentricity between the resultant of the pre-compressive force and the neutral axis of the retrofitted specimen is taken into account via an additional bending moment M_e. This eccentricity $e_{N.A}$ is equal to 13 mm. The moment is deconstructed into a pair of equivalent normal forces F_{eq} with an internal lever-arm equal to half the thickness of the masonry bricks t_b. Finally, these equivalent normal forces are distributed over an area equal to height times half the thickness of the masonry brick (210 mm · 50 mm).

Table 7.4: Loading conditions additional numerical analyses. Influence of pre-compression eccentricity.

Level of pre-compression	Uniform load	Additional loading	Resulting pre-compression	Unit
-0.2	-0.2	± 0.044	-0.156 ; -0.244	N/mm^2
-0.6	-0.6	± 0.132	-0.468 ; -0.732	N/mm^2
-1.0	-1.0	± 0.22	-0.78 ; -1.22	N/mm^2

In Table (7.4) the calculated surface loads are provided. The fourth column shows the resulting pre-compressive stresses, i.e. standard pre-compression plus or minus additional loading. It shows that still, even with the additionally applied stresses, the total specimen is loaded in compression.

All the numerical simulations resulted in converged solutions. Below the normal tractions, derived from the integration points of the unit-unit interface, are depicted for all three levels of pre-compression.

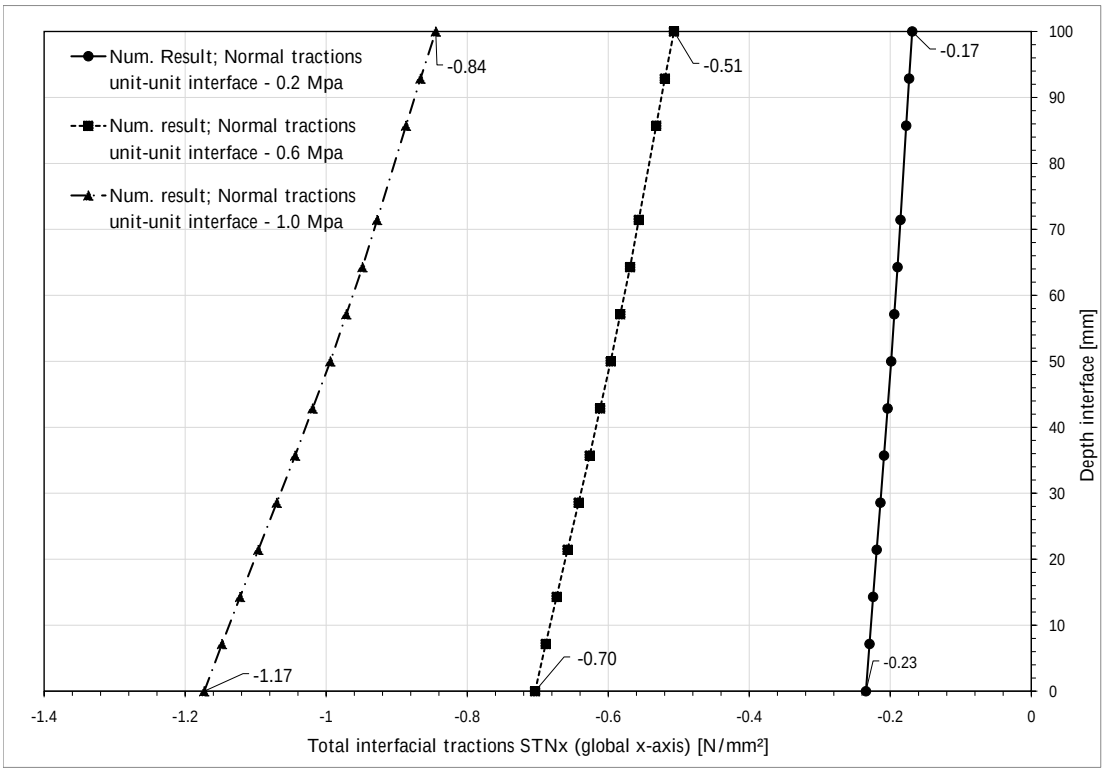

Figure 7.14: Distribution of horizontal tractions at the unit-unit interface of plain masonry triplet loaded by additional bending moment.

Figure (7.14) clearly shows that the specimen are pre-compressed by a linear distributed compressive stress. This imitates the distribution of stresses present in the unit-unit interfaces of the retrofitted masonry specimen. In Figure (7.15) the resulting force-displacement curves are plotted versus the resistance of the masonry triplets loaded uniformly. It is concluded that this non-uniform distribution of stresses does not influence the total resistance of the specimen.

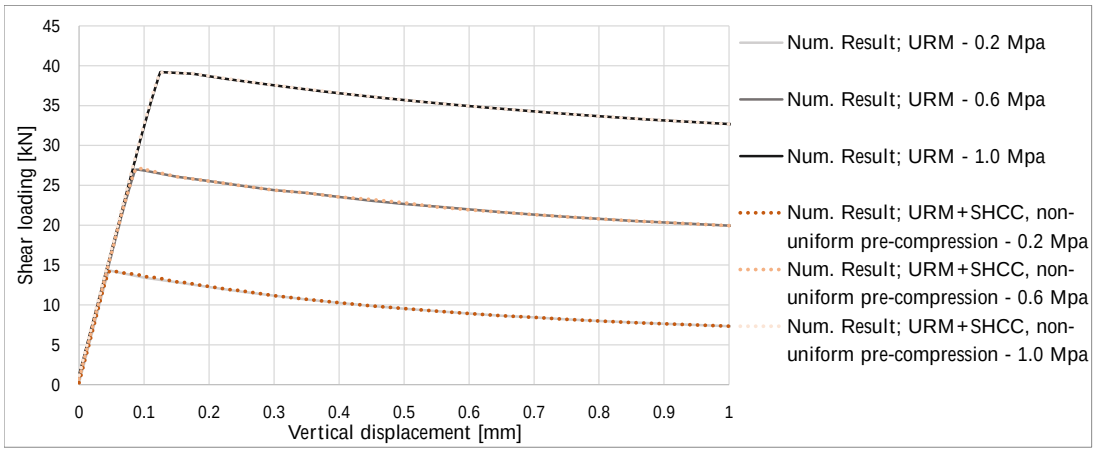

Figure 7.15: Force-displacement curves. Numerical results plain masonry triplets versus plain masonry triplets loaded by additional bending moment. Masonry material only.

The specimen loaded by the linearly distributed normal stress performs similar to the original non-retrofitted model. The average normal traction in the unit-unit interface is governing for the final shear resistance, which must be taken into account when comparing the experimental results of the retrofitted specimen to the plain masonry triplets. On average, the unit-unit interface of the retrofitted specimen with a 10 mm thick SHCC overlay is loaded by compressive stress of -0.19, -0.57, and -0.95 Mpa, respectively. Taking into account the Coulomb criterion, the shear strength contribution of these two unit-unit interfaces is calculated. These values are provided in Table (7.5).

Table 7.5: Shear resistance unit-unit interface retrofitted masonry triplets.

Level of pre-compression applied	Actual pre-compression unit-unit interface [N/mm^2]	Shear resistance [kN]
$-0.2\,N/mm^2$	-0.19	14
$-0.6\,N/mm^2$	-0.57	26
$-1.0\,N/mm^2$	-0.95	38

The shear resistance of the masonry substrate can now be determined based on the average value of the actual acting normal stress distribution, calculated analytically. The shear strength is determined via equation (4.7) and (4.6). The difference with the uniformly loaded masonry is not significant. The linearly distributed pre-compression does not influence the resistance of the retrofitted masonry specimen in the unit-mortar joints.

7.4. Influence interfacial bond strength SHCC-masonry

The second point of interest investigated is the shear bond strength between the SHCC overlay and the masonry triplet. It is concluded from the numerical analyses that this bond strength profoundly influences the shear resistance of the retrofitted specimen. However, not only the shear resistance is affected, but also the failure mechanism of the retrofitted specimen is influenced.

The influence of the SHCC-masonry interfacial bond strength is investigated via a parametric study. Figure (7.16) combines the results of multiple numerical analyses. The maximum shear force is plotted versus the $(\frac{\tau_b}{c_0})$ ratio. This ratio equals the difference between the SHCC-masonry bond strength τ_b and the cohesion of the masonry triplet c_0. It shows that the maximum shear force of the retrofitted specimen increases when the strength of the SHCC-masonry interface increases. Both of the overlay thicknesses investigated show the same linear trend.

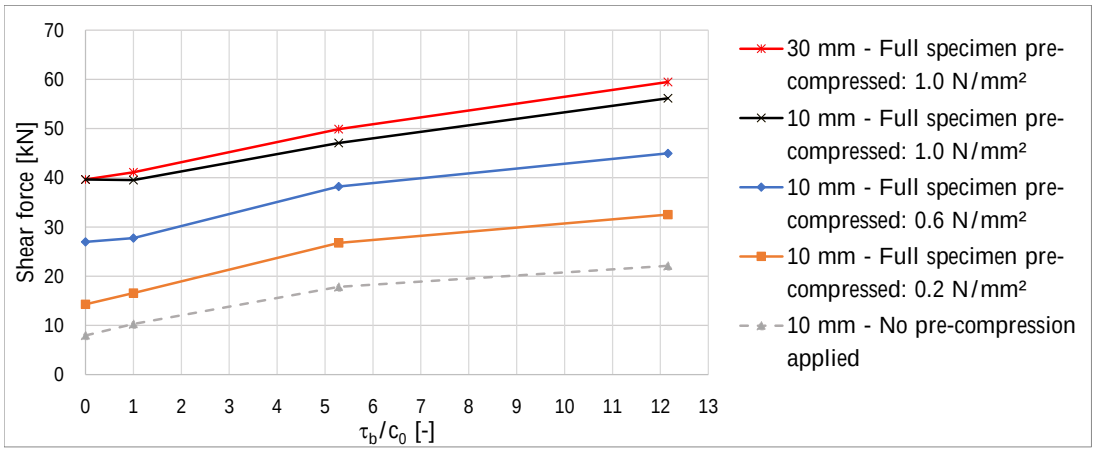

Figure 7.16: Influence shear bond strength SHCC-masonry interface on shear force resistance retrofitted specimen. Both 10 and 30 mm thick overlay represented.

The bond strength between the SHCC and the masonry influences not only the resistance of the retrofitted specimen but also the crack pattern of the overlay material. Figure (7.17) shows the crack strains in the SHCC material for two specimen. These specimens are retrofitted with a 10 mm thick overlay and have a SHCC-masonry bond strength equal to 1.0 and 2.3 Mpa, respectively. No pre-compression is applied. In this way, the influence of applied pre-compression is neglected. The higher level of bond strength results in more activation of the SHCC overlay material. All specimen with a $\frac{\tau_b}{c_0}$ ratio equal to 1.0 do not show any sign of cracking. Also, the interfacial bond strength for the retrofitted specimen with a 30 mm thick overlay does not influence the cracking behaviour. None of these specimen show cracks in the overlay.

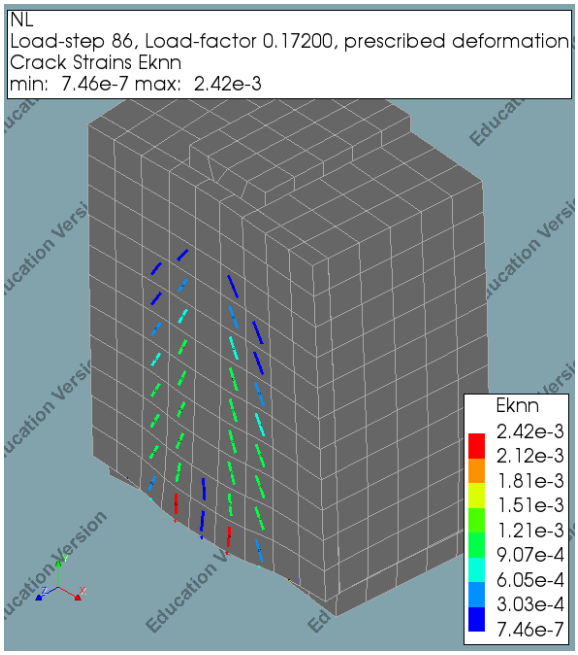

(a) Isometric view cracking strains SHCC overlay. No pre-compression applied. Overlay thickness = 10 mm. SHCC-masonry bond strength = 1.0 N/mm^2.

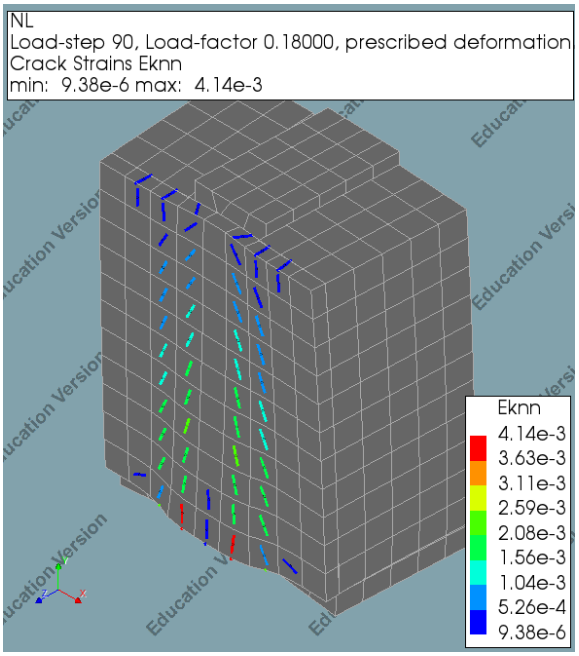

(b) Isometric view cracking strains SHCC overlay. No pre-compression applied. Overlay thickness = 10 mm. SHCC-masonry bond strength = 2.3 N/mm^2.

Figure 7.17: Influence SHCC-masonry bond strength on cracking pattern 10 mm thick SHCC overlay.

7.5. Influence material properties SHCC

In the previous analyses, the SHCC mixture from literature [7] is taken into account. This paragraph discusses the possible influences of the material properties of the retrofitting material.

The SHCC mixture used in this experimental campaign is stronger compared to the mixture considered in, for example, [7]. Both the initial and ultimate cracking strength are higher, i.e. $3.6\,N/mm^2$ and $4.6\,N/mm^2$ versus $2.19\,N/mm^2$ and $2.20\,N/mm^2$, respectively. In Figure (7.18) the uniaxial tensile stress-strain diagram of both mixtures is shown. Only specimens without the application of pre-compression are analysed.

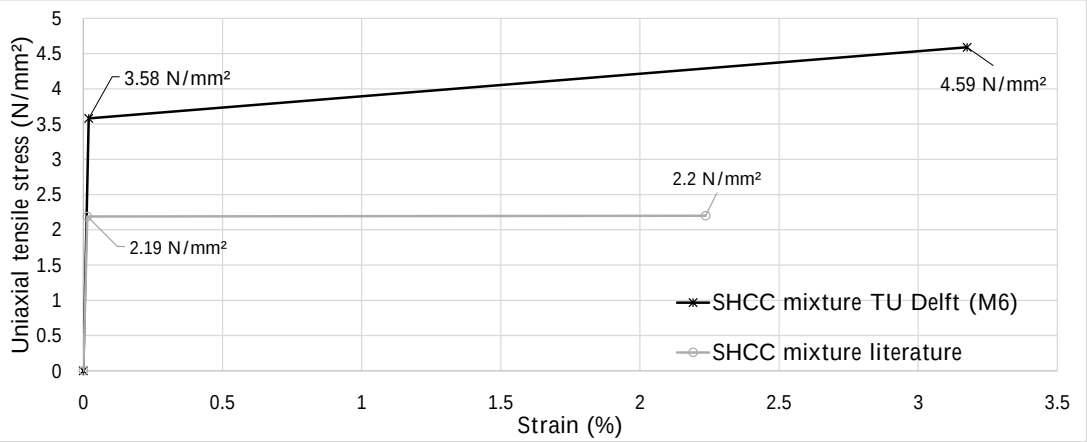

Figure 7.18: Tensile stress-strain curves M6 mixture [41] and mixture used in literature [7].

In Figure (7.19) the crack strains in the 10 mm thick overlay are shown. As discussed in paragraph 7.4, a higher strength interface between the overlay and the masonry results in a more distributed crack pattern with larger cracking strains. The specimen retrofitted with the stronger overlay material show a smaller magnitude of cracking strains. Also, cracks are present in a smaller area of the overlay. This becomes clear when comparing Figure (7.19) and (7.17). The cracking strains are up to one magnitude smaller.

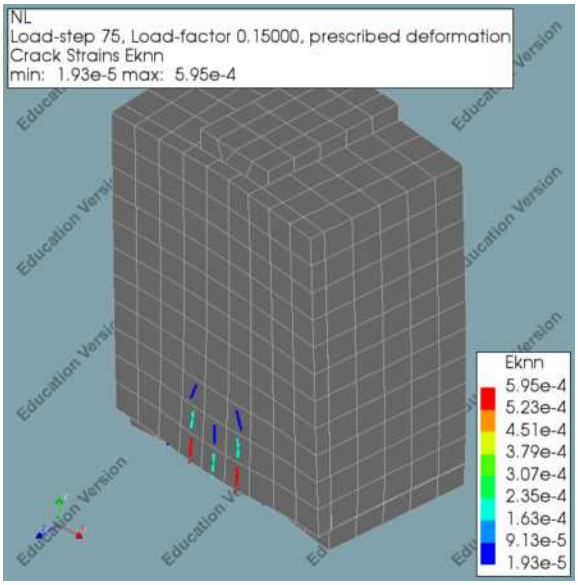

(a) Isometric view cracking strains SHCC overlay. No pre-compression applied. Overlay thickness = 10 mm. SHCC-masonry bond strength = 1.0 N/mm^2.

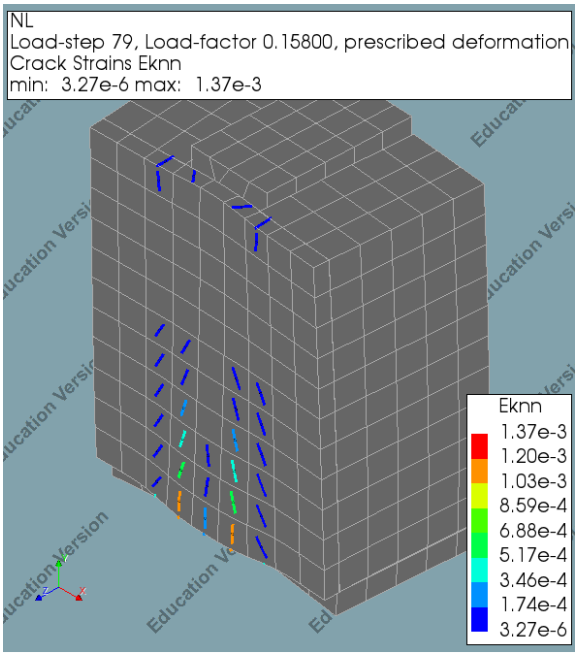

(b) Isometric view cracking strains SHCC overlay. No pre-compression applied. Overlay thickness = 10 mm. SHCC-masonry bond strength = 2.3 N/mm^2.

Figure 7.19: Cracking strains SHCC mixture used in this experimental campaign.

The used SHCC mixture in this experimental campaign requires high bond strengths to be activated. None of the specimen with a SHCC-masonry bond strength equal to 0.1892 N/mm^2 show any cracks, for any of the loading conditions. This is similar to the previously investigated SHCC mixture. Thus, both mixtures are too strong to be activated if a low strength interface is present.

7.6. Influence overlay thickness

A numerical model with an overlay thickness equal to 5 mm is investigated. The SHCC material properties corresponding to the mixture used in this experimental campaign are considered. When the SHCC-masonry bond strength is considered equal to the cohesion of the masonry, no cracking of the thin overlay is shown. This outcome is similar to all other analyses discussed earlier. Application of even thinner overlays is not considered. However, using the SHCC mixture from literature, in combination with the thinner 5 mm overlay thickness, is taken into account.

The additional model considered contains a 5 mm thick single-sided overlay. The interfacial bond strength between the overlay and the masonry triplet is taken equal to the cohesion of the masonry, i.e. the lowest value considered. None of the specimen considered earlier showed cracking with this value of interfacial strength. Using this thinner overlay, the lower strength SHCC, and the lowest value of the SHCC-masonry bond strength resulted in minor cracking strains present at the bottom of the overlay. Figure (7.20) shows the cracking strains at peak resistance.

This conclusion corresponds to the equation provided in [8]. See equation 3.3. With this low value of the SHCC-masonry bond strength, very thin overlays are required to obtain ductile failure of the retrofitted specimen.

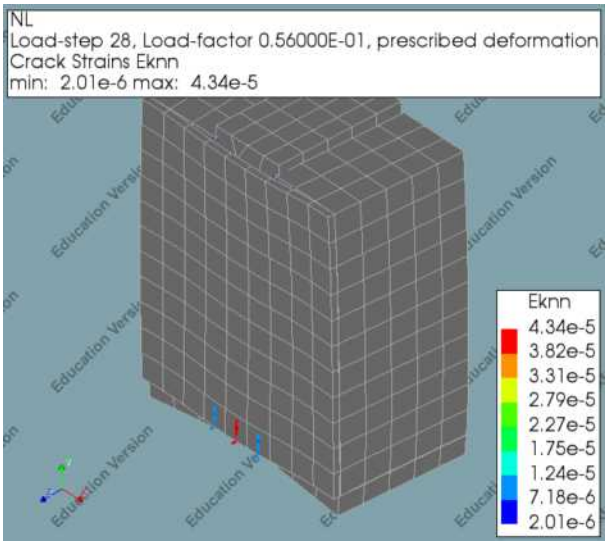

Figure 7.20: Cracking strains thin 5 mm overlay with low SHCC-masonry bond strength.

7.7. Influence eccentricity shear loading

The last parameter investigated is the eccentricity of the vertical hydraulic jacket. This jacket is loading the retrofitted specimen vertically. The top surface area of the central masonry unit is loaded only. However, just as for the applied pre-compression, the resulting force is not coinciding with the location of the neutral axis of the retrofitted specimen. The influence of this loading eccentricity is investigated with the help of numerical analyses. In Figure (7.21) the mesh of the numerical model considered is shown.

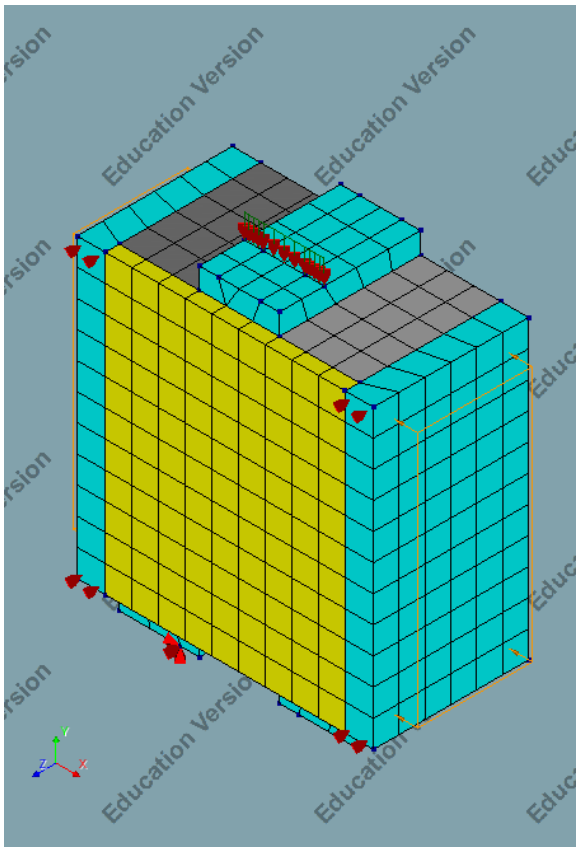

(a) Isometric view mesh.

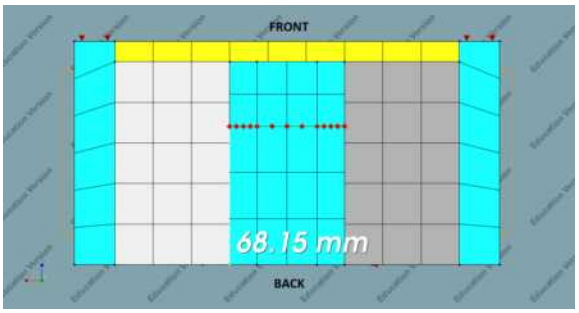

(b) Top view mesh.

Figure 7.21: Mesh numerical model considered to investigate influence eccentricity vertical hydraulic jacket.

The loading of the vertical jacket is changed to a line load at the neutral axis of the retrofitted cross-section. The stiffness of the top steel loading plate is increased to avoid unrealistic deformations of the numerical model. In these analyses the pre-compression is applied to the full retrofitted specimen. This is corresponding to the experimental setup considered in this research. In Figure (7.21) the force-displacement curves of two analyses are depicted. The interfacial bond strength between the SHCC overlay and the masonry is taken equal to $2.30\,\mathrm{N/mm^2}$.

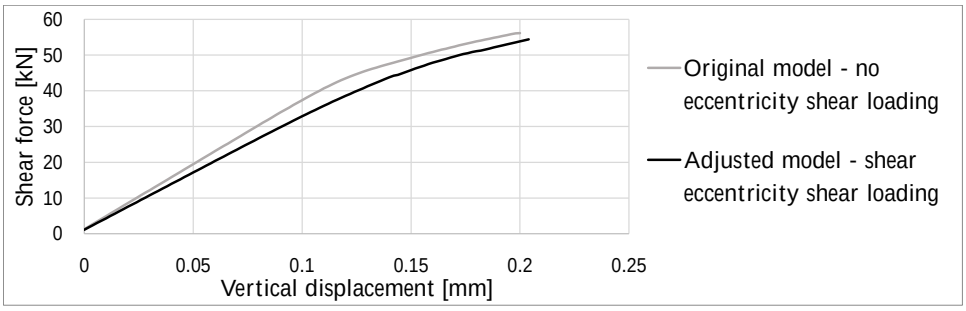

Figure 7.22: Force-displacement curve original and eccentrically loaded model. Grey = original model, black = numerical model with shear loading eccentricity.

It is shown that no large influences are present because of the eccentric vertical loading. The peak resistance is slightly underestimated if the vertical hydraulic jacket is loading the retrofitted specimen in its neutral axis.

8 Discussion

In this chapter, both the experimental and numerical results are discussed. The influence of different parameters is addressed.

8.1. Shear strength retrofitted masonry triplets

From the initial experiments performed, none of the retrofitted specimens showed increased shear resistance (or ductility) over the plain masonry triplets. Additionally, it is concluded that the surface preparation, overlay thickness, and curing conditions did not influence the experimental results.

Possible influence factors are investigated with the help of additional experiments and numerical analyses. The influence of the strength of the interfacial bond, between the SHCC overlay and the masonry substrate, is investigated both experimentally and numerically. The influence of the applied pre-compression, and SHCC mixture used, are examined via numerical analyses alone.

8.1.1. Influence interfacial bond strength SHCC-masonry interface

The importance of the interfacial bond strength, between the SHCC overlay and the masonry substrate, is investigated with additional experiments. Some of the already tested specimens are glued back together. The application of the glue is done with great care, and cleaning of the surfaces is done thoroughly for all specimen. However, still, many variations in the experimental results are present. It is questioned if the glued interfaces are of equal quality for all the different specimen. Because these specimens are tested before not all surfaces are perfectly straight anymore, possibly causing difficulties for the bonding between the glued elements, especially for the SHCC-masonry interface. After the initial testing phase, mortar material remained stuck to the overlay, making it difficult to obtain a perfect alignment between this overlay and the masonry triplet. All of these factors will have resulted in the high level of heterogeneity shown in the experimental results.

Only two of the glued retrofitted specimen showed an increase in resistance. Similar results are found when comparing these experimental results to the additional numerical simulations. With the help of these numerical analyses, the influence of the interfacial bond strength is investigated. From these analyses, it is concluded that higher bond strength, between the overlay material and the masonry triplet, will result in higher shear resistance of the retrofitted specimen. Only when this SHCC-masonry bond strength is sufficient the SHCC can be activated.

The exact bond strength of the glued interfaces is unknown. However, glueing the already failed unit-mortar interfaces will result in the failure of the two, non-glued, interfaces, resulting in similar shear strength as for the plain masonry triplets. Thus, only the SHCC-masonry interface is strengthened by the glue. This coincides with the numerical results.

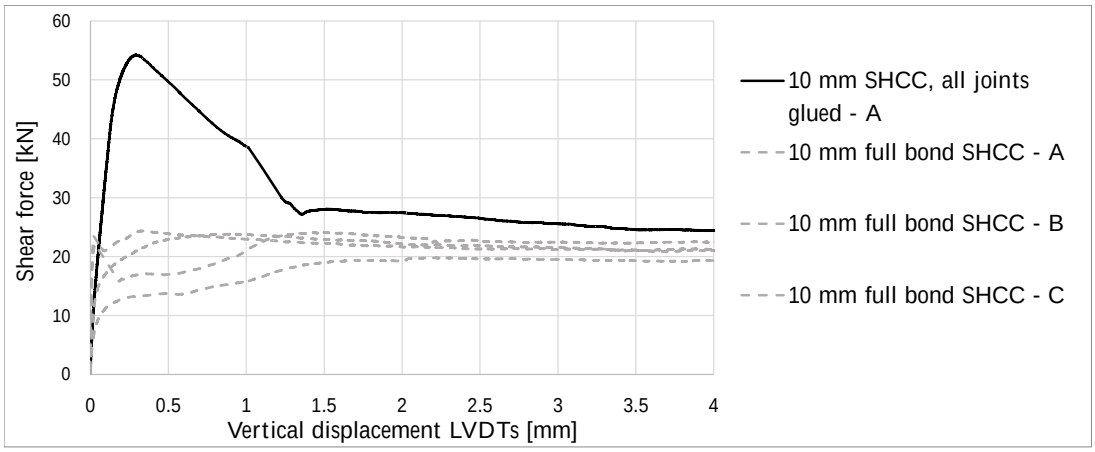

(a) Force-displacement curves additional experiments; 10 mm SHCC overlay with glued interface(s), pre-compression = 0.6 N/mm^2. Grey = initial tested retrofitted specimen. Black = glued retrofitted specimen.

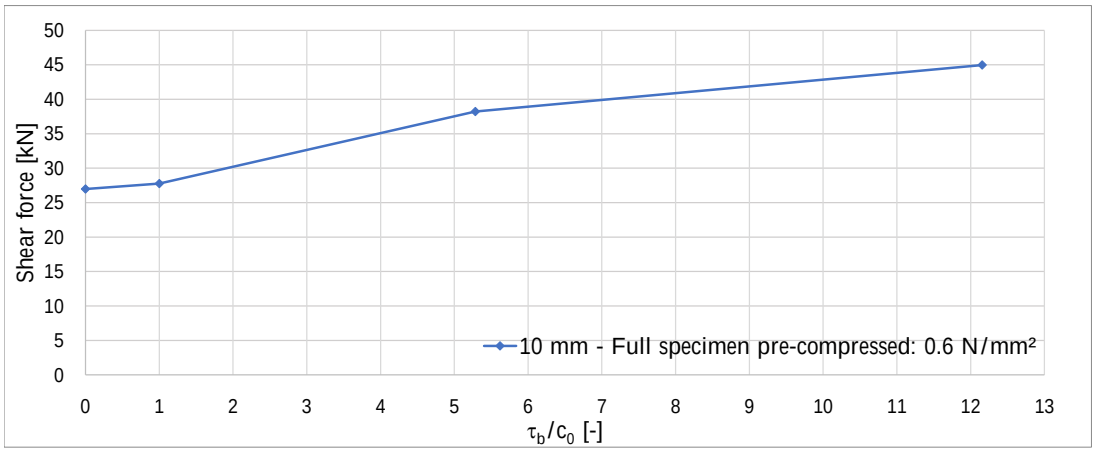

(b) Influence shear bond strength SHCC-masonry interface on shear force resistance retrofitted specimen. Only result for 10 mm thick overlay shown. Pre-compression (0.6 Mpa) applied to full retrofitted specimen.

Figure 8.1: Force-displacement curve experimental results and numerical results. Influence of SHCC-masonry bond strength investigated.

In Figure (8.1a), the force-displacement relationship of one of the glued specimen is shown. This specimen has a 10 mm thick overlay. Both the unit-mortar and the SHCC-masonry interfaces are glued. The full (glued) retrofitted specimen is pre-compressed by a distributed force equal to $-0.6\,\mathrm{N/mm^2}$. The numerical model with a $\frac{\tau_b}{c_0}$ ratio equal to 12.2 shows the best correspondence with the experimental result.

Additionally, comparing the results of the digital image correlation and the numerical model also shows similarities in terms of the cracking of the overlay material. In Figure (8.2) the von Mises strain field is shown for this particular specimen. A broad crack pattern is shown in the SHCC material. The corresponding numerical model also shows this large amount of cracks present in the overlay, see Figure (8.3). In Figure (8.3a) the cracking strains at the front side of the SHCC overlay are shown. The cracking strains are greater, and distributed over a larger area, at the backside of this overlay, see Figure (8.3b). For this numerical model, the full retrofitted specimen is pre-compressed. The bond strength for the SHCC-masonry interface is taken equal to $2.3\,\mathrm{N/mm^2}$ ($\frac{\tau_b}{c_0} = 12.2$). The material properties of the SHCC overlay are taken equal to the mixture used in this research.

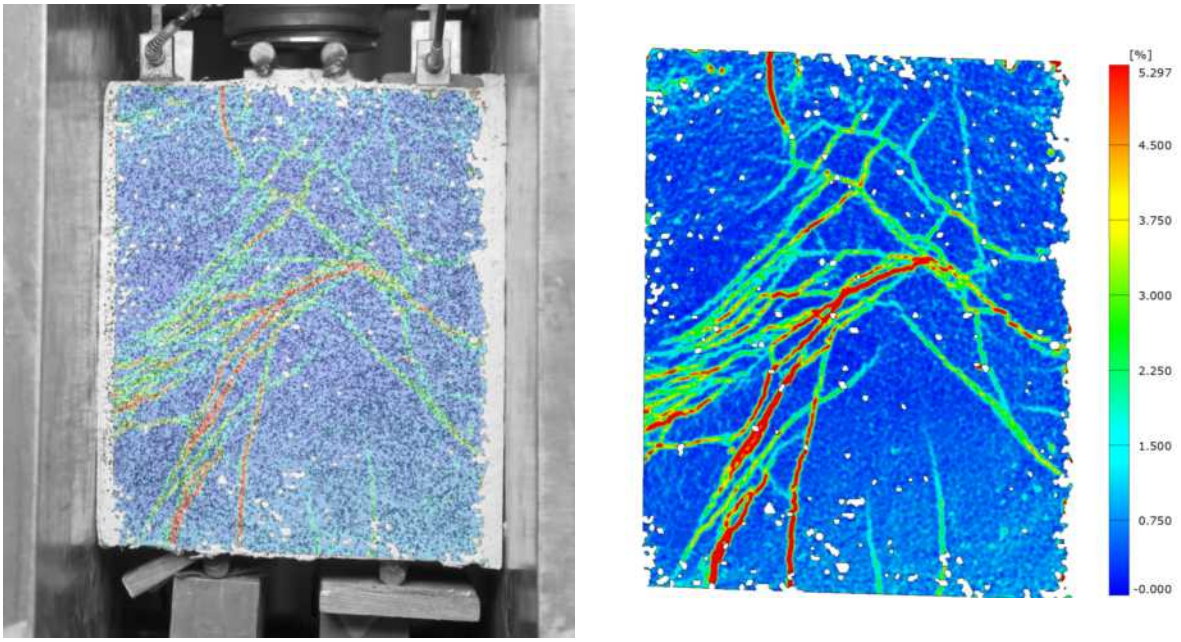

Figure 8.2: Von Mises strain field calculated with DIC compared with numerical result. Cracking of glued, 10 mm thick, overlay shown. Pre-compression = 0.6 Mpa, applied to full retrofitted specimen.

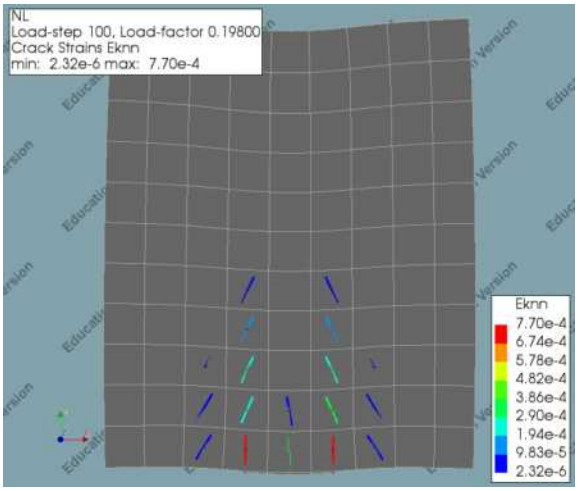

(a) Cracking strains SHCC overlay, front side. Overlay thickness 10 mm. Pre-compression applied to full retrofitted specimen, 0.6 Mpa.

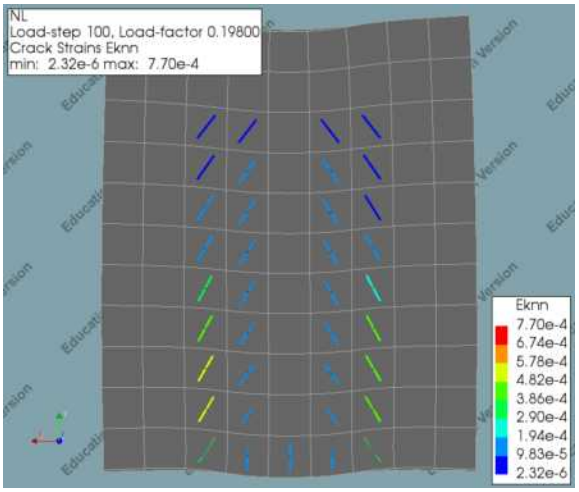

(b) Cracking strains SHCC overlay, back side. Overlay thickness 10 mm. Pre-compression applied to full retrofitted specimen, 0.6 Mpa.

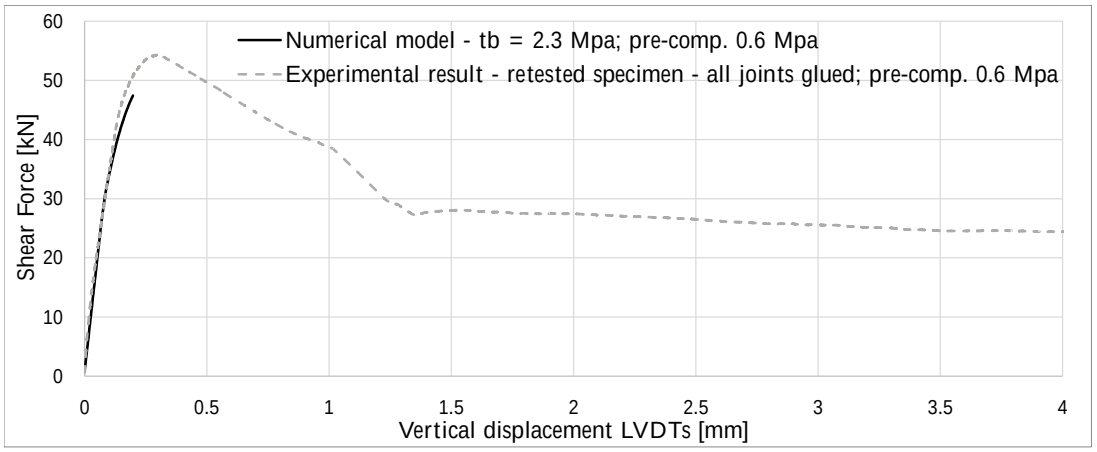

(c) Force-displacement curve numerical and experimental result. Grey = experimental result glued specimen. Black = Numerical result.

Figure 8.3: Numerical results crack pattern and force-displacement curve pre-compressed retrofitted specimen. Pre-compression = 0.6 Mpa, applied to full retrofitted specimen. Material properties SHCC equal to mixture used in this research.

In Figure (8.3c), the force-displacement relationship of the glued specimen is plotted versus the numerical result. Good correspondence is shown in the linear elastic stage of the specimen. The numerical model underestimates the peak resistance. Also, the numerical model shows brittle failure directly after peak resistance, resulting in divergence.

In conclusion, both the experimental and numerical results show that higher interfacial bond strength between the SHCC overlay and the masonry triplet will result in higher shear strength and the activation of the overlay material. This level of pre-compression did not disable the ability of the overlay to crack. Additionally, for this experimental campaign, it is shown that the initially assumed interfacial bond strength between the overlay and the masonry is correct, i.e. $0.1892\,\mathrm{N/mm^2}$. This low strength of the interface results in a marginal increase in strength, see Figure (8.1b), and is not able to activate cracking of the overlay material.

8.1.2. Influence application of pre-compression

Via additional numerical analyses, the influence of the applied pre-compression is investigated. The method of application is also considered.

This influence is also partly investigated with the help of additional experiments. In these additional experiments, the pre-compression is only applied to the masonry triplet. However, still, pre-compressive stresses are introduced in the overlay, restricting it from cracking. Two of the additionally tested specimen do show cracking of the overlay. One of these specimens is discussed in the previous paragraph. The second specimen contains a 10 mm thick overlay, which is cured in non-sealed curing conditions. During the initial testing phase of this particular specimen, vertical cracks in the overlay material are noticed with the DIC, see Figure (8.4).

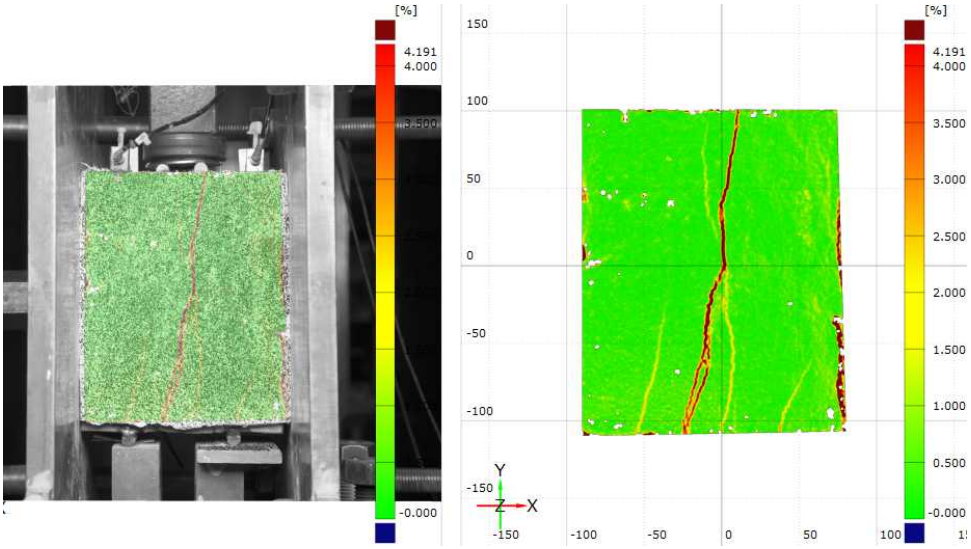

Figure 8.4: Cracks overlay after initial testing phase. Specimen number 42. Retrofitted masonry triplet with 10 mm thick SHCC overlay. Cured in non-sealed curing conditions.

The vertical cracks showed up after the initial testing phase and might have resulted from the non-sealed curing conditions. During re-testing of this specimen, now with glued interfaces, these vertical cracks initiated the final horizontal crack pattern in the glued overlay. In Figure (8.5b) this final crack pattern is shown.

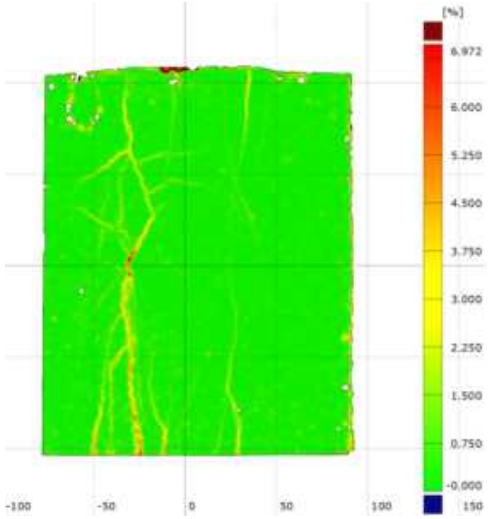

(a) Crack pattern glued SHCC overlay at peak resistance. Vertical crack coinciding with the crack found during initial phase of testing.

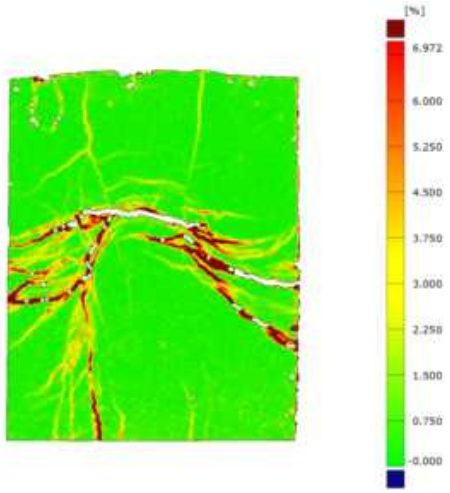

(b) Final crack pattern glued SHCC overlay DIC analysis.

(c) Picture specimen after re-testing with glued interfaces.

Figure 8.5: Crack pattern pre- and post-peak SHCC overlay. Pre-compression equal to 1.0 N/mm^2. Pre-compression applied to masonry surface only.

Because of the existing cracks before re-testing, this final cracking of the overlay cannot be directly related to the different method of application of pre-compression.

Numerical analyses show that the application of pre-compression negatively influences the cracking behaviour of the overlay material. If pre-compression is applied to the full specimen, high SHCC-masonry bond strength is required to activate cracking in the overlay. Neglecting the presence of pre-compression will result in cracking of the SHCC, even for lower bond strength values. However, this will also directly influence the shear resistance of the masonry triplet itself.

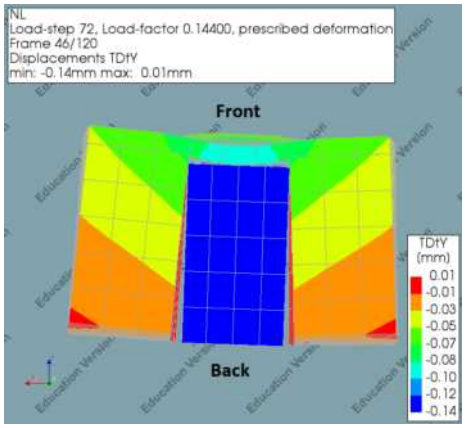

Figure 8.6: Top view deformed mesh at peak shear load.

If no constraints are applied to the specimen, bending of the retrofitted specimen will occur, see Figure (8.6) These additional deformations are initiated by the difference in stiffness between the masonry and the SHCC overlay. Bending of the specimen will introduce high tensile stresses in the masonry material and curvature of the overlay material. Not using pre-compression will, therefore, result in experimental data not directly representative of the shear strength of the retrofitted material.

For actual structures only pre-compressive stresses in the masonry are present. The overlay is stress-free after application. Phased numerical analyses are used to investigate this specific case. In Figure (8.7) the principle stresses in the SHCC overlay, at peak resistance, are shown for the two different cases with the applied pre-compression. The results of the highest level of pre-compression are shown. The material properties of the overlay are corresponding to the mixture used in this research. The SHCC-masonry bond strength is taken equal to 2.3 N/mm^2.

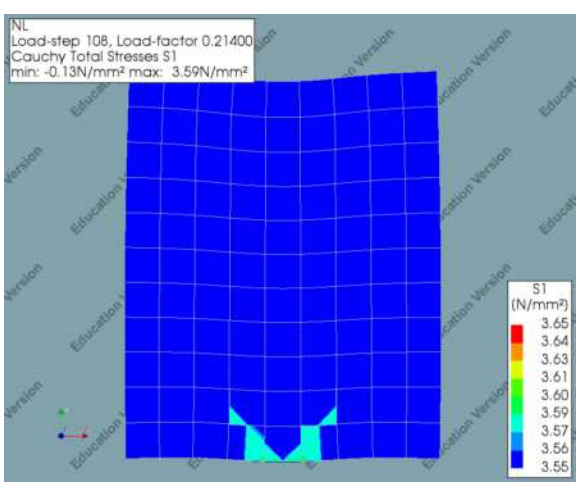

(a) Principle stresses front side SHCC overlay. Pre-compression = 1.0 Mpa. Full specimen pre-compressed.

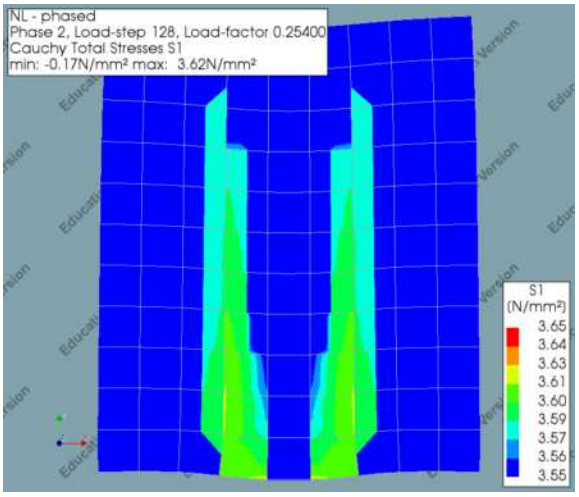

(b) Principle stresses front side SHCC overlay. Pre-compression = 1.0 Mpa. Only masonry triplet pre-compressed.

Figure 8.7: Principle stresses front side SHCC overlay, (a) Pre-compression applied to full retrofitted specimen, (b) Pre-compression only applied to masonry triplet (phased-analysis). Pre-compression equal to 1.0 Mpa.

In Figure (8.7) the values of the legend are specified to have a minimum equal to $3.55\,N/mm^2$ (blue). The maximum value depicted equals $3.65\,N/mm^2$ (red). The first cracking strength of the overlay material equals $3.58\,N/mm^2$. It is clearly shown that the method of application for the pre-compression highly influences the amount of tensile stresses to be present in the overlay. The experimental setup used in this research has negatively influenced the possibility of the overlay material to crack.

8.1.3. Influence material properties SHCC

In this experimental campaign a SHCC mixture with, compared to the literature, high first cracking strength is considered. With the help of the numerical analyses, it is concluded that this mixture only shows cracking if the bond strength between the SHCC and the masonry is sufficiently high.

For most of the numerical models considered no cracking of the overlay is present if the SHCC material is similar to the mixture used in this experimental campaign. The tensile stresses in the overlay do not reach the first cracking strength. Only if the bond strength between the masonry triplet and the overlay material is sufficient (e.g. $2.3\,N/mm^2$) cracks in the overlay can be expected. This is shown in Figure (8.8).

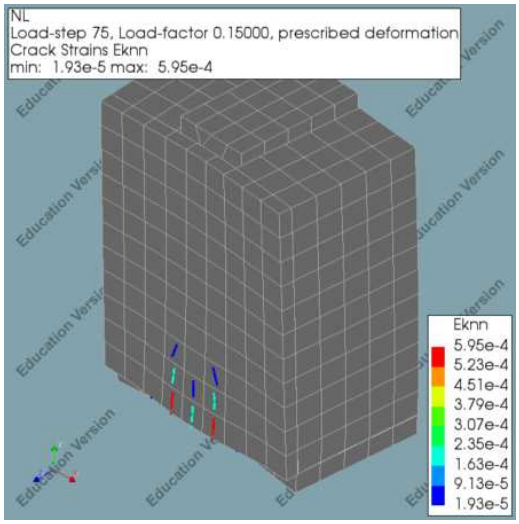

(a) Isometric view cracking strains SHCC overlay. No pre-compression applied. Overlay thickness = 10 mm. SHCC-masonry bond strength = 1.0 N/mm^2.

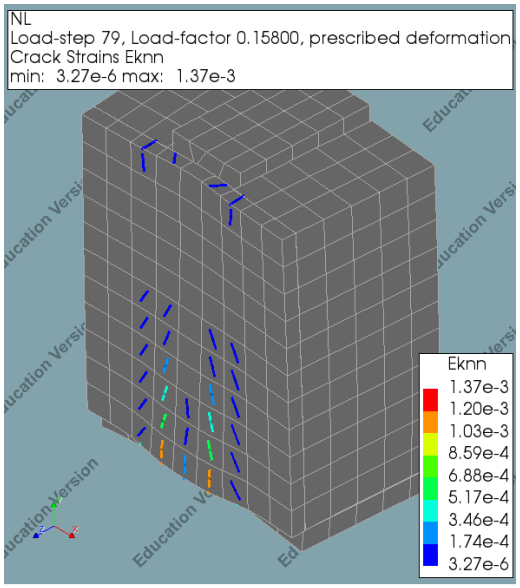

(b) Isometric view cracking strains SHCC overlay. No pre-compression applied. Overlay thickness = 10 mm. SHCC-masonry bond strength = 2.3 N/mm^2.

Figure 8.8: Cracking strains SHCC mixture used in this experimental campaign. No pre-compression applied to specimen.

However, comparing these results to similar results, taking into account the SHCC mixture from literature [6], more overlay material is activated. In Figure (8.9) the crack pattern in the SHCC overlay is shown. The influence of the tensile strength of the overlay material is shown by a comparison of these two figures. The mixture with the higher tensile strength (used in this research) shows fewer cracks in the overlay.

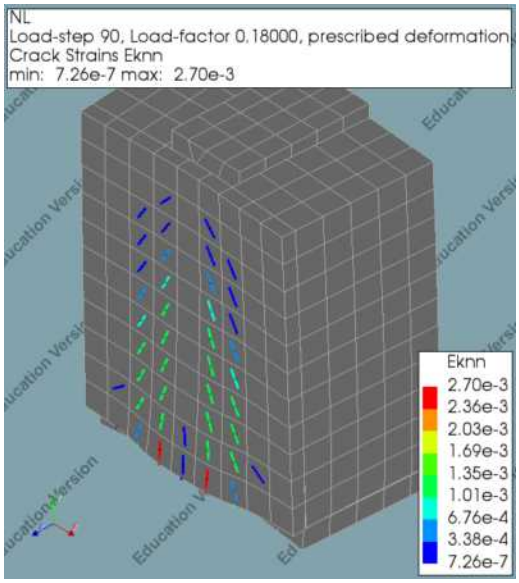

(a) Isometric view cracking strains SHCC overlay. No pre-compression applied. Overlay thickness = 10 mm. SHCC-masonry bond strength = 1.0 N/mm^2.

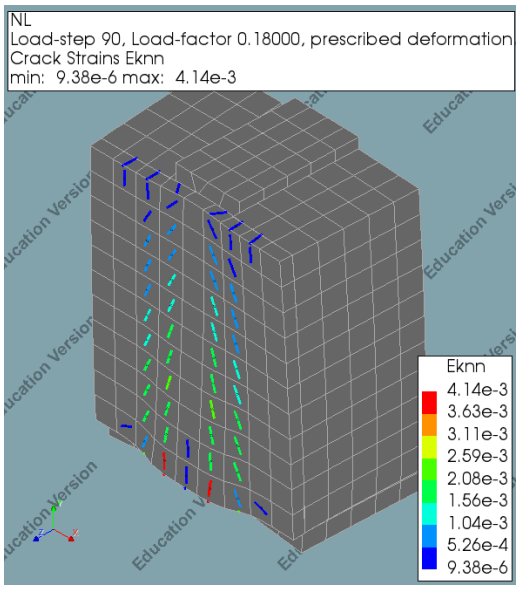

(b) Isometric view cracking strains SHCC overlay. No pre-compression applied. Overlay thickness = 10 mm. SHCC-masonry bond strength = 2.3 N/mm^2.

Figure 8.9: Cracking strains SHCC mixture used in [6]. No pre-compression applied to specimen.

8.1.4. Influence overlay thickness

With the help of the equation provided in [38] the critical thickness of the SHCC overlay can be determined. This equation is repeated below.

$$t_s \leq \frac{t_b \cdot \tau_b}{2 \cdot \tau_s} \tag{8.1}$$

This equation is governed by both the bond and shear strength of the SHCC overlay material. Assuming the bond strength between the SHCC and the masonry to be equal to the cohesion of the masonry substrate ($0.1892\,N/mm^2$), it is shown that this critical thickness approaches zero. Making use of this retrofitting approach impossible. If the same masonry material and surface preparations are considered, using a thinner overlay will therefore not result in the activation of the overlay material. This corresponds to the experimental results shown in this research.

This critical thickness is an artefact of the experimental campaign performed in [6]. It is shown with the numerical analyses that the proposed equations do hold. However, in the proposed equations, the applied pre-compression is not taken into account for the shear strength of the SHCC. The importance of the SHCC-masonry bond strength, SHCC material properties and the applied pre-compression are governing for the performance of the retrofitting approach considered.

8.2. Flexural strength retrofitted masonry beams

From the flexural tests, two distinct failure modes are observed. Most of the specimen failed by debonding of the masonry units. The debonding of the masonry units is governed by the interfacial bond strength between the SHCC overlay and the masonry substrate.

From the shear tests, it is concluded that low bond strength at the SHCC-masonry interface is present for the specimen investigated. The numerical models analysed correspond to the experimental results, if low bond strength is considered. Both the masonry triplets and the masonry beams are built and prepared with the same materials, therefore, this low bond strength is assumed to be present for the retrofitted beam specimen as well.

Only two specimens displayed flexural failure. The force-displacement curves are shown in Figure (8.10). The retrofitted masonry beam with the 30 mm thick overlay shows an increased flexural strength. However, a sharp decrease in strength is also present for this specimen. This indicates that, just as for the masonry triplets, a thinner overlay is beneficial for ductile failure.

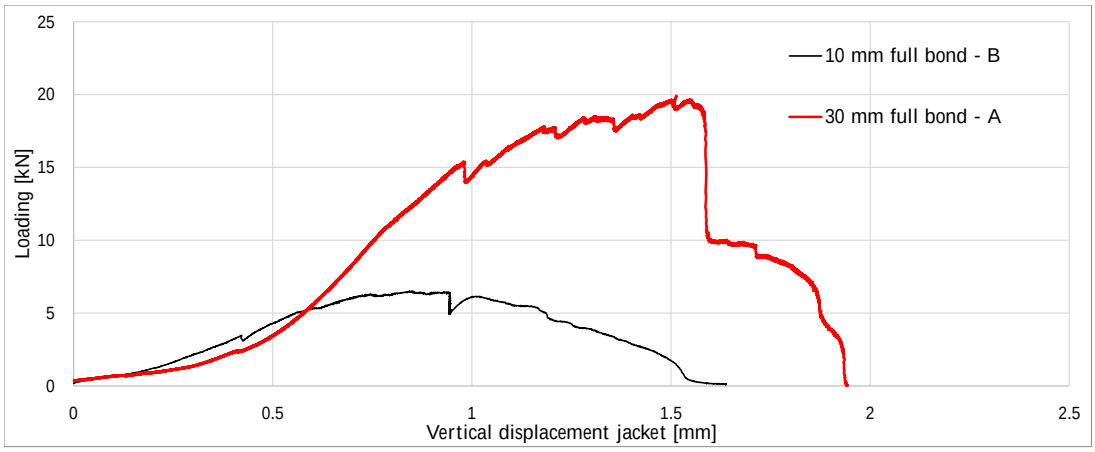

Figure 8.10: Force-displacement curve flexural tests. Both specimen failed in flexural failure. Black = retrofitted masonry specimen with 10 mm full bonded overlay. Red = retrofitted masonry specimen with 30 mm full bonded overlay.

The interfacial bond strength, between the SHCC and the masonry substrate, is determined analytically. For this analytical calculation the DIC results are analysed further. By means of the following equation the shear bond strength of the SHCC-masonry interface is derived.

$$\tau = \frac{V \cdot ES}{b \cdot EI} \tag{8.2}$$

The loading at peak resistance is taken into account via V. This is equal to half the total resistance. The shear stresses are determined at the SHCC-masonry interface. The width of the masonry beams is accounted for via the parameter b. This is equal to 210 mm. The bending stiffness of the total retrofitted masonry beam is considered EI. For these calculations it is assumed all of the failure is governed by the loss of strength at the SHCC-masonry interface. This is a rough estimate, since not all of these eight specimen failed by pure debonding of the overlay. The DIC results, at peak resistance, are shown in Appendix F.

Table 8.1: Analytical results shear bond strength flexural strength.

Specimen nr.	Overlay thickness [mm]	Bonding	Curing	Peak resistance [kN]	Bond strength [N/mm^2]
4	10	Full bond	Sealed	7.37	0.17
8	10	Debonded	Sealed	6.55	0.15
12	10	Full bond	Non-sealed	8.63	0.20
7	30	Full bond	Sealed	12.32	0.33
10	30	Debonded	Sealed	8.46	0.23
11	30	Debonded	Sealed	6.58	0.18
13	30	Full bond	Non-sealed	10.29	0.27
	Average				**0.22**

From the analytical calculations it is concluded that the bond strength between the SHCC overlay and the masonry substrate is similar to the cohesion of the masonry material, i.e. 0.22 N/mm^2. This magnitude corresponds to the cohesion of the masonry material. It is concluded that also the flexural strength of the retrofitted masonry material is governed by the low interfacial bond strength between the two materials.

8.3. Numerical models considered

In this research two seperate numerical investigations are performed. For the first analyses the combined shearing-cracking-crushing interface model is used for both the unit-unit and the SHCC-masonry interfaces. For the additional numerical analyses a different structural interface is considered for the SHCC-masonry interface, i.e. the Coulomb friction model. For both models similar numerical quantities for both the cohesion, friction angle, and dilatancy angle are taken into account (i.e. 0.1892 N/mm^2, 0.647 rad, and 0.647 rad, respectively).

A comparison of the two models is done in terms of the resulting force-displacement curves, see Figure (8.11). It is shown that the models using a Coulomb friction model for the SHCC-masonry interface underestimates the shear force resistance. A brittle gapping behaviour is assumed for this model. Because of this assumed interface model, no intermediate (and residual) yield surfaces are present for this interface. The resistance of an interface element is reduced to zero if it has reached the yield strength. This result in a quicker decay of strength.

Additionally, using this interface model allows for converging solutions for all levels of pre-compression. This is not possible if the combined shearing-cracking-crushing interface model is considered.

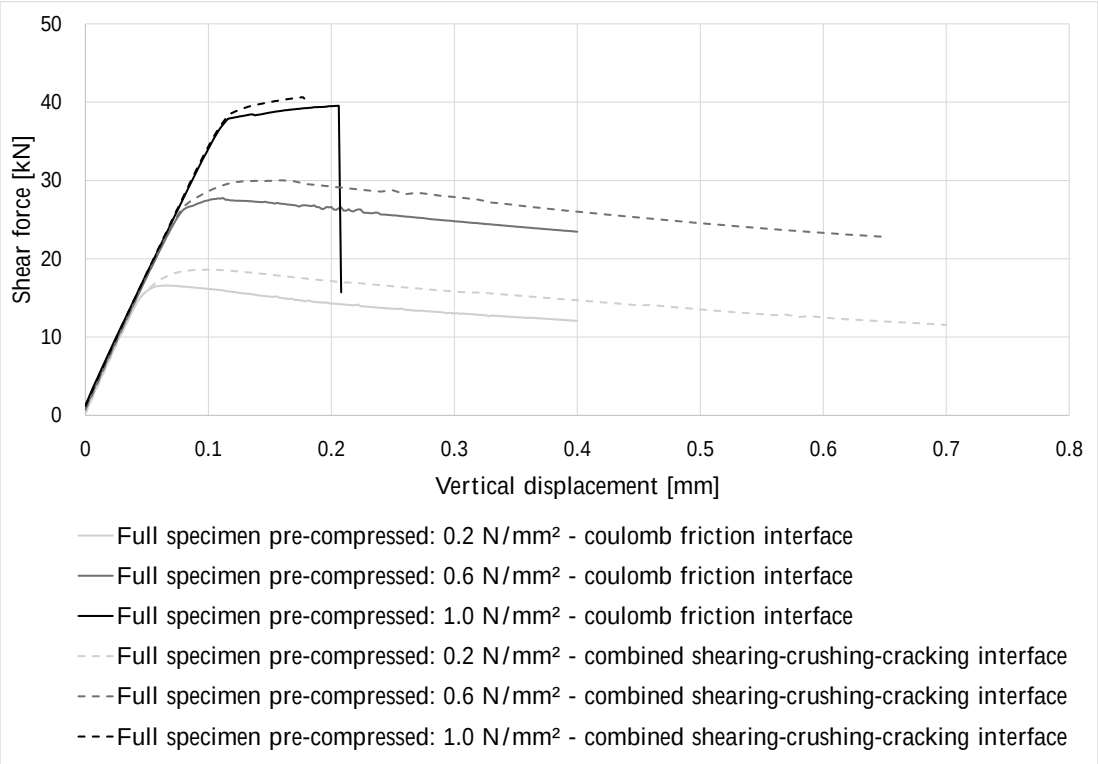

Figure 8.11: Force-displacement curves numerical models considered. Solid curves = Coulomb friction model, dotted = combined interfaces. Cohesion SHCC-masonry interface = $0.1892\,N/mm^2$.

The results shown in Figure (8.11) correspond to the numerical models for which the cohesion of the SHCC-masonry interface is taken equal to $0.1892\,N/mm^2$. Analysing higher values for this quantity is not possible if the combined interface model is considered at the SHCC-masonry interface, see Figure (8.12). The peak resistance is underestimated if high levels of pre-compression are applied to the full retrofitted specimen.

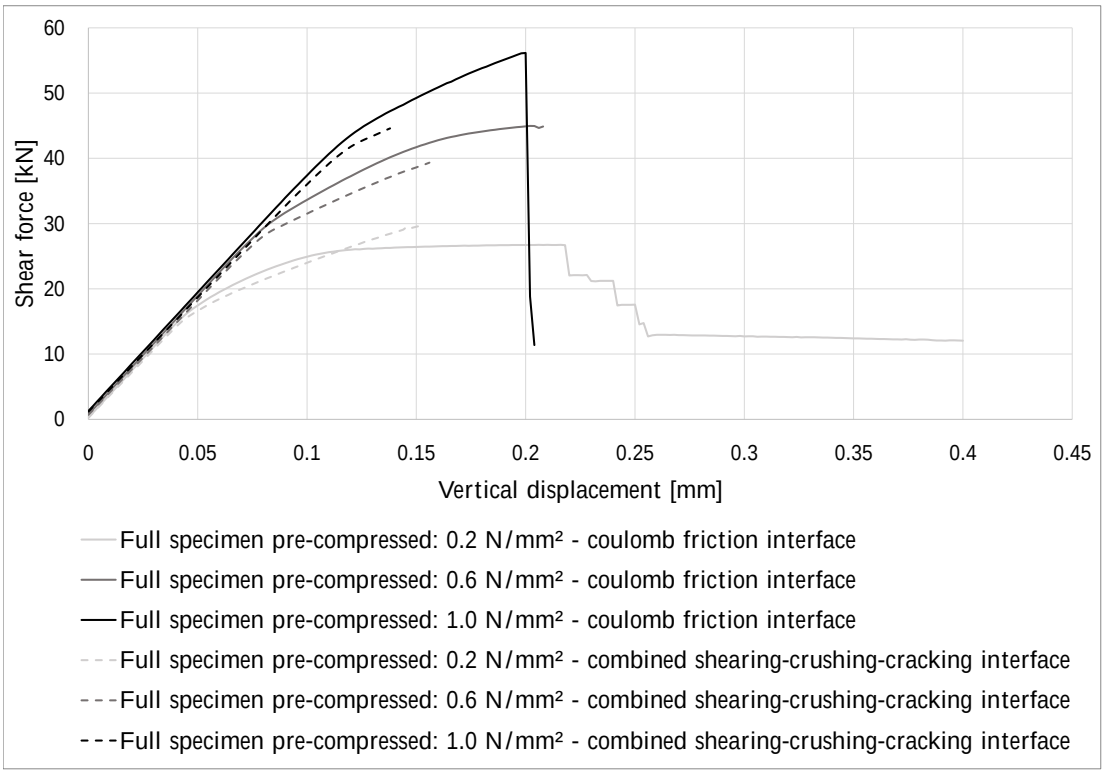

Figure 8.12: Force-displacement curves numerical models considered. Solid curves = Coulomb friction model, dotted = combined interfaces. Cohesion SHCC-masonry interface = 2.30 N/mm^2.

In conclusion, the inially used numerical model, with the combined interface model for both the unit-unit and SHCC-masonry interfaces, showed satisfying results for low strength interfaces. Because of the applied pre-compression, the shear strength of the unit-unit interfaces increased, causing it to fail after the SHCC-masonry interface. Softening of these unit-unit interfaces is governing for the post-peak behaviour, corresponding to the experimental results. Using this interface model, for the interface between the overlay and the masonry substrate, provides satisfying results if low strength interfaces are present. The Coulomb friction model is required if greater magnitudes for the shear bond strength of the SHCC-masonry interface is present. With the help of this latter numerical model the experimental results of literature are reproduced effectively.

9

Conclusions and Recommendations

In this final chapter of the report, a short overview of the considered research method is provided. The research question is answered. Additionally, recommendations are given for future research.

9.1. Conclusions

The main goal of this research is to investigate the material behaviour of unreinforced clay masonry, retrofitted with a single-sided SHCC overlay. The applied overlay must introduce additional strength and ductility to the masonry substrate.

With the help of experimental tests, the material properties of the retrofitted masonry material are investigated. Small scale experiments are performed to determine both in-plane and out-of-plane material characteristics of the retrofitted masonry. Additional experiments and numerical analyses resulted in the identification of several parameters influencing this retrofitting procedure. Conclusions to the research question, as stated in paragraph 1.3, are summarised below.

9.1.1. Material behaviour retrofitted masonry

From the experimental and numerical results, it is concluded that the application of a single-sided overlay can increase both the strength and ductility. The performance of the overlay is related to the material properties of this overlay and its bonding properties to the masonry substrate. In this experimental campaign, low bond strength, between the retrofitting material and the masonry, resulted in negligible strength improvements under shear loading conditions. The applied overlay did result in higher capacities for the out-of-plane flexural tests. However, also for these specimen, the low bond strength between the SHCC and the masonry, resulted in unfavourable failure mechanisms.

From the numerical models, it is concluded that an improved bond, between the SHCC and the masonry, will result in higher strength (and ductility) for the retrofitted material under shear loading conditions. Not verified by the numerical model is the flexural strength of the retrofitted masonry beams. With DIC, it is concluded that the flexural tests are governed by the debonding of the masonry units from the overlay material. It is assumed that an increased bond strength with the overlay will also improve the flexural strength of the retrofitted masonry.

The used experimental setup for the shear strength tests does not correspond to the literature (and actual structures). The applied pre-compression, required for an accurate representation of the masonry material under shear loading conditions, resulted in high compressive stresses in the overlay material, reducing the possibility for the SHCC to be activated through cracking. A more realistic loading condition is considered via phased numerical analyses. In these analyses, only the masonry substrate is pre-compressed. Initially, no stresses are present in the overlay. Still, even under these more realistic loading conditions, no cracking of the SHCC is activated. With the help of the numerical analyses it is shown that even without this pre-compression, the applied overlay will not crack under shear loading conditions, because the first cracking strength of the

SHCC mixture considered is too high and the bond strength with the masonry substrate is too weak.

In this research a SHCC mixture with a first cracking strength equal to $3.58\,N/mm^2$ is considered. Because of the low interfacial bond strength, between the overlay and the masonry, this magnitude of tensile stresses is not obtained in the SHCC. It is shown with the numerical analyses that a mixture with lower first cracking strength will result in the activation of cracks, even at lower interfacial bond strengths.

The thickness of the retrofitting overlay will determine the final failure mechanism of the retrofitted specimen. A thicker overlay results in more brittle behaviour. Debonding of the overlay is governing. However, still, a sufficient bond strength is required between the overlay and the masonry to ensure an increase in shear resistance. Finally, for the retrofitted triplet tests, the eccentric loading of both the applied pre-compression and the shear loading did not influence the experimental results.

In short, the experimental results obtained are not corresponding to the mentioned references. With numerical simulations, the shear tests are modelled, and several parameters are investigated. It is shown that the following parameters will influence the cracking behaviour of the SHCC overlay: SHCC-masonry bond strength, SHCC tensile strength, and the application of pre-compression. The former two are governing for the activation of the retrofitting overlay. The out-of-plane flexural strength of the retrofitted masonry beams is improved, but higher capacities can be obtained with a stronger interface between the SHCC and the masonry substrate. Finally, the simplified micro-modelling approach adopted in this research showed to be able to determine the global behaviour of the retrofitted masonry triplets. Requirements of the material properties can be determined based on this modelling procedure.

9.2. Recommendations and future work

The experimental results of both the initial and additional experimental campaign form the basis for the recommendations and future work. Additionally, thoughts are given on follow-up projects for which this report forms the initial starting point.

- **Perform numerical analyses before experimental campaign**

  It is shown that the simplified micro-modelling approach provides satisfying results for both the plain and the retrofitted masonry triplets. With the help of these numerical analyses, the required material properties can be estimated before performing any experiments.

- **Development of new SHCC mixture**

  The material properties of the considered SHCC mixture must be investigated and adjusted accordingly. For practical retrofitting purposes, the mixture must be applied to vertical surfaces. This is not possible with the current mixture. A sprayable version will be optimal.

- **Investigation surface preparation masonry substrate**

  It is shown in the literature that the moisture content of the masonry material is of high importance for the bond strength with the overlay material. In this experimental campaign, wet cloths are used to pre-wet the masonry material. However, in this manner, the moisture content of the masonry is uncertain. It is thought to be beneficial to investigate the importance of this moisture content of the masonry substrate and determine the possible influences on the retrofitting approach considered.

- **Using DIC during experiments**

  During this research, the usage of DIC is showed to be highly effective. The failure mechanisms of the specimen analysed can be investigated in great detail. Additionally, since the DIC does not require to be connected to the specimen, no influences of the measurement device are to be expected.

Bibliography

[1] D. Addessi, S. Marfia, E. Sacco, and J. Toti. Modeling Approaches for Masonry Structures. Technical report, 2014.

[2] C. J. Adendorff, W. P. Boshoff, and G. P.A.G. Van Zijl. Characterisation of crack distribution of strain-hardening cement composites (SHCC) under imposed strain. *Advances in Cement-Based Materials - Proceedings of the International Conference on Advanced Concrete Materials*, (May):215–221, 2010. doi: 10.1201/b10162-32.

[3] G. Andreotti, F. Graziotti, and G. Magenes. Detailed micro-modelling of the direct shear tests of brick masonry specimens: The role of dilatancy. *Engineering Structures*, 168:929–949, 2018. ISSN 18737323. doi: 10.1016/j.engstruct.2018.05.019.

[4] Thi-Loan Bui, Xuan-huy Nguyen, and A. Si Larbi. Proceedings of the 4th Congrès International de Géotechnique - Ouvrages -Structures. *Cement and Concrete Research*, 7(3):1–7, 2016. ISSN 00088846. doi: 10.1007/978-981-10-6713-6. URL http://xypex.co.th/assets/test{_}reports/carbonation/carbonation{_}McGrathPF.pdf{%}0Ahttp://dx.doi.org/10.1016/j.jnucmat.2012.12.030{%}0Ahttp://dx.doi.org/10.1016/j.jnucmat.2014.01.015{%}0Ahttp://dx.doi.org/10.1016/j.clay.2012.09.023{%}0Ahttp://dx.doi.org/10.1016/j.m.

[5] Paolo Caporossi, Paolo Mazzanti, and Francesca Bozzano. Digital image correlation (DIC) analysis of the 3 December 2013 Montescaglioso landslide (Basilicata, southern Italy): Results from a multi-dataset investigation. *ISPRS International Journal of Geo-Information*, 7(9), 2018. ISSN 22209964. doi: 10.3390/ijgi7090372.

[6] L. de Beer and G. P.A.G. van Zijl. SHCC OVERLAY AS RETROFITTING STRATEGY FOR LOAD-BEARING MASONRY SEISMIC RESISTANCE. Technical report, 2016.

[7] D. J.A. de Jager and G. P.A.G. van Zijl. Computational Assessment of SHCC overlay Retrofitting of Unreinforced Load Bearing Masonry for Seismic Resistance. Technical report, 2018.

[8] D. J.A. de Jager and G. P.A.G. van Zijl. Improved Ductility of SHCC Retrofitted Unreinforced Load Bearing Masonry Seismic Resistance. Technical report, 2018.

[9] A. Dehghani, G. Fischer, and F. Nateghi-Alahi. Structural behaviour of small scale masonry elements strengthened with engineered cementitious composites. Technical report, 2015.

[10] DIANA FEA. DIANA User's manual, version 10.3, 2019.

[11] Mohamed A Elgawady and Pierino Lestuzzi. A review of conventional seismic retrofitting techniques for URM. *13th International Brick and Block Masonry Conference*, pages 1–10, 2004. URL http://imacwww.epfl.ch/GenieParasismique/EDOC{_}ST09/Course{_}6/old/89ElGA13-IBMaCstateoftheart.pdf.

[12] Mohamed A Elgawady, P Lestuzzi, and M Badoux. A review of retrofitting of unreinforced masonry walls using composites. *Proc., 4th International Conf. ...*, (July):1–8, 2004. URL http://www.researchgate.net/publication/37447218{_}A{_}Review{_}of{_}Retrofitting{_}of{_}URM{_}Walls{_}Using{_}Composites/file/60b7d51a2e3409523f.pdf.

[13] Mohamed A Elgawady, P Lestuzzi, and M Badoux. Seismic behavior of URM walls retrofitted using Shotcrete. *2006 NZSEE Conference*, (November 2016), 2006.

[14] E. Esmaeeli, E. Manning, and J. A.O. Barros. Strain hardening fibre reinforced cement composites for the flexural strengthening of masonry elements of ancient structures. Technical report, 2013.

[15] R. Esposito, S. Jafari, G.J.P. Ravenshorst, H.R. Schipper, and J. G. Rots. Influence of the behavior of calcium silicate brick and element masonry on the lateral capacity of structures. *10th Australasian Masonry Conference*, 2018.

[16] F. Ferretti, C. Mazzotti, R. Esposito, and J. G. Rots. Shear-sliding behaviour of Masonry, Numerical micromodeling of Triplet Tests. Technical report, 2018.

[17] F. Graziotti, U. Tomassetti, A. Rossi, S. Kallioras, M. Mandirola, E. Cenja, A. Penna, and G. Magenes. Experimental campaign on cavity walls systems representative of the Groningen building stock. Technical report, 2015.

[18] F. Graziotti, U. Tomassetti, S. Kallioras, A. Penna, and G. Magenes. Shaking table test on a full scale URM cavity wall building. Technical report, 2017.

[19] F. Graziotti, A. Penna, and G. Magenes. A comprehensive in situ and laboratory testing programme supporting seismic risk analysis of URM buildings subjected to induced earthquakes, 2018.

[20] Alper Ilki, Medine Ispir, Fundagul As, Cem Demir, and Nahit Kumbasar. Frp Retrofit of Walls Constructed With Historical Bricks. *Challenges for Civil Construction*, (May 2014), 2008.

[21] T. Kamada and V.C. Li. The effects of surface preparation on the fracture behaviour of ECC/concrete repair system. Technical report, 2000.

[22] Y. M. Lim and V. C. Li. Durable repair of aged infrastructure using trapping mechanism of engineered cementitious composites. Technical report, 1997.

[23] Paulo B Lourenço. *Computational strategies for masonry structures*, volume 70. 1996. ISBN 9040712212. doi: ISBN90-407-1221-2. URL `http://www.narcis.nl/publication/RecordID/oai:tudelft.nl:uuid:4f5a2c6c-d5b7-4043-9d06-8c0b7b9f1f6f`.

[24] Paulo B Lourenço and J. G. Rots. Multisurface Interface Model for Analysis of Masorny Structures. Technical report, 1997.

[25] M. Lukovic and Prof.dr.ir. Hordijk D.A. Literature review on new concrete types; A start on exploring their opportunities for Dutch infrastructure. Technical report, 2017.

[26] F. Messali, R. Esposito, S. Jafari, G. Ravenshorst, P. Korswagen Eguren, and J. G. Rots. A multiscale experimental characterisation of Dutch unreinforced masonry buildings. Technical report, 2018.

[27] J. G. Rots, F. Messali, R. Esposito, S. Jafari, and V. Mariani. Computational Modelling of Masonry with a view to Groningen Induced Seismicity. Technical report, 2016.

[28] S. Sharma, U. Tomassetti, L. Grottoli, and F. Graziotti. OUT-OF-PLANE TWO-WAY BENDING SHAKING TABLE TESTS ON SINGLE LEAF AND CAVITY WALLS. Technical report, 2018.

[29] Ming Hsiang Shih and Wen Pei Sung. Application of digital image correlation method for analysing crack variation of reinforced concrete beams. *Sadhana - Academy Proceedings in Engineering Sciences*, 38(4): 723–741, 2013. ISSN 02562499. doi: 10.1007/s12046-013-0141-5.

[30] U. Tomassetti, A.A. Correia, F. Graziotti, A. I. Marques, M. Mandirola, and P. X. Candeias. COLLAPSE SHAKING TABLE TEST ON A URM CAVITY WALL STRUCTURE REPRESENTATIVE OF A DUTCH TERRACED HOUSE. Technical report, 2017.

[31] Ö. S. Türkmen, B. T. De Vries, S. N. M. Wijte, and A. T. Vermeltfoort. Quasi-static cyclic in-plane testing of masonry walls strengthened with a single-sided fabric-reinforced cementitious matrix overlay and flexible anchorage. *Journal of Building Pathology and Rehabilitation*, 4(1), 2019. ISSN 2365-3159. doi: 10.1007/s41024-019-0043-y. URL `https://doi.org/10.1007/s41024-019-0043-y`.

[32] K. van Breugel, C. R. Braam, C. Van der Veen, and J. Walraven. Concrete Structures under Imposed Thermal and Shrinkage Deformations - Theory and Practice. 2016.

[33] R. van der Pluijm. *Out-Of-Plane Bending of Masonry - Behaviour and Strength*. PhD thesis, 1999.

[34] K. Van Thienen-Visser and J. N. Breunese. Induced seismicity of the Groningen gas field: History and recent developments. *Leading Edge*, 34(6):664–671, 2015. ISSN 19383789. doi: 10.1190/tle34060664.1.

[35] G. P.A.G. van Zijl. Modeling masonry shear-compression: Role of dilatancy highlighted. *Journal of Engineering Mechanics*, 130(11):1289–1296, 2004. ISSN 07339399. doi: 10.1061/(ASCE)0733-9399(2004)130:11(1289).

[36] G. P.A.G. van Zijl. Improved mechanical performance: Shear behaviour of strain-hardening cement-based composites (SHCC). *Cement and Concrete Research*, 37(8):1241–1247, 2007. ISSN 00088846. doi: 10.1016/j.cemconres.2007.04.009.

[37] G. P.A.G. van Zijl and L. de Beer. An SHCC Overlay Retrofitting Strategy for Unreinforced Load Bearing Masonry. Technical report.

[38] G. P.A.G. van Zijl and L. de Beer. Sprayed Strain-Hardening cement-based composite overlay by shear strengthening of unreinforced load-bearing masonry. Technical report, 2018.

[39] G. P.A.G. van Zijl and D. J.A. de Jager. Improved ductility of SHCC retrofitted Unreinforced Load Bearing Masonry via a strip-debonded approach. Technical report, 2019.

[40] En Hua Yang, Shuxin Wang, Yingzi Yang, and Victor C. Li. Fiber-bridging constitutive law of engineered cementitious composites. *Journal of Advanced Concrete Technology*, 6(1):181–193, 2008. ISSN 13468014. doi: 10.3151/jact.6.181.

[41] J. Zhou, S. Qian, M. G.S. Beltran, G. Ye, K. van Breugel, and V. C. Li. Development of engineering cementitious composited with limestone powder and blast furnace slag. Technical report, 2010.

[42] Jian Zhou. *Performance of Engineered Cementitious Composites for Concrete Repairs*. 2011. ISBN 9789090259505.

A

Compressional strength SHCC mixture used

In this Appendix the experimental results of the compressional strength of the SHCC mixture used is summarized. The results of all individual specimen are provided. Uniaxial compression tests are performed on SHCC cubes (40x40x40 mm). Additionally, the averaged result, and the corresponding coefficient of variation, are shown.

Table A.1: Experimental results compressional strength SHCC mixture.

Specimen nr.	Compressional Strength	Unit
1	38.7	N/mm^2
2	31.4	N/mm^2
3	47.4	N/mm^2
4	46.6	N/mm^2
5	33.7	N/mm^2
6	43.4	N/mm^2
7	39.1	N/mm^2
8	40.8	N/mm^2
9	34.3	N/mm^2
10	36.1	N/mm^2
11	36.3	N/mm^2
12	34.4	N/mm^2
Average:	38.5 (0.128)	N/mm^2

B

Failure mechanisms non-retrofitted clay masonry triplets

In this Appendix the different failure mechanisms observed in the non-retrofitted masonry triplets are discussed. By means of digital image correlation better understanding into the development of localized failure patterns is achieved.

Linking the fast amount of photos to the corresponding force-displacement curve of the investigated masonry specimen is of high importance. This is done with great care, since any deviation might lead to misleading results.

Not all photos taken by the camera are used in this analysis. The experiments are performed in a displacement controlled manner with a loading rate equal to 0.005 mm/s. Using all pictures, keep in mind that a picture is taken every five seconds, will result in a lot of data with comparable results. Most of the experiments used up to 700 pictures. Using every 10^{th} picture seemed to be sufficient. Additionally, the used software (GOM Correlate) is computationally demanding, making the use of all the photos nearly impossible.

In the figures below the force-displacement curves of the three plain masonry triplets analyses are shown. Points of interest are selected from these f-u curves and the corresponding (analysed) DIC picture is linked. The analysed surface components of GOM Correlate are plotted for these different points of interest. The equivalent Mises strains are shown. As mentioned in section 3.4.3, this quantity provides the best results with respect to the introduction of cracks.

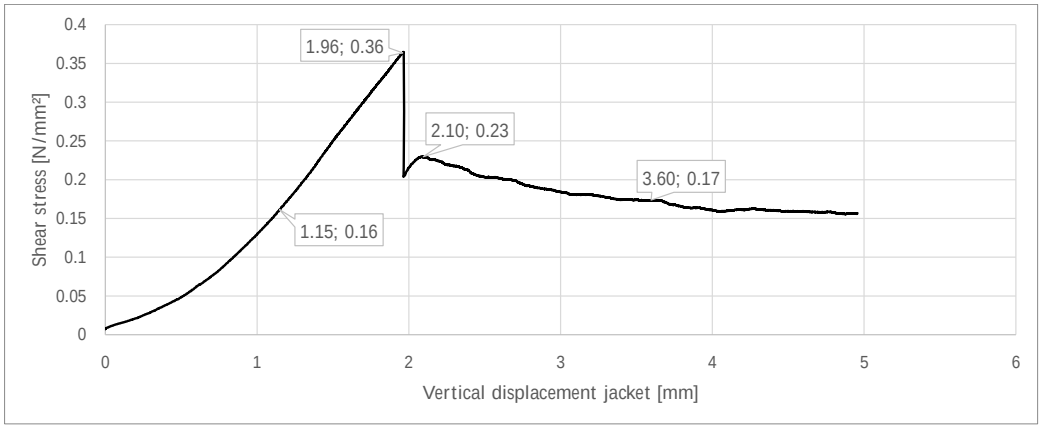

(a) Stress-displacement curve (non-retrofitted) masonry triplet.

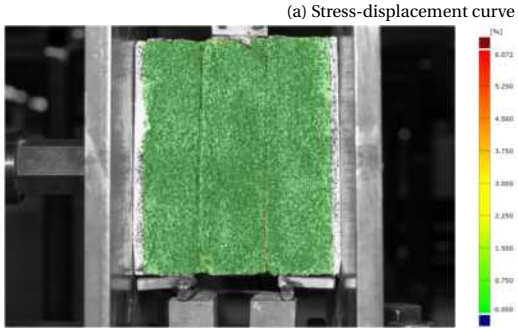

(b) First point of interest, pre-peak (A).

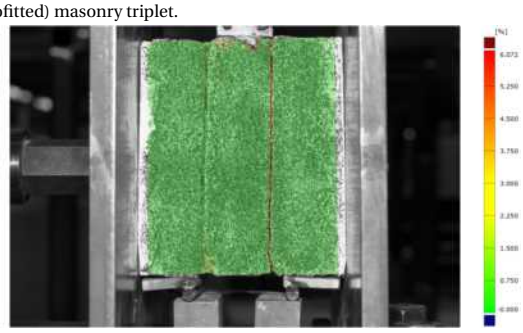

(c) Second point of interest, peak resistance (B).

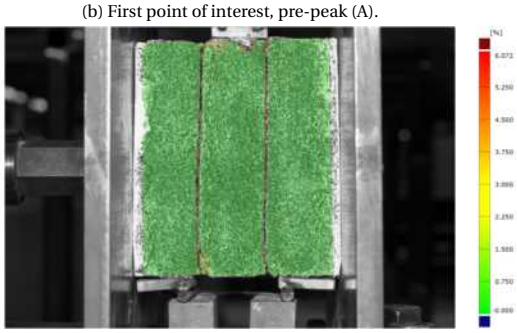

(d) Third Point of interest, post-peak (C).

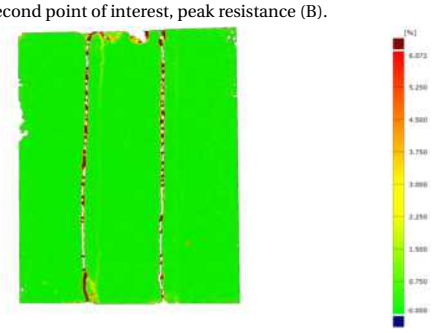

(e) Fourth point of interest, post-peak (D).

Figure B.1: Mises equivalent strains pre- and post-peak. Pre-compression equal to 0.2 N/mm^2.

In the figure above the shear stresses in the mortar-unit interface are plotted against the vertical displacement of the jacket for the lowest pre-compression level, 0.2 Mpa. The first point of interest, located in the linear elastic regime of the specimen, allready shows the initiating of failure at the interface between the bottom right hand side of the central unit and the connecting mortar joint. Thus, a non-symmetrical failure pattern is allready observerd. At peak resistance, Figure (B.1b), this initiated failure in the right hand side unit-mortar interface is progressed up to the total height of the specimen. As shown in the force-displacement curve, this initiated a sharp decrease in resistance. Also, in the same force-displacement curve, a second peak in resistance is depicted, located just after the first (main) peak. This second peak is related to the failure of the left unit-mortar interface, see Figure (B.1c). In the post-peak regime vertical relative displacements of the central masonry unit are governing.

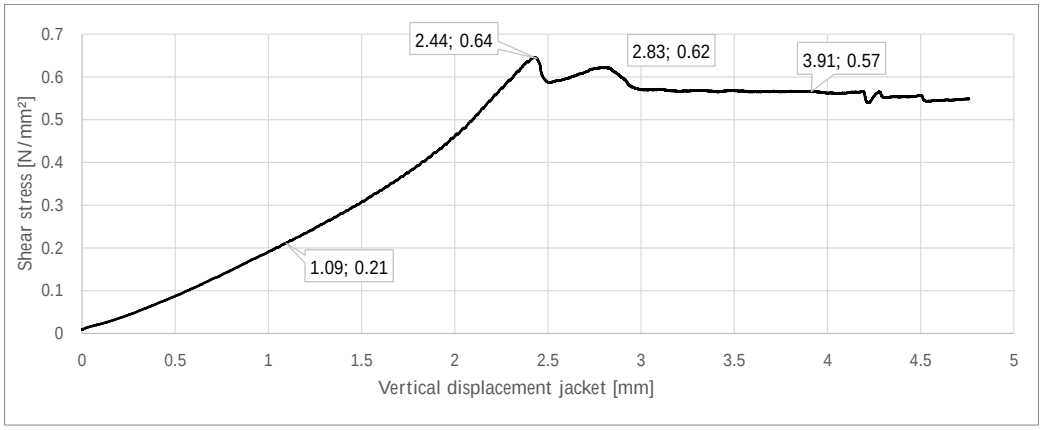

(a) Stress-displacement curve (non-retrofitted) masonry triplet.

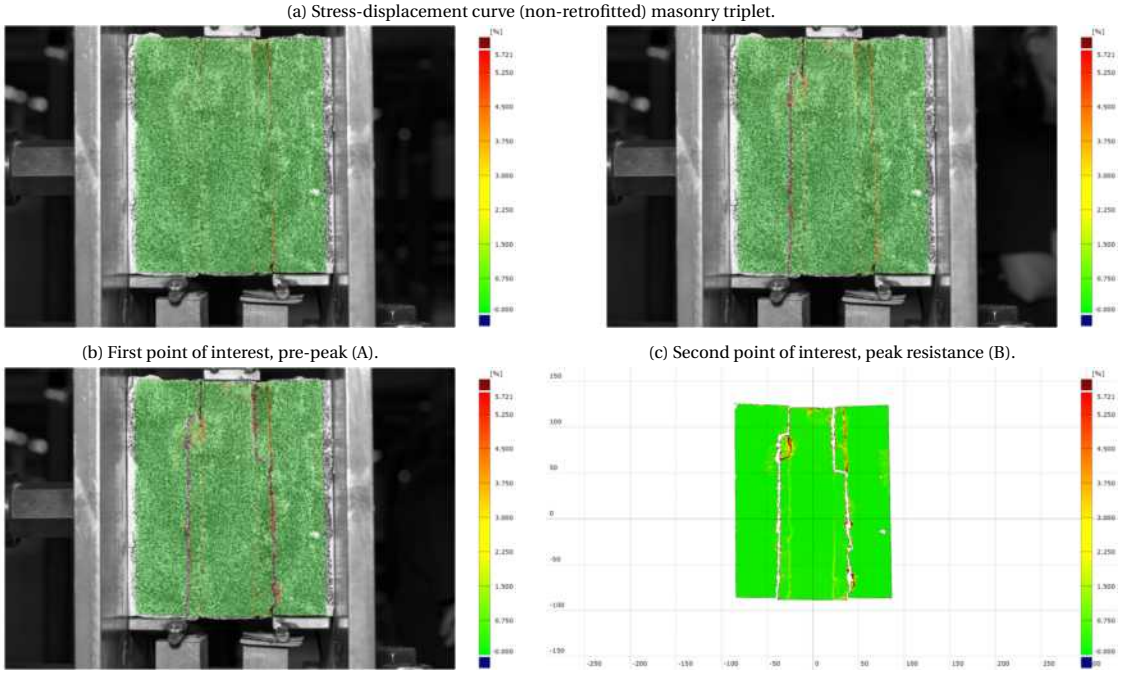

(b) First point of interest, pre-peak (A).

(c) Second point of interest, peak resistance (B).

(d) Third Point of interest, post-peak (C).

(e) Fourth point of interest, post-peak (D).

Figure B.2: Mises equivalent strains pre- and post-peak. Pre-compression equal to $0.6\,N/mm^2$.

For the specimen tested with a pre-compression level equal to $0.6\,N/mm^2$ this non-symmetric type of failure is also governing. Again, the failure is initiated at the bottom right unit-mortar interface. However, the highest strains are present at the interface between the right mortar joint and the right masonry unit, instead of the central unit. At peak loading the main stress concentrations are shifted from the mortar joint located on the right side of the specimen towards the interfaces located left of the central unit. Additionally, failure of the left mortar joints itself is noticed. This is shown by the high level of strains in the left mortar joint itself. Just as for the lower pre-compression level a second peak is present in the force-displacement curve, corresponding to the failure of the second mortar-unit interface, see Figure (B.2d). At the top of the specimen the mortar-unit interface, between the mortar joints and the central unit, failed. This is different compared to the lower level of pre-compression. In the case of this lower pre-compression the failure of the interfaces remained on one side of the mortar joints, as is shown in Figure (B.1).

As for the intermediate pre-compression level ($0.6\,N/mm^2$) failure of the unit-mortar interface on both sides of the mortar joint is present for a pre-compression level equal to $1.0\,N/mm^2$. Failure is initiated at the left mortar joint, see Figures (B.3b) and (B.3c). Different to the other two pre-compression levels, no second peak is shown in the force-displacement curve. However, just after the peak resistance has been reached the interfaces

of the right mortar joint fail. Similarly to the previously discussed results, failure of the mortar material itself is observed for this level of pre-compression.

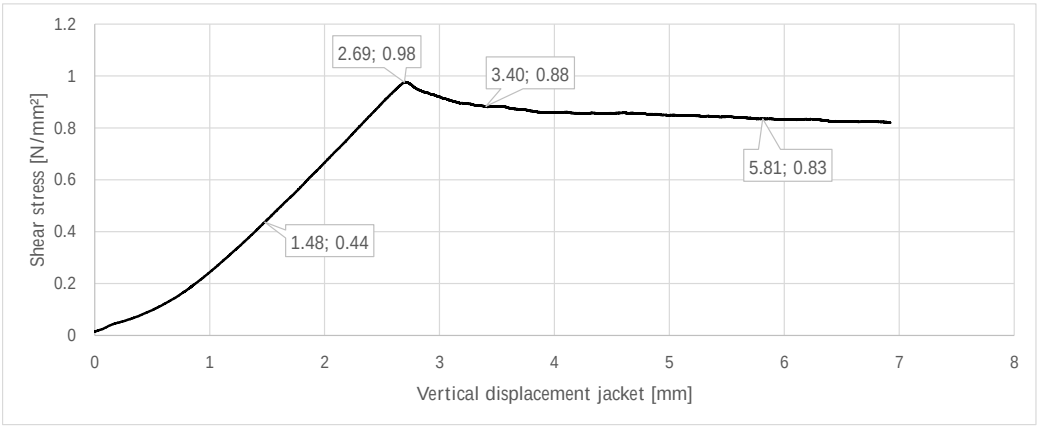

(a) Stress-displacement curve (non-retrofitted) masonry triplet.

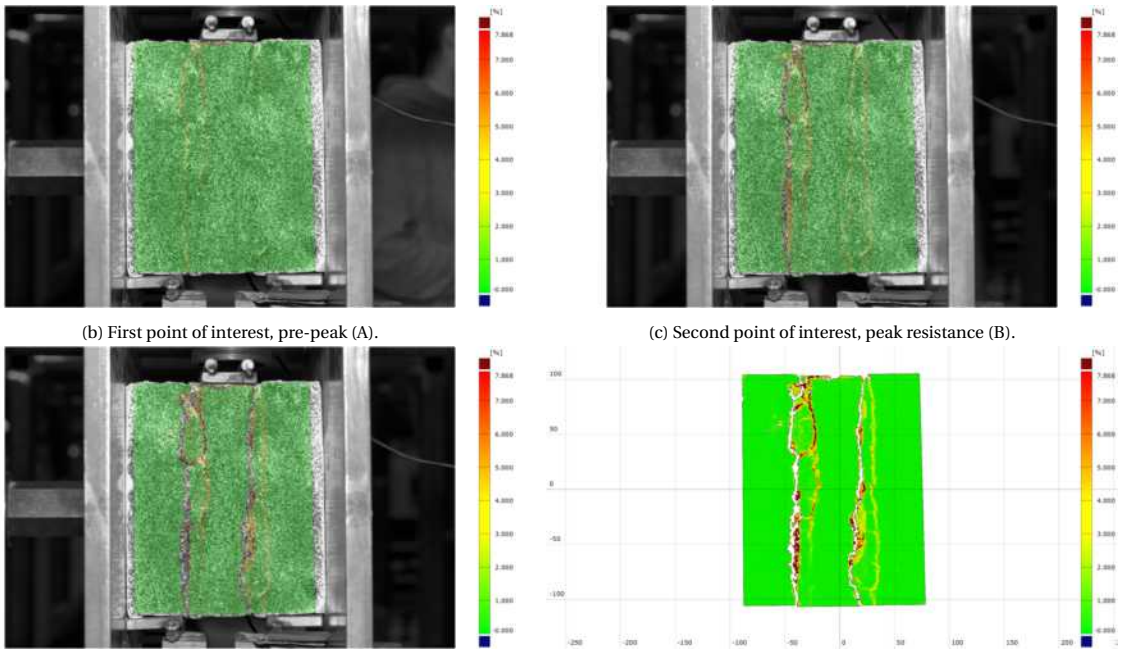

(b) First point of interest, pre-peak (A).

(c) Second point of interest, peak resistance (B).

(d) Third point of interest, post-peak (C).

(e) Fourth point of interest, post-peak (D).

Figure B.3: Mises equivalent strains pre- and post-peak. Pre-compression equal to 1.0 N/mm^2.

Below some additional figures are presented using a different type of representation of the same results, as shown above. For all the three different pre-compression levels the analysed pictures corresponding to the first two loadsteps are depicted. The surface of interest (displaying the strains) is visualized in a rotated position. The front of the masonry specimen is facing towards the right side of this report (rotation equal to 45°). Via these additional figures the initiation of failure becomes more clear.

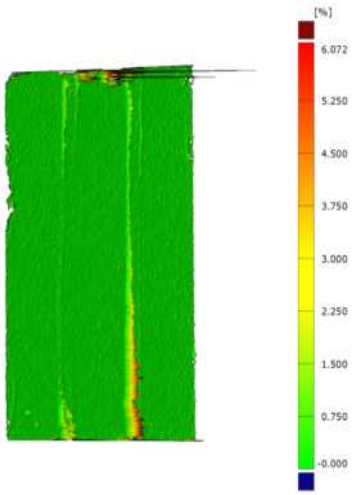

(a) Exaggerated display of strains, linear elastic stage loadstep (A). Pre-compression level = 0.2 N/mm^2.

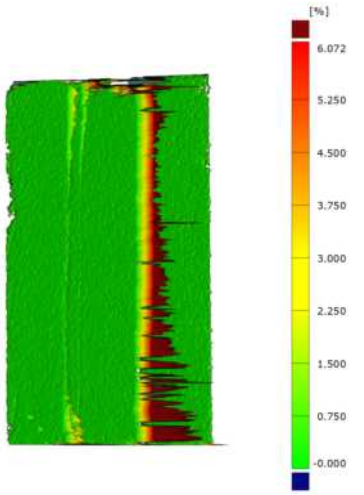

(b) Exaggerated display of strains, peak resistance loadstep (B). Pre-compression level = 0.2 N/mm^2.

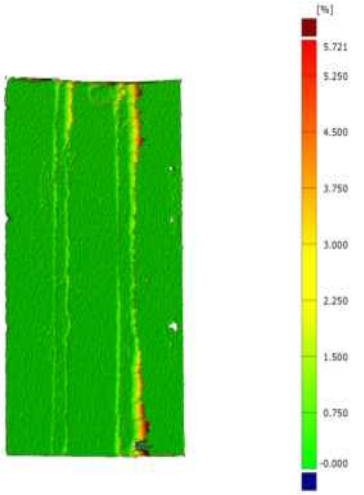

(c) Exaggerated display of strains, linear elastic stage loadstep (A). Pre-compression level = 0.6 N/mm^2.

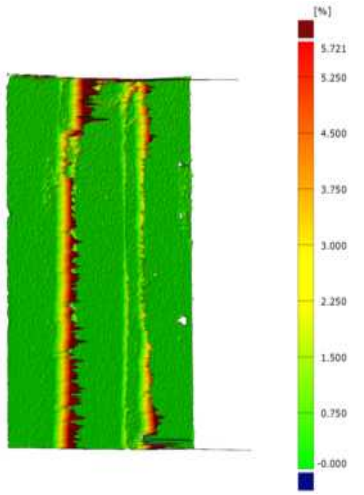

(d) Exaggerated display of strains, peak resistance loadstep (B). Pre-compression level = 0.6 N/mm^2.

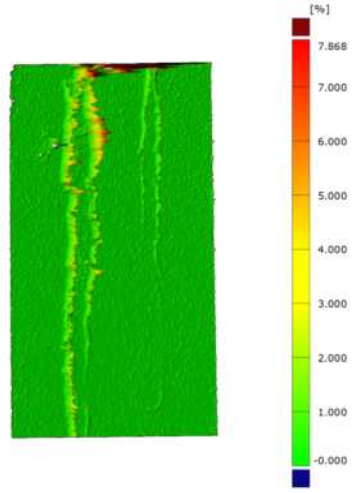

(e) Exaggerated display of strains, linear elastic stage loadstep (A). Pre-compression level = 1.0 N/mm^2.

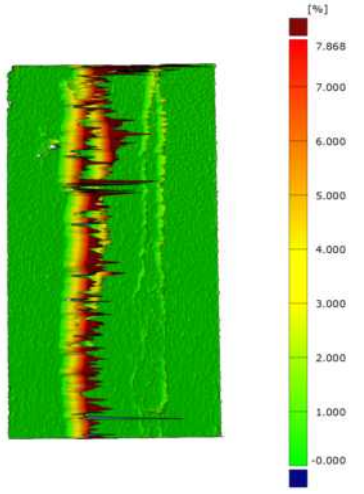

(f) Exaggerated display of strains, peak resistance loadstep (B). Pre-compression level = 1.0 N/mm^2.

Figure B.4: Additional figures equivalent mises strains pre-peak and peak resistance all pre-compression levels.

C

Accuracy test DIC technique applied

C.1. Shear triplet tests non-retrofitted masonry triplets

To gain insight in the accuracy, and determine if the DIC approach is a valid tool to use for these type of experiments, a simple accuracy test is performed in which the vertical displacements measured by the hydraulic jacket, the vertical LVDTs, and the corresponding output of the DIC are compared. Additionally, the measured uplift of the masonry units, as measured by the horizontal LVDT, is compared to the DIC results.

In GOM correlate it is possible to perform a point-wise inspection, i.e. calculation of the required quantities for a single point inside the surface of interest. By means of these inspection points the vertical and horizontal displacements are determined. In total 10 different inspection points are created, see Figure (C.1). Points 1 up to 8 are used for the relative vertical displacement of the middle masonry unit. Point 9 and 10 are used for determination of the horizontal displacement (or uplift) of the masonry units.

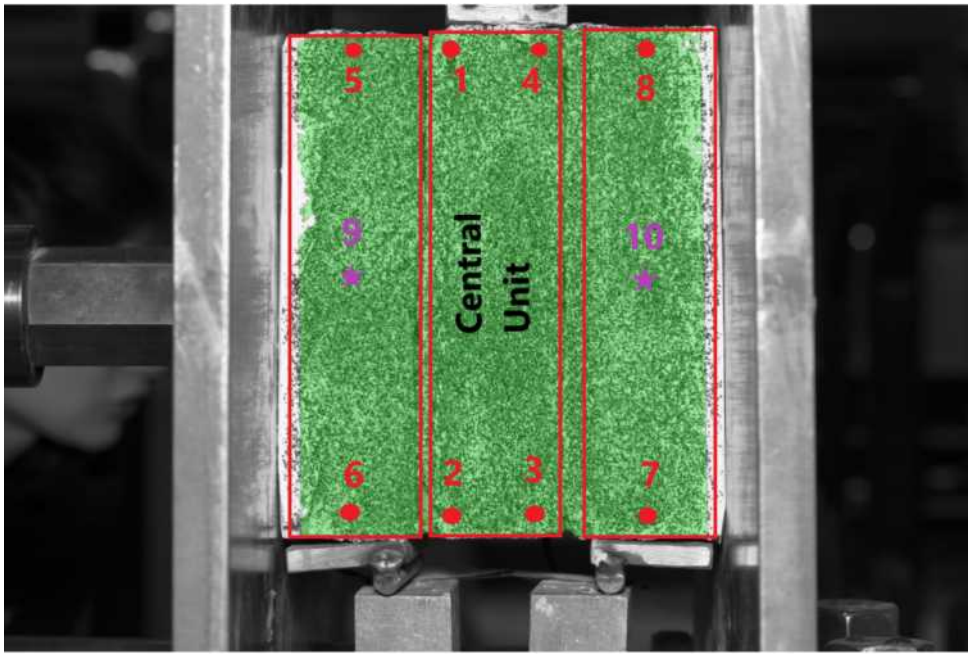

Figure C.1: Measuring points DIC analysis.

Recal Figure (3.14) showing the setup of both the vertical and horizontal LVDTs used during the experiments. The DIC is based on the front side of the specimen, however, the LVDTs are placed on the other side. It is assumed that no differences in displacements, between the front and the back of the specimen, are present.

Vertical LVDT number 1 corresponds to the inspection points 3, 4, 7, and 8. The second vertical LVDT is compared to inspection points 1, 2, 5, and 6. The measurement data of the horizontal LVDT is compared to inspection points number 9 and 10.

In Figure (C.2) three different subfigures are provided, one for each pre-compression level. In these figures the shear stress is plotted against the measured vertical deformation. The vertical deformation, as measured by the hydraulic jack, is represented by the black curves. It is shown these specific curves represent the largest magnitude of vertical deformation, for which possible reasons are provided earlier. The averaged value of the relative vertical deformation measured by the two vertical LVDTs is represented by the grey curves. The red dotted lines relate to the output data of the DIC software. The average vertical deformation of inspection points 5 and 6 is subtracted from the averaged vertical deformation measured in the points 1 and 2, generating the relative vertical motion of the left hand side of the middle brick. The same procedure is used to determine the relative vertical motion of the right hand side of this same unit. Inspection points 3, 4, 7, and 8 are used for this side of the specimen. The averaged value of the left and right inspection points is considered and plotted by means of the red dotted curves in Figure (C.2). This specific curve represents the relative vertical displacement of the central masonry unit, with respect to the total specimen, similarly to the averaged measurement data of the two vertical LVDTs.

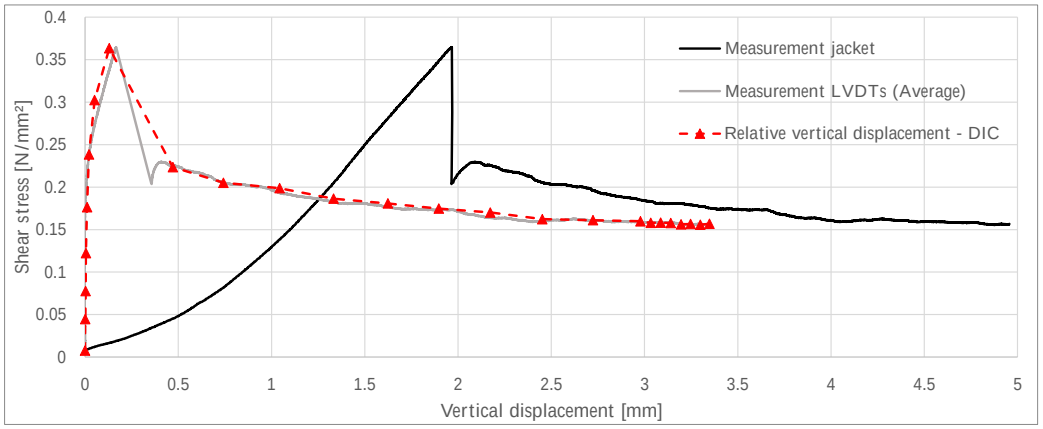

(a) Stress-displacement curve, 0.2 Mpa.

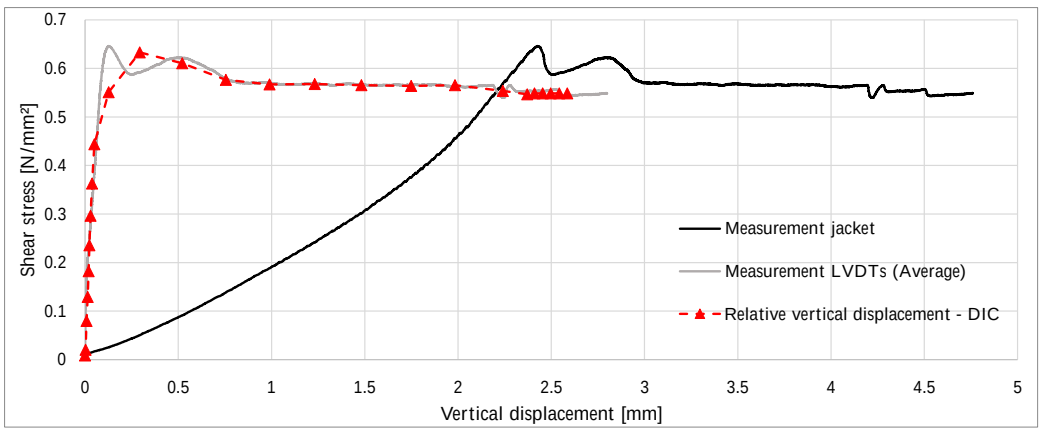

(b) Stress-displacement curve, 0.6 Mpa.

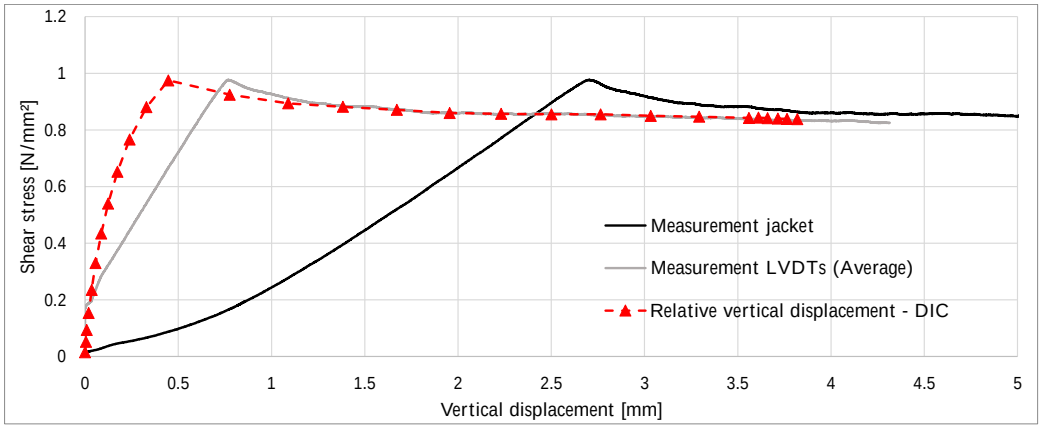

(c) Stress-displacement curve, 1.0 Mpa.

Figure C.2: Stress-displacement curves. Accuracy test DIC analysis.

It is shown in the figure above that using DIC allows for a representative determination of the relative vertical deformations of the non-retrofitted masonry triplets. Especially for the pre-compression levels equal to $0.2\,\mathrm{N/mm^2}$ and $0.6\,\mathrm{N/mm^2}$ this is the case. The vertical deformation of the specimen tested with the highest level of pre-compression is note as accurate. The DIC results in more stiff behaviour, compared to the measurement data of the LVDTs. However, the vertical displacements measured by the two vertical LVDTs seem to be less stiff compared to the other two pre-compression levels, making it questionable if these measurement data are accurate.

Additionally, in Figure (C.2b) it is shown that the DIC results don't exactly match the LVDT data around the peak resistance, i.e. the two distinct peaks obtained from the LVDTs is not shown from the DIC. A possible explaination of this fact is related to the number of pictures taken into account in the DIC. As mentioned, for this analysis every 10^{th} picture of the camera is used. This equals to an interval of 50 seconds between the different DIC pictures analysed. From the timestamp of the experimental data it is known that the time interval between the two consecutive peaks equals ± 74 seconds, quite similar to the interval between the pictures analysed. Using more pictures will introduce a better representation of the measurement data, since more data is included. Further research into a more accurate result is not part of this report.

As mentioned, the ability of the DIC to measure the uplift of the masonry units is also considered. In the figure below the results are shown for all the pre-compression levels. The LVDT measurement data is represented by the solid black and grey curves. The DIC results are plotted with red curves. For this case the DIC output is shown to be less representative, compared to the relative vertical deformations. The lower two pre-compression levels are somewhat well represented by the DIC. However, the results of the highest pre-compression level vary a lot. The normal displacement of the masonry units, as measured by the DIC, are underestimated. For a pre-compression level equal to $0.6\,\mathrm{N/mm^2}$ even negative tangential displacements are observed by the DIC for the initial loading stages.

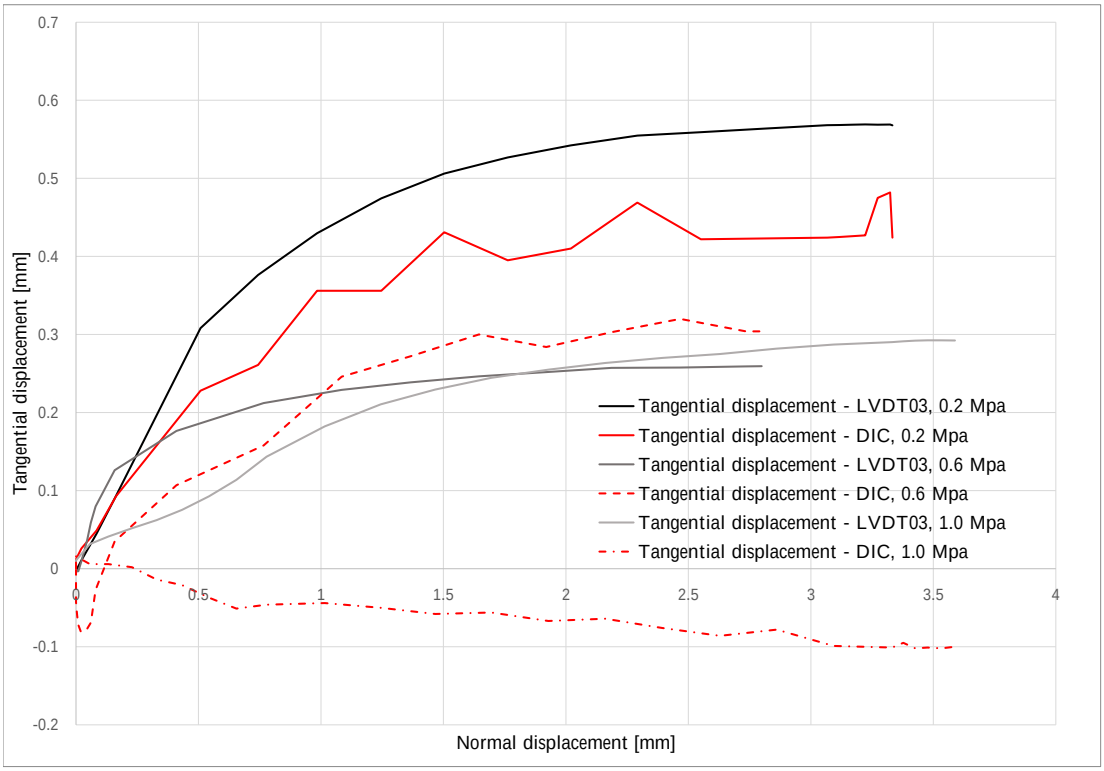

Figure C.3: Tangential versus normal displacements. LVDT data versus DIC output.

C.2. Flexural strength tests retrofitted masonry beams

To investigate the accuracy of the used DIC the vertical displacements captured by this analysis are taken into consideration. Both the vertical hydraulic jacket and the LVDT are influenced by the setup used for this experimental campaign. The former one is influenced by the steel frame of the total setup and the latter by the uplift of the outside masonry units. However, the camera used for the DIC is not influenced by any of these factors. Because of this reason the results of the DIC might be a good tool to use to determine the actual vertical displacements of the different specimen.

A similar procedure, as used for the analysis of the masonry triplets, is considered. Three measurement points are used in the GOM Correlate software to determine the vertical deformation of the centre of the retrofitted beams. These three points coincide with the connection/measuring points of the vertical LVDT applied (LVDT04).

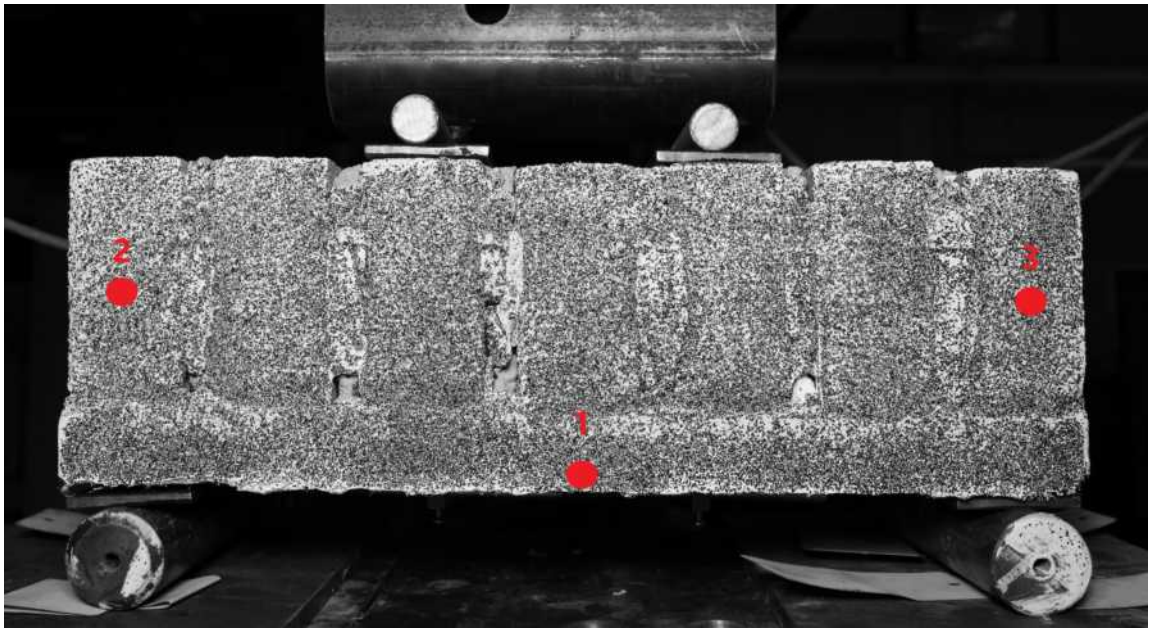

Figure C.4: Measuring points DIC analysis.

The vertical LVDT measures the relative displacement of the middle section of the specimen, compared to the 'fixed' locations at the outer edges. Via Excel the same procedure is used, i.e. the average vertical motion captured in measurement points 2 and 3 is subtracted from the vertical displacement determined in point 1. In the figure below the force-displacement curves of both specimen discussed above are depicted. In these figures both the vertical displacement measured by the jacket, the vertical LVDT, and the relative vertical displacement determined via DIC are shown.

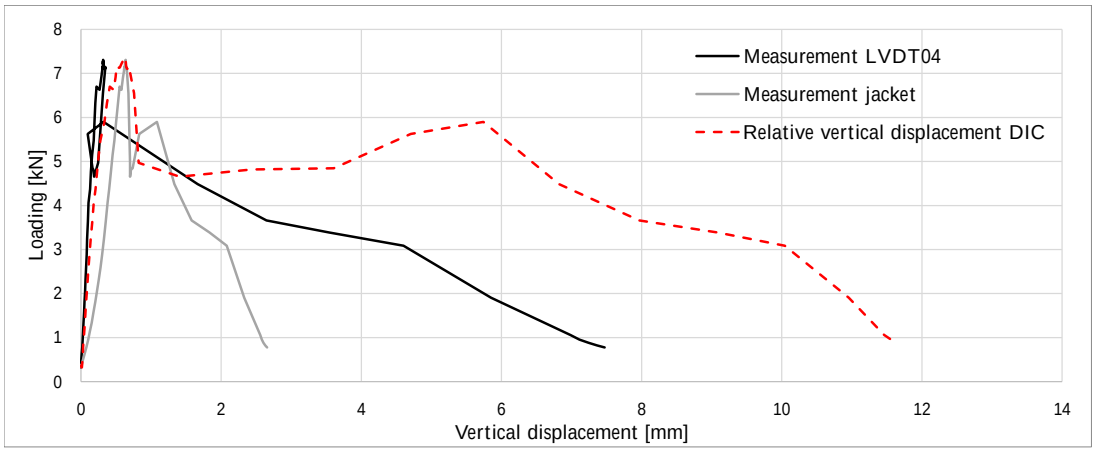

(a) Vertical displacements specimen number 4; 10 mm full bond - A. Shear type of failure.

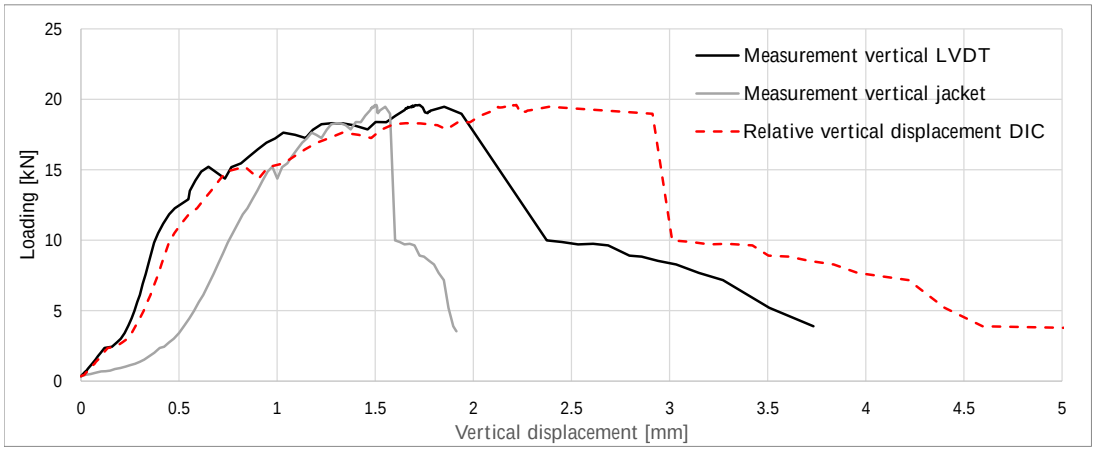

(b) Vertical displacements specimen number 6; 30 mm full bond - A. Flexural failure.

Figure C.5: Comparison vertical deformations measured by different instruments, flexural tests.

From Figure (C.5) it is clearly shown that the relative vertical displacement of the bottom centre of the masonry beams is not well estimated by the DIC, especially for specimen number 4. As mentioned, this particular specimen failed by the debonding of one of the outside masonry units, directly influencing the measurement data of the vertical LVDT. Since the most left outside unit moves upward, the average vertical displacement of measurement points 2 and 3 is highly influenced. Uplift of one of the fixation points of the vertical LVDT results in increased measurement data (increased elongation of the aparatus). This is clearly shown in the post-peak behaviour.

For the second specimen analysed, however, the results determined via the DIC are beter representative of the measurement data of the vertical LVDT.

The differences in accuracy of the DIC results is explained by the Figure shown below. From Figure (C.6a) it is clearly shown that the vertical motion of the left masonry unit (i.e. measurement point 2) becomes negative after the peak loading. This particular masonry unit debonded from the SHCC overlay causing it to move in upward direction, directly influencing the measurement data of the vertical LVDT by increasing in magnitude. Figure (C.6b), however, shows that the DIC analysis captured a rigid body motion of the total specimen in the first loading step. This rigid body motion is taken into account by subtracting the average value of point 2 and 3 from the data captured in measurement point 1. It is shown that the two outside measurement points don't displace significantly after this initial step. However, still, as shown in Figure (C.5b), the relative vertical displacement of this specimen is overestimated by the DIC. It is noted that the difference in measurement data

only occurs after the peak resistance, before this the relative vertical deformation is well estimated.

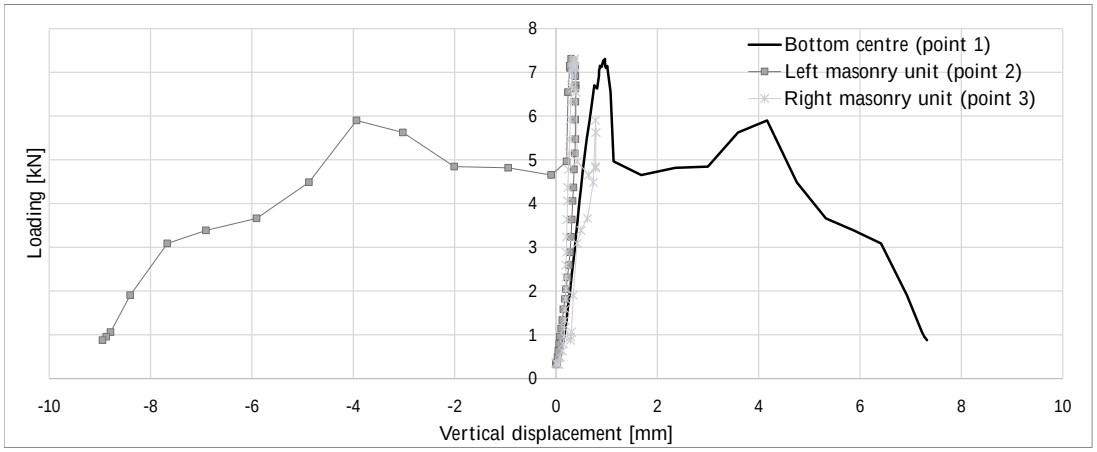

(a) Vertical displacements measurement locations specimen number 4; 10 mm full bond - A.

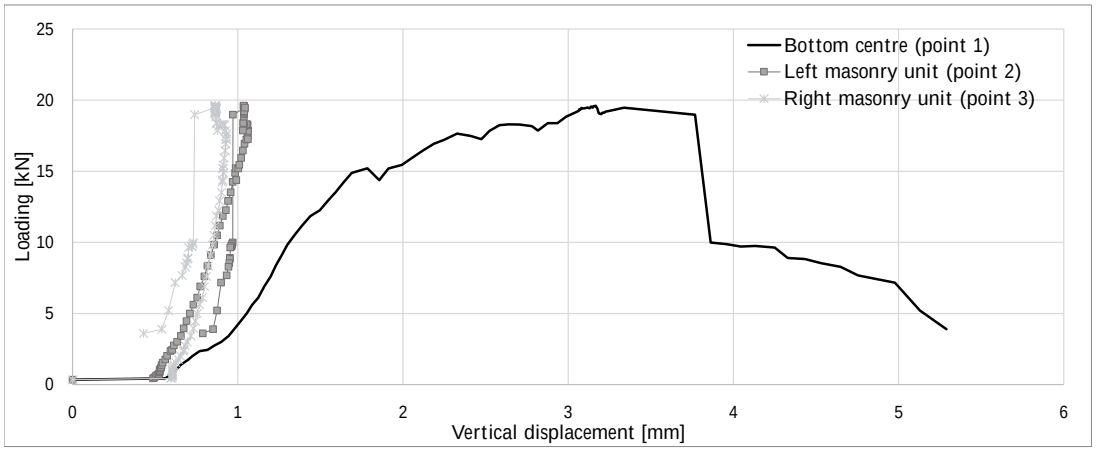

(b) Vertical displacements measurement locations specimen number 6; 30 mm full bond - A.

Figure C.6: Vertical displacements measurement points DIC, flexural tests.

D

DIC results retrofitted shear triplets

In this Appendix some of the DIC results corresponding to the retrofitted shear triplet tests are presented. Not all the results are shown. For every type of specimen analysed the governing results are depicted.

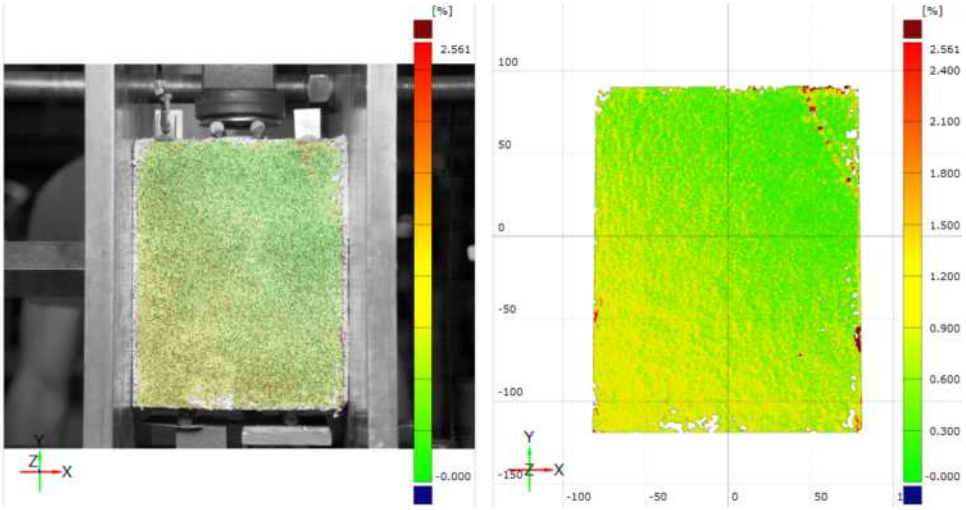

Figure D.1: Post-peak state SHCC overlay. Specimen number 4, 10 mm full bonded SHCC. Pre-compression level = 0.6 Mpa.

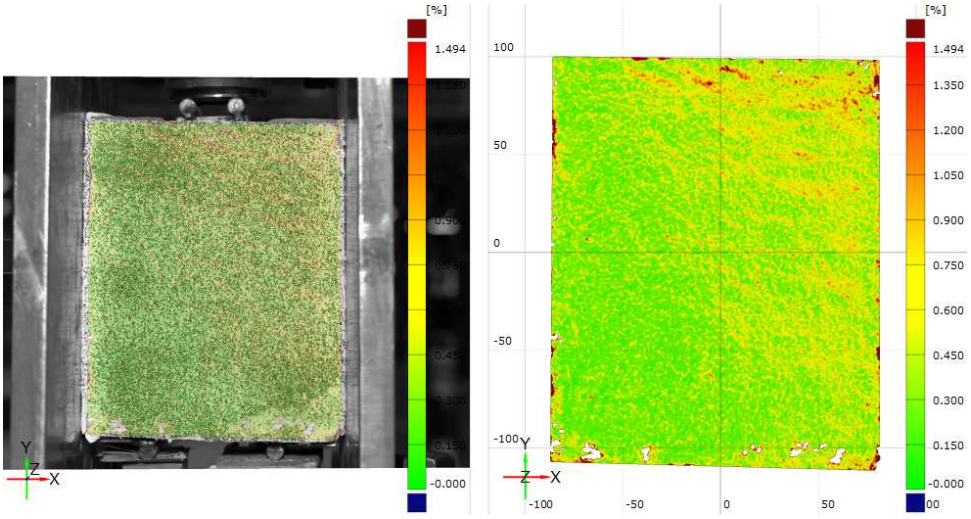

(a) Specimen number 9.

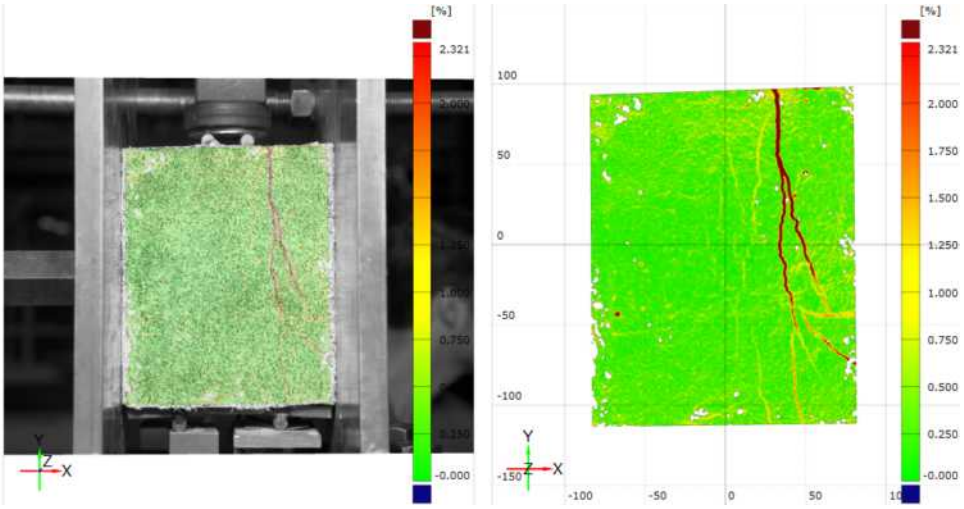

(b) Specimen number 36

Figure D.2: Post-peak state SHCC overlay. Specimen number 9 and 36, 10 mm full bonded SHCC. Pre-compression level = 1.0 Mpa.

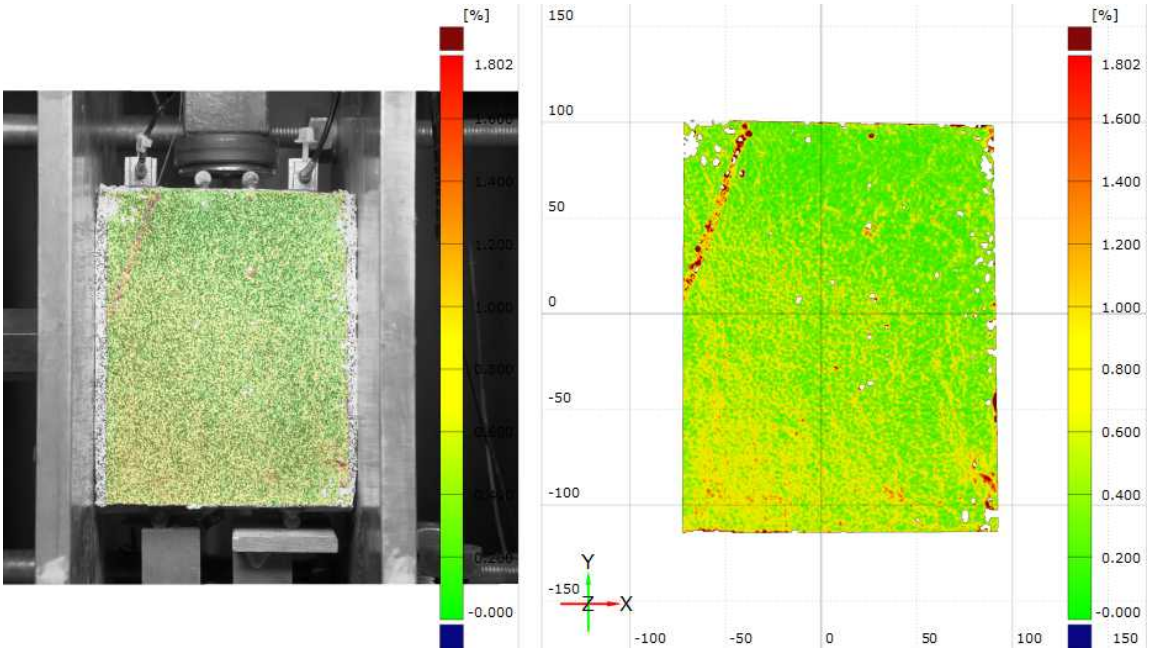

(a) Specimen number 11.

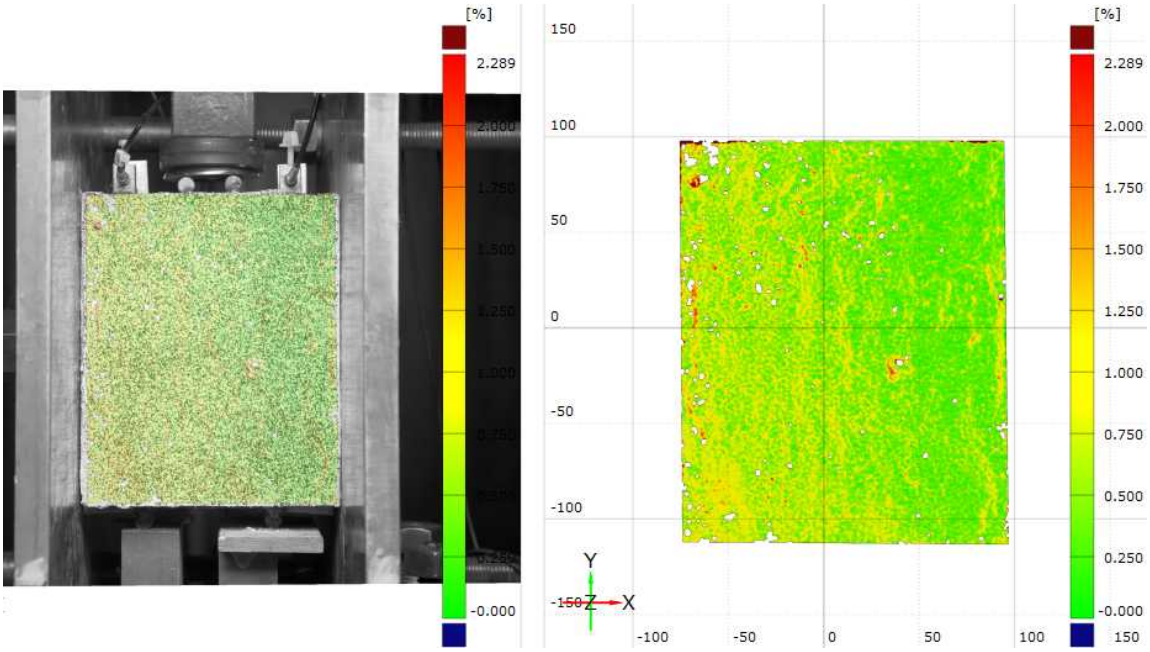

(b) Specimen number 12.

Figure D.3: Post-peak state SHCC overlay. Specimen number 11 and 12, 30 mm full bonded SHCC. Pre-compression level = 0.2 Mpa.

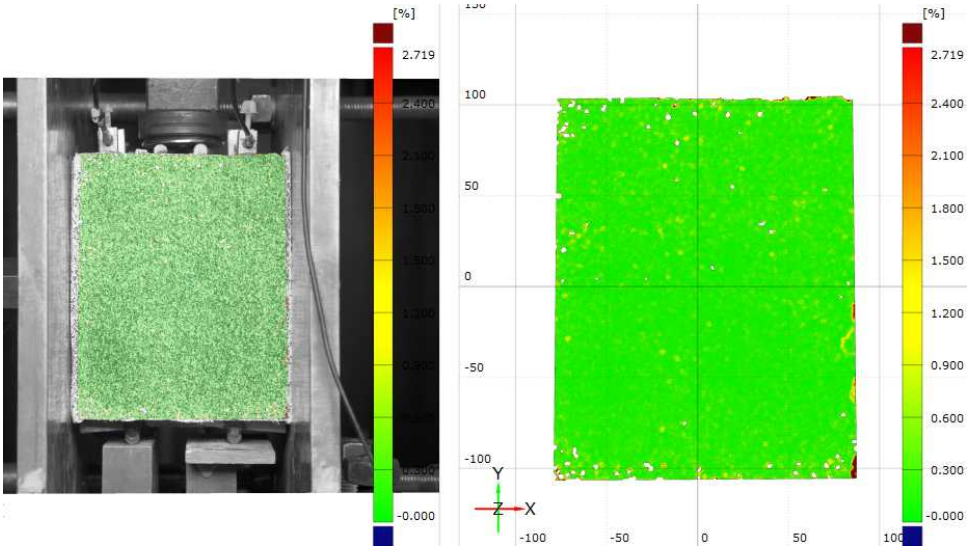

(a) Specimen number 13.

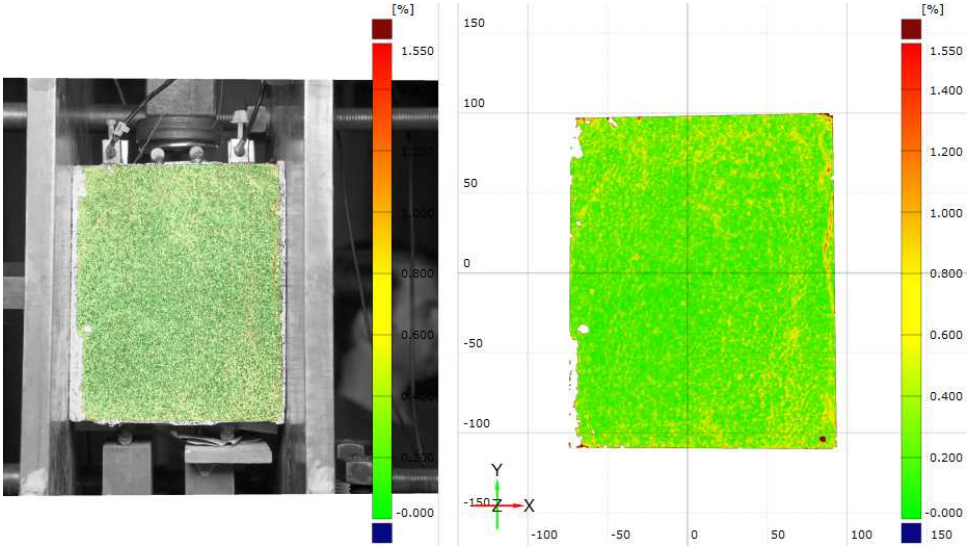

(b) Specimen number 15.

Figure D.4: Post-peak state SHCC overlay. Specimen number 13 and 15, 30 mm full bonded SHCC. Pre-compression level = 0.6 Mpa.

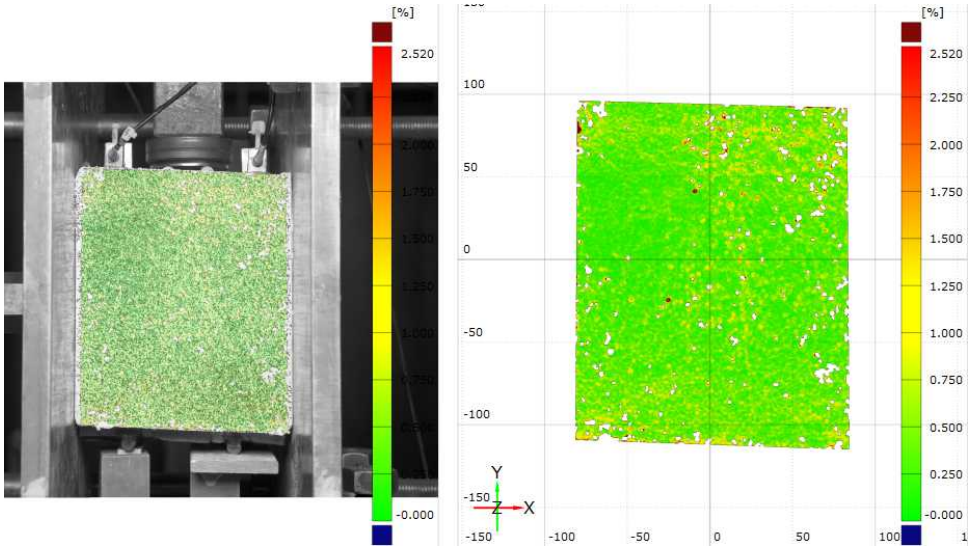

(a) Specimen number 18.

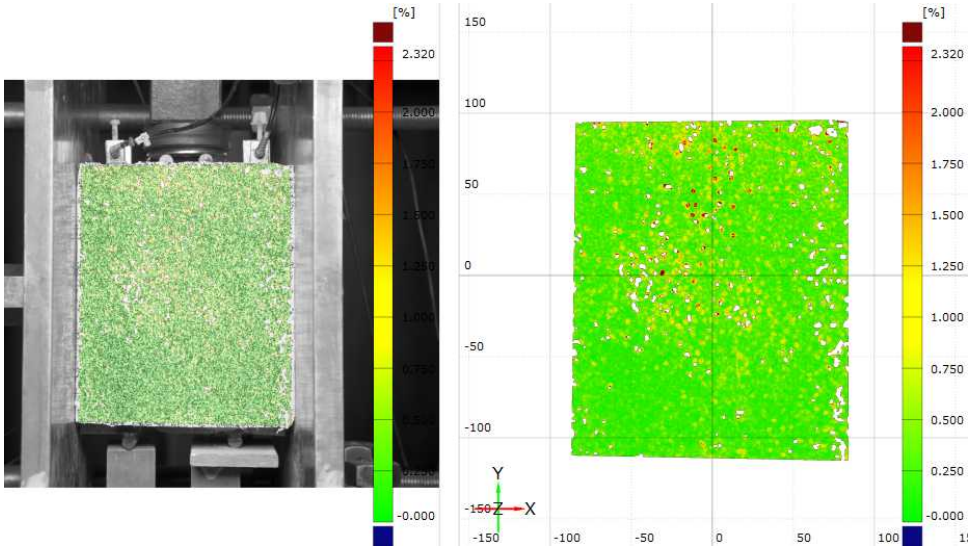

(b) Specimen number 39.

Figure D.5: Post-peak state SHCC overlay. Specimen number 18 and 39, 30 mm full bonded SHCC. Pre-compression level = 1.0 Mpa.

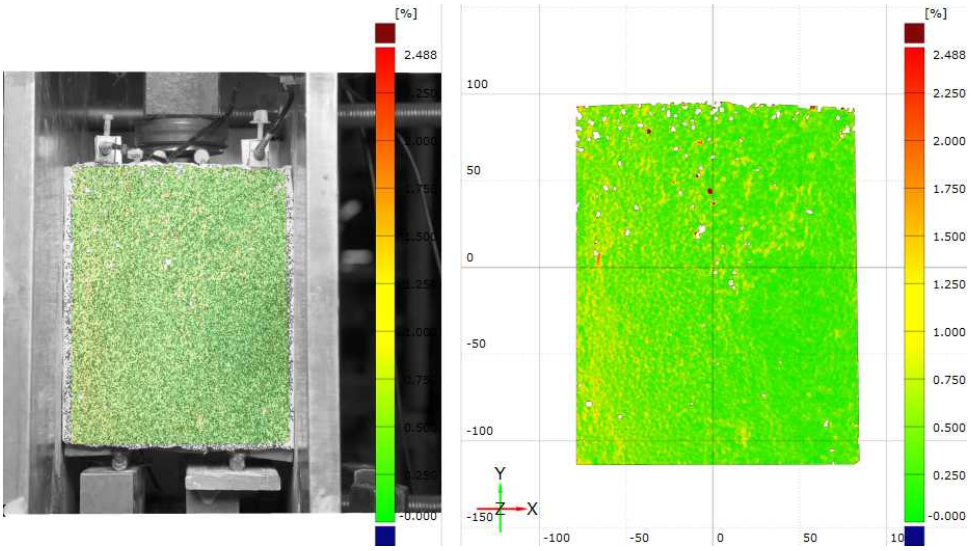

(a) Specimen number 19.

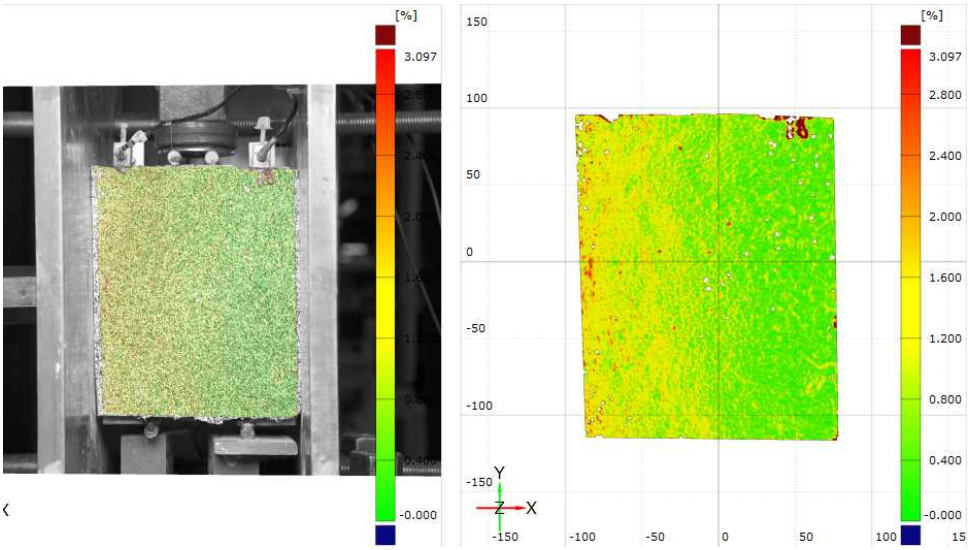

(b) Specimen number 40.

Figure D.6: Post-peak state SHCC overlay. Specimen number 19 and 40, 10 mm debonded SHCC. Pre-compression level = 0.2 Mpa.

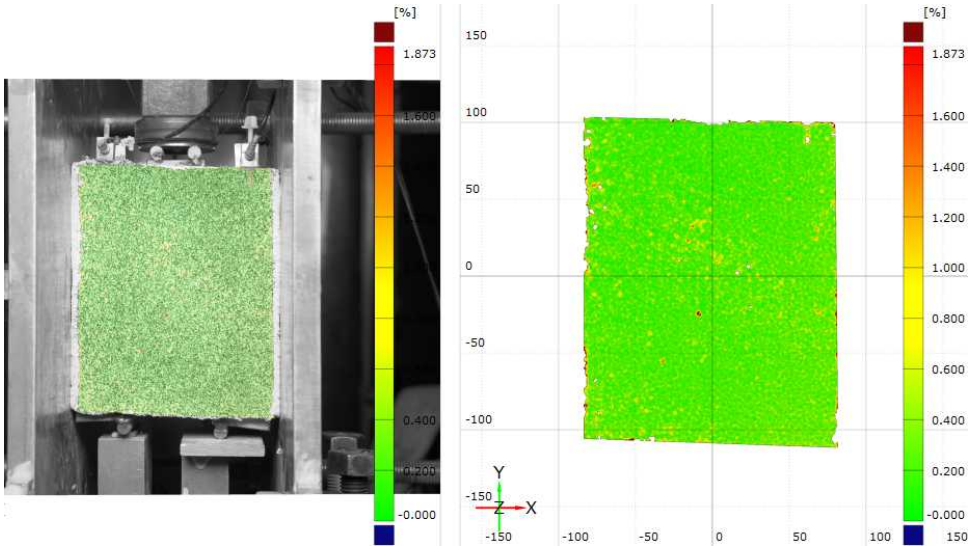

(a) Specimen number 23.

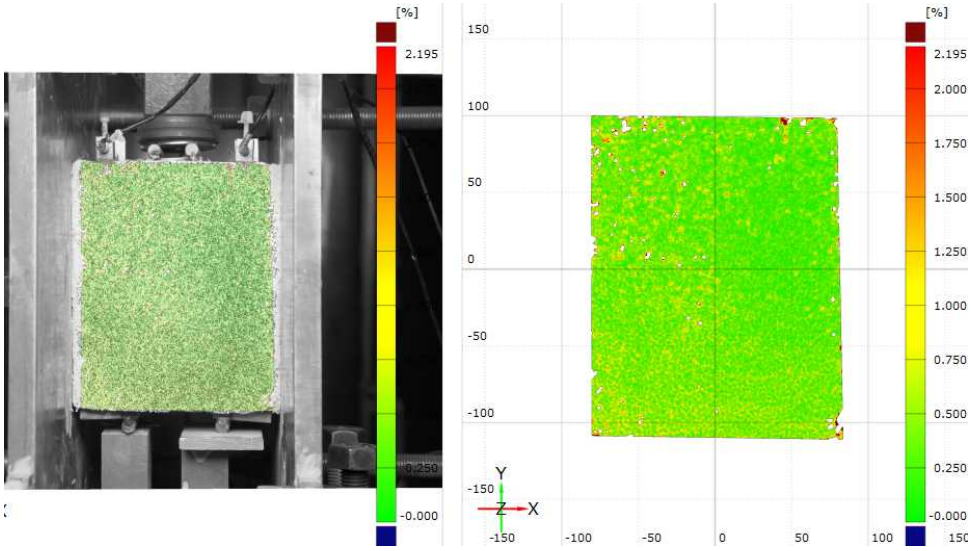

(b) Specimen number 41.

Figure D.7: Post-peak state SHCC overlay. Specimen number 23 and 41, 10 mm debonded SHCC. Pre-compression level = 0.6 Mpa.

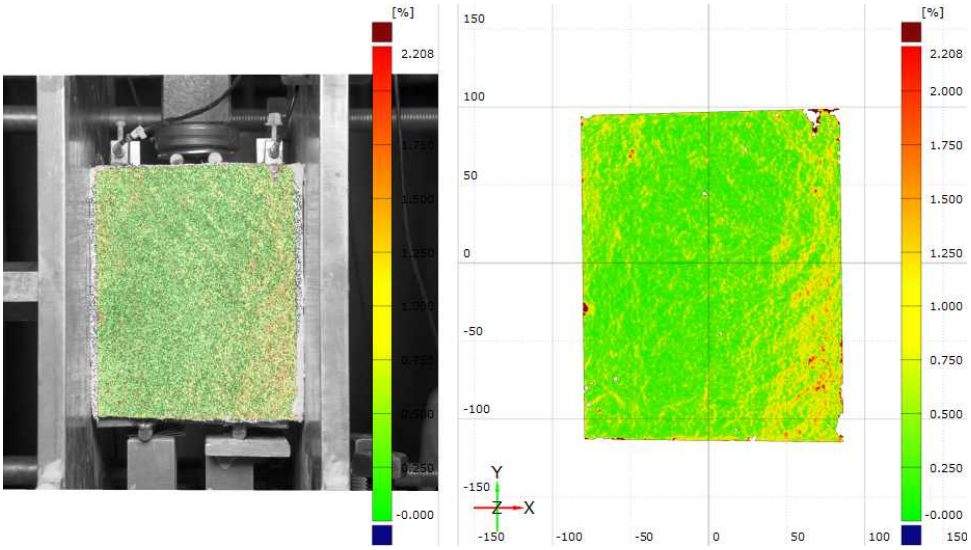

Figure D.8: Post-peak state SHCC overlay. Specimen number 26, 10 mm debonded SHCC.Pre-compression level = 1.0 Mpa.

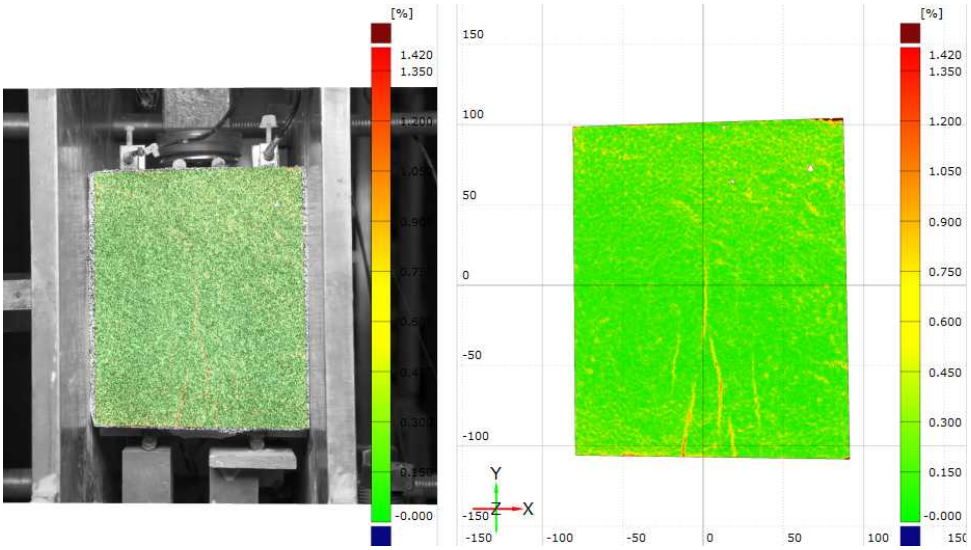

Figure D.9: Post-peak state SHCC overlay. Specimen number 29, 30 mm debonded SHCC. Pre-compression level = 1.0 Mpa.

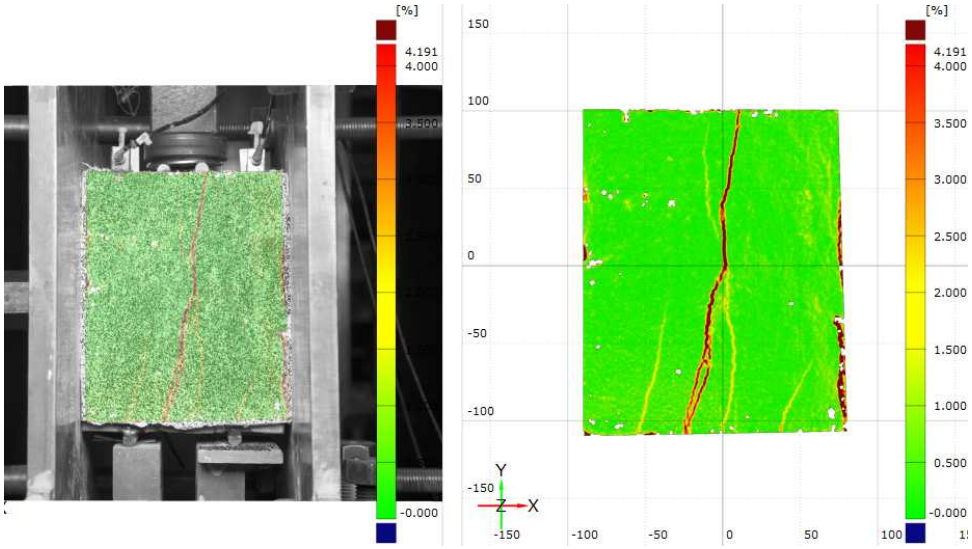

(a) Specimen number 42.

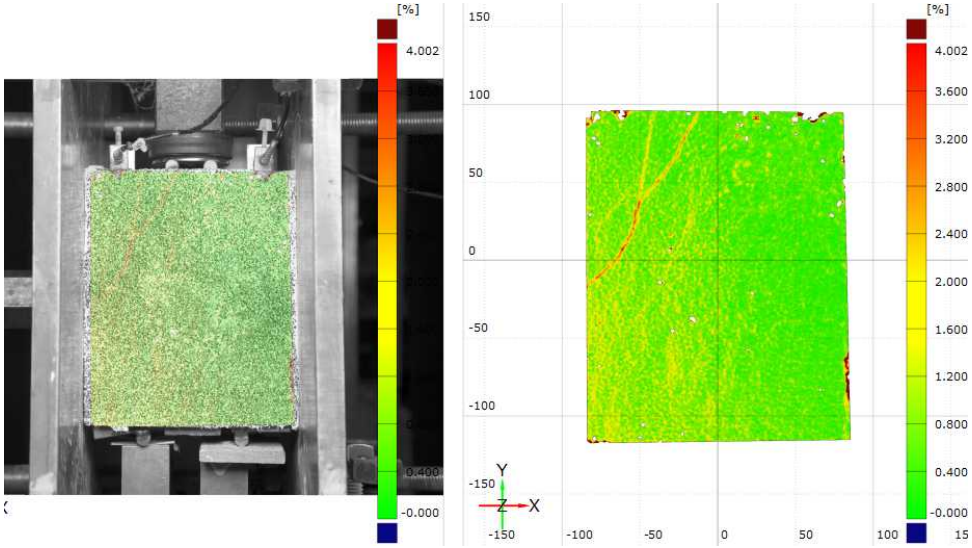

(b) Specimen number 44.

Figure D.10: Post-peak state SHCC overlay. Specimen number 42 and 44, 10 mm full bond SHCC, non-sealed curing conditions. Pre-compression level = 1.0 Mpa.

E

Analysis numerical results shear strength plain masonry triplets

E.1. Two-dimensional simplified micro-model clay masonry triplet

First, the accuracy of the two-dimensional model is discussed. Below the force-displacement curve obtained from the numerical analysis is plotted versus the experimental results. All three pre-compression levels are taken into account. The vertical displacements of the experimental results shown relate to the average value of the two vertical LVDTs, measuring the vertical relative displacement of the central masonry unit. The experimental results are plotted by means of black and grey curves. The numerical results are visualized by means of red curves.

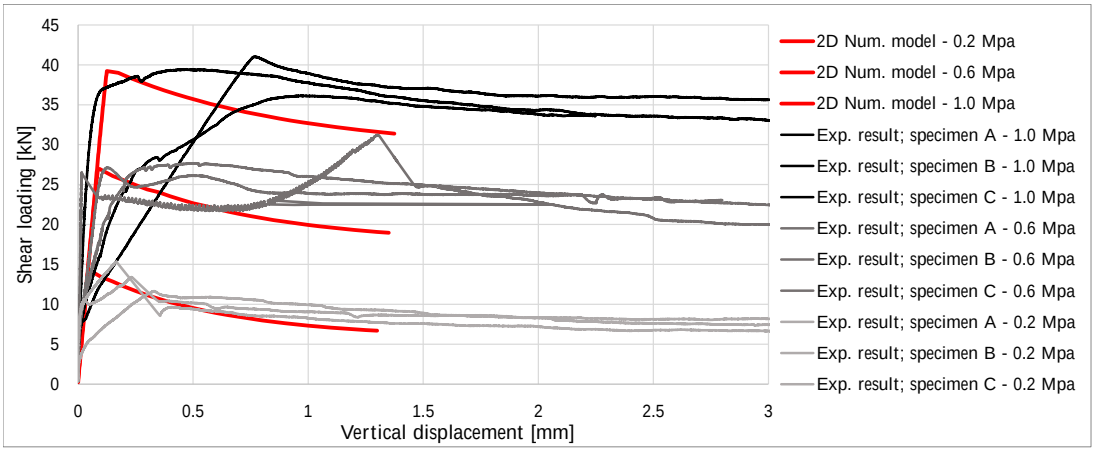

Figure E.1: Force-displacement curve. 2D numerical simulation versus experimental results. Three pre-compression levels.

From this figure it is concluded that the numerical model, in terms of peak resistance, performs in good agreement with the experimental results. However, the post-peak behaviour is best represented for the lowest pre-compression level. The decay in resistance is too quick for the higher pre-compression levels. By means of a parametric study the influence of several parameters is taken into account. This is discussed in the following sections.

Besides the overall force-displacement relationship the stress distributions at the non-linear unit-unit interfaces are investigated. The tractions of one of the two interfaces are considered. Due to symmetry conditions no differences in any quantity are to be expected between these two interfaces. In the figures below these tractions are plotted versus the height of the unit-unit interface. In total five points of interest are determined from the force-displacement curve. These five points coincide with the points used for the analysis of DIC

data in the previous chapter. Using similar points of interest opens up the possibility of combining the all the different type of results, i.e. experimental data, DIC results, and numerical results, possibly resulting in a better understanding of the actual failure mechanisms.

Below the interfacial tractions are depicted for the different coordinates of the force-displacement curve. The results of all three pre-compression levels are analysed and discussed. Additionally, the shear and normal tractions at the unit-unit interface are plotted in the $\tau - \sigma$ plane. The multi-surface interface model is also depicted in the same figure, enabling the possibility to determine if there are stress (traction) combinations are at the yield surface, and for which loadstep(s). These combinations of tractions are only plotted for a limited amount of elements over the height of the interface, the lowest value (0) corresponding to the bottom of the specimen and the highest value (210) related to the top of the specimen. The other data is related to intermediate points in between the top and bottom of the specimen. The absolute value of the shear tractions are plotted.

All the tractions are derived from the integration points of the finite elements. Displacements are taken from the nodal values.

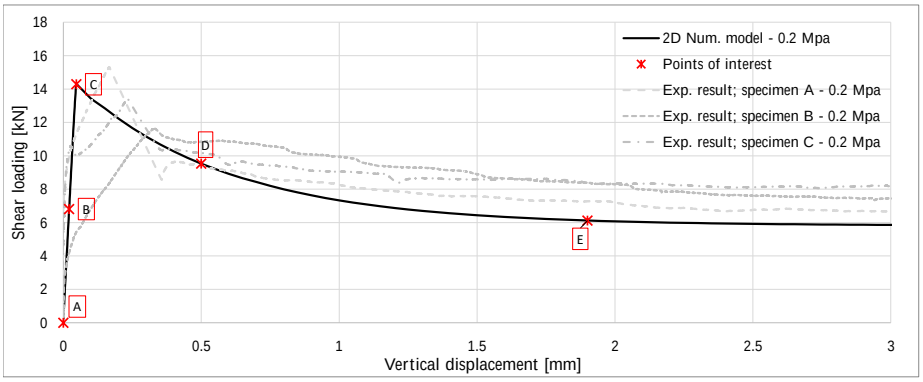

(a) Force-displacement curve experimental results and numerical model. Pre-compression level = 0.2 Mpa.

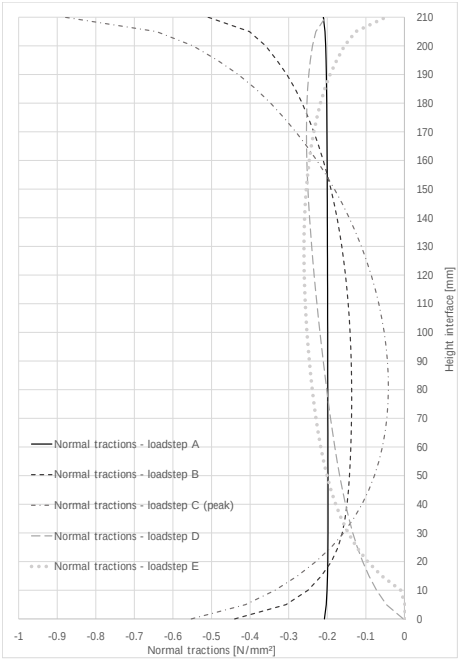

(b) Normal tractions unit-unit interface for different loadsteps.

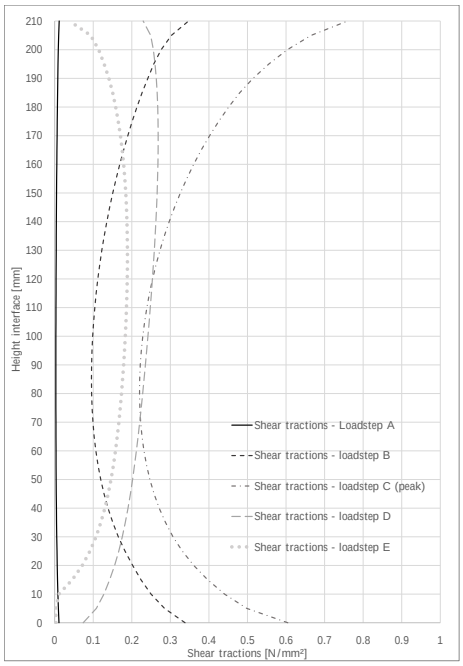

(c) Shear tractions unit-unit interface for different loadsteps.

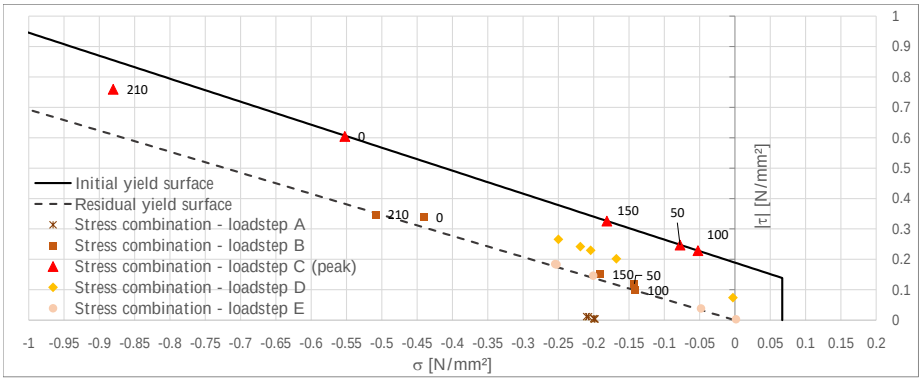

(d) $\tau - \sigma$ plane with initial and residual yield surfaces. Additional numbers plotted correspond to the height along the investigated interface.

Figure E.2: Stress distribution unit-unit interface 2D numerical model non-retrofitted clay masonry. Pre-compression = 0.2 Mpa.

In the figure above the results for the lowest pre-compression level are shown. It is noted that both the normal and shear tractions are nonlinearly distributed over the height of the unit-unit interfaces, as expected from [16]. Also, in Figure (E.2d), the shear and normal tractions are plotted versus the yield criteria of the interface model for the different selected loading steps. The compressional cap is not shown in this figure since the compressional strength of the interface is much higher (i.e. 13.11 N/mm^2) compared to the acting normal tractions. In this figure it is clearly shown that at peak resistance (loadstep C) the combination of tractions are on the initial yield surface of the interface model used. For the following two loading steps it can be seen that the analysed points move down to a intermediate yield surface (loadstep D, yellow points) and, finally, to the residual yield surface. In the figures below similar results are shown for the other two pre-compression levels.

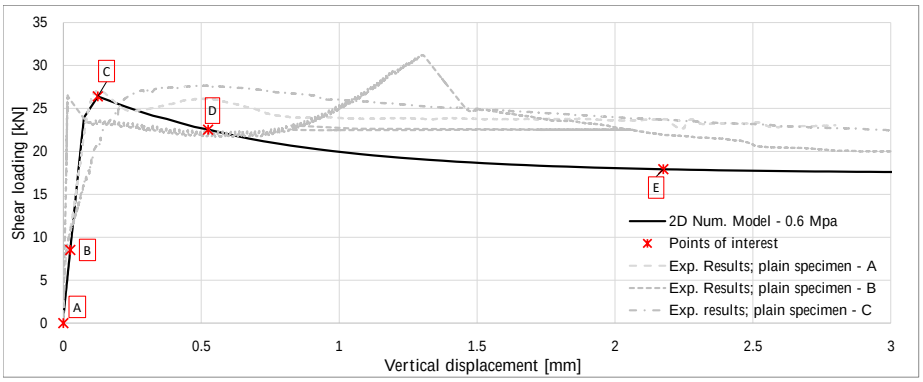

(a) Force-displacement curve experimental results and numerical model. Pre-compression level = 0.6 Mpa.

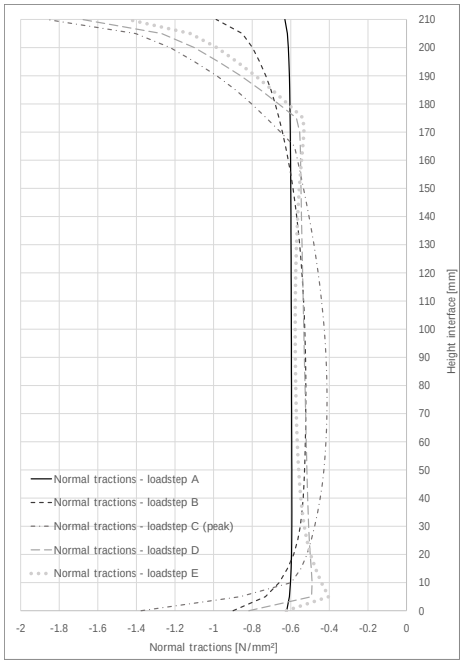

(b) Normal tractions unit-unit interface for different loadsteps.

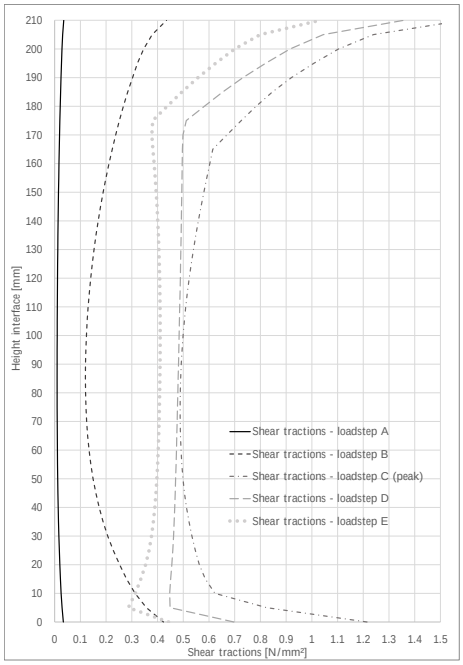

(c) Shear tractions unit-unit interface for different loadsteps.

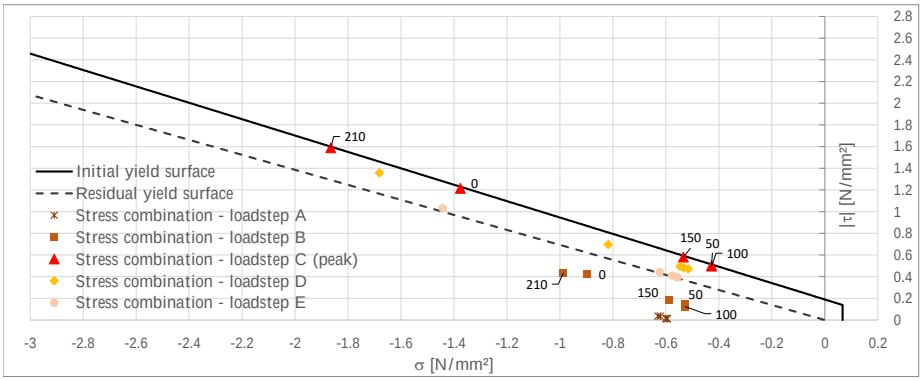

(d) $\tau - \sigma$ plane with initial and residual yield surfaces. Additional numbers plotted correspond to the height along the investigated interface.

Figure E.3: Stress distribution unit-unit interface 2D numerical model non-retrofitted clay masonry. Pre-compression = 0.6 Mpa.

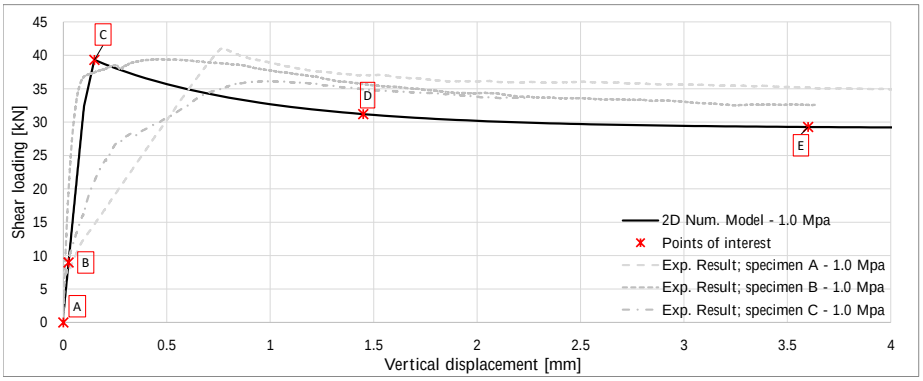

(a) Force-displacement curve experimental results and numerical model. Pre-compression level = 1.0 Mpa.

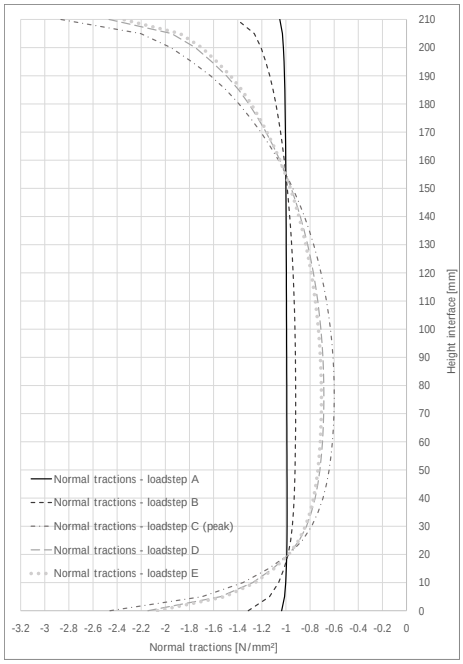

(b) Normal tractions unit-unit interface for different loadsteps.

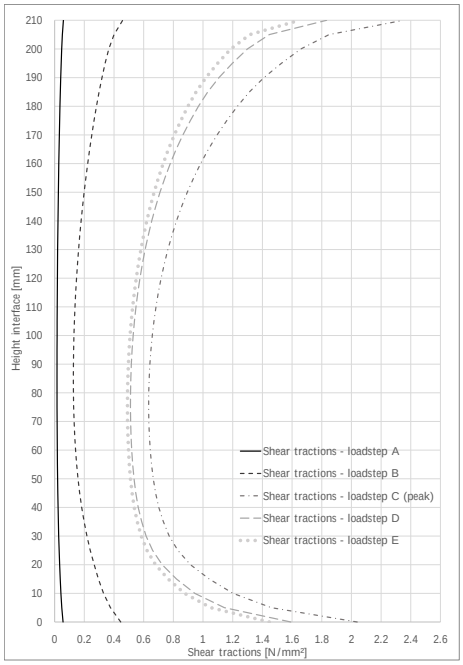

(c) Shear tractions unit-unit interface for different loadsteps.

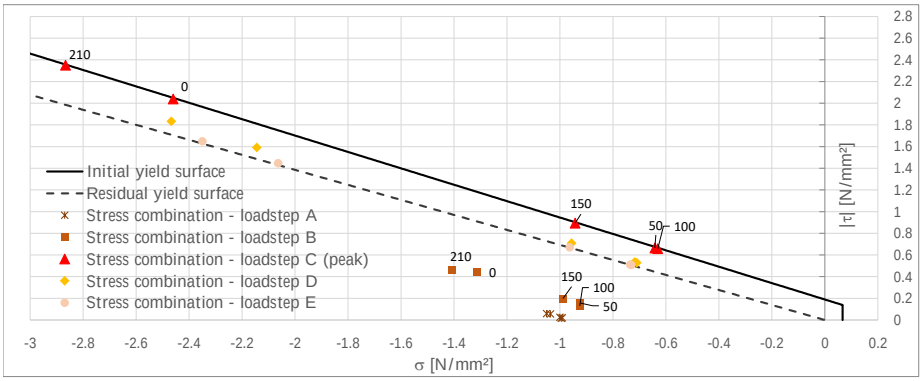

(d) $\tau - \sigma$ plane with initial and residual yield surfaces. Additional numbers plotted correspond to the height along the investigated interface.

Figure E.4: Stress distribution unit-unit interface 2D numerical model non-retrofitted clay masonry. Pre-compression = 1.0 Mpa.

From the figures above it is shown that all the pre-compression levels result in similar results with respect to the non-linear stress distributions and point of yielding. However, one difference must be noted. Comparing the normal and shear traction distributions of all three pre-compression levels it is noticed that only for the lowest pre-compression level these curves 'flip' in direction after the peak resistance, i.e. the highest values of the tractions don't remain at the bottom and the top of the interface. This is not the case for the other two pre-compression levels. This is similar to the numerical results presented in [16].

From the numerical results it is concluded that, at peak resistance, the $\tau - \sigma$ combinations are located at the Coulomb-friction yield surface. No yielding due to compressional of tensile stresses is observed.

In addition to the force-displacement relationships and stress-distributions along the unit-unit interfaces, also the accuracy of the numerical model with respect to the dilatant behaviour of the masonry is tested. During the experiments this uplift (or normal displacement) is measured via a horizontal LVDT (LVDT03). The horizontal displacement, determined at equivalent locations as the connections points of this LVDT, are retrieved from the two-dimensional numerical model. From Figure (E.5) it is clearly shown that the dilatant behaviour of the URM masonry triplets is not well captured by the numerical model at all. This is similar to

the results presented in [16]. For more information the reader is referred to the literature.

The current model examined is not fitted to the experimental data. With the help of a parametric study more representing results can possible be obtained. This, performing a parametric study to fit the numerical results to the experimental ones, is not in the scope of this report and will therefore not be discussed. Additionally, it must be noted that the experimental results represent non-symmetric failures (i.e. failure of the specimen is initiated in one of the unit-mortar interfaces). The numerical model is only able to represent symmetric failure modes where both unit-unit interfaces fail simultaneously. However, it is assumed this will not influence the goal of this numerical research.

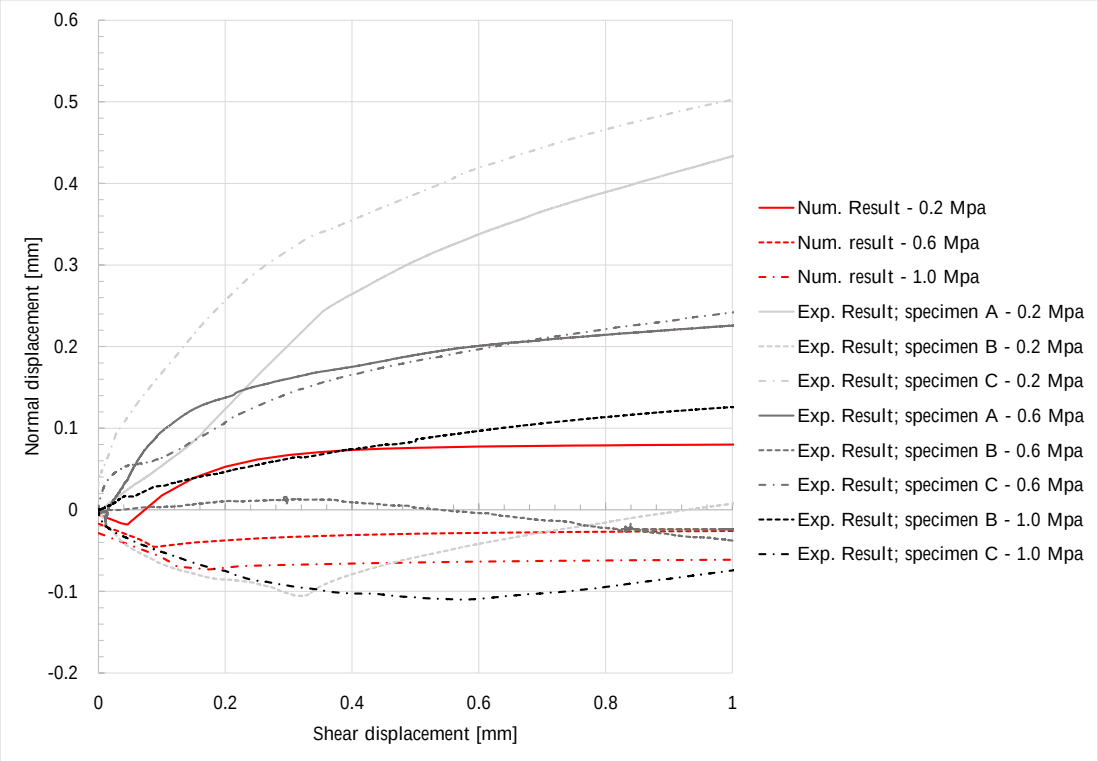

Figure E.5: Tangential versus normal displacements numerical and experiment results.

E.2. Three-dimensional simplified micro-model plain clay masonry triplet

Besides two-dimensional models also three-dimensional simplified micro-models are made for the non-retrofitted masonry. Below the numerical results of these models are compared to their two-dimensional counterparts. The force-displacement curves are plotted for all pre-compression levels, see Figure (E.6). The results of the 2D and 3D models are represented by solid curves and dotted lines, respectively. It is clearly shown that the results are exactly similar to each other.

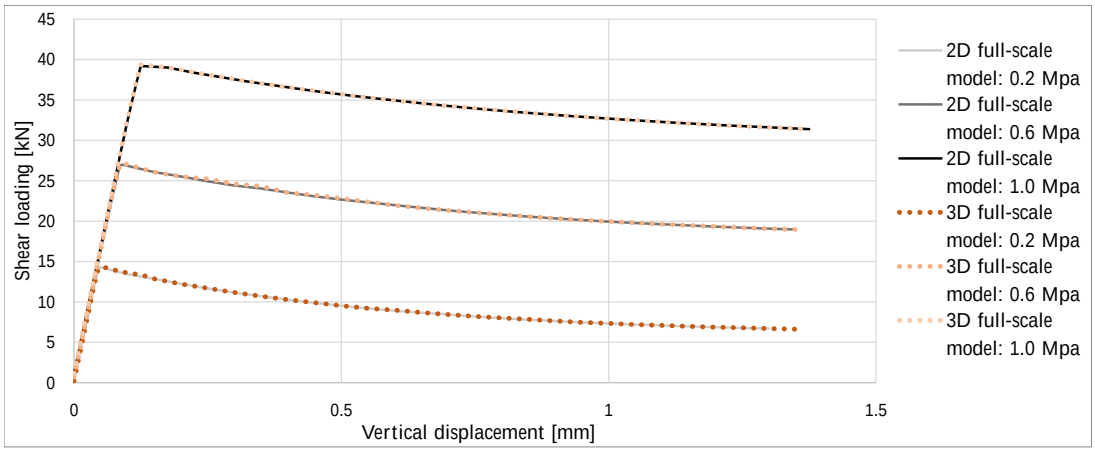

Figure E.6: Force-displacement curves 2D versus 3D models.

The stress distribution at the unit-unit interface is only depicted for the lowest level of pre-compression. Because of the three-dimensional geometry, the unit-unit interfaces become 2D surfaces, adding one extra direction of shear tractions. For the visualisation of these tractions one single vertical section is considered at halfway the depth of the specimen, see Figure (E.7) below. This assumption, i.e. considering only one section for the stress distribution, is sound since no imperfections are present and the model is symmetric. The stresses at the considered section are well representing the actual stress-state in the total unit-unit interface.

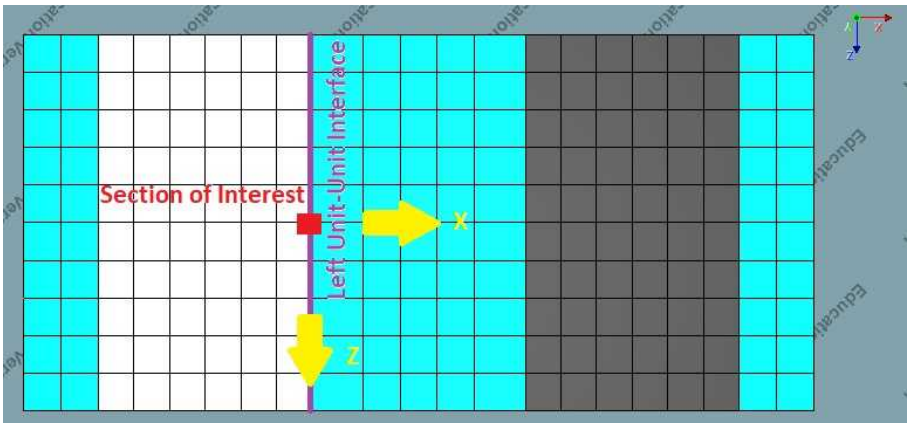

Figure E.7: Vertical section 3D simplified micro-model clay masonry triplet. Top view FE model. Global axes shown with yellow arrow.

Below the distribution of the different tractions in the unit-unit interface are depicted for the same load-steps as used in Figure (E.2). These loadsteps can be used for this 3D model as well, as it is shown in Figure (5.4) no differences are present in the force-displacement curves between the 2D and 3D models. The tractions are provided in terms of the global axes of the numerical model.

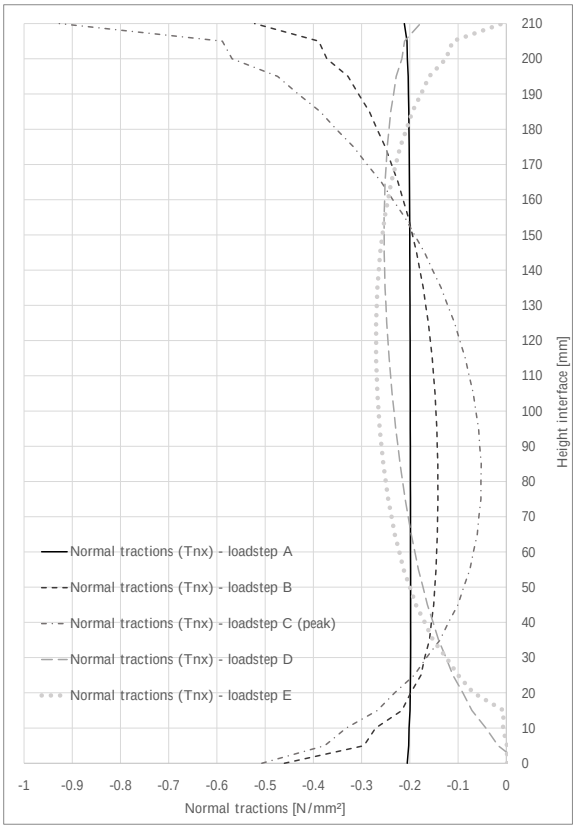

(a) Normal tractions unit-unit interface in global x-direction.

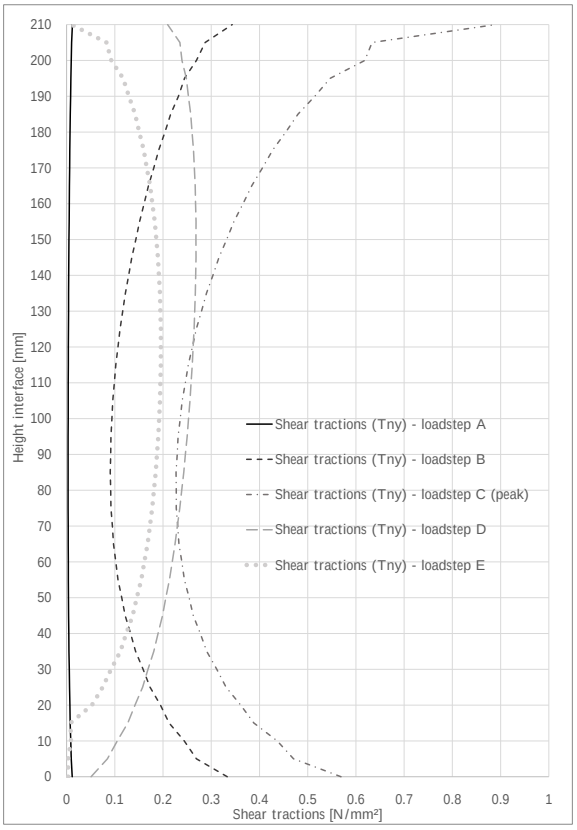

(b) Shear tractions unit-unit interface in global y-direction.

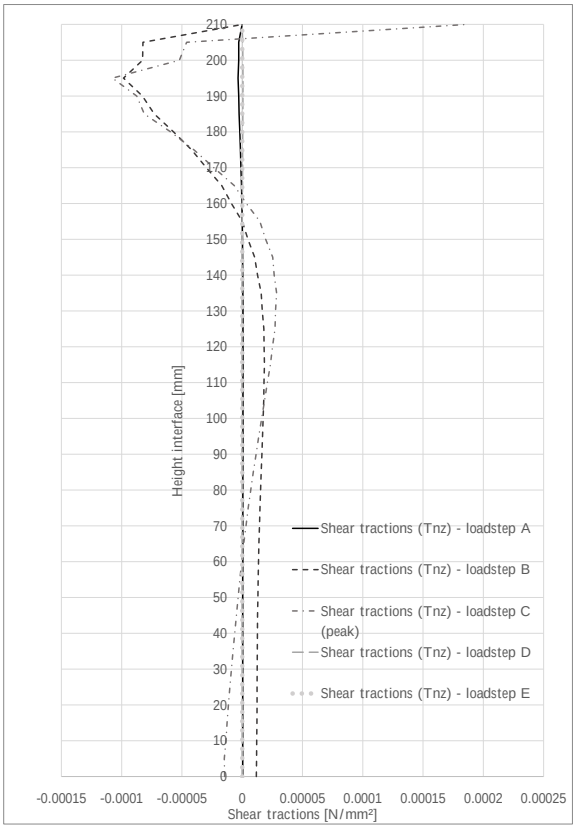

(c) Shear tractions unit-unit interface in global z-direction.

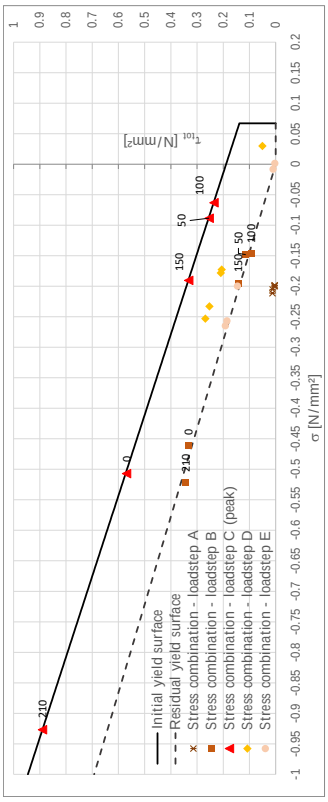

(d) $\tau - \sigma$ plane with initial and residual yield surfaces.

Figure E.8: Stress distribution unit-unit interface 3D numerical model non-retrofitted clay masonry. Pre-compression = 1.0 Mpa.

By comparing Figure (E.2) and (E.8) it is shown that, as expected, similar results are present for both the 2D and 3D model. As mentioned, for the 3D model one additional direction of shear tractions is taken into account, see Figure (E.8c) above. It is shown that in this direction no significant shear tractions develop for all loading stages considered. The total shear traction is determined via the following equation:

$$\tau_{tot} = \sqrt{\left(T_{ny}\right)^2 + \left(T_{nz}\right)^2} \tag{E.1}$$

In which T_{ny} and T_{nz} represent the shear tractions in the two global directions of the FE model. Because the shear tractions in the global Z-direction are negligible the equation simplifies to the equation shown below. This is equal to the 2D case examined earlier.

$$\tau_{tot} = T_{ny} \quad \text{if} \quad T_{nz} \rightarrow 0 \tag{E.2}$$

Finally, it is concluded that both the 2D and 3D models are able to simulate the global failure of the URM specimen. Exact dilatant behaviour is not of interest for this research.

E.3. Parametric study numerical simulation

The nonlinear interface model used for the unit-unit interface is complex, since it combines three different failure modes. Modelling these different failure modes requires a great amount of input parameters. Fitting of the numerical results to the experimental results must be done in a critical manner, i.e keeping in mind the physical meaning of the input parameters. In Figure (E.1) it is shown that the numerical models do not exactly represent the experimental results for levels of pre-compression. However, one can also argue these initial results are already quite satisfactory. Still, investigating some of the parameters is done via additional numerical simulations. This (small-scale) parametric study is focussed on the input parameters related to the simplified unit-unit interface. These interfaces are considered to be governing since all the non-linear behaviour is atributed to these two interfaces. Additionally, since the failure modes are mainly governed by the shear failure of these interfaces, parameters related to this failure mode are focal point of this part of the study. The different parameters corresponding to this failure mode are provided in Table (5.5).

A vast amount of numerical analyses are performed to investigate the possibility of a 'better' fit of the experimental results. It is not in the author's interest to describe all the different parameters adjusted, and their corresponding result. Therefore, the results of this study are summarized in Figure (E.9). In this figure the results related to the lowest pre-compression level are depicted. However, this picture is applicable for all three levels of pre-compression.

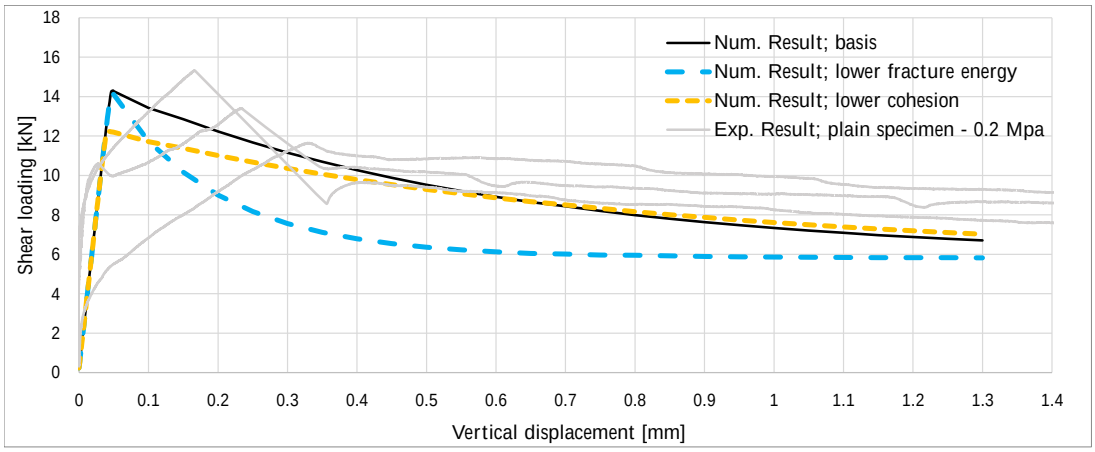

(a) Visualisation influence lowering cohesion c_0 and mode-II fracture energy G_f^{II}.

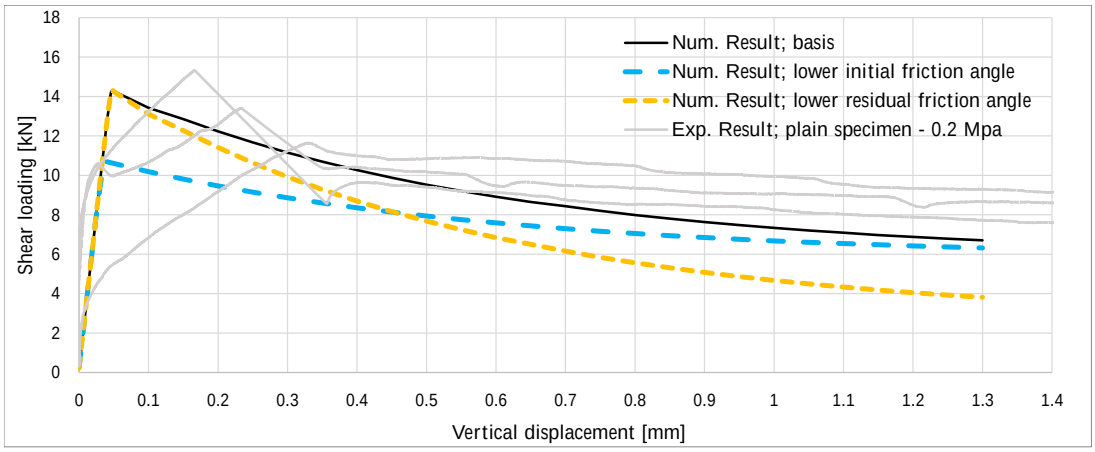

(b) Visualisation influence initial and residual friction angle (ϕ_0 and ϕ_r).

Figure E.9: Visualisation influence individual parameters shearing failure unit-unit interface.

Lowering of the cohesion simply lowers the maximum shear strength of the specimen, i.e. the peak shear force moves down. As to be expected from equation (4.7). The mode-II fracture energy is determined via two parameters (a and b). The former one influences the fracture energy over the different pre-compression levels, this is clear from equation (4.8). The second parameter (b) is the base value present for all levels of pre-compression. Lowering this value decreases the area under the force-displacement curve, see the blue curve in Figure (E.9a). Both the initial and residual friction angles influence the numerical results significantly. Lowering (or increasing) one of these input parameters will cause a 'rotation' of the numerical force-displacement curve along it's residual or peak strength, respectively. Lowering the residual friction angle results in a lower shear force at the horizontal tail of the curve. A lower initial friction angle lowers the peak resistance, but the residual shear strength, i.e. height of the horizontal tail, remains unchanged.

F

Digital Image Correlation retrofitted masonry beams

In this Appendix the DIC results of the retrofitted masonry beams are depicted. The von Mises strain field at peak resistance is shown for all specimen failing the non-flexural manner.

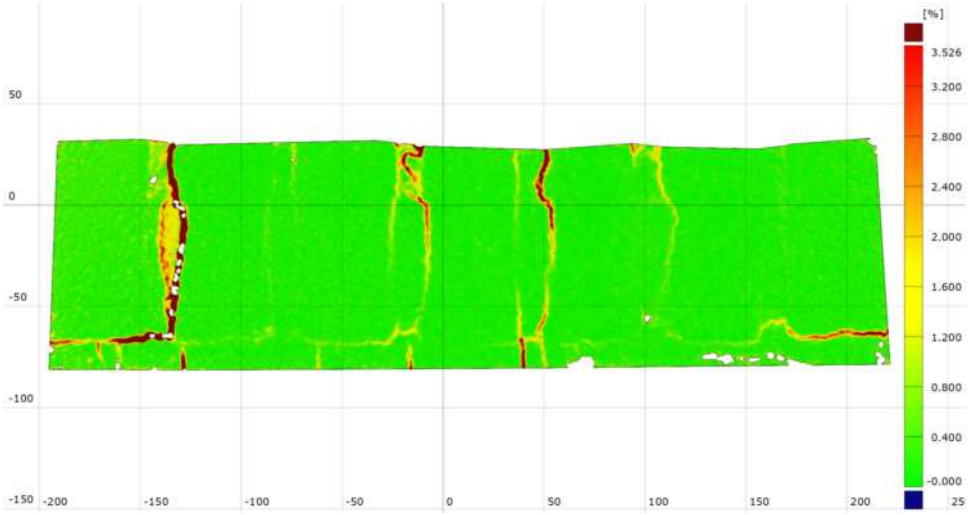

(a) 10 mm full bond overlay.

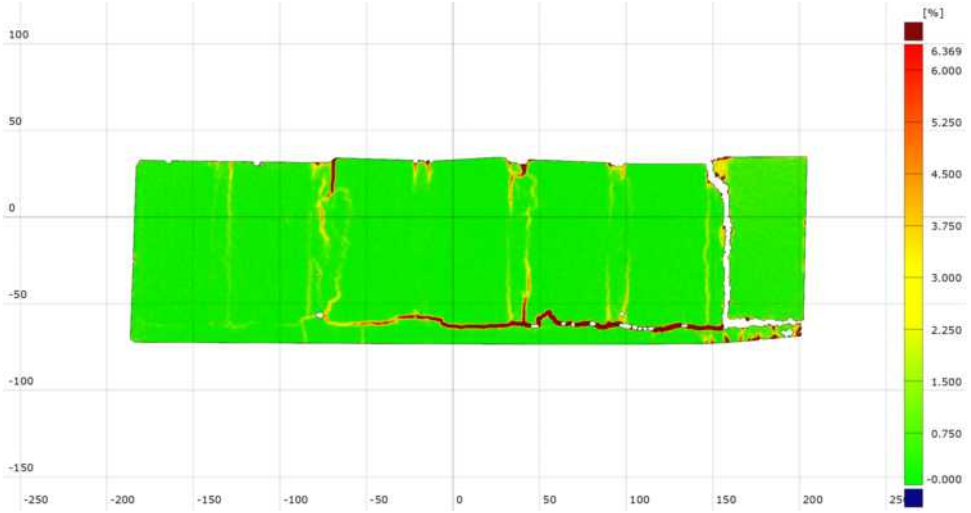

(b) 10 mm debonded overlay.

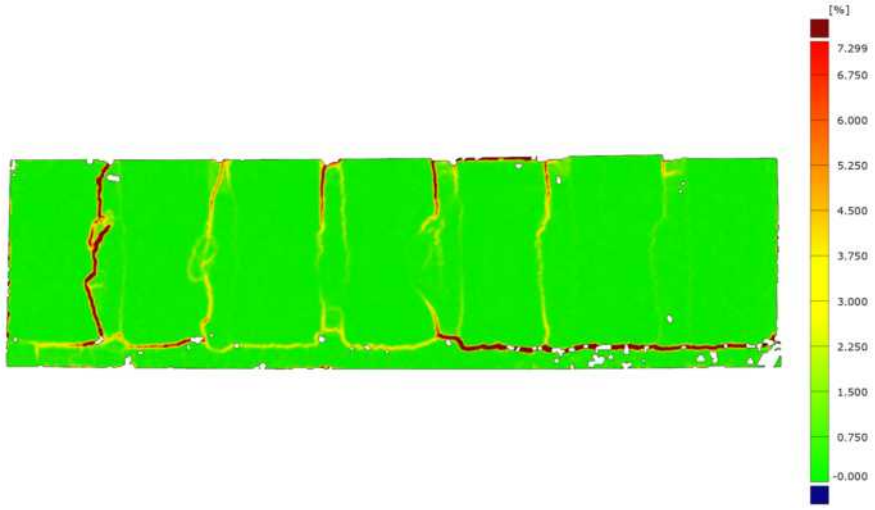

(c) 10 mm full bond overlay. Non-sealed curing conditions.

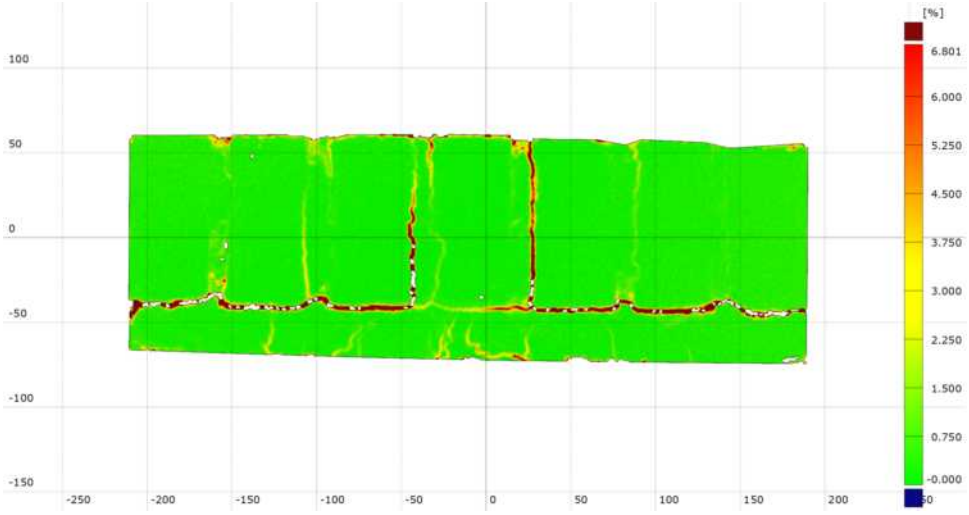

(d) 30 mm full bond overlay.

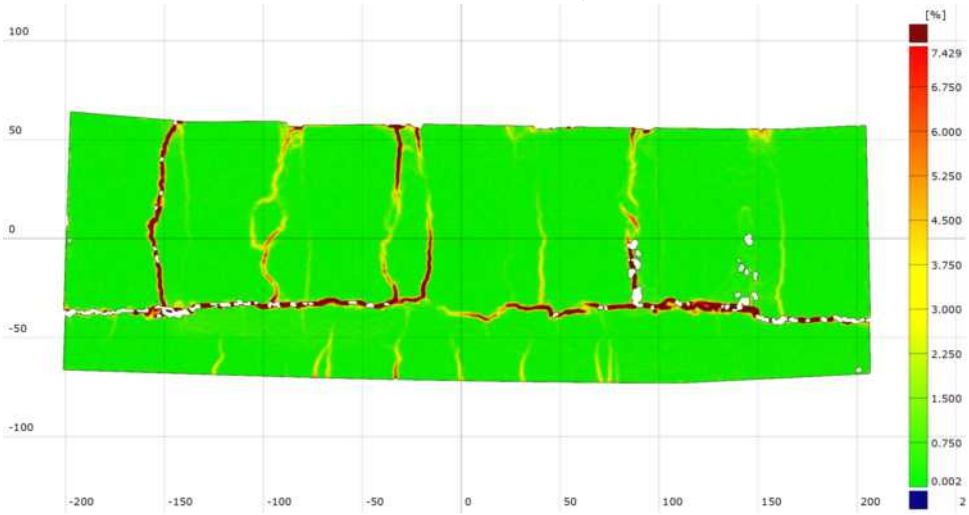

(e) 30 mm debonded overlay - A.

(f) 30 mm debonded overlay - B.

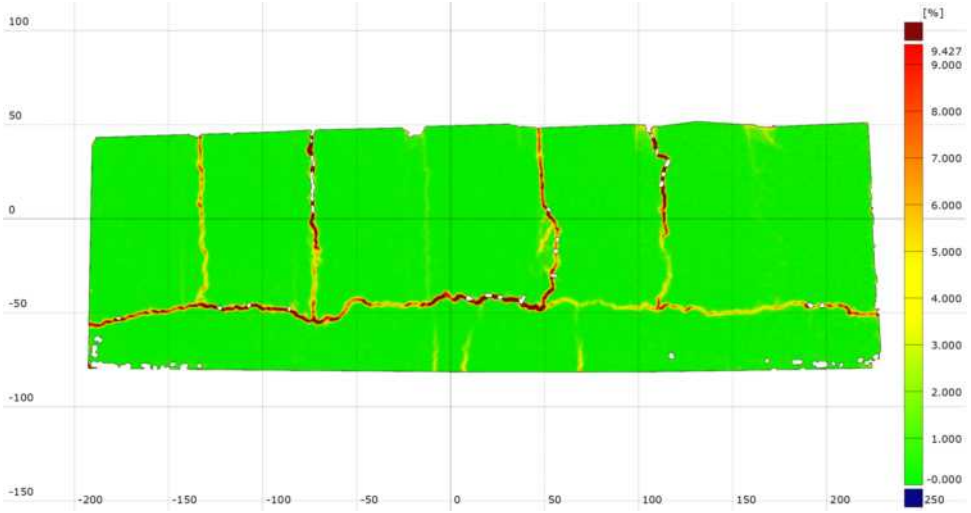

(g) 30 mm full bond overlay. Non-sealed curing conditions.

Figure F.1: Von Mises strain field DIC at peak resistance. Results for retrofitted masonry beams failed by debonding of masonry substrate.